



European Commission's 7th Framework Programme
Grant Agreement N°: 603521

Project Acronym: **PREFACE**

Project full title: **Enhancing prediction of tropical Atlantic climate and its impacts**

Instrument: Collaborative Project

Theme: ENV.2013.6.1-1 – *Climate-related ocean processes and combined impacts of multiple stressors on the marine environment*

Start date of project: 1 November 2013

Duration: 48 Months

Deliverable Reference Number and Title:

D 4.1

“Velocity, temperature, salinity variability in the equatorial Atlantic: Analysis of available moored observations from equatorial subsurface and PIRATA moorings including data from 23°W, 10°W, and 0°E acquired within different projects before PREFACE”

Lead work package¹ for this deliverable: GEOMAR

Organization name of lead contractor for this deliverable: GEOMAR

Due date of deliverable: 31.10.2014

Actual submission date: 23.10.2014

Project co-funded by the European Commission within the Seven Framework Programme (2007-2013)		
Dissemination Level		
PU	Public	X
PP	Restricted to other programme participants (including the Commission Services)	
RE	Restricted to a group specified by the Consortium (including the Commission Services)	

¹ Beneficiary = partner institute in PREFACE; see below: Table “List of beneficiaries”.

CO	Confidential, only for members of the Consortium (including the Commission Services)	
-----------	--	--

Contribution to project objectives – with this deliverable, the project has contributed to the achievement of the following objectives (see Annex I / DOW, Section B1.1.):

N.º	Objective	Yes	No
1	Reduce uncertainties in our knowledge of the functioning of TA ² climate, particularly climate-related ocean processes (including stratification) and dynamics, coupled ocean, atmosphere, and land interactions; and internal and externally forced climate variability.	X	
2	Better understand the impact of model systematic error and its reduction on s2d ³ climate predictions and on climate change projections.		X
3	Improve the simulation and prediction TA climate on seasonal, and longer time scales, and contribute to better quantification of climate change impacts in the region.	X	
4	Improve understanding of the cumulative effects of the multiple stressors of climate variability, greenhouse induced climate change (including warming and deoxygenation), and fisheries on marine ecosystems, functional diversity, and ecosystem services (e.g., fisheries) in the TA.		X
5	Assess the socio-economic vulnerabilities and evaluate the resilience of the welfare of West African fishing communities to climate-driven ecosystem shifts and global markets.		X

Deviation from planned efforts for this deliverable:

(PLEASE ONLY COMMENT IF THERE WERE DEVIATIONS FROM THE ORIGINAL PLAN⁴ IN PERSON-MONTHS PER BENEFICIARY⁵ AND/OR WORK PACKAGE FOR ACHIEVEMENT OF THIS DELIVERABLE)

List of Beneficiaries	
N.º	Name
1	UNIVERSITETET I BERGEN (UiB)
2	KOBENHAVNS UNIVERSITET (UCPH)
3	CENTRE EUROPEEN DE RECHERCHE ET DE FORMATION AVANCEE EN CALCUL SCIENTIFIQUE (CERFACS)
4	INSTITUT DE RECHERCHE POUR LE DEVELOPPEMENT (IRD)
5	METEO-FRANCE (CNRS-MF)
6	UNIVERSITE PIERRE ET MARIE CURIE - PARIS 6 (UPMC)

² TA = Tropical Atlantic

³ s2d = seasonal to decadal

⁴ See [List of person-months, nature and dissemination level of deliverable](#)

⁵ Beneficiary = partner institute in PREFACE; see below: Table “List of beneficiaries”.

7	HELMHOLTZ ZENTRUM FUR OZEANFORSCHUNG KIEL (GEOMAR)
8	INSTITUT FUER OSTSEEFORSCHUNG (IOW)
9	JOHANN HEINRICH VON THUENEN-INSTITUT, BUNDESFORSCHUNGSINSTITUT FUER LAENDLICHE RAEUME, WALD UND FISCHEREI (TI)
10	CHRISTIAN-ALBRECHTS-UNIVERSITAET ZU KIEL (CAU)
11	UNIVERSITA CA' FOSCARI VENEZIA (UNIVE)
12	WAGENINGEN UNIVERSITY (WU)
13	HAVFORSKNINGSINSTITUTTET (IMR)
14	UNI RESEARCH AS (Uni Research)
15	FUNDACIO INSTITUT CATALA DE CIENCIES DEL CLIMA (IC3)
16	UNIVERSIDAD COMPLUTENSE DE MADRID (UCM)
17	THE UNIVERSITY OF READING (UREAD)
18	INSTITUTO NACIONAL DE INVESTIGACAO PESQUEIRA (INIP)
19	MINISTRY OF FISHERIES AND MARINE RESOURCES (MFMR)
20	UNIVERSITY OF CAPE TOWN (UCT)
21	INSTITUTO NACIONAL DE DESENVOLVIMENTO DAS PESCAS (INDP)
22	INSTITUT NATIONAL DE RECHERCHE HALIEUTIQUE (INRH)
23	INSTITUT SENEGALAIS DE RECHERCHES AGRICOLES (ISRA-CRODT)
24	UNIVERSITE CHEIKH ANTA DIOP DE DAKAR (UCAD)
25	UNIVERSITE D'ABOMEY-CALAVI (UAC)
26	CENTRE DE RECHERCHES OCEANOLOGIQUES (CRO)
27	UNIVERSITY OF NIGERIA (UNN)
28	UNIVERSITE LIBRE DE BRUXELLES (ULB)

R. Kopte¹, P. Brandt¹, B. Bourlés², M. Rouault³

¹ *GEOMAR, Helmholtz Centre for Ocean Research Kiel, Germany*

² *Centre IRD de Brest, Plouzané, France*

³ *Mare Institute, University of Cape Town, Cape Town, South Africa*

Report summary

The variability of the tropical Atlantic has been investigated in a number of recent studies. Using repeated ship sections and moored ADCP observations of the upper ocean at 23°W Brandt et al. (2014) estimate the Equatorial Undercurrent (EUC) transport and analyze seasonal to interannual variations of the EUC (see section 2). A similar EUC transport estimate is derived by Johns et al. (2014) for the 10°W section. By combining observations at 23°W, 10°W, and 0°E Johns et al. (2014) describe the seasonal cycle and interannual variability of the EUC across the Atlantic basin (see section 3). The fate of the EUC in the eastern equatorial Atlantic was studied based on hydrographic and current data by Kolodziejczyk et al. (2014) (section 4). The mean meridional currents in the central and eastern equatorial Atlantic are investigated in a study by Perez et al. (2013), using shipboard ADCP measurements along 23°W and 10°W. On longer time scales, the tropical cells are found as the dominant feature of the meridional circulation in the upper 100 m (see section 5). Hummels et al. (2014) investigate the mixed layer heat budget at four locations within the Atlantic Cold Tongue (ACT) region. The inclusion of the diapycnal heat flux estimated from an extensive data set of microstructure profiles appears to be a dominant cooling term during the establishment of the ACT (see section 6). Furthermore, the temperature and salinity changes in the mixed layer during the onset of the cold tongue season 2011 have been studied by a dedicated cold tongue experiment and described in Schlundt et al. (2014) (see section 7).

These studies and associated field campaigns have been funded and supported by a number of international programs, for example as part of the recently completed Tropical Atlantic Climate Experiment (TACE, Brandt et al. (2013)), an international CLIVAR program (<http://www.clivar.org/organization/atlantic/tace>), and the ongoing Prediction and Research moored Array in the Tropical Atlantic (PIRATA, Bourles et al. (2008)), as well as the African Monsoon Multidisciplinary Analysis (AMMA) with its oceanographic components including EGEE (Gulf of Guinea climate and ocean circulation study, Bourles et al. (2007)).

In the following a brief description and update of the available database that has been acquired during the last years under support of the above-mentioned programs is given as well as a brief outlook on the next aspects of tropical Atlantic variability that will be investigated within PREFACE WP4.1.

1 Overview of current database and brief outlook

1.1. Database

1.1.1. Moored ADCP observations

An array of moorings equipped with ADCP current meters (among other instruments) has been maintained in the tropical Atlantic since end of 2001 with varying spatial and temporal coverage (see Fig. 1.1 for details). The long-term observations at 23°W have been maintained by GEOMAR (Germany)) and by IRD (Institut de Recherche pour le Développement, France, as part of PIRATA), those at 10°W have been installed by the University of Miami (US) and by IRD and at 0°E by the University of Miami with contribution by EGEE/AMMA and PIRATA (IRD). Furthermore, shorter observational periods are available at 35°W, and 21.5°W (installed by GEOMAR). Details on the instrumentation of the moorings can be found for example in Brandt et al. (2014) and Johns et al. (2014).

After the last mooring service in May 2014, continuous observations of the EUC now span more than a decade, indicating variability on a wide range of time scales, from high-frequency to interannual (Fig. 1.2).

Especially for the TACE period (2007-2011) the dataset of moored ADCP observations yields high spatial resolution. Simultaneous measurements are available at 23°W, 10°W, and 0°E for several latitudes (compare Fig. 1.1), which makes this period particularly interesting for the study of propagating signals along the equator.

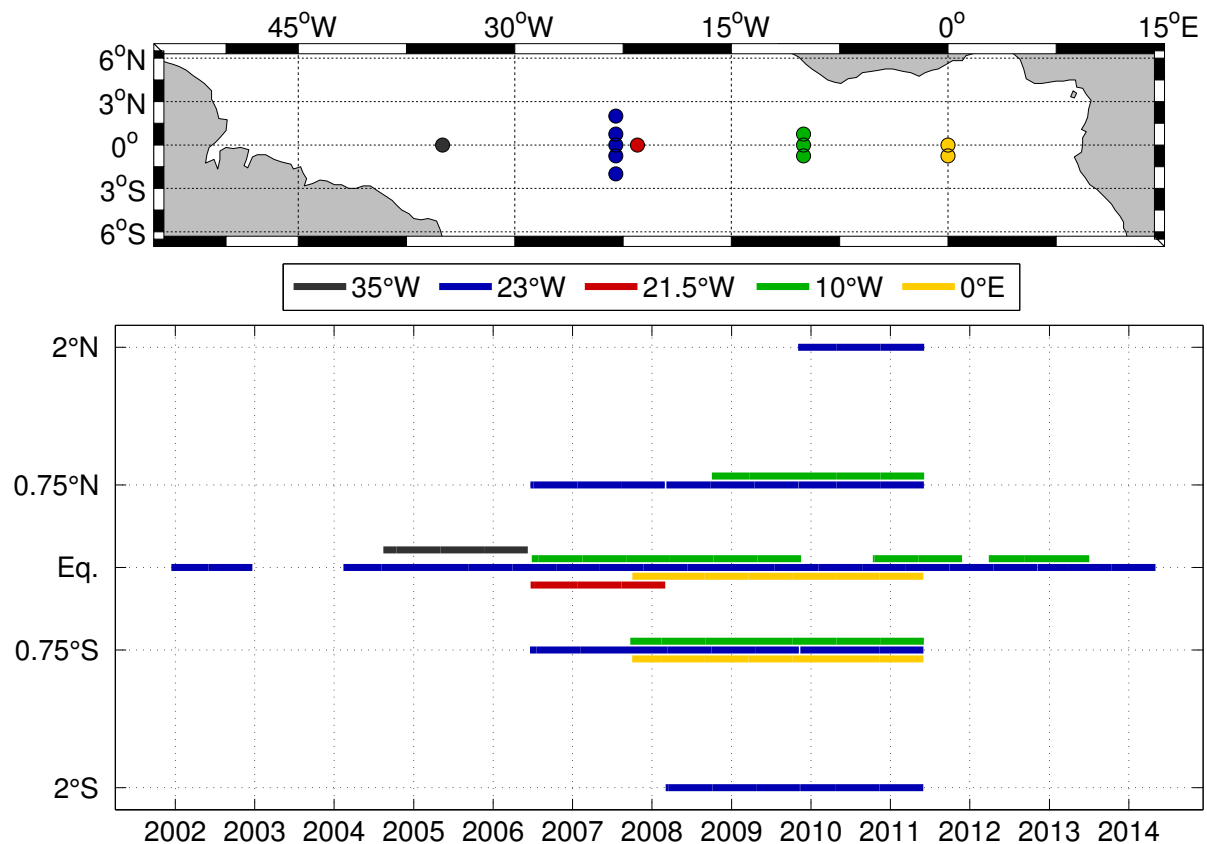


Fig. 1.1: *top*: Positions of moored ADCP observations in the tropical Atlantic, *bottom*: Timeline of observations.

Using repeated ship sections along 23°W and 10°W allows the calculation of EUC transport time series, as done by Brandt et al. (2014); Johns et al. (2014) (see section 2 and section 3, respectively). The updated EUC transport time series for 23°W is shown in Fig. 1.3, indicating strong intra-seasonal, seasonal and interannual variability.

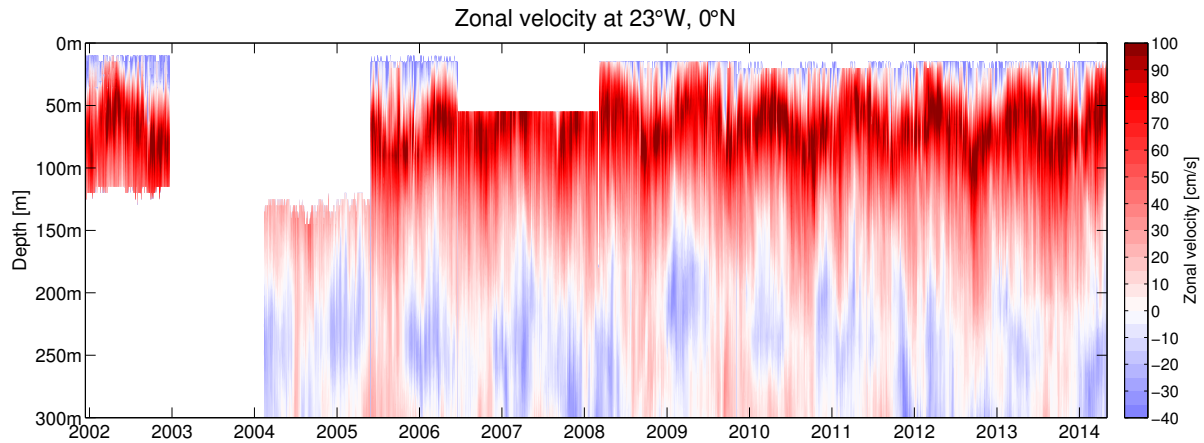


Fig. 1.2: Zonal velocity at 23°W, 0°N acquired between December 2001 and May 2014.

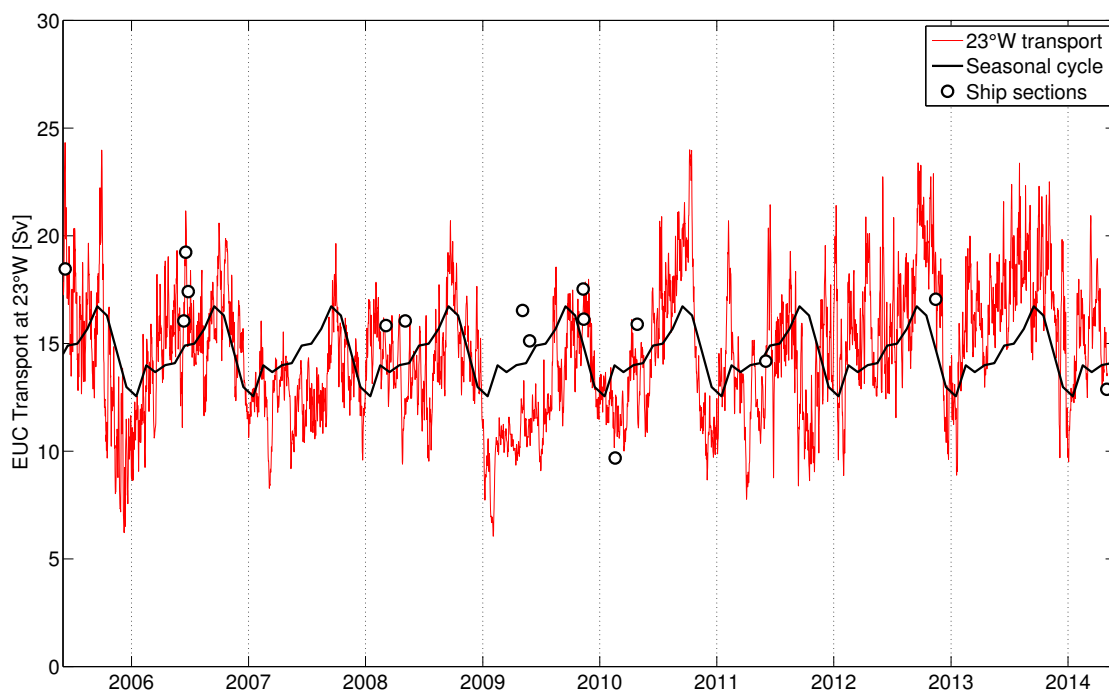


Fig. 1.3: EUC transport at 23°W updated for the last deployment period Nov 2012 - May 2014 (red line). The black line represents the monthly mean seasonal cycle. Circles denote transport estimates from ship sections. For details on the calculation see Brandt et al. (2014) or section 2.

1.1.2. PIRATA subsurface temperature and salinity

PIRATA buoys/moorings have collected surface meteorological data as well as temperature and salinity measurements of the upper ocean since 1998. Fig. 1.4 shows the available temperature and salinity data at the four equatorial mooring positions for this time period.

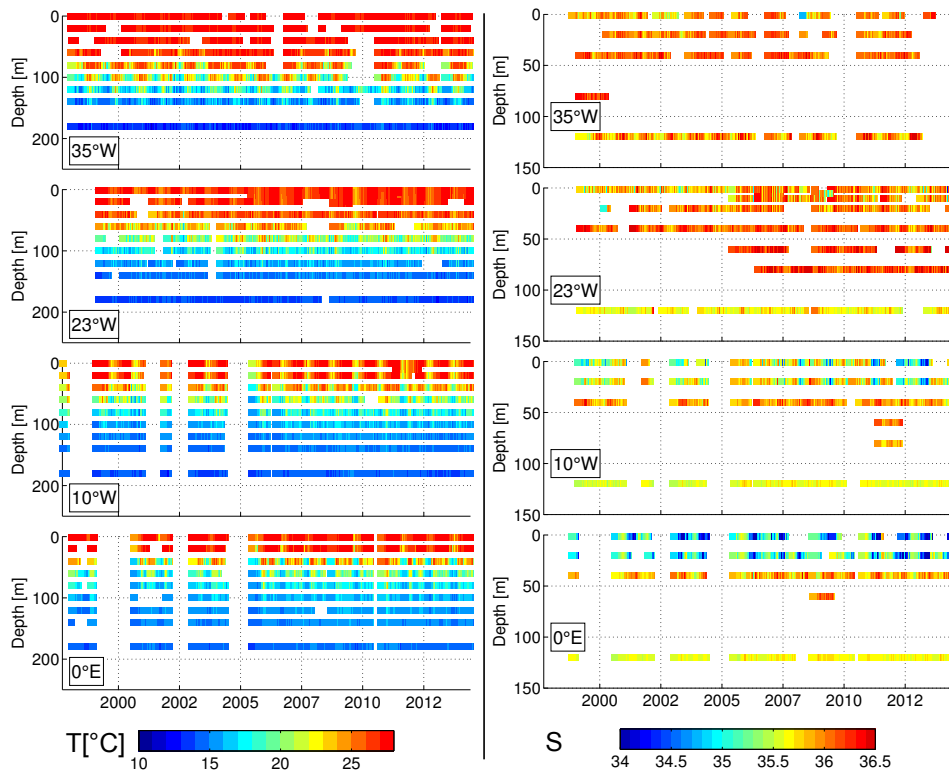


Fig. 1.4: Temperature (left) and salinity (right) time series as collected by the PIRATA moorings at 35°W, 23°W, 10°W, and 0°E. Note the different depth scales for the temperature and salinity plots.

1.1.3. Auxiliary datasets

Various satellite products can be used to obtain additional information on oceanic and atmospheric parameters in the region of interest, also on larger spatial scales. For, example, gridded maps (horizontal resolution of 0.25°) of sea level anomalies (SLA) are produced by *Ssalto/Duacs* and distributed by *Aviso*, with support from *Cnes* (<http://www.aviso.altimetry.fr/duacs/>) with several temporal resolutions, which can be used to study propagations of wave signals. Maps of SST are available either from NOAA (Optimum Interpolation-SST, a blend of satellite and in-situ measurements 1981-present, <http://www.ncdc.noaa.gov/sst>) or from the Tropical Microwave Imager TMI onboard the Tropical Rainfall Measuring Mission TRMM (since 1999, www.ssmi.com/tmi). Regarding wind stress, direction and speed, the Cross-Calibrated Multi-Platform (CCMP) Ocean Surface Wind Vector Analyses (Atlas et al. 2010) provide consistent, gap-free long-term time-series from July 1987 to June 2011.

1.2. Outlook

Within PREFACE WP4.1 the above-described database will be used to study the influence of equatorial Kelvin wave propagations on the equatorial and coastal upwelling regions.

Fig. 1.5 shows the presence of both eastward propagating Kelvin waves and westward propagating Rossby waves in the AVISO data (Fig. 1.5 *bottom left*). In a climatology of band passed SLA along an equatorial and southern wave track (Fig.

1.5 top left), continuous and recurrent eastward propagations as far as 15°S are apparent (Fig. 1.5 right).

In the next steps interannual variability in the Kelvin wave activity and its causes and consequences will be investigated, as well as related oceanic variability that might have been recorded in the moorings.

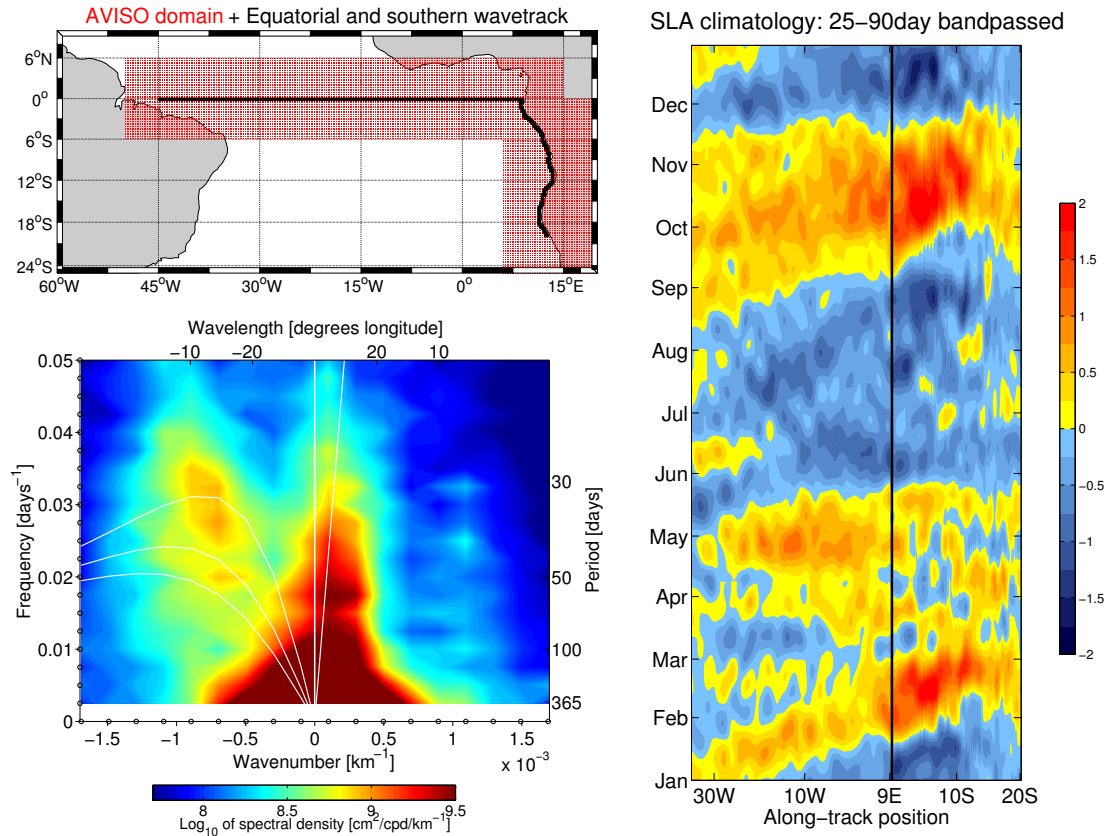


Fig. 1.5: **Top left:** Used AVISO domain and selected equatorial and southern wave track; **Bottom left:** Mean wavenumber-frequency spectrum of SLA from the equatorial belt (5°S-5°N) indicating the presence of Rossby and Kelvin waves; **Right:** Climatology (1994-2013) of SLA for the equatorial and southern wave track.

2 The Equatorial Undercurrent in the central Atlantic and its relation to tropical Atlantic variability

Authors: P. Brandt, A. Funk, A. Tantet, W.E. Johns, J. Fischer

The Equatorial Undercurrent (EUC) is among the strongest currents of the tropical ocean (Cromwell et al. 1954; Metcalf et al. 1962). It is generated at the subsurface under predominantly Easterlies in the equatorial Pacific and Atlantic Oceans and flows opposite to the wind following the depth-dependent eastward pressure gradient. The full three-dimensional structure of the EUC, which can only be explained by including viscous and inertial effects, is associated with strong horizontal flow divergences that are particularly responsible for the supply of the eastern equatorial upwelling (Qiao and Weisberg 1997; Schott et al. 1998). In the Atlantic, the EUC is supplied almost exclusively from the southern hemisphere. It transports oxygen-rich and high-saline water masses from the western boundary eastward (Brandt et al. 2011a; Kolodziejczyk et al. 2009; Metcalf et al. 1962; Schott et al. 1998). The transport of the Atlantic EUC contributes to both the equator-crossing warm water pathway of the meridional overturning circulation (Ganachaud and Wunsch 2000; Lumpkin and Speer 2003), and the subtropical cell connecting the subduction regions of the subtropics with the equatorial upwelling (McCreary and Lu 1994; Schott et al. 2004).

The Atlantic EUC undergoes a strong seasonal cycle with vertical excursions mainly associated with the vertical movement of the thermocline as revealed by moored observations at the equator (Brandt et al. 2006; Giarolla et al. 2005; Provost et al. 2004). Earlier moored observations from February 1983 to October 1985, while showing a seasonally varying vertical migration of the EUC core, could not reveal a repeated seasonal cycle of the EUC transport due to pronounced interannual variability (Weisberg et al. 1987). Shipboard observations are still inconclusive concerning the seasonal cycle of the Atlantic EUC transport mainly due to the presence of large intraseasonal variability associated with tropical instability waves (TIWs) and wind-generated Kelvin waves (Athie and Marin 2008; Bunge et al. 2007; Han et al. 2008b; Hormann and Brandt 2009; Polo et al. 2008).

In this study by Brandt et al. (2014), additional information from moorings deployed at 23°W off the equator at 0°45'S/N as well as from 20 ship cruises along the 23°W meridian will be used to investigate the seasonal to interannual variability of the EUC. A particular focus is on key characteristics of the current such as volume transport, core velocity, core depth, and core latitude.

2.2. Data and methods

2.2.1. Shipboard data

Direct shipboard velocity observations along meridional sections crossing the equator between 23°W and 28°W were used. In total 20 sections of zonal velocity taken during different research cruises from 1999 to 2011 were analyzed. From these sections a subarea with a latitudinal range from 1°12'S to 1°12'N and a depth range from 30 to 300m was selected. The subarea covers almost the full extent of the EUC

and includes the locations of the three moorings that will be discussed in the next section (Fig. 2.1). The mean EUC core at 23°W is shifted slightly southward with respect to the equator to about 0°10'S and is located at a depth of about 87 m (Fig. 2.1). We assume that the shipboard zonal velocity sections, which do vary due to the presence of oceanic variability on intraseasonal to interannual time scales, contains the dominant EUC variability pattern. We will use in the following the dominant variability pattern of the zonal velocity from the shipboard velocity section to interpolate and extrapolate the moored observations.

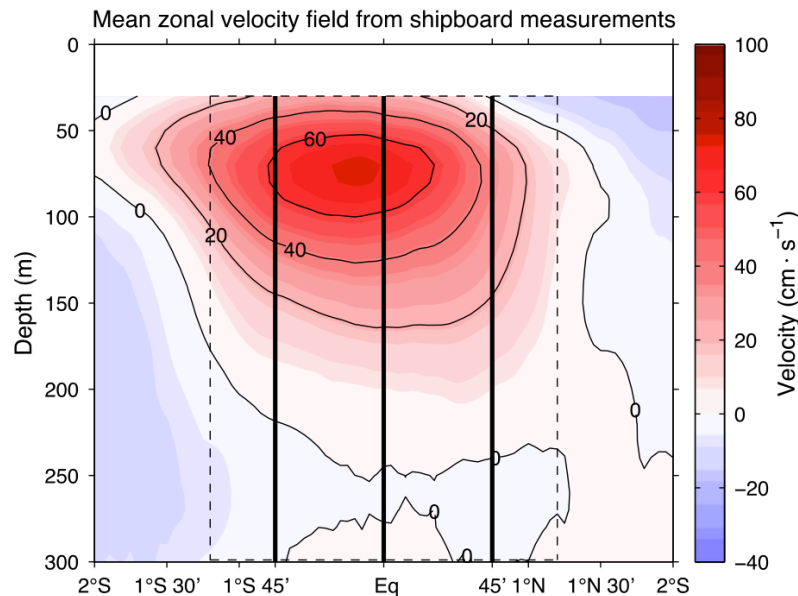


Fig. 2.1: Mean zonal velocity from 20 meridional ship sections taken from 1999 to 2011 between 23°W and 28°W. Vertical black lines mark the position of the moored observations, the dashed box marks the domain for which the velocity field will be reconstructed from moored observations.

2.2.2. Mooring data

The second dataset was obtained by an equatorial current meter mooring array along 23°W during the period May 2005 to June 2011. The mooring array consists of three moorings located at 0°45'S, equator, and 0°45'N, and was first deployed in June 2006, serviced in February 2008 and October 2009, and finally recovered in June 2011. To extend the available time series, we also use data from the equatorial current meter mooring deployed from May 2005 to June 2006. All velocities were detided using a 40h low-pass filter and subsampled to 12 h intervals. Velocity data from the equatorial mooring were previously used i) to study the mean zonal flow, its seasonal cycle, as well as intraseasonal velocity fluctuations (Brandt et al. 2006), ii) to validate high-resolutions models used to analyze the generation of TIWs (von Schuckmann et al. 2008), and iii) to analyze the interannual variability of EDJs (Brandt et al. 2008; Brandt et al. 2011b; Brandt et al. 2012). Here, for the first time, we will use off-equatorial velocity time series to obtain an integral view on the seasonal to interannual variability of the EUC and its relation to tropical Atlantic variability.

2.3. Methods

2.3.1. Reconstruction of the velocity field using HEOFs

The goal here is to construct time series of two-dimensional (latitude-depth) velocity fields from moored zonal velocity data at three locations. The construction requires an interpolation between the moorings and an extrapolation toward the boundary of the domain. To avoid excessive poleward extrapolation of the velocity fields from the mooring positions located at 0°45'S/N, we restricted the latitudinal range of the domain to 1°12' S/N. The inter-/extrapolation scheme is based on the variability patterns obtained from the 20 available ship sections. Those ship sections are assumed to represent well the variability of the zonal velocity field of the EUC. Here, we apply the Hilbert transformation (Barnett 1983) to the zonal velocity fields of the ship sections

$$\mathbf{S20} = S20 + iH(S20) \quad (1)$$

where $S20(y,z,t)$ is the three-dimensional velocity field with the spatial coordinates y and z being latitude and depth, and t referring to the time of the 20 ship sections, H is the Hilbert transform, and i the imaginary unit. By applying an empirical orthogonal function (EOF) analysis to $\mathbf{S20}$, we obtained Hilbert EOFs (HEOFs) that are composed of real and imaginary pattern (Fig. 2.2). This technique is here more suitable than traditional EOF analysis because it is capable of detecting moving features in space, like e.g. north/south or up/down migration of the EUC core. The first three patterns explain 83% of the variance contained in the ship sections. They are statistical patterns that nevertheless contain some features which correspond to EUC dynamics. For example, the first pattern that explains more than 50% of the velocity variance describes a slightly tilted vertical motion of the velocity field; the second pattern describes a more latitudinal displacement of the EUC.

To reconstruct a vector field from the moored observations, a regression is done of the HEOF patterns onto the moored observations. To find the number of leading HEOFs to be used for the reconstruction, a good compromise has to be found between simplicity and explained variance. Here we will use the first three HEOFs composed of the six patterns shown in Fig. 2.2.

2.3.2. Reconstruction of the EUC transport using the optimal width method

When interested only in the EUC transport, here defined as the integral of u with $u > 0$ over latitude and depth within the domain covering 30-300 m depth and 1°12'S-1°12'N, the optimal width (OW) method can be applied. This method is based on the calculation of the latitudinally integrated zonal velocity, $U(z,t)$, defined as the integral of u with $u > 0$ over a given latitude range. The principle of the method is to find optimal widths W_i such that:

$$U(z,t) = W_N u_N(z,t) + W_{eq} u_{eq}(z,t) + W_S u_S(z,t) \quad (2)$$

where $u_i(z,t)$ are zonal velocities with the index N/S referring to the northern/southern mooring position at 0°45'N/S and the index eq to the equatorial mooring position. The constant widths W_i are calculated by regression of the latitudinally integrated zonal velocity from the ship sections onto the zonal velocities of the ship section at the three mooring positions. The obtained latitude ranges corresponding to W_N , W_{eq} , and

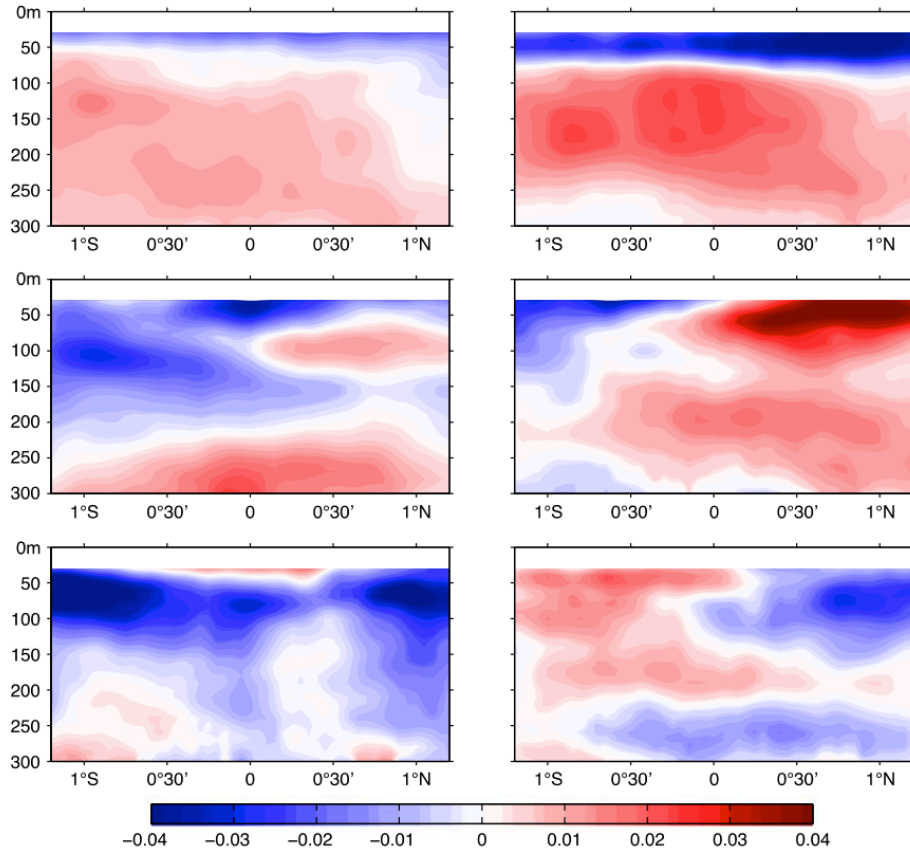


Fig. 2.2: First three HEOF patterns as calculated from 20 ship sections. Row 1-3 corresponds to HEOF 1-3; left/right column corresponds to real/imaginary pattern. HEOF 1, 2, and 3 explains 55, 16, and 12 % of the variance contained in the shipboard velocity sections.

W_S are 0.76, 0.74, and 0.79 degree latitude. In an equipartitioned domain each width would be 0.8 degree latitude. Consequently, the width of the equatorial mooring is underweighted and the sum of the three widths is less than the widths of the whole domain, which can be expected as the flow of the EUC becomes weaker toward the northern and southern boundary.

To reconstruct $U(z,t)$ from the mooring time series, zonal velocity measurements at each mooring position are required for the whole depth range (30 m to 300 m). This is usually not the case. Here we chose to fill such gaps that are also present during other mooring periods and at other locations with data obtained from the HEOF reconstruction. Integration of $U(z,t)$ over depth yields the EUC transport that can be compared with the reconstruction using the HEOF method.

2.3.3. Method validation

Here, we will use zonal velocity data from 20 meridional shipboard sections to validate the different methods applied to reconstruct full velocity sections (HEOF method) as well as EUC transport (HEOF and OW method) from moored observations. For this validation the zonal velocity data at the mooring positions are extracted from shipboard sections. The two methods are then applied to the extracted zonal velocity data and compared with results obtained from the full shipboard zonal velocity sections. We will only compare EUC transport values

calculated from the ship sections with values from the reconstructions. The EUC transport used for the validation represents an integral value of the zonal velocity variability within the section and is less affected by oceanic variability on small spatial scales. Fig. 2.3a shows the change in quality of the EUC transport calculation from the HEOF reconstruction when increasing the number of used HEOFs from one to three. The RMS difference between reconstructed and observed EUC transport reduces from 2.62 Sv when using only the first HEOF to 0.79 Sv when using the first three HEOFs, while the regression coefficient approaches 1 for larger numbers of used HEOFs. Using more than three HEOFs does not significantly improve the results. The RMS difference between reconstructed and observed zonal velocity when using the first three HEOFs is for most of the domain smaller than 5 cm/s with larger values (up to 15 cm/s) near the surface particularly near the northern and southern boundary of the domain.

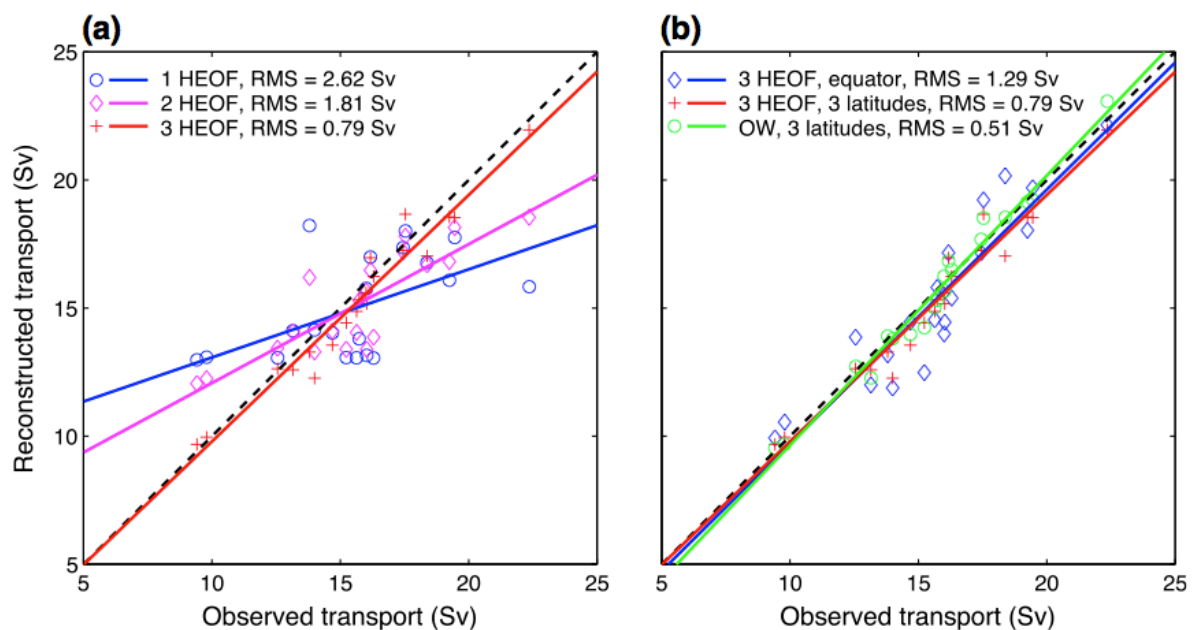


Fig. 2.3: Reconstructed versus observed EUC transport as calculated from shipboard zonal velocity data. (a) Reconstruction from zonal velocity data from the 3 mooring positions ($0^{\circ}45'N$, eq., $0^{\circ}45'S$) using the first (blue circles), the first two (purple diamonds), and the first three (red plus signs) HEOFs. (b) Reconstruction from zonal velocity data from the equator only (blue diamonds) and from the 3 mooring positions ($0^{\circ}45'N$, eq., $0^{\circ}45'S$) using the HEOF method (first three HEOFs) and from the 3 mooring positions using the OW method (green circles). The solid lines in (a) and (b) are linear regressions with RMS values as given in the legend.

For the mooring period May 2005 to June 2006 only data from the equatorial mooring are available. We will use the HEOF method also in this case to reconstruct the full zonal velocity section. Fig. 2.3b shows the quality of the HEOF reconstruction when using only data from the equator in comparison to the case when using data from $0^{\circ}45'N$, the equator, and $0^{\circ}45'S$. While the regression coefficient in both cases is similarly close to one, the RMS difference between reconstructed and observed EUC transport is clearly increased when using only equatorial data. Compared to the HEOF reconstruction the OW reconstruction results in a smaller RMS difference and in a regression coefficient even closer to one. In general, we can say that the OW method is more stable and slightly better reproduces EUC transport variability.

However, the HEOF method additionally reconstructs the full zonal velocity field and thus allows studying further characteristics of the zonal velocity field within the whole domain such as maximum zonal velocity, latitude and depth of EUC.

Fig. 2.4 shows time series of the EUC transport calculated using three different methods: 1) HEOF method with the first three HEOF applied to equatorial mooring data only, 2) HEOF method with the first three HEOF applied to data from all three moorings; and 3) OW method applied to data from all three moorings. As suggested by the method validation using shipboard velocity data, method 2 and 3 are very close; the RMS difference between both curves is $RMS = 0.65$ Sv, which can be understood as an uncertainty of the EUC transport calculation. Method 1 shows some systematic differences and increased RMS differences with respect to method 2 and 3: $RMS = 1.07$ Sv and $RMS = 1.09$ Sv, respectively. We particularly note an increase in the strength of intraseasonal fluctuations when using only equatorial mooring data for the reconstruction, the seasonal and interannual variability being less affected. Larger deviations between transport values from ship sections and reconstructions from moored observations (Fig. 2.4) are likely due to differences in methods used to derive these values: ship sections are snapshots that are completed during a day or two, while reconstructions are calculated from simultaneous and 40-h low-pass filtered moored velocity profiles. In the following we will use for the analysis of the seasonal cycle a 5 year-long time series (June 2006-June 2011) from both methods, method 2 and 3. For the analysis of interannual variability we will use a ~6-yr-long time series obtained from a combination of method 1 (May 2005-June 2006) and method 2 (June 2006-June 2011).

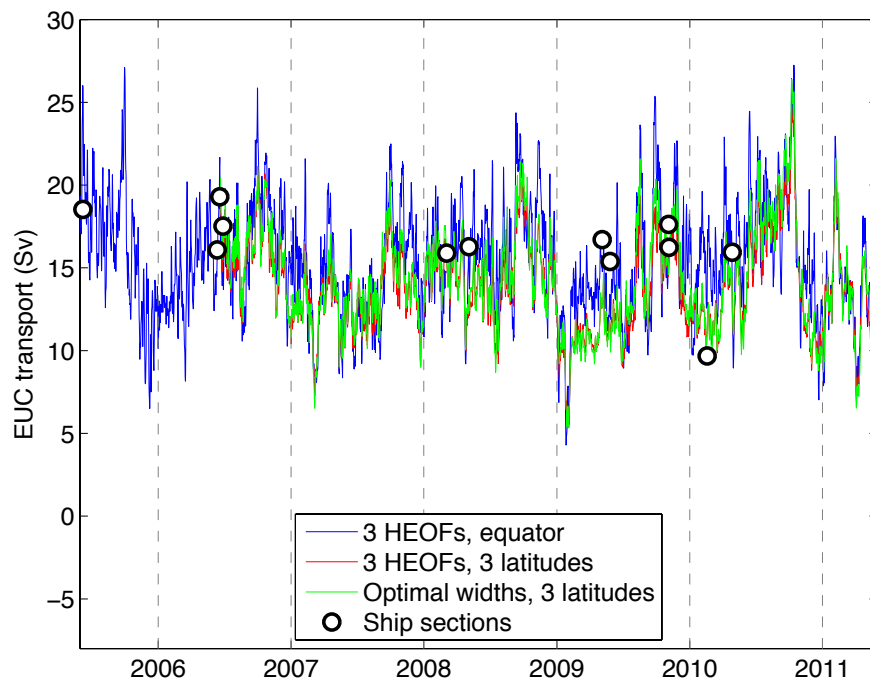


Fig. 2.4: EUC transport as calculated by applying the HEOF method with the first three HEOFs and using data from the equatorial mooring only (blue line) and from all three moorings (red line) and by applying the OW method and using data from all three moorings (green line). Also included are EUC transport values from meridional ship sections (circles).

2.4. EUC variability at 23°W

Previous observational studies on the EUC variability in the Atlantic were based on single equatorial moorings (Brandt et al. 2006; Giarolla et al. 2005; Hormann and Brandt 2009; Provost et al. 2004). Here, we want to focus on seasonal to interannual variability of different EUC characteristics such as EUC transport (Fig. 2.5), EUC core depth (Fig. 2.6), EUC maximum core velocity (Fig. 2.7), and EUC core latitude (Fig. 2.8). The estimation of these characteristics requires additional information from off-equatorial moorings. The position of the core of the EUC is here defined as the mean velocity-weighted latitude and depth of all grid points with velocities larger than 20 cm/s. This definition is applied in order to produce more stable results for the core position than one would obtain by just picking the position of maximum velocity. A variation of the velocity threshold between 10 and 30 cm/s showed that the obtained results depend only weakly on the choice of this threshold: the mean EUC core moves slightly downward/upward and northward/southward for a smaller/larger threshold.

The EUC transport is dominated by a seasonal cycle ranging from about 18 Sv in boreal autumn (maximum in September) to about 12 Sv in late boreal winter (minimum in March). The absolute extremes of the EUC transport time series are in October 2010 with about 25 Sv and in February 2009 with about 5 Sv (Fig. 2.5a). The spectrum of the EUC transport time series (not shown) has enhanced energy in the 30 to 70 days period range. While at shorter periods (30 to 40 days) TIWs might play an important role (Athie and Marin 2008; Brandt et al. 2006), longer periods (50 to 70 days) were identified by Han et al. (2008b) and Polo et al. (2008) to be associated with the presence of low baroclinic mode Kelvin waves. The strong intraseasonal fluctuations hamper the identification of the seasonal cycle of the EUC transport (and even more of its interannual variations) from shipboard observations (Fig. 2.5a). Shipboard observations show substantial variability during early boreal summer which is in general agreement with large standard deviation of monthly means from mooring data during the same season.

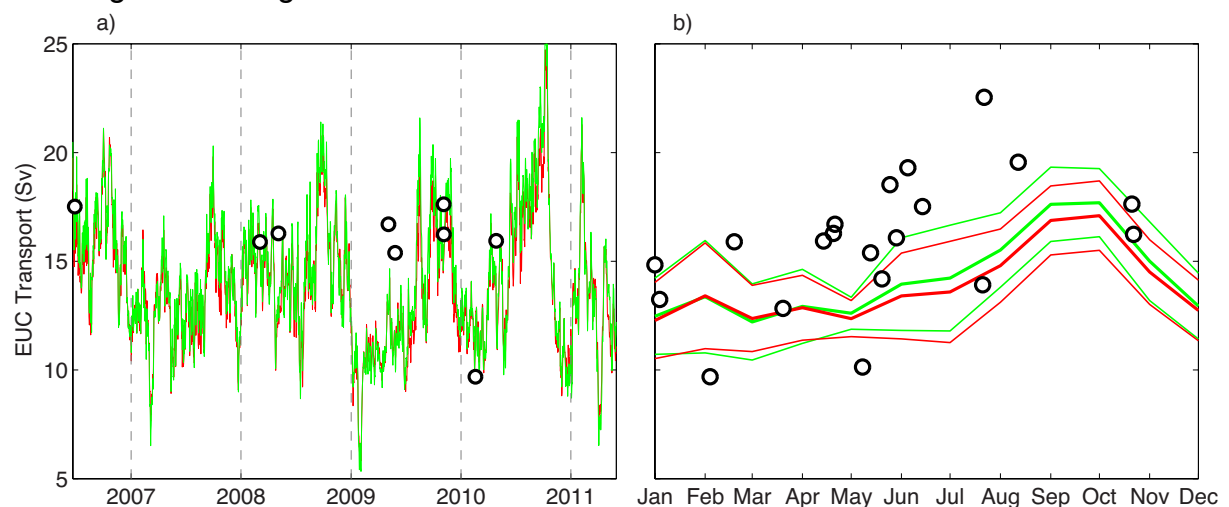


Fig. 2.5: (a) EUC transport and (b) its mean seasonal cycle with standard deviation of monthly means (thin lines) as obtained from the HEOF method (red lines) and the OW method (green lines). Shipboard measurements are marked by circles. The mean EUC transports from the HEOF and OW methods are 13.8 Sv and 14.2 Sv, respectively.

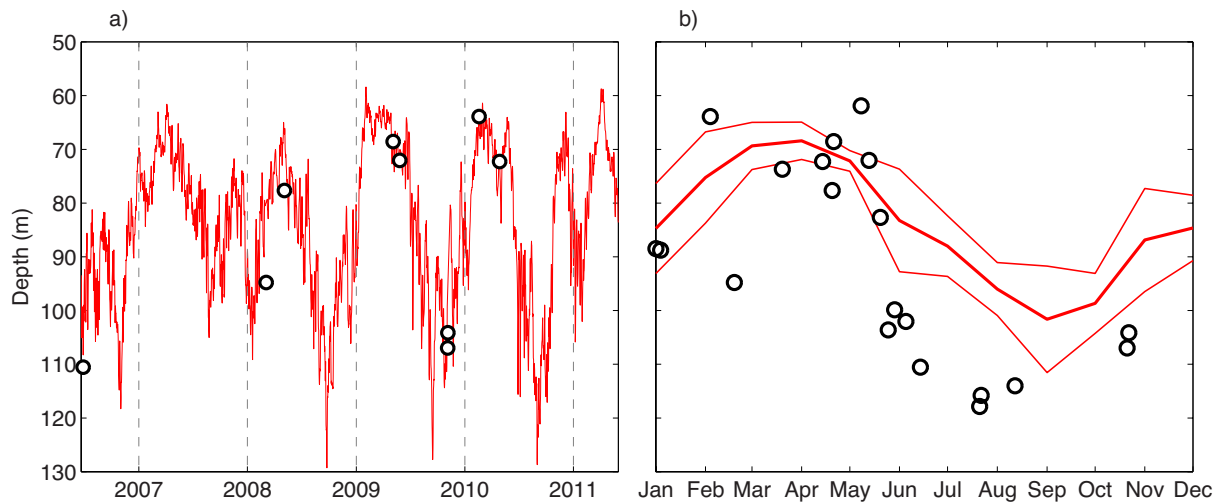


Fig. 2.6: (a) EUC core depth and (b) its mean seasonal cycle (thick line) with standard deviation of monthly means (thin lines) as obtained from the HEOF method. Shipboard measurements are marked by circles. The mean EUC core depth is 82 m.

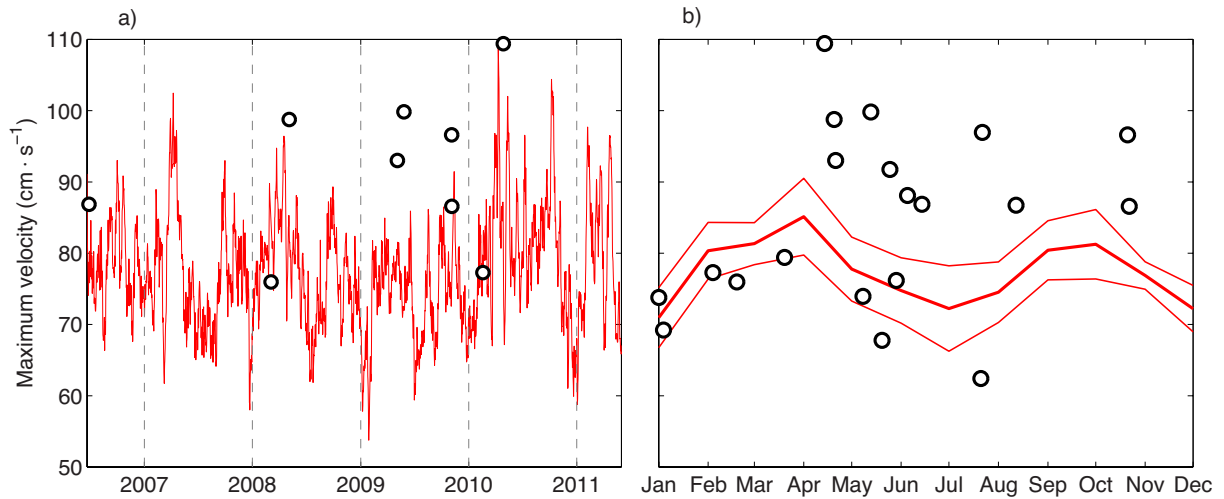


Fig. 2.7: (a) EUC maximum core velocity and (b) its mean seasonal cycle (thick line) with standard deviation of monthly means (thin lines) as obtained from the HEOF method. Shipboard measurements are marked by circles.

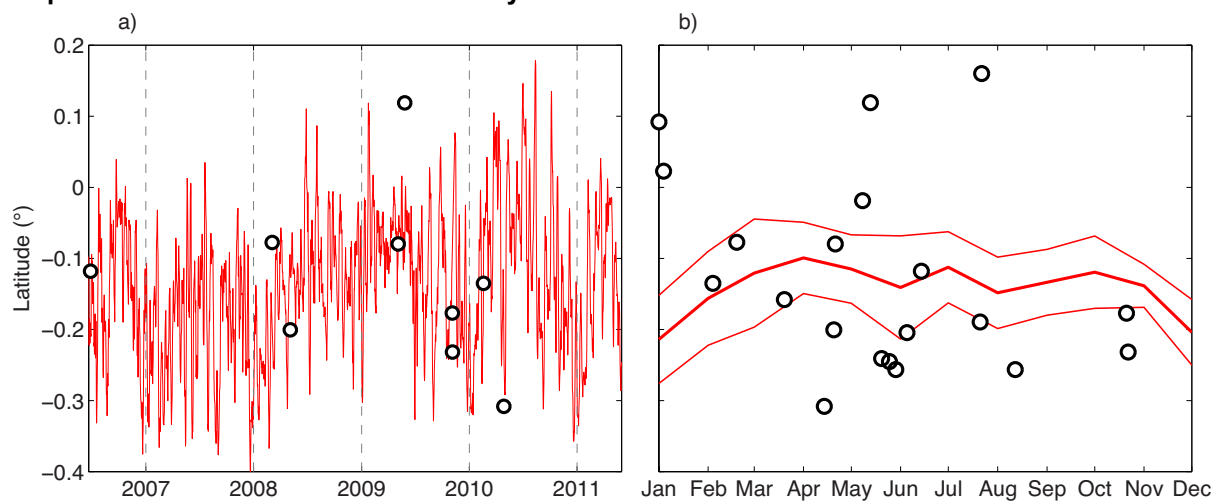


Fig. 2.8: (a) EUC core latitude and (b) its mean seasonal cycle (thick line) with standard deviation of monthly means (thin lines) as obtained from the HEOF method. Shipboard measurements are marked by circles.

An even more pronounced seasonal cycle can be found for the EUC core depth (Fig. 2.6). As similarly found by analyzing only equatorial mooring data (Brandt et al. 2006; Giarolla et al. 2005; Provost et al. 2004), the EUC is shallowest during March/April and deepest during September. Deepest EUC in the shipboard dataset is found in July/August with no measurements in September. Remarkable is the pronounced seasonal cycle of the EUC core depth in 2009 and 2010 and the weak seasonality in 2007. Years of strong (weak) seasonal cycle of EUC core depth do correspond to years with strong (weak) EUC transport seasonal cycle (cf. Fig. 2.5a and Fig. 2.6a). There seems to be a systematic difference between EUC core depth seasonal cycle from shipboard observations and moored observations during boreal summer and fall (Fig. 2.6b), but the few available shipboard sections do not unambiguously allow identifying the origin of this difference. In fact, boreal summer-fall is characterized by the largest standard deviation of monthly means, indicating strong year-to-year variations during that period. The July/August core depths from earlier ship sections, ranging between 110 and 120 m depth (Fig. 2.6b), are still in the range of values obtained from moored observations for July/August of the years 2008 to 2010 (Fig. 2.6a), indicating that the climatology derived from the shorter mooring period may not represent the true or 'typical' climatology of the core depth over a longer period of time. The quality of the reconstructed zonal velocity fields does not seem to be an issue since the comparison between shipboard and moored values for simultaneous measurements (Fig. 2.6a) shows generally good agreement between shipboard and moored EUC core depths.

The reconstruction of the zonal velocity field using the first three HEOFs inherently includes a smoothing of the velocity field. This becomes obvious when comparing observed and moored EUC maximum core velocities: values taken from reconstructed fields are in general biased low compared to values taken from shipboard sections. However, the time series of EUC maximum core velocity is dominated by intraseasonal fluctuations (Fig. 2.7a) with a weak semiannual cycle superimposed (Fig. 2.7b). Within the seasonal cycle maximum core velocities are found in April when the EUC core is shallowest and in September/October when the EUC core is deepest.

The mean EUC core is slightly shifted south with respect to the equator (Fig. 2.8): mean position is the same as obtained from the shipboard mean, i.e. $0^{\circ}10'S$. There is no clear seasonal cycle (EUC core is farthest south during December/January), but there is interannual variability in the latitudinal excursion of the EUC core with anomalous southward displacement during 2007 and anomalous northward displacement during 2009/2010 (Fig. 2.8).

2.5. Summary and discussion

As part of the TACE program a current meter mooring array was installed in the equatorial Atlantic along $23^{\circ}W$ for a 6-year period from 2005 to 2011. It was aimed to observe the seasonal to interannual variability of the EUC. Within the seasonal cycle the EUC transport is minimum in March and maximum in September. It shows a relatively slow increase from March to September and a more rapid decrease from October to December. The depth variations of the EUC core show a more harmonic

cycle with shallowest EUC core in March and deepest EUC core in September. Seasonal variations of the maximum velocity of the EUC show instead a semiannual cycle with velocity minima in January and July and velocity maxima in April and September. Due to strong decrease in the EUC cross-section, the EUC transport is smallest in spring during the phase of maximum core velocity.

The results regarding EUC core depth and maximum velocity are in general agreement with results obtained by analyzing a subset of the equatorial velocity time series (Brandt et al. 2006; Provost et al. 2004). Previous analyses of shipboard meridional velocity sections crossing the equator at different longitudes were not completely conclusive regarding the seasonal cycle of the EUC transport (Hormann and Brandt 2007; Kolodziejczyk et al. 2009). Shipboard measurements along 35°W showed maximum EUC transport values in September with an indication of a secondary maximum in April and large variability in early boreal summer (Hormann and Brandt 2007). The analysis of 18 shipboard sections at 10°W revealed a maximum EUC transport slightly earlier in the year during August and EUC transport minima during March and November, suggesting the presence of semiannual transport variations in addition to the dominant annual harmonic (Kolodziejczyk et al. 2009).

As a last point, we want to mention the meridional migration of the EUC core. This EUC characteristic shows only weak seasonality, but instead stronger interannual variations with an anomalous southward position of the EUC core during 2007 and an anomalous northward position during 2009/2010 (Fig. 9). The timescale of such variability would be in general agreement with the 4.5-yr deep jet cycle (Brandt et al. 2011b) that was found to be consistent with equatorial basin mode oscillations (Greatbatch et al. 2012). However, to study low-frequency EUC variability that might result from the interaction of equatorial deep jets propagating their energy upward with the energetic near-surface flow, longer moored time series and/or improved numerical simulations are required.

3 Zonal structure and seasonal variability of the Atlantic Equatorial Undercurrent

Authors: W.E. Johns, P. Brandt, B. Bourlès, A. Tantet, A. Papapostolou, A. Houk

The Equatorial Undercurrent (EUC) is a quasi-permanent feature of the zonal equatorial circulation in both the Atlantic and Pacific oceans. Its main role in both oceans is to supply thermocline waters from the shallow subduction zones in the subtropics to the main upwelling zones in the central and eastern part of the equatorial basins (Schott et al. 1998; Wacongne and Piton 1992).

While in the Pacific Ocean the EUC is rather well-described from over a decade of intensive shipboard and time-series observations in the TOGA and TAO/TRITON programs (Johnson et al. 2002), the EUC in the Atlantic has remained more poorly sampled and neither its mean structure across the basin or its seasonal-to-interannual variability is understood. Particularly in the eastern part of the basin, where the EUC decays and appears to exhibit strong variability in its eastward penetration, observations are sparse and very few time series measurements have been collected. In the Pacific, the variability of the EUC is closely linked to sea surface temperature variations in the eastern cold tongue region on both seasonal and interannual (El-Niño) time scales, and it is anticipated that similar behavior may occur in the Atlantic in association with the seasonal cycle and the analogous “Atlantic Niño” phenomenon.

Despite the more limited measurements of the EUC in the Atlantic, a substantial increase in the understanding of the EUC in the western and central Atlantic has developed over the past decade. At two longitudes, near 35°W and 23°W, a sufficient number of shipboard transects across the equator have now been acquired to afford reasonable estimates of the mean EUC structure and transport at these locations (Brandt et al. 2006; Schott et al. 2003). At 35°W the EUC transports approximately 20 Sv above the density surface $\sigma_\theta = 26.8$, whereas by 23°W this transport is reduced to approximately 14 Sv. The core of the EUC is at 100 m depth at 35°W and shoals to about 85 m depth at 23°W. At both locations instantaneous core velocities are typically in the range of 80-100 cm/s.

Farther east, at 10°W, available estimates of the EUC transport from cross-equatorial sections suggest a mean value near 12 Sv (Kolodziejczyk et al. 2009), which is surprisingly similar to the 14 Sv value at 23°W in view of the expected eastward decay of the EUC in the Atlantic. Here the EUC has a core depth near 60 m, having shoaled some 40 m from the western part of the basin.

Farther yet to the east the available measurements are sparse and estimates of the EUC transport vary widely. Reported estimates from individual cruises include those of Mercier et al. (2003) at 7°W (24.6 Sv) and 2°E (12.6 Sv), Gouriou and Reverdin (1992) at 4°W (10.2 Sv), and Bourlès et al. (2002) at 0°E (6 Sv). At 0°E, Bourlès et al. (2002) found the EUC core at 50 m depth, with maximum core speeds of only 40 cm/s. More recently, Kolodziejczyk et al. (2014) found transports at 1°E ranging from 5-15 Sv, and at 6°E from 0-7 Sv.

Considerably less is known about the seasonal cycle of the EUC transport in the Atlantic compared to the Pacific. It is known that a seasonal cycle of shoaling and deepening of the EUC occurs that is similar to the behavior in the Pacific (Brandt et al. 2006; Giarolla et al. 2005). The EUC at 23°W shoals to its minimum depth in the central Atlantic (23°W) in April (~60 m), and reaches its maximum depth in about October (~90 m). A similar cycle occurs at 10°W (Kolodziejczyk et al. 2009) and also at 35°W, where the EUC routinely “surfaces” in boreal spring when the winds are weak. However, models suggest a rather different transport cycle in the Atlantic than the Pacific, characterized by two maxima – one (the primary maximum) in fall, and another (weaker) maximum in spring (Hormann and Brandt 2007; Philander and Pacanowski 1986). The transport maximum in the fall is related to the maximum in easterly wind stress that occurs in September-October in the far western part of the basin and the associated response of the zonal pressure gradient. By contrast, at 10°W, the recent analysis by Kolodziejczyk et al. (2009) indicates a summer maximum of the EUC transport, with a minimum occurring in fall. The exact nature of the seasonal cycle has been difficult to determine from the available ship-based sections due to large intraseasonal variability related to processes including transient wind forcing or Tropical Instability Waves.

In this study by Johns et al. (2014), new time series measurements of the EUC are presented, collected from moorings deployed at 23°W, 10°W, and 0° for almost a four year period, from 2007 to 2011, and used to describe the mean transport and seasonal cycle of the EUC across the basin. It is shown that a relatively simple technique can be used to reconstruct the EUC transport and vertical structure from a limited set of moorings at each longitude and produce robust estimates of its seasonal cycle and variability.

3.1 Data and methods

Several different data sets are used in this study to investigate the zonal structure and variability of the EUC, including moored Acoustic Doppler Current Profiler (ADCP) time series, shipboard ADCP and CTD sections, and temperature and salinity profile observations from Argo profiling floats and PIRATA (Prediction and Research Moored Array in the Atlantic; Bourles et al. (2008)) moorings. The main analysis is focused on the moored ADCP observations, while the other observations are used primarily to validate our methods for estimating the EUC transport from the moored observations, and to determine the distribution of the EUC transport in different density classes.

3.1.1 Moored ADCP observations

From October 2007 to May 2011, an array of moorings equipped with upward-looking ADCPs was maintained along 23°W, 10°W, and 0°E to monitor the temporal variation of the EUC at each longitude Fig. 3.1. These moorings were deployed by different groups as part of a coordinated program during the 2007-2011 International CLIVAR Tropical Atlantic Climate Experiment (TACE; Brandt et al. (2013); Brandt et al. (2014)).

Full data sets were obtained at both 23°W and 0°E for the duration of the experiment, but at 10°W there were two significant gaps. The first occurred at the 10°W , 0.75°N mooring when the mooring broke loose shortly after its initial deployment in October 2007, and could not be reinstalled until fully one year later. The second gap occurred at the 10°W , 0°N PIRATA mooring, from December 2009 to October 2010, due to a failure of the ADCP. The manner in which these gaps are dealt with in the subsequent analysis are described in section 3.2.

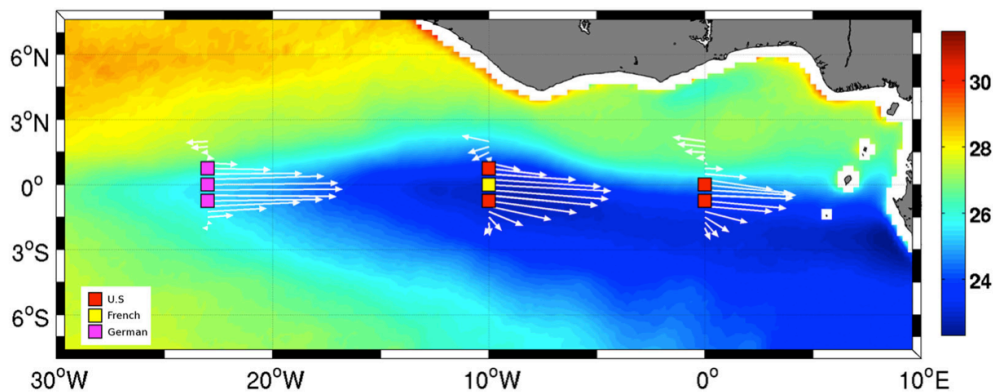


Fig. 3.1: Locations of the ADCP moorings deployed along 23°W (German), 10°W (US/France), and 0°E (US), superimposed on the climatological SST for July (from 2007 to 2011) over the tropical Atlantic, based on TMI satellite retrievals. The mean velocity vectors near the core of the EUC (80 m at 23°W , 70 m at 10°W , and 60 m at 0°E) between 2°S and 2°N , derived from the mean of available shipboard ADCP sections at each longitude, are also shown.

3.1.2 Shipboard ADCP and CTD sections

During the last 20 years a large number of cross-equatorial shipboard ADCP sections have been acquired through various national and international programs that have provided repeated sampling at (or near) four main longitudes: 35°W , 23°W , 10°W , and 0°E . Most of these results have been previously published: e.g., at 35°W by Schott et al. (2003) and Brandt et al. (2006); at $23\text{--}28^{\circ}\text{W}$ by Brandt et al. (2006) and Brandt et al. (2014); and at 10°W by Kolodziejczyk et al. (2009). In addition to these sections, we use similar compilation of sections near 0°E from recent cruises to construct mean sections of the near-equatorial zonal currents at these longitudes (Fig. 3.3). At the three westernmost longitudes there are at least 15 individual sections that go into these averages (15 sections at 35°W , 20 sections at 23°W , and 17 sections at 10°W), while at 0°E only 8 sections are available.

On many of these cruises, CTD stations were also occupied at a spatial resolution of at least 0.5° between 2°S to 2°N , which have been used in the above references to determine the EUC transport in different density classes. Here, we use a number of these available sections at 23°W (9 sections) and 10°W (8 sections) to validate methods for estimating the EUC transport in density classes from a combination of the moored ADCP measurements and equatorial density profiles derived from Argo and PIRATA observations.

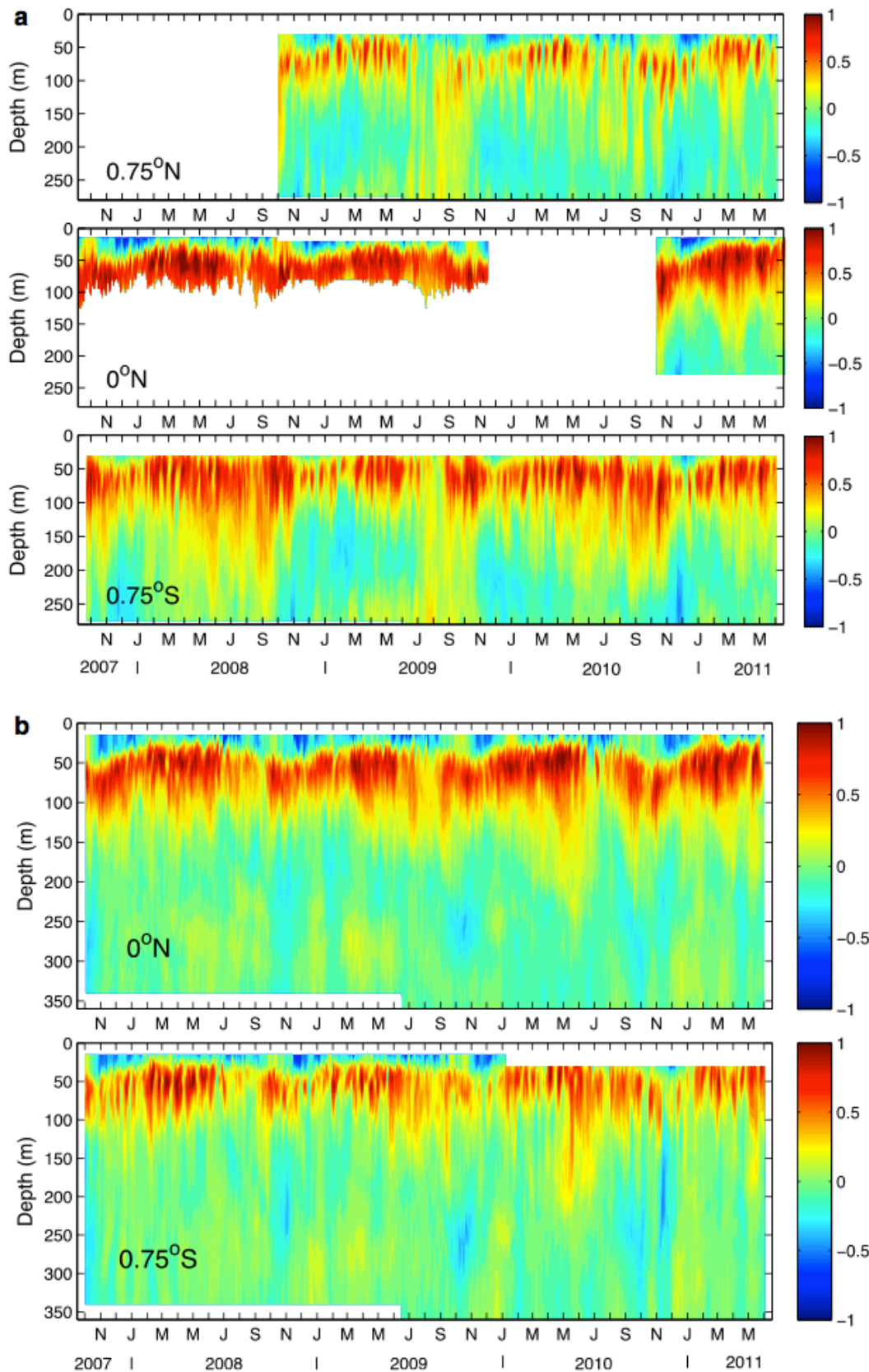


Fig. 3.2: a Zonal velocity profiles from the moored ADCP records at 10°W for the period of the observations (bottom 0.75°S; middle: 0°N, top 0.75°N). Positive velocities are eastward; color scale is in m/s. b Zonal velocity profiles from the moored ADCP records at 0°E (bottom 0.75°S; top 0°N)

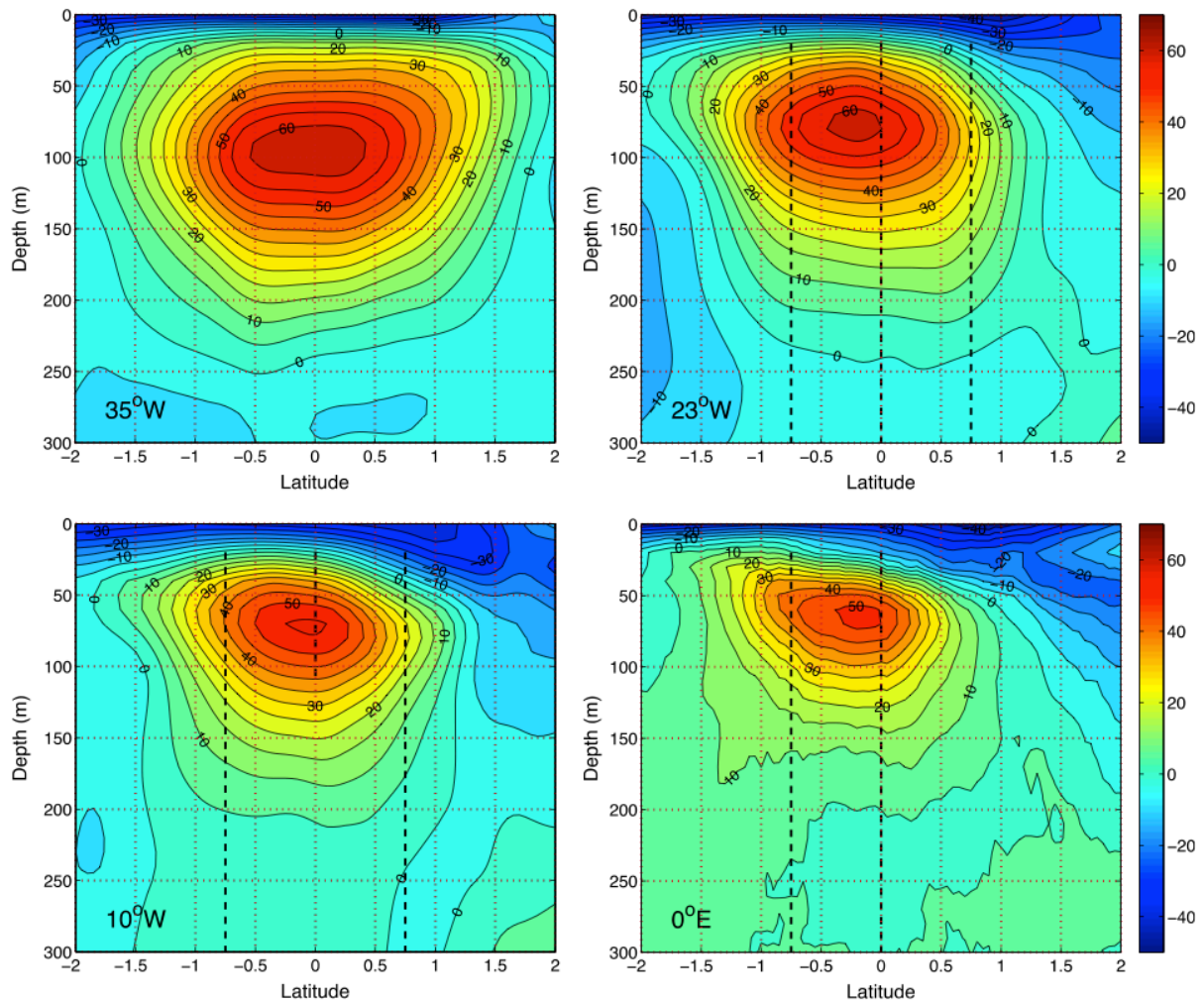


Fig. 3.3: Averaged shipboard ADCP sections across the EUC at 35°W, 23°W, 10°W, and 0°E. The locations of the ADCP moorings at each longitude and the vertical extent of the moored velocity measurements is indicated by the dashed black lines.

3.1.3 PIRATA and Argo data

Surface meteorological buoys with temperature and salinity sensors through the upper water column were maintained by the PIRATA program at each of the three longitudes, 23°W, 10°W, and 0°E, during the period of the experiment. Data recovery from these sites was generally good, except for some gaps in subsurface temperature and salinity data during 2008 and 2010 at the 0°E site. The surface (1 m) and subsurface temperature and salinity measurements at various depths on these moorings are used together with Argo profiling float data to reconstruct equatorial density profiles at each of the longitudes. The approach for merging the PIRATA and Argo data is described in section 3.2.

The Argo data used in this study is taken from the global monthly analysis produced by the Scripps Institution of Oceanography (SIO; http://sio-argo.ucsd.edu/RG_Climatology.html), which provides objectively analyzed, monthly temperature and salinity profiles over the top 2000 m on a 1° by 1° grid. Details of the analysis methodology can be found in Roemmich and Gilson (2009).

3.1.4 Reconstruction of EUC transport from moorings

The strategy for reconstructing the EUC transport from a limited set of discrete moorings is based on a relatively simple approach, in which the zonal transport profile integrated across the width of the EUC:

$$U(z) = \int_{-y_0}^{y_0} u(y, z) dy \quad (1)$$

is assumed to be represented by

$$U(z) = \sum W_n * u_n(z) \quad (2)$$

where $u_n(z)$ are the zonal velocity profiles measured by the moorings and W_n are "optimal widths" associated with each mooring. This corresponds to simply assigning a fixed width to each mooring that accounts for its respective contribution to the total EUC transport, similar to an approach used by Brandt et al. (2014). Our decision to place moorings 0.75° north and south of the equator at 10°W and 23°W was based on an initial assessment of this approach prior to the deployments using the available ADCP sections as a test bed. This analysis showed that a single equatorial mooring (with a mean meridional decay scale determined by a fit to the section transports) could track the variation in the EUC transport reasonably well, but was subject to errors as large as 5 Sv (or order 30 % errors) due to meandering of the EUC core off the equator. Using three moorings spaced between $0.6^\circ - 1.0^\circ$ off the equator reduced this error considerably (to about 10% error). There was little sensitivity to the choice of the spacing within this range, and therefore a spacing of 0.75° was adopted for the moored arrays.

To determine the final best values of the optimal widths (W_n) for the arrays, and the associated uncertainty of the method, tests were performed using all of the available shipboard ADCP sections at each longitude. The zonal velocity profiles at the exact mooring locations were extracted from each section, and the transport computed from (2) was compared to the transport derived from the actual shipboard ADCP sections. In these calculations, only positive (eastward) zonal velocities are included in the integrations and sums in (1) and (2), to exclude any contributions from westward flows adjacent to the EUC. A least squares minimization across all cruises provided the best fit values for W_n . These W_n 's are then applied to the actual moored ADCP profiles to estimate the time-varying EUC transport profile at each longitude. The moored ADCP profiles were extrapolated upward to the surface from their shallowest measurement depth (typically 20-30 m) using the same method as applied to the section data, namely, using the interpolated monthly surface drift climatology of Lumpkin and Garraffo (2005). We refer to this method hereafter as the Optimal Width (OW) method.

At 23°W , where velocity profiles spanning the full depth of the EUC were continuously available at all three latitudes (0.75°N , 0°N , and 0.75°S), the OW approach can be applied in a straightforward manner and results in optimal W_n 's of $[0.76^\circ, 0.74^\circ, 0.79^\circ]$ latitude, respectively (see further discussion in Brandt et al.

(2014)). These widths correspond fairly closely to the physical separation of the moorings, and are slightly less than the 0.8° widths that would correspond to even partitioning of the domain between 1.2°S to 1.2°N , where the bulk of the EUC is typically found.

At 0°E , there are only two moorings available for the reconstruction, at the equator and 0.75°S . The OW reconstruction yields optimal W_n 's of [0.91, 0.99] for the [0°N , 0.75°S] moorings, respectively. The overall accuracy of the reconstruction EUC transport based on the available ADCP sections at 0°E is ± 1.0 Sv.

At 10°W , a modified version of the OW method was required due to the fact that only a shallow equatorial ADCP profile is available for most of the period, as well as the data gaps. For the period between October 2007 and September 2008 - when the 0.75°N mooring was missing - we do not attempt to produce EUC transports, because the 0.75°S profile and shallow equatorial profile, in themselves, are not sufficient for a robust reconstruction. For the remainder of the record we make two different reconstructions: one derived from just the two full ADCP profiles at 0.75°S and 0.75°N , and a second that uses the data from all three moorings when the equatorial ADCP profile is available. This 3-mooring reconstruction is limited to depths ≤ 100 m (from October 2008 to November 2009) and to depths ≤ 230 m (from October 2010 to May 2011; Fig. 3.2a). For these periods the final EUC transport profile is obtained by combining the upper 3-mooring transport profile with the 2-mooring reconstructed profile over the deeper part of the water column (which we refer to as the "merged" transport profile). For the period from November 2009 to October 2010, the results rely only on the 2-mooring reconstruction. The optimal widths for the 3-mooring reconstruction were [0.71 0.81 0.79] for 0.75°N , 0°N , and 0.75°S , respectively, and for the 2-mooring reconstruction using only the off-equatorial moorings at 0.75°N and 0.75°S they were [1.31 1.39]. The larger optimal widths for the 2-mooring reconstruction are consistent with expectations, since these moorings will typically miss the maximum EUC core, and this is also reflected in the larger net meridional scale (sum of the W_n 's) for the 2-mooring reconstruction ($\sim 2.7^\circ$ latitude) versus that for the 3-mooring reconstruction ($\sim 2.3^\circ$).

3.2 EUC transport and vertical structure

3.2.1 Shipboard sections

A first view of the changing structure of the EUC across the basin is provided by the averaged shipboard ADCP sections (Fig. 3.3). These mean sections have been described previously in several studies (Brandt et al. 2006; Kolodziejczyk et al. 2009; Schott et al. 2003), but it is the first time that they have been shown together in one place. The mean section at 0°E compiled in this study is a new addition and is based mostly on sections acquired during the 2005-2007 French EGEE program in the Gulf of Guinea, as part of the AMMA program (e.g., Bourles et al. (2007)).

Consistent with previous observations, the EUC core shoals across the basin, from a core depth of about 90 m at 35°W to 65 m at 0°E . The width of the EUC also decreases across the basin and the mean core velocity decreases slightly from >0.6 ms^{-1} to about 0.5 ms^{-1} . These sections represent geographic (Eulerian) averages and

therefore the peak velocities at the EUC core are considerably weaker than seen in individual sections, where the velocity maxima are typically between $0.8 - 1.0 \text{ ms}^{-1}$. The meridionally-elongated velocity core and much larger overall width at 35°W is due in part to broadening of the mean flow distribution at 35°W by significant lateral meandering of the EUC just after it retroflects eastward from the North Brazil Undercurrent. In these sections, the EUC core is found slightly south of the equator at the three easternmost longitudes, suggesting only a small and relatively uniform displacement of about 0.2° from the equator, even in the eastern part of the basin. The strong and coherent zonal flow pattern associated with the EUC is contained mostly above 200-250 m, and its lower limit also shoals along with the velocity core, to depths of about 150 m at 0°E .

3.2.2 Mooring data

The time series of the EUC transport profile constructed from the moorings using the OW method described in section 3.1.4 are shown in Fig. 3.4, and show several notable features. First, at each longitude, the core of the EUC exhibits a seasonal vertical migration, being shallowest in boreal spring months (March-May) and deepest in boreal fall (September-October). This behavior is most pronounced in the west (23°W) and generally decreases toward the east. Associated with this deepening EUC core in fall is a much deeper extension of the eastward flow below the EUC core, which is clearly evident at 23°W and 10°W but not clearly at 0°E . This deeper EUC structure can also be seen in the individual zonal velocity profile at 10°W , 0.75°S during 2008 (Fig. 3.2a), even though we do not produce a EUC transport reconstruction at 10°W for this period. The timing and duration of this deep extension varies somewhat from year to year, but it generally emerges in boreal summer (July-August) and lasts through about the end of October. During these periods, significant eastward transport extends to depths of ≥ 300 m, while in boreal spring the eastward EUC flow is confined mostly above 150 m.

A second feature that can be noticed in Fig. 3.4 is that the EUC core intensity is generally weakest in boreal summer (June-August) at all longitudes, which coincides with the onset and seasonal development of the Atlantic cold tongue. This behavior is more pronounced in the east, especially at 0°E , and also at 10°W , where it follows a sustained period of maximum EUC core intensity in boreal spring (March-May).

In addition to these seasonal changes there is considerable short-term variability throughout the records. The dominant time scales of this variability are generally between 12-60 days, associated with Tropical Instability Waves and other modes of equatorial variability that have been previously described (e.g., von Schuckmann et al. (2008), Athie and Marin (2008), Athie et al. (2009); Perez et al. (2012)). The meridional component of velocity at each of the longitudes shows relatively high coherence throughout this band, and is mostly symmetric about the equator (i.e., in-phase between the equatorial and off-equatorial sites). Zonal velocity anomalies are mainly out of phase across the equator on these time scales, which, to first order, reflects the meandering of the EUC in response to these meridional velocity perturbations. This out of phase relationship is difficult to see in Fig. 3.2 due

to the long time span of the records, but is clearly evident when the time scale is expanded to more closely examine individual events. On longer time scales from 80 days up to annual, the zonal velocity anomalies become more in-phase with each other and reflect seasonally-coherent changes in the intensity and structure of the EUC. It is noteworthy also that the ADCP records at 0°E - which represent the first long-term records of the EUC in the eastern Gulf of Guinea - show that the EUC remains essentially tied to the equator at this location and that it has not shifted significantly south of the equator at this location as is depicted in some models.

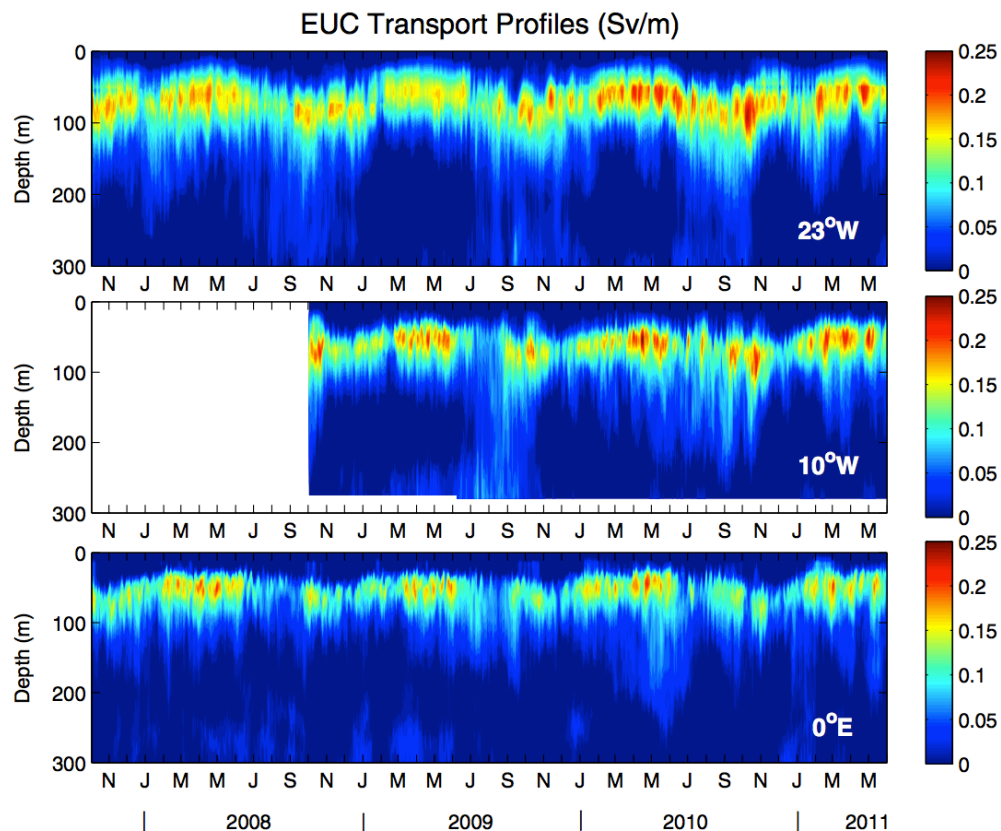


Fig. 3.4: EUC transport profiles (Sv/m) derived from the moorings at 23°W, 10°W, and 0°E. The EUC transport reconstruction is not attempted at 10°W for the first year of the observations, when the 0.75°N, 10°W mooring was missing.

The time-mean profiles of the EUC transport at each longitude are shown in Fig. 3.5, where it can be seen that the EUC core shoals progressively to the east, from 75 m at 23°W to 55 m at 0°E. The transport at the EUC core is largest at 23°W and decreases by about 10% and 30%, respectively, at 10°W and 0°E, relative to that at 23°W. Below the EUC core the transport remains higher at 23°W than 10°W until about 200 m, while at 0°E the transport profile shows almost a uniform reduction of ~ 0.01 Sv/m relative to 10°W. In the region above the EUC core the transport profiles are nearly identical across all longitudes.

The mean transports for the EUC derived from these measurements, integrated to 300 m, are 14.3 ± 0.6 Sv, 12.1 ± 0.9 Sv, and 9.4 ± 0.6 Sv, at 23°W, 10°W, and 0°E, respectively, where the given uncertainties represent standard errors. These uncertainties are based on the number of available degrees of freedom in each transport time series, determined by the length of the time series divided by twice the

integral time scale of the transport variability (which is approximately 27 days at 23°W, 24 days at 10°W, and 21 days at 0°E). The associated standard deviations of the transport are 3.2 Sv at 23°W, 4.1 Sv at 10°W, and 3.0 Sv at 0°E. The larger uncertainty at 10°W is a result of both its larger transport variability and the shorter length of time series available at that longitude. If one includes in these error estimates a random measurement uncertainty of ± 1 Sv, then the overall uncertainties for the above mean transports increase by only about 5%, which indicates that the errors in the transport reconstruction associated with the OW method add little to the total uncertainty. The uncertainties in the mean transport at each longitude are therefore essentially governed by the natural variability of the EUC transport.

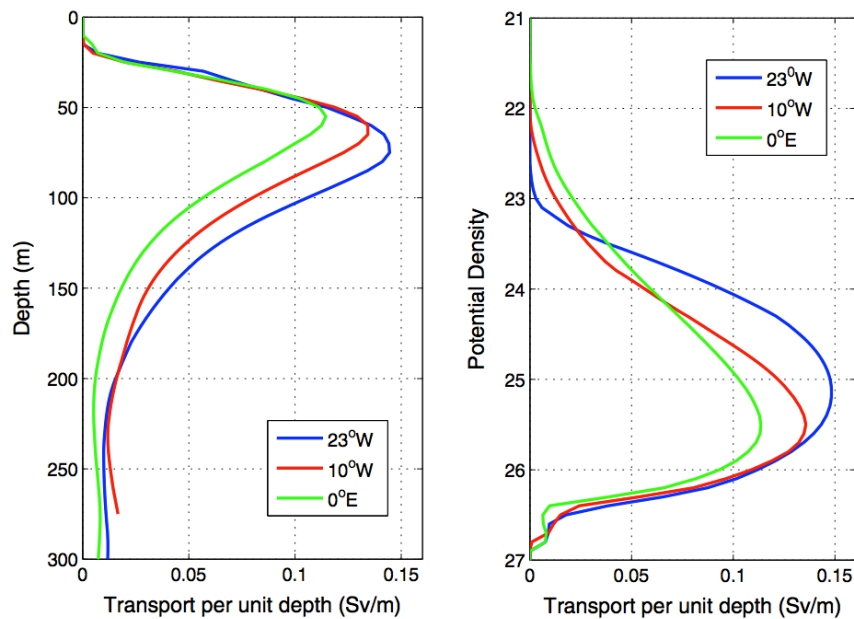


Fig. 3.5: Mean EUC transport profiles (Sv/m) at 23°W, 10°W, and 0°E, plotted versus depth (left) and versus potential density (ρ_h) (right)

To compare these results with previous estimates of the EUC transport, it is desirable to break the total transport down into different density classes, rather than a single depth integrated value. In order to accomplish this, we utilize the SIO monthly Argo analysis described in section 3.1.3, together with the available PIRATA moored temperature and salinity data during the measurement period, to construct density profiles at the equator at each longitude. The Argo data provide high-resolution vertical profiles of temperature and salinity, but may occasionally be inaccurate due to sparse regional sampling, whereas the PIRATA data are from discrete depths and sometimes have temporal gaps. To obtain the most accurate possible density profiles, a simple correction scheme was applied to the monthly Argo profiles, as follows. At each PIRATA measurement depth, the differences between the Argo and monthly-mean PIRATA temperature and salinity data are used to construct an "error" profile for the Argo data, that is linearly interpolated between the PIRATA measurement depths. This error profile is then added back into the Argo profiles to obtain a corrected Argo profile. These corrected temperature and salinity profiles pass through all the measured PIRATA points, but are otherwise consistent with the

vertical structure of the continuous Argo profiles. The required corrections to the Argo profiles were small, less than 1°C RMS. for temperature and 0.2 RMS for salinity, which indicates that the Argo profiles themselves are remarkably accurate (even though the SIO analysis does not utilize any of the PIRATA data). During periods when no simultaneous PIRATA data were available for this correction, the mean error (i.e., the mean error profile from all of the available Argo-PIRATA comparisons at that longitude) was used instead to correct those Argo profiles. Monthly density profiles at the equator were then constructed at each longitude from these corrected Argo temperature and salinity profiles. These density profiles are then used to transform the EUC transport profiles, measured as a function of depth, into density coordinates.

The corresponding mean EUC transport profiles in density coordinates at each longitude are shown in Fig. 3.5b. The peak transport occurs near $\sigma_\theta = 25.1$ at 23°W and near $\sigma_\theta = 25.5$ at both 10°W and 0°E. Thus while the EUC core is physically deeper at 23°W (Fig. 3.5a), it occurs at a lighter mean density. The eastward shoaling of the EUC core in depth space - but trending toward higher densities - reflects a more rapid shoaling of the main pycnocline toward the east than the EUC velocity core, which is analogous to the observed EUC structure in the Pacific (Johnson et al. 2002). An alternate presentation of the same results is shown in Fig. 3.6, where the transports are accumulated into even density classes of 0.1 kgm⁻³. The maximum EUC transport in this representation occurs in the density class $\sigma_\theta = 26.3$ at each longitude, which reflects the greater thickness of isopycnal layers below the core of the EUC. The main differences between the profiles are above $\sigma_\theta = 25.5$ where the transports decrease toward the east. In particular there is significant transport above $\sigma_\theta = 24.5$ at 23°W which decreases markedly by both 10°W and 0°E. Below the transport maximum at $\sigma_\theta = 26.3$, the transport at 0°E also decreases relative to that at 23°W and 10°W.

The transports in four main density classes that have been used to describe the regional characteristics of the EUC in previous studies (e.g., Brandt et al. (2006); Kolodziejczyk et al. (2009)) are listed in Tab. 1. These classes correspond to a "surface" layer ($\sigma_\theta < 24.5$), an "upper thermocline" layer ($24.5 < \sigma_\theta < 25.5$), a "lower thermocline" layer ($25.5 < \sigma_\theta < 26.5$), and a "deep thermocline" layer ($26.5 < \sigma_\theta < 26.8$), after Kolodziejczyk et al. (2009). The upper and lower thermocline layers contain the main contributions to the EUC transport in the regions above and below the EUC velocity core, respectively, and these are often grouped together into a single "thermocline layer" EUC transport (e.g., Schott et al., 2003; Brandt et al., 2006). The transport in the thermocline layer is identical at 23°W and 10°W (10.2 Sv), but there is a relative decrease (increase) in the upper (lower) thermocline component at 10°W. At 0°E the thermocline transport is reduced to 8.0 Sv, with both the upper and lower thermocline contributions decreasing from 10°W. The results obtained from our mooring-based analysis compare very well with the earlier estimates at 23°W and 10°W derived from ship sections (Tab. 1), essentially confirming the results of Brandt et al. (2006) and Kolodziejczyk et al. (2009) at these longitudes, and indicating that those estimates did not suffer greatly from aliasing of the ship sections by intraseasonal variability. The measurements at 0°E, however,

provide fundamentally new information on the EUC transport and vertical structure in the eastern Gulf of Guinea, where the available ship sections have been too limited to construct representative annual estimates.

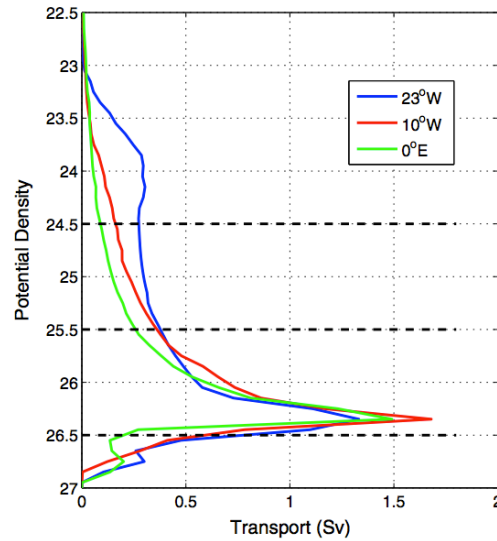


Fig. 3.6: Mean EUC transport profile in density classes, at 0.1 kg/m³ intervals, at 23°W, 10°W, and 0°E, derived from the mooring-based EUC transport profiles and PIRATA-corrected ARGO density profiles at each longitude.

Density class	σ -range	This study			Brandt et al. (2006)		Kolodziejczyk et al. (2009)
		23°W	10°W	0°E	35°W	23°W	10°W
Surface	<24.5	3.0	1.1	0.8	5.4	3.1	0.4
Upper thermocline	24.5–25.5	3.1	2.4	1.6	14.6	10.7	2.5
Lower thermocline	25.5–26.5	7.1	7.8	6.4			8.3
Deep thermocline	26.5–26.8	1.1	0.8	0.6			0.9
Total		14.3	12.1	9.4	20.0	13.8	12.1

Tab. 1: Transports (in Sv) in density classes, from this study compared with previous estimates from averaged ship sections at the various longitudes (from Brandt et al. (2006) and Kolodziejczyk et al. (2009)).

3.2.3 Seasonal cycle of the EUC

A climatological seasonal cycle is derived for the EUC transport profile at each longitude by averaging together all of the data from the available records by the month of observation (Fig. 3.7). These seasonal cycles represent the climatological average over 3.7 years of data at 23°W and 0°E but only over 2.7 years at 10°W. The features described earlier in the time series are clearly evident: (1) a semi-annual cycle in the intensity of the EUC core transport, with maxima in boreal spring and fall; (2) an annual vertical migration of the EUC core with shallowest (deepest) depths in boreal spring (fall); and (3) a deep extension of the eastward flow beneath the core of the EUC in boreal summer to early fall at both 23°W and 10°W.

The semi-annual cycle of the core intensity is most pronounced in the eastern part of the basin, where the two maxima are separated by a progressively weakening core intensity during boreal summer. The spring maximum tends to be better

sustained across the basin while the fall maximum decays more sharply, especially at 0°E. Therefore in terms of the absolute EUC core intensity, as well as its seasonal behavior across the basin, the spring maximum is considered the primary maximum and the fall maximum a secondary maximum.

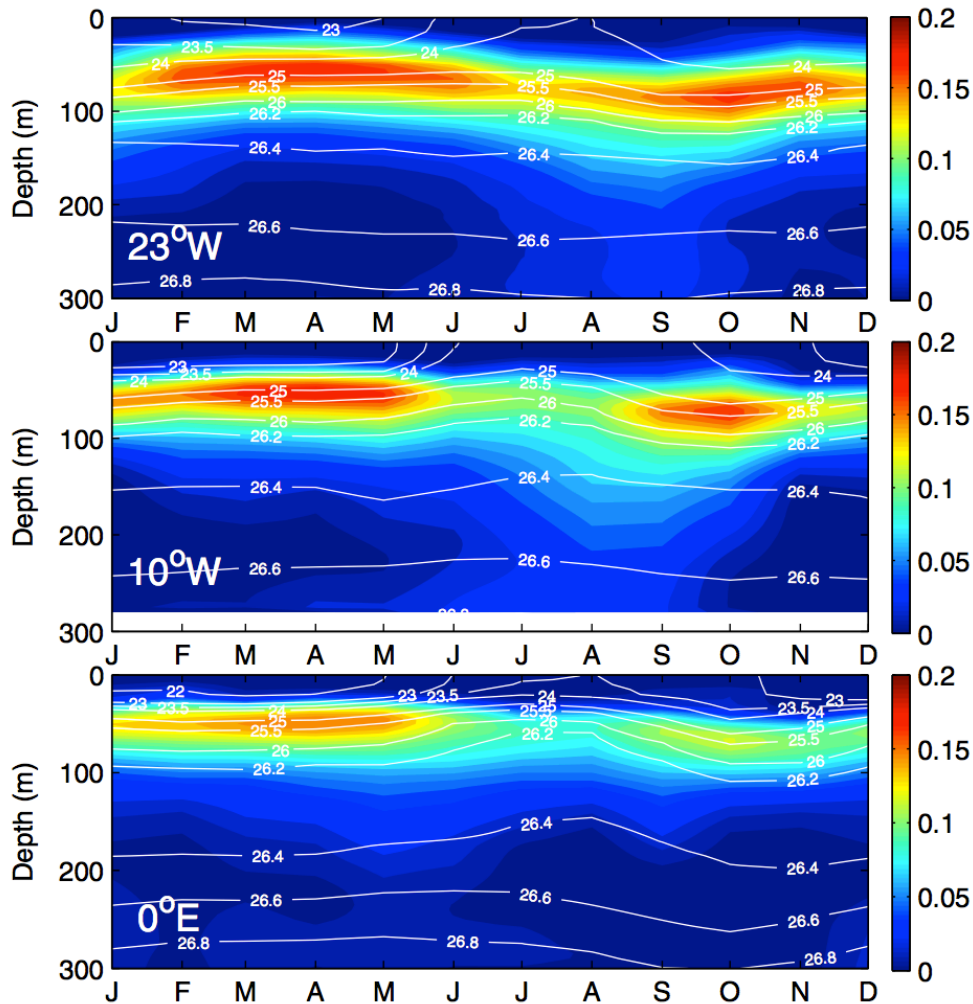


Fig. 3.7: Monthly-mean EUC transport profiles (Sv/m) at 23°W, 10°W, and 0°E. Density contours derived from the PIRATA-corrected ARGO temperature and salinity data, averaged over the TACE time period (2007–2011), are shown in thin white lines.

The seasonal cycle of the total (0 - 300 m) EUC transport at each longitude is illustrated in Fig. 3.8 where it is superimposed on the transport time series from each measurement year. At 23°W the transport exhibits a single broad maximum in September, with otherwise nearly constant total transport from boreal winter through spring (December to June). The reverse is true at 0°E, where the seasonal maximum occurs in boreal spring (April-May), and the transport is nearly constant from August through January. In between these longitudes, at 10°W, a semi-annual cycle is evident, with maxima in September (primary) and April (secondary), and a relatively sharp minimum in November-December. The amplitude of the seasonal variability is about 5 Sv (peak-to-peak) at 23°W and 0°E and about 10 Sv at 10°W. The instantaneous transports range from about 5 - 25 Sv at 23°W and 10°W, consistent with the range of observed transports from individual ship sections at

these longitudes (Brandt et al., 2006; Kolodziejczyk et al., 2009). At 0°E the transports vary from about 5 to 20 Sv.

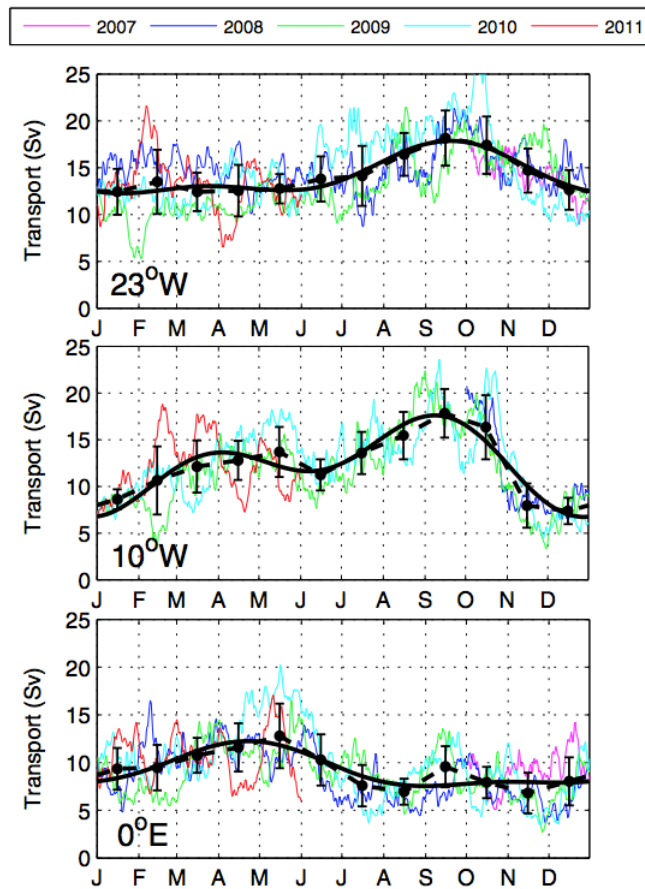


Fig. 3.8: EUC transport (0–300m) at each of the observed longitudes, for individual years (colors; see legend), with monthly means and standard deviations shown as black symbols with error bars. The respective seasonal cycles derived from fits of the data to an annual plus semi-annual harmonic are shown in the bold solid lines.

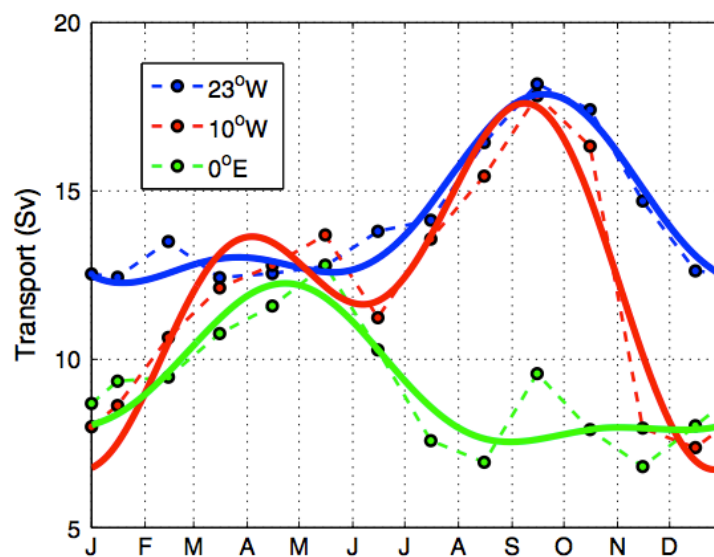


Fig. 3.9: Monthly means (symbols) and seasonal harmonic cycle of the 0–300 m EUC transport, overlain from Fig. 3.8 at each of the longitudes.

The seasonal cycles at all three longitudes are overlain in Fig. 3.9, where it can be seen that the transports at all locations are roughly the same during boreal spring, approximately 12-13 Sv, when the EUC core is relatively intense and shallowest across the whole basin (Fig. 3.7). During boreal fall, the transports at 23°W and 10°W are again similar, at about 18 Sv, but the transport at 0°E is nearly 10 Sv weaker at this time. There is some indication of a secondary maximum in the September monthly mean transport at 0°E, associated with the secondary fall maximum in the upper EUC core at that time, but it is not clearly present in all years and is not a feature of the seasonal harmonic cycle.

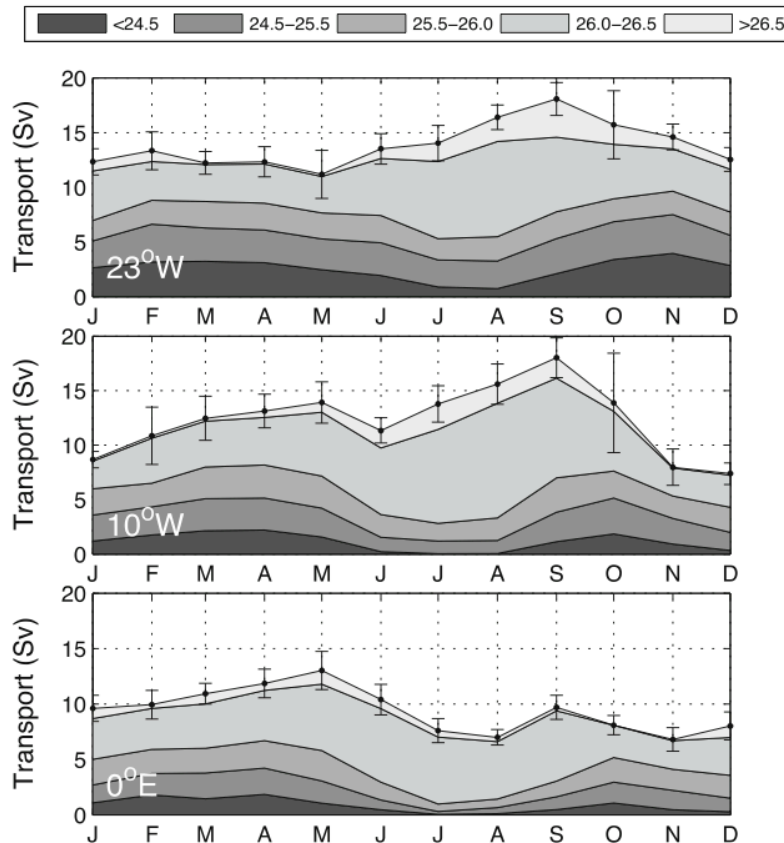


Fig. 3.10: Seasonal cycle of the EUC transport in density classes, shown as cumulative transport from the lowest (shallow) to highest (deeper) density classes. $\sigma_\theta < 24.5$ corresponds to the “surface” layer, $\sigma_\theta = 24.5\text{--}25.5$ to the “upper thermocline” layer, $\sigma_\theta = 25.5\text{--}26.5$ to the “lower thermocline” layer (split here into two sub-layers), and $\sigma_\theta = 26.5\text{--}26.8$ to the “deep thermocline”, following Kolodziejczyk et al. (2009). The dots with error bars at the top of each plot show the total EUC transport and its standard error for each month.

The depth-integrated transport of the EUC does not reveal the changing vertical structure of the EUC transport, which is illustrated more clearly in Fig. 3.10 where the transports are broken down into density classes. The transports in the surface and upper thermocline layer all reach a minimum in boreal summer, and nearly vanish at 0°E during July-August. This reduction is compensated at both 23°W and 10°W by an increase in the lower thermocline layer transport that begins in June and peaks in August. Most of this transport occurs in the deeper part of the thermocline ($\sigma_\theta = 26.0\text{--}26.5$), and there is also a further contribution from $\sigma_\theta > 26.5$ at this time. At 0°E the behavior is somewhat different, with the peak in lower thermocline transport

actually occurring in May, but showing a less pronounced seasonal variation than at 23°W or 10°W. Thus, during the summer upwelling season, the transport in the upper portion of the EUC is substantially reduced at all locations, and this reduction becomes progressively larger toward the east so that by 0°E almost all of the transport occurs in the lower thermocline.

3.3 Discussion and conclusions

New observations of the Equatorial Undercurrent in the central and eastern part of the Atlantic are presented based on moored current measurements collected during 2007-2011 along 23°W, 10°W, and 0°E. These observations provide, for the first time, a clear description of the seasonal cycle of the EUC across the basin, which had before relied mainly on ship sections that can be affected by seasonal sampling biases and strong intraseasonal fluctuations.

The mean transport of the EUC at 23°W is 14.3 ± 0.6 Sv, decreasing to 12.1 ± 0.9 Sv at 10°W and 9.4 ± 0.6 Sv at 0°E. The character of the seasonal cycle changes moving eastward: at 23°W the strongest EUC transport occurs in boreal fall, at 10°W the EUC transport shows a semiannual cycle with a maximum in boreal spring and fall, while at 0°E the EUC has a single spring maximum. The maximum core intensity within the upper part of the EUC occurs in boreal spring at all longitudes, and at this time (April) the EUC transport is almost uniform, at about 12-13 Sv, all across the basin. The weakest EUC core intensity occurs during the boreal summer cold tongue phase at all locations.

As noted by Arhan et al. (2006), there is potential confusion in the literature when discussing the seasonal cycle of the EUC, depending on whether it is the total transport or the maximum intensity (core speed) that is being considered. Our observations show that the maximum in core intensity occurs across the basin in boreal spring (April), while there is a secondary maximum in the fall (October) at both 23°W and 10°W, and a transport maximum at 23°W and 10°W that occurs slightly earlier, in September. This transport maximum is associated in part with the intensified upper core of the EUC in boreal fall, but derives in large part from a deeper extension of the EUC into the lower thermocline in late summer and early fall at those longitudes. The study by Philander and Pacanowski (1986), in fact, does show two seasonal maxima in the velocity core of the EUC, which take place in April-May and November at 30°W and have about equal strength (~ 0.8 m/s), and in October and February at 0°E, where the October maximum is significantly stronger (~ 0.6 m/s vs. 0.3 m/s in February). These were the only two longitudes studied in that paper. On the other hand, Arhan et al. (2006) find only a fall maximum in core intensity, and the core intensity is actually a minimum across the whole basin in boreal spring (their Fig. 6). Furthermore, the models that do predict a secondary maximum in the EUC transport (Hormann and Brandt, 2007; Arhan et al., 2006) or EUC core intensity (Philander and Pacanowski, 1986) in the eastern part of the basin, seem to get this at the wrong time, in January or February instead of April. Therefore, we conclude that the observed spring maximum in EUC core intensity across the whole basin, and the fact that this leads to an actual transport maximum in spring at 0°E, is not a feature that is correctly reproduced by the available models.

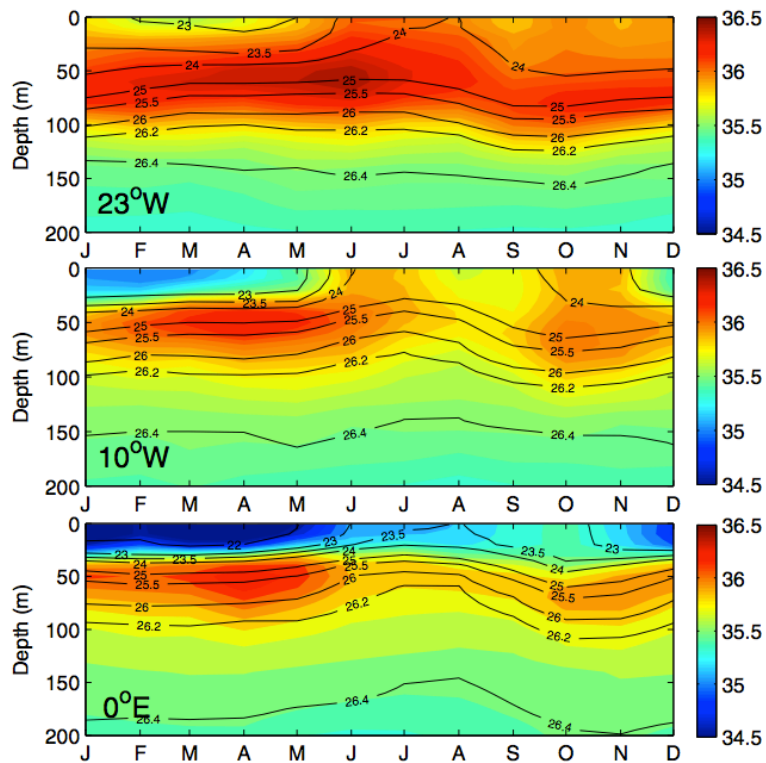


Fig. 3.11: Monthly-mean salinity profile variability at the equator for the TACE period (2007–2011), from 0 to 200 m, derived from the PIRATA-corrected Argo data at 23°W, 10°W, and 0°E. Density contours are overlain in black.

The existence of a spring maximum in the EUC in the eastern part of the basin also has support in hydrographic observations. Since the SEQUAL-FOCAL experiment (e.g. Hisard and Hénin (1987)), it has been known that the thermocline salinity maximum associated with the EUC is strongest in the eastern equatorial Atlantic in late winter to spring, and we find in our analysis of the Argo data at 0°E (Fig. 3.11) that this consistently occurs between March-May, exactly when the EUC core intensity and transport are a maximum there. This is consistent with the notion that the high salinity core of the EUC - originating from the subtropics and mostly entering the EUC at the western boundary - is more effectively transported across the basin during boreal spring when the EUC core intensity is at a maximum. A second salinity maximum occurs in October-November at 0°E (and at 10°W) when the EUC re-accelerates after its summer minimum (Fig. 3.11). The Argo data, and previous observations, also show clearly that the EUC salinity maximum is strongly eroded, or can even disappear, in boreal summer, due to the strong mixing that occurs at the top of the EUC during the development of the cold tongue. Surface mixed layer salinities also reach their seasonal maximum over most of the central and eastern Atlantic between June - November (Fig. 3.11). This is consistent with the weaker upper EUC observed in boreal summer, which is presumably also retarded by downward mixing of westward surface momentum and also by the relaxed zonal pressure gradient in the eastern part of the basin during summer.

The fate of the high salinity waters carried in the EUC, especially in boreal spring when they are carried farthest eastward into the Gulf of Guinea, remains uncertain. Historical studies of the EUC in the eastern Gulf of Guinea have generally

concluded that the EUC penetrates in the mean to the eastern boundary where it feeds coastal undercurrents both to the north and south of the equator (Hisard and Hénin 1987; Wacongne and Piton 1992). However, the more recent cruises conducted in the Gulf of Guinea, including a U.S. cruise in June 2009 in support of our mooring operations that extensively sampled the EUC across the basin, have shown the presence of westward flowing, high-salinity cores flanking the EUC in the Gulf of Guinea during boreal summer and fall (Kolodziejczyk et al. 2014). The salinity in these westward flows is comparable to the salinity of the EUC core itself, and can only come from the EUC, since there is no other source of such high salinity waters in the Gulf of Guinea. We hypothesize that these high salinity waters are remnants of the high salinity EUC core waters that are advected most strongly into the eastern Gulf of Guinea during boreal spring, which are then recirculated back in these westward flows toward the central part of the basin. The portion of the EUC fed into these westward recirculations may actually be larger than the amount that reaches the African coast and can escape the Gulf of Guinea through the Gabon-Congo Undercurrent flowing southward along the eastern boundary (Mercier et al. 2003; Wacongne and Piton 1992), as suggested by Kolodziejczyk et al. (2014).

4 Seasonal variability of the equatorial undercurrent termination and associated salinity maximum in the Gulf of Guinea

Authors: N. Kolodziejczyk, F. Marin, B. Bourlès, Y. Gouriou, H. Berger

Recent observational studies have described the mean properties of the EUC in the Atlantic between the western boundary and 0°E (Bourlès et al. 2002; Brandt et al. 2006; Johns et al. 2014; Kolodziejczyk et al. 2009; Schott et al. 1998; Stramma and Schott 1999). The core of the EUC is characterized by maximum salinity and dissolved oxygen concentrations, while the mean EUC transport is seen to progressively weaken eastward from 20.9 Sv at 35°W to 9.1 Sv at 0°W (Johns et al. 2014; Schott et al. 1998). East of 0°E, in spite of sparse recent measurements (Hummels et al. 2013), the fate of the EUC remains still poorly documented.

Both numerical and observational studies indicate that the EUC is subject to a strong seasonal cycle (Arhan et al. 2006). At 10°W, Kolodziejczyk et al. (2009) observed two maxima of the EUC transport from individual cruises: the strongest (up to 30.0 Sv) during boreal summer and early fall, and the weakest (up to 14.8 Sv) during boreal winter, but the full seasonal cycle of the EUC transport at that longitude could not be resolved due to the absence of observations during the boreal spring. More recently, Johns et al. (2014) confirmed this semi-annual cycle of the EUC transport at 10°W from current-meter moorings, but the boreal summer maximum was found to be weaker (~18 Sv) than in Kolodziejczyk et al. (2009), and the second maximum (~14 Sv) was observed in boreal spring. In the central and eastern equatorial Atlantic, the thermocline and EUC seasonal variability is mainly associated with the basin scale adjustment to the zonal wind forcing over the equatorial Atlantic (e.g., Giarolla et al. (2005); Johns et al. (2014); Katz (1984); Kolodziejczyk et al. (2009); Philander and Pacanowski (1986); Wacongne (1989)). East of 0°E, due to sparser observations, the seasonal variability of the EUC termination remains an open question.

Moreover, previous observations have shown a strong seasonal variability of salinity in the thermocline in the eastern equatorial Atlantic. From hydrological measurements collected during 1982–1984, Gouriou and Reverdin (1992) identified the presence of a tongue of high salinity waters during boreal spring over the whole width of the Atlantic Ocean. This tongue reached the eastern boundary, and spread meridionally from 5°S to 5°N. Mercier et al. (2003) also observed extra-equatorial salinity maxima around 3°S–N within the upper thermocline during boreal spring 1995 at 3°E, associated with westward circulations surrounding the EUC. During boreal summer, this equatorial salinity maximum is found to weaken or even disappear (Gouriou and Reverdin 1992; Hisard and Morlière 1973; Verstraete 1992).

The EUC additionally exhibits a year-to-year variability over the whole equatorial Atlantic, as evidenced from observations carried out during boreal summer of different years (Bourlès et al. 2002; Gouriou and Reverdin 1992). Hormann and Brandt (2007) pointed out strong correlations between the interannual variability of the EUC and the South Equatorial Current (SEC) west of 10°W, and SST in the eastern Atlantic Cold Tongue (ACT) during the boreal summer. The anomalous cold

(warm) SST in the ACT is associated with a stronger (weaker) EUC and SEC transports west of 10°W. However, Hormann and Brandt (2007) did not address explicitly the interannual variability of the EUC east of 10°W, and observations were until recently too sparse to document it.

In this study, observations from recent oceanographic cruises, during which simultaneous measurements of currents and hydrology were obtained along meridional sections between 10°W and 6°E, are analyzed to describe the fate and seasonal variability of the EUC and its associated salinity maximum in the Gulf of Guinea (GG; defined here as the region extending from 15°S to 5°N and from 15°W to 15°E). These measurements are complemented by observations from PIRATA moorings and from ARGO profiling floats, and by a high-resolution Ocean General Circulation Model (OGCM) simulation of the tropical Atlantic Ocean.

4.1. Observations and model

4.1.1. Data

4.1.1.1. Cruises

The data used in this study were collected in the Gulf of Guinea in 2000 during EQUALANT-2000 cruise (Bourles et al. 2007), and from 2005 to 2007 during 6 repetitive cruises in the framework of EGEE (Etude de la circulation océanique et des échanges océan-atmosphère dans le Golfe de Guinée) (Bourles et al. 2007) as part of the AMMA (African Monsoon Multidisciplinary Analysis) program (Redelsperger et al. 2006).

During these cruises, 19 meridional hydrological sections, including measurements of zonal and meridional currents from Ship-mounted Acoustic Doppler Current Profilers (SADCP), were carried out along 10°W, near 2°E and along 6°E. Temperature, salinity and dissolved oxygen measurements were collected from CTD-O₂ SeaBird probes along each section at a spatial resolution of at least 0.5° in latitude. En-route SADCP measurements cover the depth range from 20 m down to about 150 m (EGEE1 and EGEE2) or 350 m (other cruises). Absolute referencing was provided by Global Positioning System (GPS) navigation. SADCP data were first hourly-averaged, then linearly interpolated onto a regular grid with a resolution of 0.1° in latitude and 1 m in depth. The standard error of the hourly-averaged velocities, $S_E = STD/\sqrt{N}$ (estimated as the STD of the hourly mean velocity divided by square root of the sample size, N , i.e. the number of data used in the hourly mean estimates), is around 1 cm s⁻¹ on average for each cruise.

For validation purpose, we also used the velocity and hydrographic data of 17 historical cruises carried out at 10°W between 1997 and 2007 and described in Kolodziejczyk et al. (2009). Note that the 10°W sections from EQUALANT-2000 and EGEE 1-to-6 are common to the present paper and Kolodziejczyk et al. (2009). These data allow a validation of the mean sections of zonal velocity and salinity at 10°W, and of the seasonal cycle of the transport at 10°W estimated with the model output.

4.1.1.2. PIRATA moorings

In the framework of the PIRATA program (Bourles et al. 2008), 2 meteo-oceanic moorings are maintained since 1997 along the equator in the eastern Atlantic, namely at 10°W and 0°E. These moorings provide daily time series of temperature at 11 depth levels from the surface down to 500 m depth, with a 20 m resolution from the surface down to 140 m depth; and of salinity at 6 levels from surface to 120 m depth with a 20 m resolution. The mean seasonal cycles of temperature and salinity were calculated for each PIRATA buoy location and for each depth from the complete time series (covering the period September 1997– August 2013). The data sets suffer from numerous gaps (refer to <http://www.brest.ird.fr/pirata/> for details on the PIRATA datasets), but at least 7 complete years of temperature and salinity data were available at most depths at 10°W and 0°E. Note however that there is only about 1 year of salinity measurements at 60 m (at 10°W and 0°E) and at 80 m (at 0°E), and no salinity data at 80 m at 10°W. In particular, there is no salinity measurement at these depths in June–August at 10°W and in April at 0°E.

4.1.1.3. Argo floats

The hydrological profiles from Argo floats used in this study have been downloaded from the Coriolis Data Center (<http://www.coriolis.eu.org/>). A climatological test was applied to the data set, and followed by a visual control of suspicious profiles in the framework of the “Global Ocean Surface Salinity Calibration and Validation” (GLOSCAL) project (Gaillard et al. 2009). The individual profiles available in the GG between 2004 and 2012 provide a spatial and monthly coverage since mid-2005 (more than 50 profiles per month) that is expected to be large enough to describe the seasonal variability of the temperature and salinity in this region (see also Wade et al. (2011)).

4.1.2. Model description and validation

4.1.2.1. NEMO model

In this study, we use the numerical outputs of a Tropical Atlantic configuration (30°S–30°N) of the Ocean General Circulation Model NEMO 3.1 (Madec 2008). This configuration is similar to the DRAKKAR experiment (Barnier et al. 2006). The horizontal resolution is 1/4° and there are 46 vertical levels (16 levels within the first 300 m and 10 levels in the first 100 m). This configuration is forced at its meridional boundaries (30°N–S) and its western boundary (60°W) by the 5-day outputs of the global ORCA025-G85 simulation (Barnier et al. 2006), using the “mixed” open boundary algorithm (Barnier et al. 1998; Treguier et al. 2001).

For the purpose of this study, the model includes a high-resolution sub-domain (1/12° horizontal resolution and same vertical grid) between 10.7°W and 14.5°E and between 13.7°S and 7.5°N, through the 2-way Adaptive Grid Refinement In Fortran (AGRIF; www.nemo-ocean.eu) module of the NEMO 3.1 code. This gain of resolution in the GG allows a better representation of the fine structures of the surface and subsurface, like river plumes characterized by sharp Sea Surface Salinity (SSS) fronts that could impact the SEC and EUC circulation and water masses in the

eastern GG. The boundary conditions of the AGRIF sub-domain region are provided by the larger-scale model at each time step.

The model is forced with the atmospheric fluxes of momentum, heat and freshwater provided by DRAKKAR Forcing Set 4.3 (DFS 4.3) (Brodeau et al. 2010). This dataset is a combination of ECMWF-ERA40 (European Centre for Medium-Range Weather Forecasts) 6-hourly reanalysis and observations. Radiative fluxes are provided by daily satellite measurements, while precipitations come from monthly satellite measurements. The evaporation minus precipitation (E-P) flux includes a relaxation to climatological E-P with a coefficient of $-56 \text{ mm day}^{-1} \text{ PSS}^{-1}$. The rivers' runoffs are provided by the monthly climatology of Dai and Trenberth (2002). The vertical turbulent mixing is parameterized using a TKE scheme (Blanke and Delecluse 1993) with a background vertical diffusivity coefficient equal to $10^{-6} \text{ m}^2 \text{ s}^{-1}$. Since convective mixing due to static instability cannot be represented in hydrostatic models, a TKE source is added in case of density inversion in the mixed-layer with an enhanced background vertical diffusivity coefficient set to $10^{-4} \text{ m}^2 \text{ s}^{-1}$. In the GG sub-domain ($1/12^\circ$ resolution), the horizontal friction scheme is bilaplacian, applying on horizontal surfaces with a friction coefficient equal to $-1.25 \times 10^{11} \text{ m}^4 \text{ s}^{-1}$, while diffusion is isopycnal and laplacian with a diffusion coefficient equal to $100 \text{ m}^2 \text{ s}^{-1}$.

The monthly-averaged and 5-day-averaged outputs of the simulation for the period 1993–2007 are used in this study. The model is started from rest on 1 January 1990. The initial conditions for temperature and salinity were derived from the World Ocean Atlas climatology (Antonov et al. 2010; Locarnini et al. 2010). Only model outputs after 1993 (i.e. after 3 years of spin-up) are considered.

The present study will mostly focus on the main properties and transports within the upper thermocline (defined as the within the $\rho_\theta = 24.5\text{--}26.2$ isopycnal layer), where the EUC core and the associated salinity maximum lie, or within the thermocline (defined as the within the $\sigma_\theta = 24.5\text{--}26.5$ isopycnal layer), where most of the EUC transport takes place. For each 5-day output of the model, we first determine the depths of the two isopycnals from the linear interpolation of the vertical density profile at each gridpoint, and then average (for mean fields) or integrate (for transports) the model fields between these two depths (taking into account the thickness of the vertical grid cells). We checked that the 24.5, 26.2 and 26.5 isopycnals never outcrop in the eastern equatorial Atlantic.

4.1.2.2. Model validation

For details on the model validation see Kolodziejczyk et al. (2014).

4.2. Evidence of a westward recirculation of the EUC salinity maximum in June 2007

In this section, we focus on the observations of currents, salinity and dissolved oxygen acquired in June 2007 in the Gulf of Guinea during the EGEE5 cruise (Fig. 4.1). The meridional sections of salinity along 10°W , 2.3°E and 6°E (Fig. 4.1d–f) reveal, within the upper thermocline layer (defined here between the 24.5 and 26.2 isopycnals), the presence of high salinities (exceeding 36.0) both at the equator and off the equator (near 3°N and 3°S at 2.3°E), as previously evidenced by Gouriou and

Reverdin (1992). At the equator, high salinities are observed along the three sections at the depth of the EUC core (Fig. 4.1d–f) and coincide with high dissolved oxygen concentrations (up to $120 \mu\text{mol kg}^{-1}$; Fig. 4.1g–i). At 10°W , it is worth noticing that the strong salinities that are visible south of 4.5°S around the 24.5 isopycnal (Fig. 4.1a, d), in the region of the eastward South Equatorial Undercurrent (SEUC) do not result from the recirculation of the EUC in the eastern GG. They are likely the signature of the subtropical water masses from the south Atlantic advected by the SEUC (Kolodziejczyk et al. 2009), and are thus beyond the scope of the present study.

The EUC maximum velocity decreases eastward from 70 cm s^{-1} to 40 cm s^{-1} (Fig. 4.1d–f), while the thermocline EUC transport first increases from 8.3 Sv to 11.6 Sv between 10°W and 2.3°E , and subsequently decreases to 4.4 Sv at 6°E . Note that both eastward velocities and high oxygen concentrations extend below $\sigma_\theta = 26.2$ (down to the 26.5 isopycnal) at 10°W and 2.3°E , i.e. deeper than the salinity maximum of the EUC core which is confined to the upper thermocline (Fig. 4.1d, g).

At 6°E , salinities exceeding 35.9 and dissolved oxygen concentrations greater than $150 \mu\text{mol kg}^{-1}$ cover the whole latitude range of the meridional section (between 1°S to 2.5°N) in the upper thermocline (Fig. 4.1i), in contrast with the EUC that remains confined between 1°N and 1°S (Fig. 4.1c). Between 1°N and 2.5°N , high salinities are associated with a westward current, which strongly suggests that EUC water masses spread poleward and recirculate westward near that longitude.

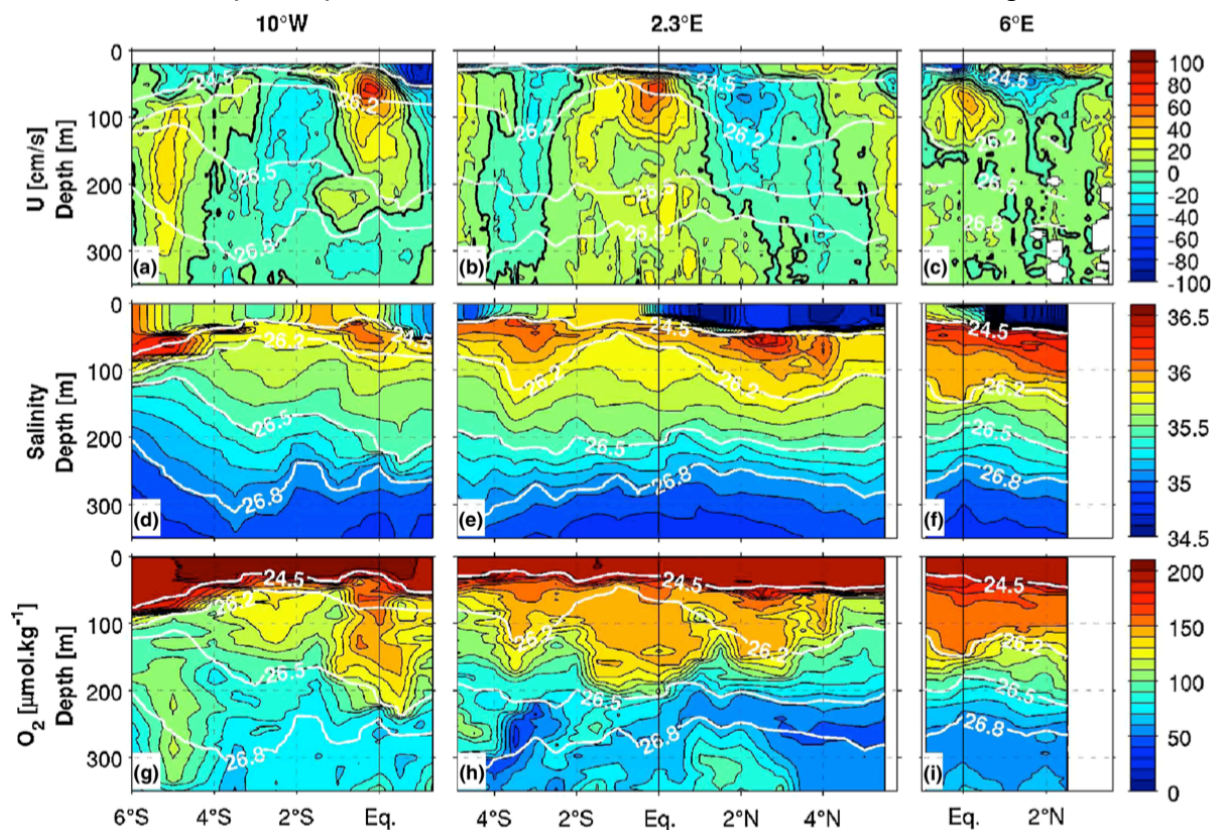


Fig. 4.1: Meridional sections at 10°W (left column), 2.3°E (central column) and 6°E (right column) of zonal (upper, in cm s^{-1} ; isotach 0 in bold), salinity (middle) and dissolved oxygen (lower, in $\mu\text{mol kg}^{-1}$) as measured during the EGEE5 cruise in June 2007. Isopycnals 24.5, 26.2, 26.5 and 26.8 are superimposed in solid white lines.

At 2.3°E, this extra-equatorial westward recirculation of EUC water masses is more clearly identified through the presence of two maxima of salinity (up to 36.2) and oxygen ($140 \mu\text{mol kg}^{-1}$) near 3°S and 3°N, with values comparable with those at 6°E. Contrary to 6°E, the high salinity cores off the equator are clearly distinct from the equatorial salinity maximum related to the EUC core (Fig. 4.1e). The total transports of these westward flows within the upper thermocline are 5.5 and 2.0 Sv respectively north and south of the equator, leading to a total extra-equatorial westward transport of 7.5 Sv in the upper thermocline. These results are comparable with the observations made in March 1995 at 3°E by Mercier et al. (2003).

At 10°W, a westward current is still found in the thermocline between 1°S and 3°S (Fig. 4.1a). This current is still associated with a relative maximum of oxygen (up to $120 \mu\text{mol kg}^{-1}$), but no longer with a local salinity maximum. However, the horizontal distribution of salinity and oxygen in the upper thermocline at 2.3°E and 10°W around 3°S strongly suggests the continuity of the westward extra-equatorial circulations of saline water masses originating from the EUC.

4.3. Seasonal variability of the upper EUC water mass

We now focus on the time evolution of vertical average of salinity and the zonal transport in the upper thermocline ($\sigma_\theta = 24.5\text{--}26.2$ isopycnal range) - i.e. where the salinity maximum associated with the EUC core is confined - as observed from all the individual Argo profiles available from 2004 to 2012 (Fig. 4.2) and seven cruises available from June to November between 2000 and 2007 (Fig. 4.3).

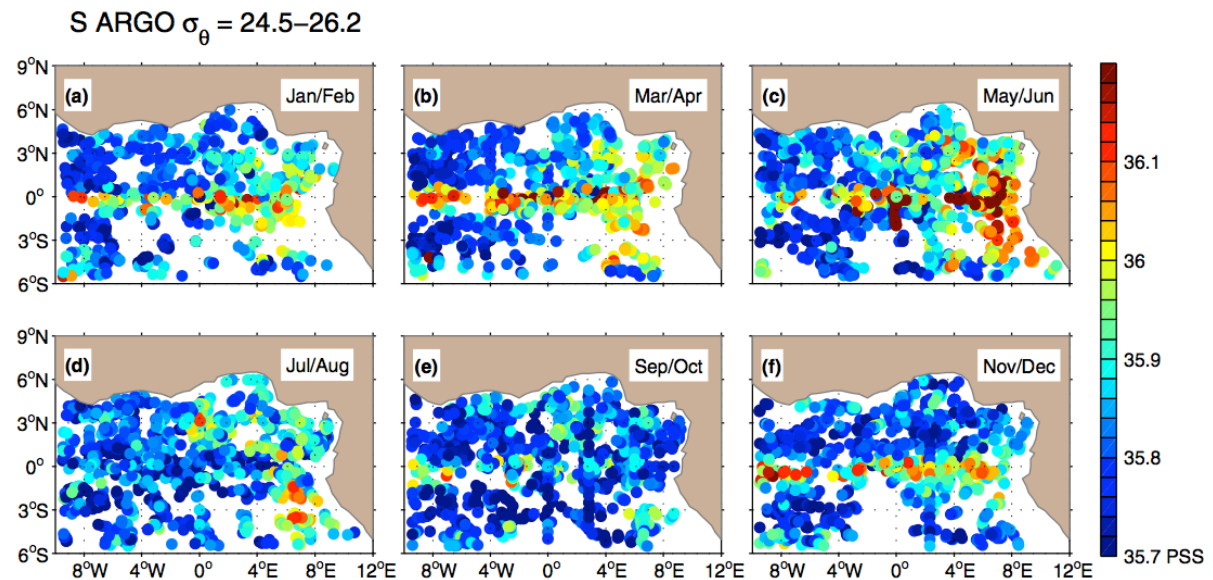


Fig. 4.2: Bi-monthly climatology of mean upper thermocline salinity (*shaded color*; in PSS) from each available Argo profiles in the GG between 2004 and 2012.

In the GG, the coverage of Argo profiles is sufficient to depict the climatological seasonal variability of the mean salinity within the upper thermocline (Fig. 4.2). In spite of possible intra-seasonal and inter-annual variability in the data, a robust seasonal cycle is observed. From January– February to May–June (Fig. 4.2a–c), the upper thermocline is characterized by a tongue of high saline water masses (up to 36.1 PSS) along the equator (within a $\pm 1.5^\circ$ latitude band) extending over the whole

GG. In the eastern GG, these saline water masses progressively spread off the equator, and westward along 3°N–S until May–June. During July–August (Fig. 4.2d), the mean salinity in the upper thermocline dramatically weakens down to 35.7 PSS along the equator, while the extra equatorial maxima of salinity remain present east of 0°E. From September–October (Fig. 4.2e–f), the equatorial salinity maximum first reforms west of 0°E, before extending again over the whole GG in November–December (Fig. 4.2), while the extra-equatorial maxima progressively disappear during this season.

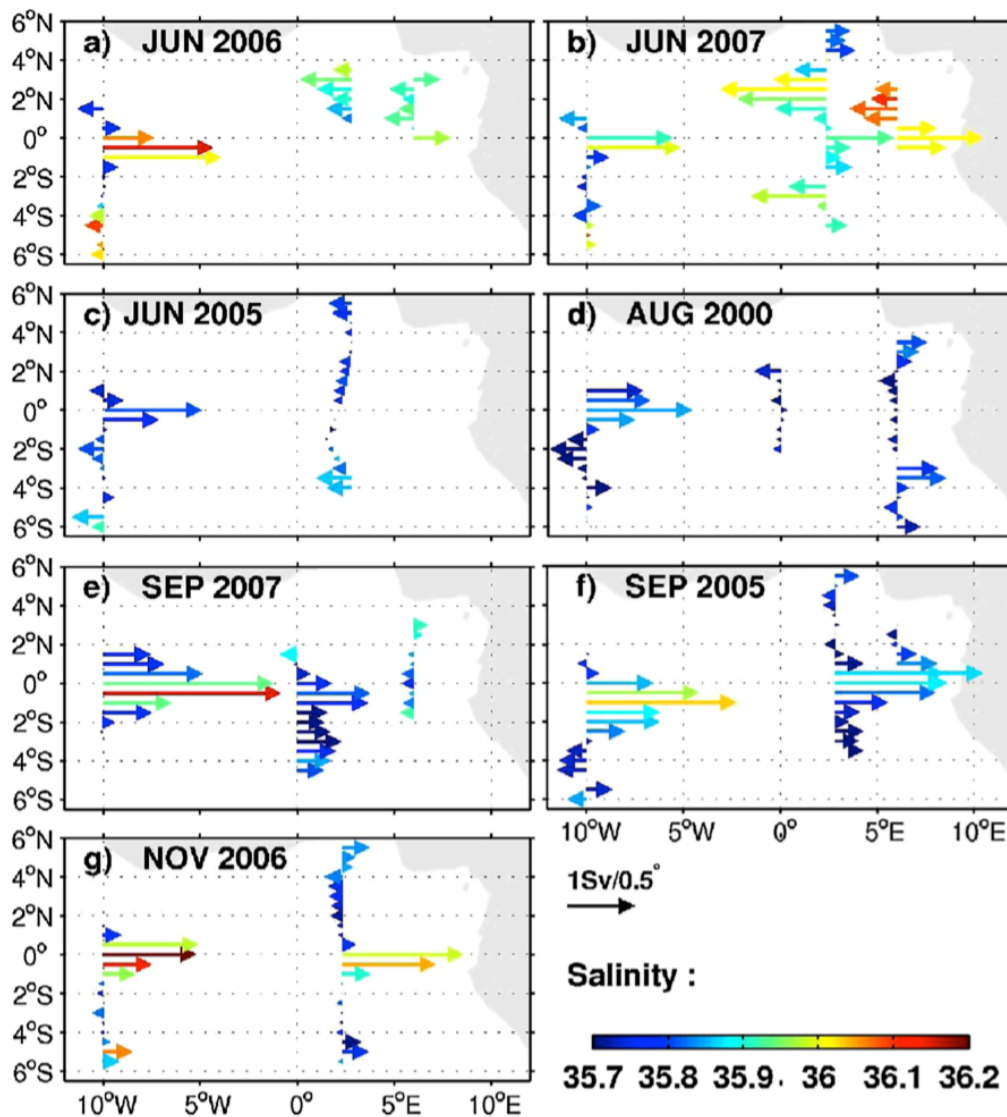


Fig. 4.3: Zonal transport per 0.5° of latitude (*arrows*; in Sv) and mean salinity (*color*; in PSS) in the upper thermocline (24.5–26.2 isopycnal layer) during each cruise.

The seven cruises carried out in the GG between 2000 and 2007 allow us to describe the salinity and the associated horizontal transport distribution during the summer to fall season. During June 2006 and 2007, the year-to-year distribution of salinity and transport presents qualitatively common features (Fig. 4.2a, b), e.g. the EUC is observed along the equator from 10°W to 6°E with salinities greater than 35.9. As described in the previous section, westward recirculations are observed north and south of the equator in June 2007 at 2.3°E and north of the equator at 6°E, transporting salty waters with comparable salinity values as for the EUC at the

equator (Fig. 4.2b). A similar recirculation is suggested north of the equator across 6°E and 2.5°E in June 2006 (Fig. 4.3a), but there is no data for this cruise to confirm its existence in the southern hemisphere. During June 2006 and 2007, the salinity distribution agrees qualitatively well with the seasonal one given from Argo data (Fig. 4.2c).

Nevertheless, during June 2005 and August 2000 (Fig. 4.3c, d), the salinity distribution clearly differ from the seasonal picture given from Argo data during May–June (Fig. 4.2c) and July–August (Fig. 4.2d), whereas the horizontal distribution of transports are alike during June 2005 and August 2000. During both cruises, the EUC is only present at 10°W, but the associated salinity maximum is weaker than the corresponding bi-monthly distribution suggested in Argo data. At 2.3°E (in June 2005) and 0°E (in August 2000), zonal transports at the equator are weak, even westward, suggesting that the upper EUC does not penetrate in the eastern GG during these two cruises. In June 2005 at 2.3°E, extra-equatorial salinity maxima are weaker than the ones obtained in May–June from Argo data, and associated with weak westward transports. In August 2000 at 6°E, weak extra-equatorial salinity maxima are observed on both sides of the equator near 3°S and 3°N, associated with eastward flows. The June 2005 and August 2000 cruises data strongly suggest that interannual variability may strongly modulate the mean seasonal variability deduced from Argo measurements.

In September 2005 and 2007 and November 2006 (Fig. 4.2e–g), the EUC is again observed in the upper thermocline with a high salinity signature, in agreement with salinity Argo distribution during this year period (Fig. 4.2e, f). In early September (2007), the upper EUC does not reach 6°E and salinity is weaker than 35.8 near 0°E (Fig. 4.3e). In contrast, in late September (2005), the EUC is present from 10°W to 6°E, and carries salinity of about 35.9 at 2.3°E and 6°E (Fig. 4.2f). In November 2006 (Fig. 4.3g), the EUC is associated with salinities greater than 36.0 at 2.3°E. This suggests a progressive eastward penetration of the EUC and saline water masses along the equator from late boreal summer to mid boreal fall, thus supplying again the GG with high salinity waters of subtropical origin. In agreement with Argo data, neither salinity maximum nor intense westward recirculations are observed off the equator during these three cruises.

4.4. Seasonal variability of the EUC termination in the model

4.4.1. EUC termination and circulation of saline water masses

To infer in more details the horizontal structure of the upper thermocline circulation in the GG and overview its complete seasonal cycle, we now analyze the bi-monthly climatological horizontal distribution of mean salinity and transports within the upper thermocline, calculated from the 1993–2007 NEMO simulation (Fig. 4.4).

From May to November (Fig. 4.4c–f), the seasonal evolutions of zonal transport and salinity in the upper thermocline are qualitatively in good agreement with the descriptions provided in the previous section: (i) the EUC slightly weakens from May, then strongly diminishes and disappears east of 5°E during July–August (Fig. 4.4c–d). It strengthens in September–October when it is present again until the African coast (Fig. 4.4e); (ii) extra-equatorial westward transport are intensified between 2°

and 3° in both hemispheres from May to July (Fig. 4.4c–d); (iii) a strong salinity maximum is present near the equator in May–June (Fig. 4.4c), is largely eroded in July–August (Fig. 4.4d) and reappears from the west in September (Fig. 4.4e); (iv) extra-equatorial salinity maxima are observed from May to August near 3°N and 3°S (Fig. 4.4c, d). These extra-equatorial high salinities are spatially connected to the EUC salinity maximum in May–June in the eastern half of the GG (Fig. 4.4c). Then they persist in time, despite the disappearance of the EUC salinity maximum in boreal summer, until appearing as local salinity maxima near 4°S and 4°N in July–August. During late summer and fall, the southern salinity maximum slightly moves southward, probably advected by the poleward transport (Fig. 4.4d–f). The close qualitative agreement between the bi-monthly climatology from the model and the in-situ observations (Fig. 4.2, Fig. 4.3) confirms that the model is able to reasonably reproduce the salient features of the seasonal cycle in the upper thermocline.

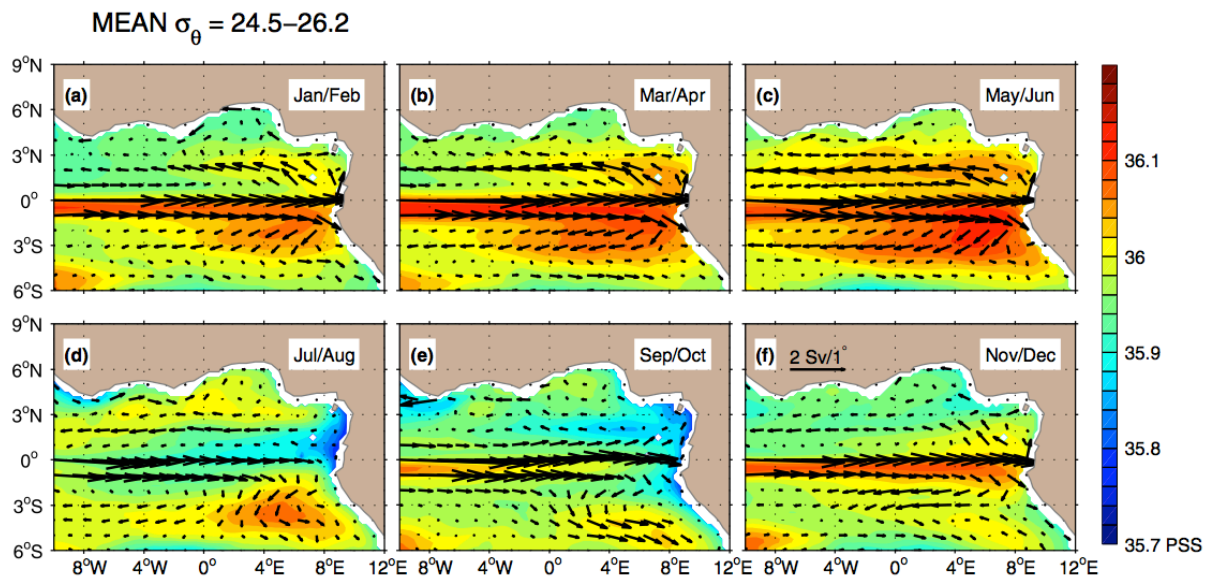


Fig. 4.4: Bi-monthly climatology of the transport per unit of latitude/longitude (arrows; scaling provided in the bottom/right panel) and mean salinity (shaded color) in the 24.5–26.2 isopycnal layer in the model.

The model outputs allow us also to describe the poorly documented variability of the upper EUC termination and salinity from November to May. During this period, the upper EUC transports high subtropical saline waters along the equator to the eastern GG (Fig. 4.4f,a–c). At the African coast the EUC flow and its associated saline waters bifurcate meridionally and progressively reform the extra-equatorial maxima between 1.5–3.5°N–S. From January–May, the extra-equatorial westward flow in the upper thermocline transports the saline waters masses westward (Fig. 4.4a–c).

Note that, in the southern hemisphere a very small poleward transport along the African coast is observed in the upper thermocline, amounting to only 0.2 ± 0.6 Sv across 5°S between 9°E and the coast. Between May and August, the southward export along the African coast is 0.2 Sv while the salinity maximum is eroded in this region. This transport along the African coast is even observed to reverse in September–November (~ 0.2 Sv northward), while the salinity is minimum. The poleward transport is maximum during the winter (~ 0.4 Sv in December–February),

while the salinity re-increases south of the equator along the African coast. Thus, although a direct export of EUC water masses along the African coast found in the model in the coastal GCUC, as previously suggested by Wacongne and Piton (1992), it only represents a very small part of the EUC transport. The EUC recirculates primarily in the westward extra-equatorial branches of the SEC.

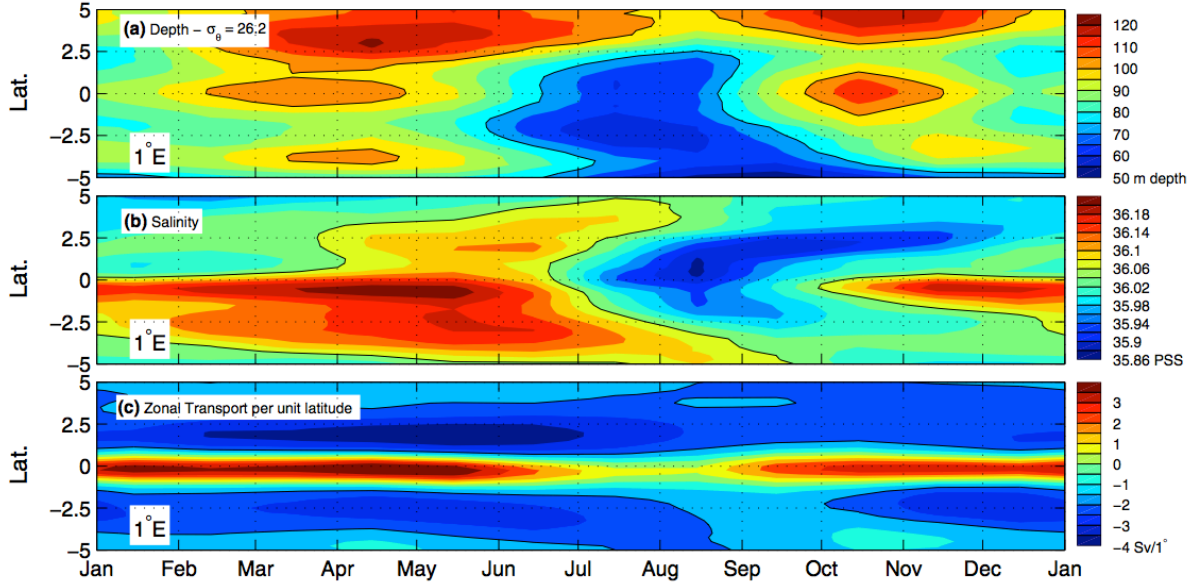


Fig. 4.5: Time-latitude diagrams of the mean seasonal cycle at 1°E between 5°S-N of a) $\sigma_\theta = 26.2$ isopycnal depth (in m, *black contour* interval is 20 m), b) vertically-averaged salinity within the upper thermocline (*black contour* is 36 PSS) and c) zonal transport per unit latitude in the upper thermocline (in Sv/1°, *black contour* is 0 Sv/1°).

In order to better describe the seasonal evolution of the upper thermocline in the GG, we computed the monthly climatology of the depth of the thermocline (materialized here by $r_h = 26.2$ isopycnal depth), the vertically-averaged salinity and the zonal transport in the upper thermocline in time-latitude diagrams along 1°E in the center of the GG (Fig. 4.5). At the equator, the depth of the $\sigma_\theta = 26.2$ and the salinity both exhibit two minima during a climatological year, with the salinity lagging the $\sigma_\theta = 26.2$ depth by about 1 month (Fig. 4.5a, b). For instance, a first strong minimum in the $\sigma_\theta = 26.2$ depth is observed from June–July to September, while it is observed from July to October for the salinity. The $\sigma_\theta = 26.2$ depth experiences a second weaker minimum in December, leading the second salinity relative minimum observed in January (Fig. 4.5a, b). On the other hand, the upper EUC transport shows only one minimum in July–August (Fig. 4.5c).

Off the equator, the $\sigma_\theta = 26.2$ depth is also subject to a semi-annual cycle, with a first strong maximum in March–April and a second maximum of weaker amplitude in October–November (Fig. 4.5a). In contrast, the extra-equatorial salinity exhibits a dominant annual cycle, with minimum values from September to January (Fig. 4.5b). At the equator during the late spring, the salinity decreases concomitantly to the $\sigma_\theta = 26.2$ depth and transport, and leads the more progressive poleward erosion of the salinity maxima. Off the equator, from December until the following summer, the salinity maxima are reformed around 2.5°N–S, concomitantly to the deepening of the $\sigma_\theta = 26.2$ depth and the increase of the westward transports (Fig. 4.5a–c).

The cycle of these three quantities suggests different processes for the boreal summer erosion of the salinity maxima in the GG. At the equator, the strong shallowing of the upper thermocline may contribute to bring its waters near the surface and to increase the vertical shear between the EUC and the surface westward SEC, leading to an enhanced mixing with the surface fresher waters. On the other hand, the dramatic weakening of the EUC transport, starting in late boreal spring, interrupts the supply of saline waters toward the GG. In order to get more insight into the contribution of both advection and mixing in the erosion of saline water, we have computed, in the next section, the seasonal salinity budget in the upper thermocline of the eastern GG.

4.4.2. Seasonal box-averaged salinity budget in the upper thermocline

In order to quantify the role of the ocean circulation (i.e. upper EUC and extra-equatorial recirculation) for the seasonal salinity budget of the upper thermocline, the eastern GG (between 4°W and the African coast) has been decomposed into 3 boxes (Fig. 4.6): an equatorial box (box 1) between 1.5°S and 1.5°N to represent the upper EUC contribution, a northern box (box 2) between 1.5°N to 5°N and a southern box (box 3) between 1.5°S and 5°S to represent the contributions of the extra-equatorial recirculations on both sides of the equator.

To facilitate the comparison with Fig. 4.4, we define the mean upper thermocline salinity S_v inside each box as:

$$S_v(t) = \frac{1}{v} \int_{y_S}^{y_N} \int_{x_W}^{x_E} \int_{-h_2}^{-h_1} S(x, y, z, t) dx dy dz \quad (1)$$

where v is the total volume of the upper thermocline inside the box.

$$v = \int_{y_S}^{y_N} \int_{x_W}^{x_E} \int_{-h_2}^{-h_1} dx dy dz \quad (2)$$

and $S(x, y, z, t)$ is the local salinity at each grid point, y_S and y_N the latitudes of the southern and northern limits of the box, x_W and x_E the longitudes of the western and eastern limits of the box, and $h_1(x, y, z, t)$ and $h_2(x, y, z, t)$ the depths of the $\sigma_\theta = 24.5$ and $\sigma_\theta = 26.2$ isopycnals which delimit the upper thermocline.

The salinity budget applied to S_v writes:

$$\begin{aligned} \frac{dS_v}{dt} = & -\frac{1}{v} \left[\int_{y_S}^{y_N} \int_{-h_2}^{-h_1} u(S - S_v) dz dy \right]_{x_W}^{x_E} \\ & - \frac{1}{v} \left[\int_{x_W}^{x_E} \int_{-h_2}^{-h_1} v(S - S_v) dz dx \right]_{y_S}^{y_N} \\ & - \frac{1}{v} \langle w_1^c (S_1 - S_v) \rangle + \frac{1}{v} \langle w_2^c (S_2 - S_v) \rangle + Res \end{aligned} \quad (3)$$

where u and v are the zonal and meridional components of the velocity. The bracket operator denotes the horizontal average over the box: $\langle . \rangle = \int_{x_W}^{x_E} \int_{y_S}^{y_N} . dx dy$. Finally, w_1^c and w_2^c are the diapycnal velocities across the $\sigma_\theta = 24.5$ and $\sigma_\theta = 26.2$ surfaces defined as:

$$w_i^c = w_{-h_i} - \frac{\partial h_i}{\partial t} - u \frac{\partial h_i}{\partial x} - v \frac{\partial h_i}{\partial y} \quad (4)$$

where $i = \{1, 2\}$ denotes the $\sigma_\theta = 24.5$ and $\sigma_\theta = 26.2$ surfaces and w_{h_i} is the local vertical velocity at depth h_i . The salinity budget (3) is computed offline from the 5-day outputs of the model. In this section, we will only present the monthly climatology of each term of Eq. (3) for the different boxes.

The lhs term of Eq. (3) represents the rate of change of the mean upper thermocline salinity inside the box (in PSS month⁻¹). The first and second rhs terms represent the zonal and meridional divergence of salinity flux in the box. The third and fourth rhs terms represent the cross-isopycnal advective flux of salinity; and *Res* is the residual term induced by the vertical and horizontal diffusivity, and all nonlinear processes that are filtered out in the 5-day outputs of the model. Note, in particular, that the contributions of the intra-seasonal variability, that is known to be important near the equator in the GG (e.g.: Athie and Marin (2008) Coëtlogon et al. (2010); Han et al. (2008a); Jouanno et al. (2013)), to the meridional eddy fluxes (Coëtlogon et al. 2010; Peter et al. 2006) or to the vertical turbulent mixing above the EUC (Jouanno et al. 2013), cannot be estimated correctly from the 5-day outputs of the model and will thus be included in the residual term.

In Box 1 (Fig. 4.6a), the salinity change rate reveals two maxima/minima during a climatological year (Fig. 4.6a, red curve) with a first strongest minimum in June–July (-0.08 PSS month⁻¹) and a second weaker in December (-0.01 PSS month⁻¹). This agrees with the seasonal evolution of the equatorial salinity maximum in the upper thermocline depicted in the previous sections (see Fig. 4.4, Fig. 4.5). From September to May, the zonal advection of the salinity (Fig. 4.6a, solid blue curve), mainly due to the zonal divergence in the EUC salinity flux, explains the largest part of this semi-annual cycle. It is partly compensated by the meridional recirculation of EUC salinity in the eastern GG (dashed blue curve). The weakening of the EUC zonal salinity flux and the enhancement of the meridional divergence of the salinity flux contributes to about 25 % of the salinity loss in June–July, during which the residual term (Fig. 4.6a, solid and dashed black curve) dominates the salinity budget. This suggests that the erosion of the salinity maximum in the EUC core during the cold tongue season is mainly due to enhanced mixing. Note the significant contribution, in April–June, of the diapycnal advective salinity flux mainly through the $\sigma_\theta = 24.5$ surface, that acts to increase salinity and largely compensate the residual term during boreal spring.

The salinity budget in the northern Box 2 is depicted in Fig. 4.6b. In contrast with the equatorial Box 1, the salinity change rate (Fig. 4.6b, red curve) presents a predominant annual cycle characterized by a salinity increase from October to April (maximum 0.02 PSS month⁻¹), and a salinity decrease from May to October (minimum -0.04 PSS month⁻¹). During the winter–spring season, the salinity increase

is mainly explained by the meridional advection of salinity into the box (Fig. 4.6b, dashed blue curve), while during the boreal late spring and summer, the loss is mainly explained by the residual term (Fig. 4.6b, dashed black curve), i.e. mixing. The diapycnal flux of salt remains negligible throughout the year (Fig. 4.6b, green curve).

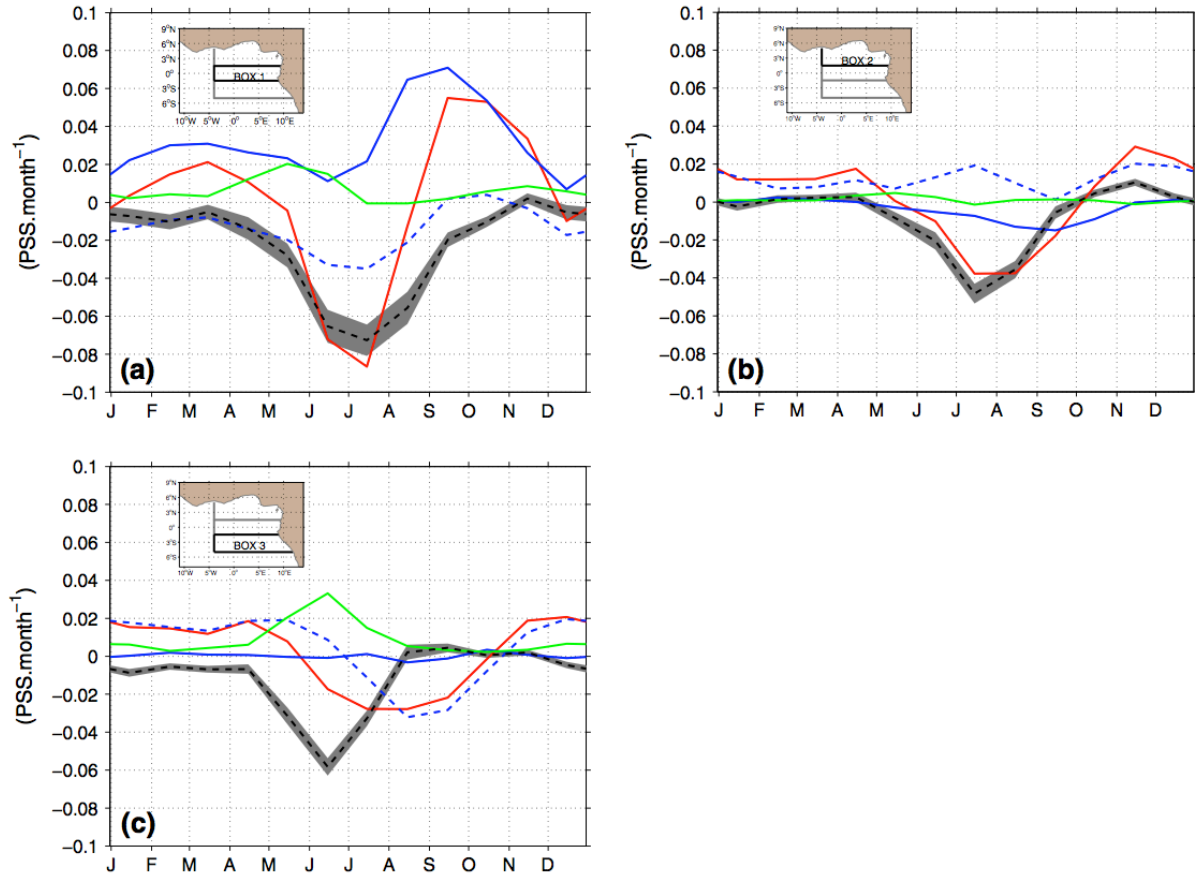


Fig. 4.6: Seasonal box-averaged salinity budget (in PSS month⁻¹) within the $\sigma_\theta = 24.5\text{--}26.2$ layer in the equatorial box 1 (a), the northern box 2 (b) and the southern box 3 (c), as defined in each subfigure mini-map. The box-averaged salinity budget is decomposed in the salinity change rate (red), zonal (solid blue) and meridional (dashed blue) salinity divergence, the salinity divergence due to diapycnal velocities (green) and the residual terms with its uncertainty (black)

In the southern Box 3 (Fig. 4.6c) as for the northern box 2, the salinity change rate (Fig. 4.6c, red curve) shows a dominant annual cycle with a freshening from May to October (minimum -0.03 PSS month⁻¹), and an increase of salinity from September to April (maximum 0.02 PSS month⁻¹), i.e. in phase with the northern and equatorial boxes. The meridional advection of salinity (dashed blue curve) from the EUC recirculation explains the salinity increase from October to April as for the two other boxes. In contrast, from August to October, the meridional advection of salinity across 5°S is the main contributor to the freshening. This freshening can be explained by the southward displacement, in late summer and fall, of the southern salinity maximum, that is observed in the south–eastern part of the GG around $4\text{--}6^\circ\text{S}$ in Fig. 4.4d, e. The residual term only contributes from April to August, participating to the erosion of the salinity maximum in boreal summer, and is partly compensated by the cross-isopycnal advective flux.

In summary, the strong diminution of salinity noticed during the late spring and summer in the equatorial box 1 is firstly explained by the residual term. This term represents the vertical and horizontal mixing that contributes to the bulk of erosion in the upper equatorial thermocline (about 75 %), plus the possible effect of meridional eddy flux due to intra- seasonal variability. The dramatic weakening of the salinity advection by the EUC at 4°W contributes also to about 25 % of the diminution of equatorial salinity. In the extra-equatorial boxes, the mixing term appears also to play a dominant role in eroding the salinity maxima during the late spring and summer, while meridional advection acts to supply extra-equatorial maxima of salinity with saline waters from the EUC in winter and spring. It is also interesting to note the north–south asymmetry during the erosion of extra-equatorial salinity maxima: north of the equator, the salinity erosion is mainly due to mixing, while south of the equator the salinity maximum is first partially eroded by mixing (between May–July) then advected southward.

4.4.3. Role of equatorial zonal wind

In this section, we diagnose the potential mechanisms that could explain the dominant role of the mixing in the seasonal variability of the EUC termination and associated salinity maximum erosion in the eastern GG from the model. As shown by several previous studies (e.g., Arhan et al. (2006); Ding et al. (2009); Hormann and Brandt (2007); Jouanno et al. (2011a); Katz (1984); Kolodziejczyk et al. (2009); Verstraete (1992)), the equatorial zonal wind forcing plays a leading role by driving the surface current and the seasonal baroclinic adjustment of the upper eastern equatorial Atlantic, i.e. by strengthening the vertical shear between the surface and subsurface currents.

Fig. 4.7 presents the seasonal variability of the zonal wind stress (averaged between 1.5°S–N) along the equator. East of 30°W, it shows a seasonal cycle with two maxima/ minima, which acts to seasonally increase (from May to August and from October to January) and decrease (from January to April and from August to October) the permanent Easterlies west of 10°W. In the GG, between 5°W and 5°E, this semi-annual cycle leads to a seasonal reversal of the zonal wind stress between

5°W and 5°E, with strongest Easterlies in May–June and strongest Westerlies in September, and secondary extrema of zonal wind stress anomalies in November (weak Easterlies) and January– February (weak Westerlies). Note the phase lag between the semi-annual cycles west of 10°W and east of 10°W.

We now discuss the seasonal cycle of the EUC and its associated saline waters in the light of the

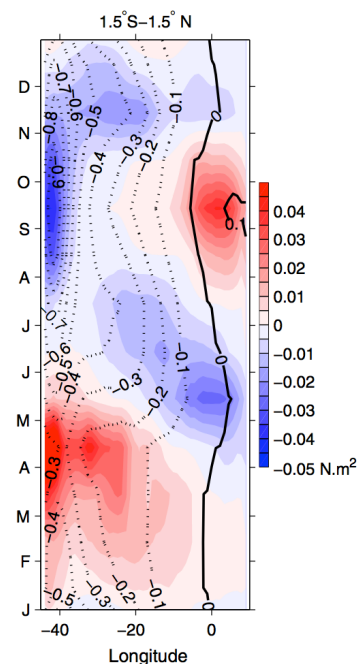


Fig. 4.7: Longitude-time diagram of the mean seasonal anomaly of the zonal wind stress (colors) and total mean zonal wind stress (contours) averaged between 1.5°S–N and between 45°W and 10°E computed from 1993–2007 DFS wind forcing dataset. Unit is N m⁻²

seasonal variability of the equatorial zonal wind and the surface currents. Fig. 4.8 depicts the mean seasonal cycle for the surface zonal currents and upper thermocline depth - materialized by the $\sigma_\theta = 26.2$ isopycnal depth (first column; Fig. 4.8 a, e, i), the vertically-averaged zonal velocities (second column; Fig. 4.8 b, f, j) and salinity (third column Fig. 4.8 c, g, k) in the upper thermocline, and the vertical shear of zonal velocities computed from the surface current and the upper thermocline vertically-averaged velocities (last column; Fig. 4.8 d, h, l).

At the equator, the semi-annual cycle of the zonal wind stress forces a semi-annual cycle of the zonal current at the surface, that manifests by a westward intensification in boreal spring–summer and during November, and an eastward reversal during early fall and winter (Fig. 4.8e; color shading). The seasonal variability of the upper thermocline depth anomalies also presents a semi-annual cycle in quadrature (3-month phase lag) with the semi-annual cycle of the surface current (Fig. 4.8 e). This lag is characteristic of the linear basin mode adjustment to the semi-annual cycle of the equatorial wind stress described in Cane and Moore (1981) or Ding et al. (2009). During the late spring–summer and November–December periods, the intensification of the surface currents and the shallowing of the upper thermocline are concomitant with the erosion of the EUC velocity and its associated salinity maximum (Fig. 4.8 f, g). Hence, as the surface current increases and the thermocline heaves up, the vertical shear between the EUC and the surface current is strongly enhanced at the equator (Fig. 4.8h).

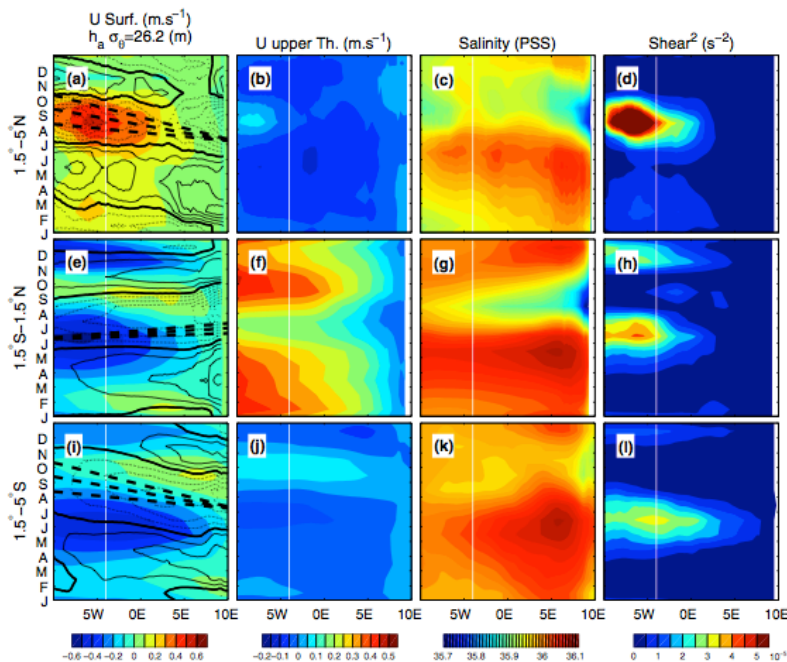


Fig. 4.8: Longitude-time diagrams of mean seasonal cycle of (a) the surface zonal velocities (in m s^{-1}) and the seasonal anomaly of the $\sigma_\theta = 26.2$ depth (in m; CI = 5 m; positive anomalies are in solid line); (b) the EUC mean velocities in the upper thermocline (in m s^{-1}); (c) mean salinity in the upper thermocline (in PSS); and (d) the mean vertical shear (in s^{-2}) between the upper thermocline and the surface averaged between 1.5°N – 5°N . The white line at 4°W materializes the western boundary of the boxes in Fig. 10. (e–h) same as (a–d), but between 1.5°S – 1.5°N . (i–l): same as (a–d), but between 5°S – 1.5°S . The dashed black lines represent the characteristics of the propagation speed respectively for a Kelvin wave of the first (2.14 m s^{-1}), second (1.24 m s^{-1}) and third (0.86 m s^{-1}) baroclinic modes (e); and for long Rossby waves of the first (0.71 m s^{-1}), second (0.41 m s^{-1}) and third (0.29 m s^{-1}) baroclinic modes (in a and i)

North and south of the equator, the upper thermocline depth anomalies (Fig. 4.8a, i) show a seasonal cycle associated with a more marked annual component than at the equator (Fig. 4.8e). In the southern hemisphere, the surface zonal velocities exhibit a semi-annual cycle comparable with those along the equator (Fig. 4.8e, i), while in the northern part of the GG, the currents are mostly eastward with a more marked annual cycle (Fig. 4.8a). The upper thermocline depth anomalies exhibit a westward propagation visible in Fig. 4.8 a and i, that is slower in the southern hemisphere (between second and third baroclinic mode) than in the northern hemisphere (less than the first baroclinic mode). In the upper thermocline layer, the currents are westward on both sides of the EUC and exhibit a weak variability (Fig. 4.8b, j), while the salinity experiences a dominant annual cycle with a weakening from late spring to winter (Fig. 4.8c, k). In the southern hemisphere, the vertical shear of the zonal velocities is enhanced following a semi-annual cycle that is in phase, though of lesser amplitude, with the one at the equator (Fig. 4.8 l, h). In contrast, in the northern hemisphere, the vertical shear is intensified during the westward intensification of the surface currents during the late winter and summer (Fig. 4.8d).

At the equator, these diagnostics suggest that the salinity maximum in the eastern GG is supplied by the EUC, and that the salinity content and the EUC are subject to the same seasonality. In the surface layer above the EUC, the semi-annual cycle of the SEC is associated with the basin adjustment of a second baroclinic basin mode to the semi-annual cycle of the equatorial zonal wind (Ding et al. 2009). This adjustment manifests by the acceleration of the SEC between 5°N–S due to the propagation of westward Rossby waves from the eastern boundary of the GG, that transport the saline water masses westward on the both flanks of the EUC during the boreal late spring. The adjustment is compatible with the propagation velocities observed at the equator and in the southern hemisphere, but not in the northern hemisphere. This discrepancy is probably due to the effects of the northern coast in the GG that dramatically modifies the meridional structure of the equatorial waves (Cane and Sarachik 1983). During the late boreal spring and summer, the intensification of the westward equatorial wind accelerates the SEC at the surface and heaves the thermocline up at depth. The upper thermocline is pinched off and the EUC saline water masses are simultaneously eroded. It results that no more saline waters can be advected in the eastern GG and recirculate in the extra-equatorial branches. The decrease of EUC transport, along with the erosion of its associated salinity maximum, can thus be explained by the vertical mixing induced by the stronger vertical shear between the surface and upper thermocline currents during boreal spring and fall, in agreement with results by Jouanno et al. (2011a).

4.5. Discussion and conclusion

This study describes in a first part the time evolution of EUC water masses during boreal summer in the eastern equatorial Atlantic from a new set of in situ observations including both currents and salinity measurements. It provides strong observational evidence of the existence of an intense seasonal variability of the circulation and salinity in the upper thermocline in the GG from boreal late spring to

fall. The more striking signature of this variability is the presence of westward extra-equatorial recirculations of EUC water masses in late boreal spring (early summer) and the absence of a direct supply of EUC saline water masses from the west in mid and late summer. This is due to (i) the progressive weakening of the upper thermocline EUC in the GG in boreal summer, and (ii) the concomitant erosion of the salinity maximum west of the GG induced by the outcropping of the thermocline in the mixed layer (Verstraete 1992) and/or by enhanced vertical diffusion in the surface layer (Gouriou and Reverdin 1992; Jouanno et al. 2011b). All seven cruises and Argo observations used in this study support this seasonal cycle. Some observed differences between repeated sections however suggest some inter-annual and/or intra-seasonal variability (Marin et al. 2009).

In situ cruises observations used in this study were mostly collected between June and November, thus preventing us from analyzing the complete seasonal cycle of the upper thermocline circulation. Therefore, in order to study the complete seasonal variability of the termination of the EUC and the fate of associated saline waters in the GG, we used validated NEMO model outputs from 1993 to 2007 and compared them with the repeated cruises sections, as previously done at 10°W by Kolodziejczyk et al. (2009).

Simulations of the upper layers of the eastern equatorial Atlantic Ocean are known to be strongly sensitive to the parameterization of the vertical mixing (Blanke and Delecluse 1993; Pacanowski and Philander 1981; Wacongne 1989). Considering the high sensitivity of the EUC properties to the vertical viscosity in the models (Böning and Kröger 2005), vertical mixing is suspected to be responsible for the bias in salinity observed in the upper thermocline in the model, and the discrepancy of the stratification and EUC strength reported in the model validation section. However, in boreal summer the model is qualitatively consistent with the variability observed in our data set but also in several previous observations in the region (Bourlès et al. 2002; Gouriou and Reverdin 1992; Hisard and Morlière 1973; Mercier et al. 2003; Verstraete 1992), thus confirming the seasonal cycle suggested by the sparse observations.

The analysis of the mean seasonal variability of the upper thermocline has established a robust seasonal cycle. The model allowed us to quantify the seasonal salinity budget in the upper thermocline in the eastern GG. It appears first that the amount of saline waters in the upper thermocline of the GG is strongly dependent of the upper EUC transport that contributes to feed the eastern GG and extra-equatorial salinity maxima, mainly during the boreal spring. Such a feature is consistent with the earlier observations made in 1995 by Mercier et al. (2003). A direct poleward recirculation of the EUC water masses along the African Coast in the coastal GCUC was suggested by Wacongne and Piton (1992). Our observations do not allow to sample the GCUC which remains poorly documented in the literature (Wacongne and Piton 1992). The existence of such an along-coast EUC continuation is also suggested in the model. However, it only exports about 0.2 ± 0.6 Sv of upper thermocline water masses southward, which represents only a very small part of the EUC transport.

From May to September, the upper EUC transport in the west of the GG is minimum in the model and advects no more saline water masses into the GG, as suggested by previous observations (Gouriou and Reverdin 1992; Kolodziejczyk et al. 2009). West of 10°W, Jouanno et al. (2011a, b, 2013) demonstrated that the enhancement of vertical mixing during this season strongly contributes to the cooling of the subsurface temperature at the upper bound of the EUC. In the GG, Da-Allada et al. (2014) have recently shown from a numerical study an increase of the mixed layer salinity during boreal late spring and summer. This increase results from the dominance of the vertical diffusion of subsurface saline waters over their freshwater surface advection originating from river run off in the eastern GG during this period. Our study suggests that the intensified vertical mixing also contributes to erode the upper EUC and its salinity maximum not only west of 10°W, thus explaining the reduction of the saline waters advected in the eastern GG, but also in the GG between 4°S and 4°N to locally entrain waters from the upper EUC into the surface mixed layer. The vertical mixing may contribute to the progressive erosion of the equatorial and extra-equatorial maxima of salinity during boreal summer, in agreement with the enhancement of our residual term of salinity (loss) during this season. However, in the GG, the local vertical mixing may be not the unique mechanism responsible for the seasonal erosion of salinity, and our results indeed indicate that the contribution of horizontal advection to the seasonal cycle is also important, in particular during the second part of the year (Fig. 4.5). Though the vertical mixing is not as strong in the eastern as in the western GG, it remains a dominant contributor to the mixed layer heat budget (Jouanno et al. 2011a, b; Da-Allada et al. 2014, Berger et al. 2014) and to the upper salinity budget (Da-Allada et al. 2013). In the GG, the contribution of vertical mixing to the salinity budget in the eastern GG can also be distant, through the advection of less saline waters that have been previously freshened through turbulent vertical mixing by surface waters in the west (between 20°W and 0°E). In the easternmost part of the GG, the strong surface desalinization due to the rivers' runoff is likely to also play a significant role in the dynamical and salinity balance of the upper GG (Hisard 1973; Jouanno et al. 2011a; Da-Allada et al. 2013). Following model results from Berger et al. (2014), the lateral mixing and eddy diffusivity could also play a significant role in eroding the EUC and extra-equatorial salinity maximum. Finally, some intra-seasonal features like the 15-day variability observed near the equator in the GG (Athie and Marin 2008; Coëtlogon et al. 2010; Jouanno et al. 2013), could contribute to the erosion of salt during boreal summer.

From boreal fall to winter, the EUC appears to reinforce in the upper thermocline, bringing back saline water masses into the eastern GG, which progressively spreads along the coast in the equatorial band and supplies again the extra-equatorial salinity maxima. During December-January, the salinity and upper thermocline are slightly eroded. This is reminiscent to the reinforcement of the surface current and of the second weaker upwelling that is present from November to January in the central and eastern equatorial Atlantic, as suggested by Arhan et al. (2006), Okumura and Xie (2006), Ding et al. (2009) or Jouanno et al. (2011a).

Ding et al. (2009) have studied the seasonal cycle of the sea surface height (SSH) and surface currents in equatorial Atlantic. They have shown that the thermocline and surface currents adjust to the semi-annual cycle of the zonal wind over the Atlantic basin. The reinforcement of the wind during boreal spring and fall induces the semi-annual intensification of the surface currents and of the thermocline upwelling in the GG that is in return enhanced by a semi-annual basin mode. Some other studies (e.g., Houghton 1983; Hormann and Brandt 2007; Ding et al. 2009) have linked the seasonal variability in the upper ocean in the GG to a basin scale adjustment to the seasonal variations in easterlies. This equatorial adjustment manifests in late boreal spring by the propagation of an upwelling Kelvin wave that reflects into equatorial Rossby waves at the African coast (Ding et al. 2009; Philander and Pacanowski 1986). The semi-annual reinforcement of the surface currents plays a key role in the enhancement of turbulent mixing that erodes the upper EUC in the central Atlantic (Jouanno et al. 2011a).

An important aspect of the variability of the termination of the EUC in the GG is the fate of its saline water masses of subtropical origin involved in the larger meridional circulation of STC and TC (e.g., Blanke et al. (2002); Hazeleger and de Vries (2003); Molinari et al. (2003); Snowden and Molinari (2003); Wang (2005); Zhang et al. (2003)). The seasonal variability of the EUC termination and associated salinity maximum inferred from both the observations and the model reveals slightly different features than the STC mean circulation picture. During the first part of the year, the EUC water masses rather appears to join the eastern boundary of the equatorial Atlantic and to recirculate off the equator within the upper thermocline, without any contact with the surface. During boreal spring and summer, and November–December, the erosion of the upper EUC termination and saline waters is strongly associated with the upwelling intensity through vertical advection and mixing. The exact contribution of this seasonal cycle for the mean view of the STC would require further analysis.

5 Mean meridional currents in the central and eastern equatorial Atlantic

Authors: R.C. Perez, V. Hormann, R. Lumpkin, P. Brandt, W.E. Johns, F. Hernandez, C. Schmid, B. Bourlès

Since the late 1990s, several major field programs have been initiated to monitor the circulation, hydrography, and air-sea fluxes in the central and eastern equatorial Atlantic with moored arrays (e.g., Bourles et al. (2008)). Concurrent with these field programs, a large number of cross-equatorial cruises have been conducted primarily along 23°W and 10°W to survey zonal and meridional currents with shipboard and lowered acoustic Doppler current profilers (ADCPs) as well as temperature, salinity, and dissolved oxygen. These cruises were also used to opportunistically deploy satellite-tracked drifting buoys (hereafter “drifters”) and Argo floats. With these measurements, as well as data collected by earlier programs such as the Seasonal Response of the Equatorial Atlantic (SEQUAL) and Programme Française Océan-Climat en Atlantique Equatorial (FOCAL) programs, much has been learned about the mean cross-equatorial structure and seasonal-to-interannual variability of zonal currents, temperature, salinity, and dissolved oxygen in the upper water column in the central and eastern equatorial Atlantic (e.g., Garzoli (1987); Grodsky et al. (2005); Brandt et al. (2006); Brandt et al. (2008); Brandt et al. (2010); Hormann and Brandt (2007); Hormann and Brandt (2009); Bunge et al. (2007); Kolodziejczyk et al. (2009); Hummels et al. (2013)), but the meridional currents have yet to be examined.

Based on previous analytical and numerical modeling studies (e.g., McCreary and Lu (1994); Liu et al. (1994); Malanotte-Rizzoli et al. (2000); Hazeleger et al. (2003); Schott et al. (2004); Lohmann and Latif (2007)) and observations collected in the tropical Atlantic between 40°W and 30°W (e.g., Molinari et al. (2003)), it is expected that the mean cross-equatorial structure of the meridional currents along 23°W and 10°W will be governed by shallow overturning circulation cells known as tropical cells (TCs) which appear as near-surface, near-equatorial maxima of the much larger subtropical cells. The TCs are confined to the upper 100 m of the water column, and are characterized by wind-driven equatorial upwelling, poleward wind-driven flow in the surface limb, off-equatorial downwelling at about $\pm 3\text{--}5^\circ$ latitude, and equatorward geostrophic flow in the subsurface limb. However, this simple depiction of the flow is complicated by the presence of strong fronts bounding the seasonal equatorial Atlantic cold tongue, which exhibit large undulations due to tropical instability waves (TIWs; e.g., Duing et al. (1975); Steger and Carton (1991); Hormann et al. (2013)). The cold tongue and TIWs are typically most pronounced in boreal summer associated with increased southeasterly trade winds and enhancement of the shear between the equatorial zonal currents (e.g., Legeckis and Reverdin (1987); Steger and Carton 1991; Grodsky et al. (2005); Brandt et al. (2011a); Perez et al. (2012); Hormann et al. 2013). During this time of year, large meridional velocity fluctuations associated with TIWs can be seen in shipboard sections collected along 23°W and 10°W. Because the equatorial Atlantic circulation from the surface down to the thermocline is so profoundly influenced by westward propagating TIWs and other

mesoscale phenomena (e.g., Düing et al. 1975; Weisberg and Weingartner (1988); Menkes et al. (2002); Foltz et al. (2004); Grodsky et al. 2005; Bunge et al. 2007; Dutrieux et al. (2008); von Schuckmann et al. (2008); Jouanno et al. (2013)), to date *in situ* current measurements have been insufficient to estimate the much smaller (on the order of 10 cm s^{-1}) mean meridional currents or their seasonal variations.

Recent studies suggest that meridional currents play an important role in Atlantic meridional mode dynamics by advecting wind-driven warm ocean temperature anomalies induced immediately north of the equator towards the equatorial region and leading to so-called non-canonical Atlantic Niño events in boreal summer and fall (Lübbecke (2013); Richter et al. (2013)). During these non-canonical Atlantic Niño events, equatorial warming by meridional advection was found to be most pronounced in boreal summer between 20 m and 40 m depth (Richter et al. 2013). Meridional currents may similarly contribute to anomalous cooling events in the tropical Atlantic, such as the strong cooling observed in the ATL3 region (i.e., $20^{\circ}\text{W} - 0^{\circ}$, $3^{\circ}\text{S} - 3^{\circ}\text{N}$) from May to July 2009 (Foltz et al. (2012); Brandt et al. (2014)) by advecting subsurface cold temperature anomalies induced in the northern hemisphere.

In this study, measurements collected primarily along 23°W and 10°W during the past two decades are used for the first time to describe: (1) the long-term mean cross-equatorial and vertical structure of the meridional currents in the central and eastern equatorial Atlantic, and (2) the seasonal means during the months December to May (hereafter Dec-May) when the Atlantic cold tongue is absent or weak and June to November (hereafter Jun-Nov) when the cold tongue is most pronounced and meridional velocity may play a role in the development of non-canonical Atlantic Niño events.

5.1 Data sets, reanalysis products, and methods

5.1.1. Shipboard data

Shipboard data were obtained during March 1996 to August 2011 from 36 latitude-depth transects in the central (between 22°W and 29°W , nominally 23°W) and 19 transects in the eastern (10°W) equatorial Atlantic (Fig. 1b). Most of these sections are presented in Brandt et al. (2006); Brandt et al. (2010) and Kolodziejczyk et al. (2009), and additional sections are available from recent Prediction and Research Moored Array in the Tropical Atlantic (PIRATA) Northeast Extension (PNE; cf. Hormann et al. 2013) and Tropical Atlantic Circulation Experiment - Equatorial Undercurrent (TACE-EUC; cf. Subramaniam et al. (2013)) cruises. The individual transects resolve the flow from the near surface (typically 30 m) down to some intermediate depth (250 m or deeper). Uncertainties of hourly shipboard ADCP (SADCP) averages were estimated to be better than $2\text{-}4 \text{ cm s}^{-1}$ (Fischer et al. 2003) while the accuracy of lowered ADCP (LADCP) data was assumed to be better than 5 cm s^{-1} (Visbeck 2002). Despite the larger LADCP uncertainty, we retain these data as calibrated SADCP measurements were not available for three January sections along 23°W which represent the only realizations for this month. When both LADCP and SADCP measurements are available, the current data are merged with respect to the higher accuracy and better horizontal resolution of the SADCP measurements

– SADCP measurements are weighted up to five times more strongly than LADCP measurements. The merged data are mapped onto a uniform 0.05° latitude by 10 m depth grid using a Gaussian interpolation scheme with horizontal and vertical cutoff radii of twice the grid resolution (see Brandt et al. 2010 for details). Calibrated hydrographic parameters (temperature, salinity, and dissolved oxygen) are not available for all of the cruises along 23°W and 10°W . Hence, the ship-based ADCP measurements were merged and averaged in depth coordinates rather than isopycnal coordinates (e.g., Johnson et al. (2002)).

Although shipboard sections have been collected during all four seasons, there are seasonal sampling biases with the majority of samples collected during boreal spring along 23°W and during boreal summer along 10°W . Despite these seasonal biases, the samples along 23°W are distributed in such a way that they can be partitioned fairly evenly into boreal winter and spring (21 samples during Dec-May) and summer and fall (15 samples during Jun-Nov). There are too few samples to perform a similar meaningful seasonal breakdown along 10°W . With the exception of June 2006 when multiple sections were collected in one month, individual cruises typically occur several months apart from one another, and we assume that each section represents an independent sample. The presence of TIWs, which have periodicities of 14 to 50 days and $O(1000 \text{ km})$ zonal wavelengths (e.g., Legeckis (1977); Qiao and Weisberg (1995); Athie and Marin (2008)), allows us to assume that the meridional velocity sections collected in June 2006 are also independent of one another.

5.1.2. Drifter and Argo data

As the currents above 30 m are not well resolved by the ship-based ADCP instruments, velocity measurements obtained from satellite-tracked drifters collected in the region bounded by $30^\circ\text{W} - 8^\circ\text{W}$, $20^\circ\text{S} - 20^\circ\text{N}$ and spanning the period July 9, 1992 to June 30, 2012, as well as near-surface velocities constructed from Argo float surface trajectories from July 29, 1997 to May 7, 2013 with the YoMaHa'07 dataset, are used to estimate the mean near-surface currents. Following Lumpkin et al. (2013), an improved technique was used to distinguish drifters that have their drogue attached and follow the ocean currents at 15 m depth with relatively small wind slip from those which have lost their drogue, follow currents nearer the ocean surface, and are subject to larger wind slip. Because of the strong near-surface zonal currents and divergent meridional currents in the equatorial Atlantic, drifters do not typically remain in the region they were deployed and the total number of drifter measurements close to the equator tends to be significantly smaller than the number of measurements a few degrees poleward of the equator. Thus, simply removing the undrogued drifters from the dataset collected in the tropical Atlantic limits the ability to produce a robust estimate of the mean near-surface currents in this region. While at the surface, the Argo floats essentially behave as an undrogued drifter albeit with different wind-slip characteristics, and utilization of the YoMaHa'07 dataset allows for an additional increase in the number of near-surface velocity measurements between 30°W to 8°W and 5°S and 5°N . The Argo float surface drifts, undrogued drifters, and

drogued drifters represent 9%, 24%, and 68%, respectively, of the total drift measurements in that region.

We have applied a wind-slip correction to both drogued and undrogued drifter as well as Argo float near-surface velocity measurements (Niiler and Paduan 1995; Pazan and Niiler 2001) to combine these three types of measurements and estimate the mean 15-m currents in the central and eastern equatorial Atlantic. This corrected velocity can be expressed as:

$$u_{corrected} = u_{uncorrected} - A W_x$$

$$v_{corrected} = v_{uncorrected} - A W_y,$$

where W_x and W_y are the zonal and meridional component of wind velocity (in units of m s^{-1}) from NCEP/NCAR Reanalysis v.2 6-hourly winds and the coefficient $A = 7 \times 10^{-4}$ for drogued drifters and $A = 1.64 \times 10^{-2}$ for undrogued drifters. The coefficient for drogued drifters is the same value as used in Niiler and Paduan (1995). However, the undrogued-drifter coefficient was increased from the Pazan and Niiler (2001) value, $A = 8.6 \times 10^{-3}$, to remove a significant westward bias found in the corrected undrogued zonal velocity relative to the corrected drogued zonal velocity in the central and eastern equatorial Atlantic. The coefficient for the Argo float surface drifts, $A = 1.14 \times 10^{-2}$, is very similar to the undrogued value.

To produce mean velocity estimates along 23°W and 10°W at every 0.5° latitude, the slip corrected drifter and Argo data are grouped into 10° (at 23°W) and 4° (at 10°W) longitudinal bins and 1° latitudinal bins. These different longitudinal windows were chosen (1) to ensure sufficient samples ($N > 539$ drifter-Argo days including 69 float days at 23°W , $N > 120$ drifter-Argo days including 10 float days at 10°W) along both sections between 5°S and 5°N , and (2) to mirror the larger (7°) spread in longitudes for the cruises conducted primarily along 23°W . Within those bins, the observations are treated as time series that are fit via least-squares regression to a model composed of a time-mean value, annual and semiannual harmonics, and linear trends corresponding to the longitudinal and latitudinal distance from the bin center. This minimizes the influence of seasonal and spatial sampling biases on the combined drifter and Argo mean velocity estimates within each bin.

Constant vertical shear is assumed in the upper 30 m to linearly extrapolate the long-term mean ship-based ADCP velocity (section 5.1.1) upwards to the surface (similar to Brandt et al. (2006) and subsequent studies). This constant shear is set by the vertical gradients between the 30-m mean ADCP and the 15-m mean drifter-Argo velocities, and the resulting volume transport in the upper 30 m is equivalent to the volume transport by a well-mixed surface layer with flow in the upper 30 m given by the 15-m mean drifter-Argo velocity (i.e., zero shear). The resulting mean meridional velocity sections will hereafter be referred to as “ADCP+D”.

5.1.3. OSCAR product

Additionally, the long-term mean ship-based ADCP velocity is vertically extrapolated to the surface using the publically-available Ocean Surface Current Analysis Real time (OSCAR) product (e.g., Bonjean and Lagerloef (2002)) often used

to study the tropical Atlantic circulation (e.g., Da-Allada et al. (2013); Helber et al. (2007)). OSCAR provides an independent estimate of the depth-averaged velocity in the upper 30 m of the water column computed from remotely sensed sea surface height (SSH), surface winds, sea surface temperature (SST), and mean dynamic height topography using Ekman, geostrophic, and Stommel shear dynamics. For this study, we use the (spatially filtered) 1° gridded OSCAR product from January 1, 1993 to December 31, 2011, which is available as 5-day averages. The mean ship-based ADCP velocity is then extrapolated to the surface in the same manner as for the combined drifter and Argo data, that is assuming constant vertical shear between the 30-m mean ADCP and the mean OSCAR velocities - hereafter referred to as “ADCP+O”. This provides a means to examine the differences in the mean cross-equatorial and vertical structure of meridional velocity that result from applying a different near-surface velocity product.

5.1.4. Moored current observations

Independent current observations from moored ADCPs in the central and eastern equatorial Atlantic are also used to evaluate the mean ADCP+D currents in the upper 300 m of the water column. Moored ADCP velocity measurements are available along 23°W at 2°S, 0.75°S, 0°, 0.75°N, and 2°N, as well as along 10°W at 0.75°S, 0°, and 0.75°N as daily or 12-hourly averages. The moored ADCP measurements resolve the currents from 15 m (only at equatorial moorings) to 50 m down to an intermediate depth (most commonly 300 m), with vertical range and resolution dependent on factors such as configuration and instrument depth (e.g., Brandt et al. (2006); Brandt et al. (2008); Bunge et al. (2007); Kolodziejczyk et al. (2009); Provost et al. (2004)). Daily averages from single point current meters mounted on the 23°W, 0° - PIRATA backbone mooring at 10 m depth (and 20 m depth during 2008-2009) and the 23°W, 4°N - PNE mooring at 10 m depth provide the only other concurrent time series of velocity in the region above 20 m. Similar to the combined drifter and Argo data (section 5.1.2), the moored velocity observations are fit via least-squares regression to a model composed of a time-mean value, and annual and semiannual harmonics. The seasonal cycle is then removed from the moored data prior to estimating their means to account for potential seasonal sampling biases in the mooring records. Note, due to the only one-year 20-m current meter record at the 23°W, 0° - PIRATA mooring, the seasonal cycle from the moored ADCP data at that depth and location is used to correct for seasonal biases.

5.1.5. Reanalysis product

Output from one of the GLObal Ocean ReanalYsis and Simulations (GLORYS; Ferry et al. (2010)) products is also used to evaluate the mean meridional currents estimated from ADCP+D, ADCP+O, and mooring data along 23°W and 10°W. The GLORYS project is a cooperative initiative between Mercator Océan and the French research community to provide a series of eddy permitting global ocean simulations, based on version 3.1 of the Nucleus for European Models of the Ocean (NEMO) modeling system (Barnier et al. 2006; Madec 2008). Model equations are discretized using the standard ORCA025 configuration which has a tri-polar grid, with nominal

horizontal resolution of $1/4^\circ$ at the equator. The model has 75 vertical levels, with approximately 1-m resolution near the surface and 200-m resolution in the deep ocean. The version of GLORYS used in this study, GLORYS2V1, is forced with ECMWF ERAInterim forcing fields (Simmons et al. 2007). GLORYS2V1 assimilates remotely sensed SST and sea level height information, mean dynamic topography, and *in situ* temperature and salinity data from December 4, 1992 to December 31, 2009 via a reduced order Kalman filter (Tranchant et al. 2008; Tuan Pham et al. 1998) and a double backward incremental analysis technique (Benkiran and Greiner 2008; Bloom et al. 1996).

PIRATA and PNE temperature and salinity data are assimilated by GLORYS2V1, and as a result there is good agreement on intraseasonal to interannual time scales between the 10-m temperature and salinity observations and the global reanalysis at those sites. Although *in situ* velocity measurements are not assimilated, GLORYS2V1 produces relatively unbiased currents that are significantly correlated with the available moored 10-m velocity data at 0° and 4°N along 23°W .

5.2 Results

5.2.1. Cross-equatorial structure of meridional currents

Fig. 5.1 shows the distribution of the long-term mean meridional currents from ADCP+D along 23°W and 10°W , and compares with GLORYS2V1 meridional currents averaged from January 1, 1993 to December 31, 2009. At the surface, maximum mean poleward flow of -7.6 cm s^{-1} is observed at 1.50°S and 13.9 cm s^{-1} at 2.05°N along 23°W (Fig. 5.1a). Similarly, maximum mean poleward flow of -16.4 cm s^{-1} is observed at 3.55°S and 15.2 cm s^{-1} at 0.50°N along 10°W (Fig. 5.1b). The observed poleward surface currents in Fig. 5.1a,b are consistent with the expected mean wind-driven currents in the surface limb of the TCs based on previous TC studies in the western equatorial Atlantic and the central equatorial Pacific (e.g., Johnson et al. (2001); Molinari et al. (2003); Perez et al. (2010)). The thickness of the poleward flow in the surface limb is approximately 30 m in the northern cell and 50 m in the southern cell, consistent with the mean thermocline or pycnocline depth north of 3°S being at least 10 m shallower than south of 3°S (e.g., Brandt et al. (2006); Brandt et al. (2010); Kolodziejczyk et al. (2009)). As a result of the shallower northern cell, the presence of mean northward flow north of the equator in the surface limb is more heavily constrained by the vertical extrapolation to the drifter-Argo data (discussed further in section 5.2.2). The boundary between the surface limb of the northern and southern cells is south of the equator along both longitudes: It is found near 0.35°S along 23°W while it occurs near 1.05°S along 10°W . This off-equatorial location of the transition between the cells has been previously observed from shipboard meridional velocity observations in the western equatorial Atlantic (Molinari et al. 2003) and is consistent with maximum equatorial divergence being found approximately 1° south of the equator in observations and models (e.g., Giordani and Caniaux (2011); Helber et al. (2007); Molinari et al. (2003)).

Below the surface limb, the southward flow north of the equator along 23°W has several local maxima that are part of a broad subsurface equatorward flow between

1°N and 5°N, with strongest flow of -5.9 cm s^{-1} centered at 3.55°N and a depth of 40 m (Fig. 5.1a). This subsurface equatorward flow in the northern hemisphere is less broad in its meridional extent but stronger in magnitude along 10°W , with maximum southward flow of -8.7 cm s^{-1} at 1.6°N and a depth of 50 m (Fig. 5.1b). Subsurface northward flow is found in the southern hemisphere along 23°W , with maximum velocity of 3.6 cm s^{-1} centered at 1.25°S and a depth of 80 m (Fig. 5.1a). In contrast, strong southward flow is found in the southern hemisphere along 10°W between 2°S and the equator reaching -11.8 cm s^{-1} at 0.9°S and 40 m depth, with weaker northward flow only between 4°S and 2°S (Fig. 5.1b). The abrupt nature of this shift from northward to southward flow at 2°S along 10°W is likely due to a significant reduction in the number of samples south of 2°S .

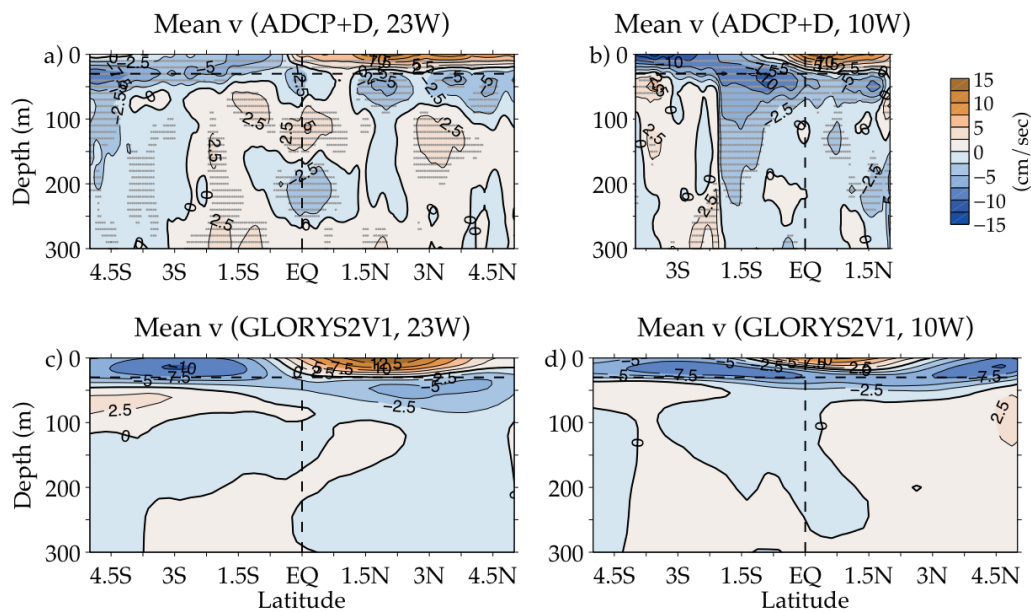


Fig. 5.1: Distribution of long-term mean (a)-(b) observed (ADCP+D) and (c)-(d) GLORYS2V1 meridional velocity along 23°W and 10°W . Mean observed velocity below 30 m (black horizontal dashed line) derived from all available ship-based ADCP measurements, and mean velocity above 30 m is vertically extrapolated to mean velocity generated from the full drifter-Argo record. Gray dots in (a)-(b) indicate statistically significant values. Contour interval is 2.5 cm s^{-1} .

The mean meridional-vertical structure of the currents from GLORYS2V1 (Fig. 5.1c,d) agrees well with the observed structure in the upper 30 m (Fig. 5.1a,b), with stronger poleward velocities north of the equator than south of the equator (14.6 cm s^{-1} compared with -8.3 cm s^{-1} along 23°W , and 10.8 cm s^{-1} compared with -7.7 cm s^{-1} along 10°W), a thinner surface limb in the northern cell than in southern cell along both longitudes, and a southward shift of the northern cell maxima as well as of the boundary between the northern and southern cells between 23°W and 10°W . Near the equator, the observed and GLORYS2V1 subsurface flow structures below 30 m and 100 m bear little resemblance to one another. However, poleward of $\pm 2^\circ$ latitude, the simulated subsurface equatorward flow in that depth range has much in common with the observed flow. Although, the weak mean meridional currents below the TCs in the observations and GLORYS2V1 share some common elements in the southern hemisphere (e.g., the transition from northward to southward flow near 2°S

along 10°W in Fig. 5.1b,d), there is no overall agreement below 100 m in the northern hemisphere.

The observed volume transport associated with the mean TCs,

$$\bar{V}_{\text{int}}(y, -D) = \int_{23\text{W}}^{10\text{W}} \int_{-D}^0 \bar{v}(x, y, z) dz dx,$$

is estimated by averaging the mean ADCP+D meridional velocity (\bar{v}) along 23°W and 10°W, multiplying by their 13°-longitude separation, and integrating over the thickness D of the upper branch of the cell,

$$\bar{V}_{\text{avg}}(y, -D) = \frac{13}{2} \times (111\text{km} \cos \theta) \int_{-D}^0 (\bar{v}(23\text{W}, y, z) + \bar{v}(10\text{W}, y, z)) dz,$$

where θ is the latitude. The observed meridional transport in the surface limb of the southern cell is larger than transport in the surface limb of the northern cell. This is apparent from Fig. 5.2a,b showing the observed meridional transport (black thick lines) in the top $D = 30$ m and 50 m, respectively, which correspond to the mean thicknesses of the surface limb of the northern and southern cells. North of the equator maximum northward transport of 2.3 Sv ($1 \text{ Sv} = 10^6 \text{ m}^3 \text{ s}^{-1}$) is found at 0.55°N (Fig. 5.2a), while south of the equator maximum southward transport of -4.6 Sv occurs at -1.95°S (Fig. 5.2b).

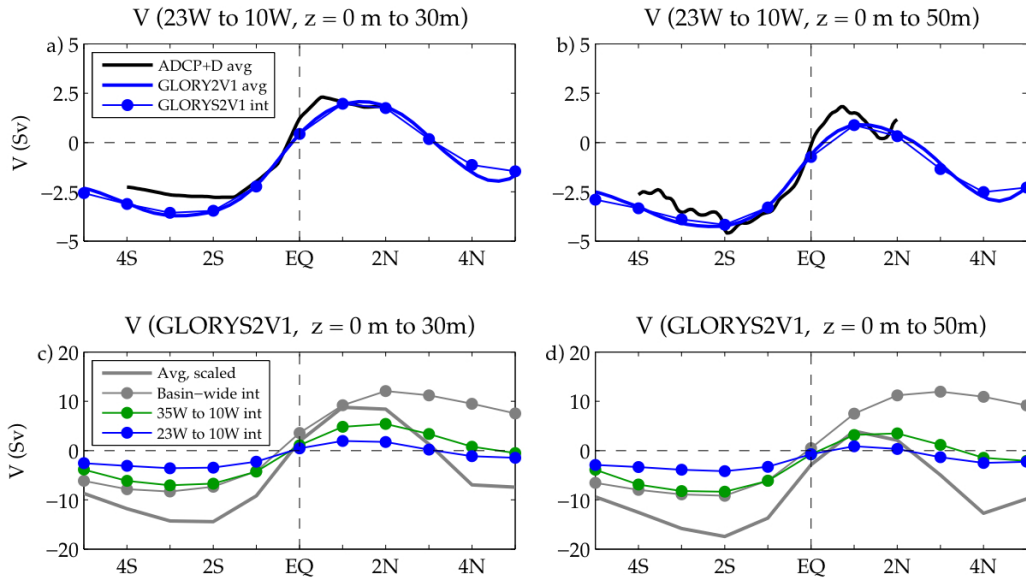


Fig. 5.2: Comparison of long-term mean meridional volume transport integrated from 0 m to 30 m (left) and 0 m to 50 m (right). (a)-(b) Meridional transport between 23°W and 10°W estimated from the average of mean ADCP+D (thick black lines) and simulated (thick blue lines) velocities along 23°W and 10°W, with the zonally-integrated simulated velocity (blue lines with circles) overlaid at select latitudes. (c)-(d) Comparison of the GLORYS2V1 meridional transport zonally integrated between 23°W and 10°W (blue lines with circles), 35°W and 10°W (green lines with circles), and across the basin (gray lines with circles) at selected latitudes, with the transport computed from the average of mean GLORYS2V1 velocities along 23°W and 10°W and scaled by the size of the basin (thick gray lines) overlaid.

The simulated meridional volume transports associated with the mean TCs, estimated from the average of the mean GLORYS2V1 meridional velocity along 23°W and 10°W, are very similar to the observed values (compare blue and black thick lines in Fig. 5.2a,b), with maximum simulated northward transport of 2.1 Sv at 1.35°N for a 30-m thick layer (Fig. 5.2a), and maximum simulated southward

transport of -4.3 Sv at -2.35°S for a 50-m thick layer (Fig. 5.2b). Note, whether the transport is estimated by zonally integrating the mean GLORYS2V1 meridional velocity at all model grid points between 23°W and 10°W (\bar{V}_{int} , blue lines with circles) or just by averaging the meridional velocity along 23°W and 10°W and multiplying by their 13° -longitude separation (\bar{V}_{avg} , thick blue lines), the simulated transports are nearly identical. This suggests that the meridional volume transport varies linearly in longitude between 23°W and 10°W .

Despite the limited observational data, we note that the range and structure in the observed variability of the meridional currents along 23°W and 10°W (Fig. 5.3a,b) is quite similar to the range and structure of the simulated variability (Fig. 5.3c,d). The variability is largest near the surface, with standard deviations at 30 m depth ranging between 10 and 27 cm s^{-1} for the ADCP data and between 12 and 20 cm s^{-1} for GLORYS2V1. For both the model and observations, the variability associated with the mean position of the northern cell tends to be larger than that of the southern cell, and the region of high variability below the surface limb of the northern cell extends deeper along 23°W (Fig. 5.3a,c) than along 10°W (Fig. 5.3b,c). The equatorial asymmetry in the variability of meridional velocity is primarily due to the asymmetric wind forcing in the region associated with the seasonal migration of the Intertropical Convergence Zone (ITCZ) complex (e.g., Helber et al. (2007)), and secondarily due to asymmetric TIW and submonthly-to-intraseasonal wind-forced variability (e.g., Athie and Marin (2008); Athie et al. (2009); Perez et al. (2012)).

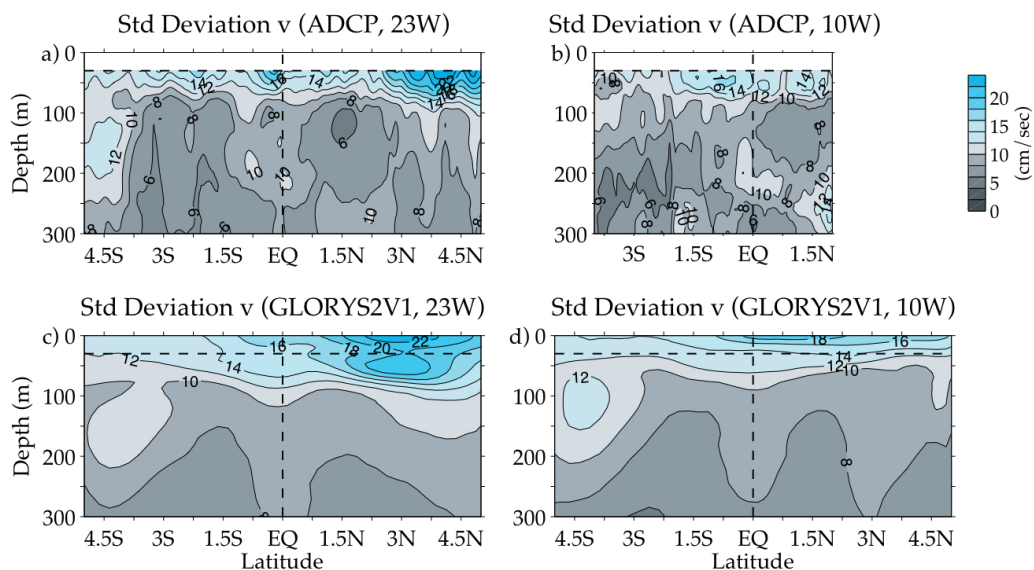


Fig. 5.3: Distribution of the standard deviation of (a)-(b) ship-based ADCP for all available ship-based ADCP measurements and (c)-(d) GLORYS2V1 meridional velocity along 23°W and 10°W . Contour interval is 2 cm s^{-1} .

5.2.2. Comparisons at discrete depths and mooring locations

For both longitudes, the mean ship-based ADCP meridional velocity blended with the mean near-surface velocity from the drifter-Argo data (ADCP+D) at 10 m (Fig. 5.4a,b) and 20 m (Fig. 5.4c,d) depth is compared with the mean ship-based ADCP meridional velocity blended with the mean OSCAR fields (ADCP+O), mean meridional velocities estimated from moored observations in the upper 20 m and the

mean GLORYS2V1 meridional velocities. The meridional structure of the mean ADCP+D meridional velocities (solid black lines) generally agrees well with that of the mean GLORYS2V1 meridional velocities (blue lines). However, the simulated magnitudes can be as much as 5 cm s^{-1} larger than the observed magnitudes along 23°W (Fig. 5.4a,c), and as much as 5 cm s^{-1} smaller than the observed magnitudes north of the equator along 10°W (Fig. 5.4b,d). The ADCP+D, ADCP+O (dashed black lines), and GLORYS2V1 currents overlap within the uncertainty with the relatively weak mean meridional velocities estimated from the moored observations at 0°N and 4°N along 23°W (green and red circles in Fig. 5.4a,c). Unfortunately, moored velocity measurements are not available where the three estimates disagree the most within the latitudes of maximum poleward flow associated with the TCs (typically between $\pm 1^\circ$ and $\pm 4^\circ$ latitude).

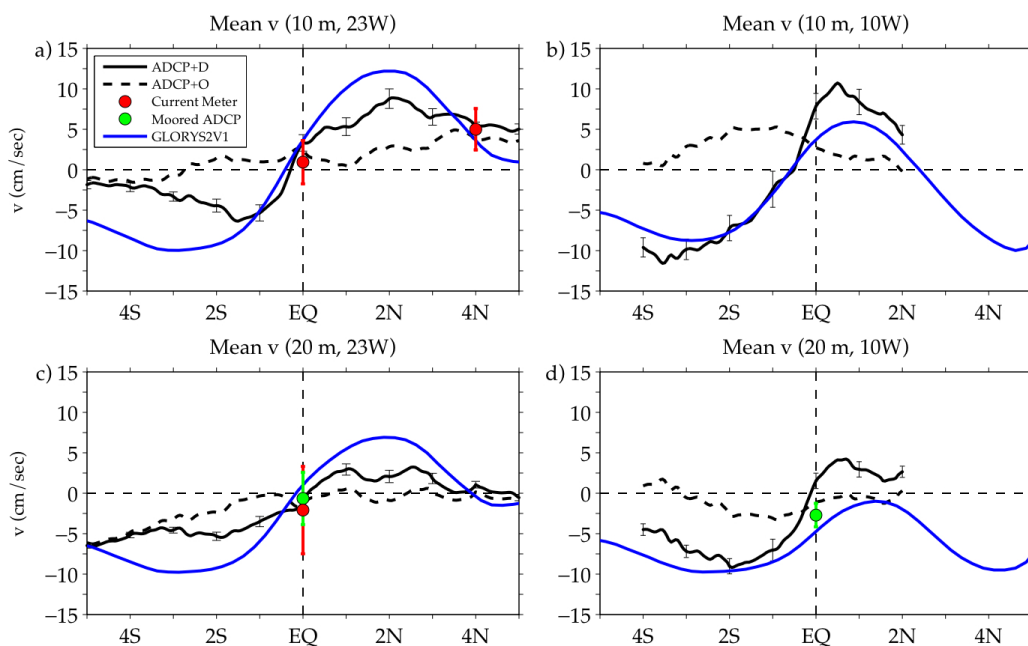


Fig. 5.4: Comparison of long-term mean ship-based ADCP meridional velocity vertically extrapolated to the drifter-Argo (ADCP+D, solid black lines) and OSCAR surface velocities (ADCP+O, dashed black lines) at (a)-(b) 10 m and (c)-(d) 20 m depth along 23°W (left) and 10°W (right). GLORYS2V1 mean meridional velocity is overlaid in blue. Mean meridional velocity derived from moored fixed-depth current meters is indicated by red circles and from moored ADCPs by green circles. Error bars denote the 95% confidence limits for the ADCP+D data and the total errors for the moored measurements.

In general, large differences are found between mean ADCP+D and ADCP+O meridional velocities at both depth levels. For example, the maximum poleward flow in ADCP+D is approximately 5 cm s^{-1} larger in magnitude than in ADCP+O along 23°W and 10°W at 10 m depth (Fig. 5.4a,b), and differs in sign from the ADCP+D velocity in the southern cell. The biased representation of the mean near-surface meridional currents in ADCP+O is consistent with a recent qualitative comparison by Da-Allada et al. (2013) of the previous version of the mean drifter annual climatology (Lumpkin and Garraffo 2005; Lumpkin and Garzoli 2005) and OSCAR velocities, and suggests that OSCAR mean meridional velocities do not adequately constrain the near-surface poleward flow in the central and eastern equatorial Atlantic. Note, if instead of extrapolating to these near-surface velocity products, the mean vertical

shear between 30 m and 40 m depth from the ship-based ADCP meridional velocity is used to extrapolate upwards as in previous studies (e.g., Johnson et al. (2001); Schott et al. (2003)), the mean surface flow would be on the order of 5 cm s^{-1} weaker along 10°W , and would be oriented southward rather than northward along 23°W (not shown). Thus, the mean vertical shear between 30 m and 40 m depth is also insufficient to adequately constrain the near-surface poleward flow.

At the nine sites along 23°W and 10°W between 2°S and 4°N where moored current measurements are available, the mean ADCP+D meridional velocity as well as the mean GLORYS2V1 meridional velocity can be further evaluated in the upper 300 m (Fig. 5.5). The mean moored ADCP meridional velocities (thick green lines) typically agree quite well with the mean ship-based ADCP meridional velocities (thick black lines) and overlap within the standard errors for each of those estimates. Exceptions are at the equator and 0.75°N along 23°W between about 75 m and 150 m depth where the ship-based ADCP estimate exhibits too strong northward flow in the EUC core region (Fig. 5.5c,d), and at 0.75°S along 10°W between 50 m and 100 m where the flow is too strong southward (Fig. 5.5g). At the 0° - 23°W mooring, the ship-based ADCP estimate also exhibits too strong southward flow below the EUC between 150 m and 250 m (Fig. 5.5c), suggesting that there are not enough ship sections to average out the mesoscale variability near the equator between 50 m and 250 m. At most sites, the mean GLORYS2V1 meridional velocities (thick blue lines) are in good agreement with both the mean moored ADCP and the fixed-depth current meter (red circles) velocity estimates, with the exception of too weak southward flow at the equator and 0.75°N along 10°W in the EUC core region between 50 m and 150 m depth (Fig. 5.5h,i).

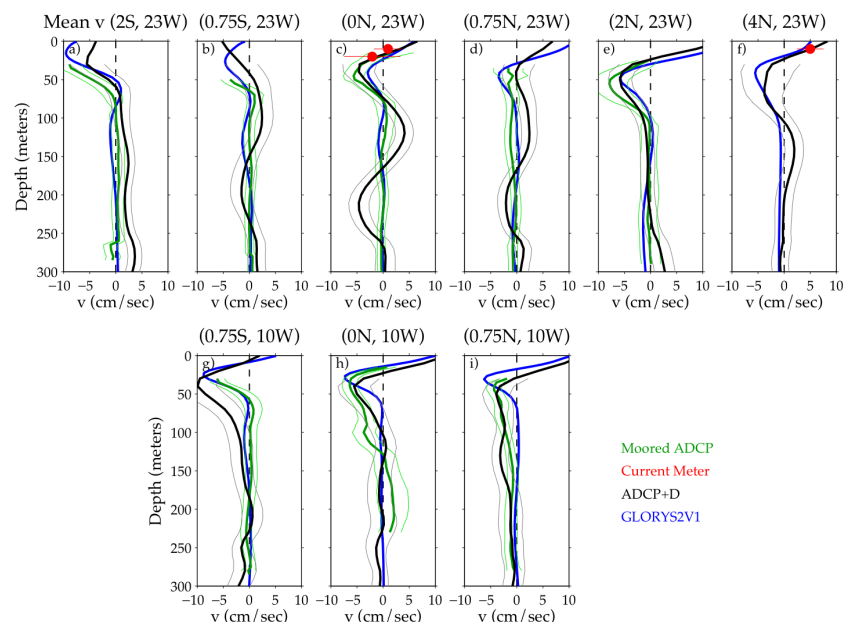


Fig. 5.5: Comparison of long-term mean ADCP+D meridional velocity (thick black lines) at various latitudes along (a)-(f) 23°W and (g)-(i) 10°W . GLORYS2V1 mean meridional currents are overlaid in blue. Mean meridional velocity derived from moored fixed-depth current meters is indicated by red circles and from moored ADCPs by thick green lines. Thin lines denote the means \pm standard errors for the ADCP+D and means \pm total errors for the moored ADCP measurements, and the error bars denote the means \pm total errors for the fixed-depth current meter measurements.

5.2.3. Seasonal comparison

The seasonal distribution of the ADCP sections (section 5.1.1) provides an opportunity to examine the meridional-vertical structure of mean meridional velocity associated with the TCs during Dec-May and Jun-Nov along 23°W (Fig. 5.6) and compare with the six-month mean drifter-Argo and GLORYS2V1 meridional velocities (Fig. 5.6 and Fig. 5.7). Although there are not enough ADCP sections along 10°W to similarly partition the ship-based ADCP meridional velocities into Dec-May and Jun-Nov averages, the six-month mean drifter-Argo and GLORYS2V1 meridional velocities can be examined along 10°W (Fig. 5.8a-d). For this reason, we do not combine the six-month mean ship-based ADCP meridional velocities with the six-month mean drifter-Argo meridional velocity estimates, but consider the two data sources separately (cf. Fig. 5.6a,b and Fig. 5.7a,b). The six-month mean meridional velocities from the moored ADCPs and fixed-depth current meters at the nine sites along 23°W and 10°W (Fig. 5.10) are also compared with the six-month GLORYS2V1 means at those locations (Fig. 5.11). Note that the six-month mean drifter-Argo and mooring estimates are generated using the harmonic fits to the data described in sections 5.1.2 and 5.1.4, respectively, rather than from the data solely in those months to reduce sampling biases.

Above 30 m depth, the mean GLORYS2V1 and drifter-Argo poleward flow associated with the upper limb of the TCs along 23°W is stronger during Dec-May than Jun-Nov (Fig. 5.6c,d and Fig. 5.7a-d). This is consistent with previous findings by Helber et al. (2007) in their seasonal analysis of OSCAR surface velocities (cf. their Fig. 5), although the magnitude of the drifter-Argo seasonal differences is much larger than the OSCAR seasonal differences. The GLORYS2V1 hydrographic fields show large seasonal variations in the zonal temperature gradients north of the equator along 23°W which set the strength of the geostrophic component of the meridional velocity, v_g . Using equatorial geostrophy (e.g., Perez and Kessler (2009), and references therein) to obtain estimates of v_g relative to an assumed level of no motion at the sea floor from the GLORYS2V1 SSH fields, reveals that there is northward geostrophic flow north of the equator along 23°W in Dec-May and southward geostrophic flow in Jun-Nov (dashed blue lines in Fig. 5.7e,f). At this longitude, the seasonal variability of the geostrophic component is larger than the seasonal variability of the ageostrophic component of meridional velocity (v_{ag} , solid blue lines in Fig. 5.7e,f), computed simply as the residual between the total near-surface velocity (Fig. 5.7c,d) and v_g , and thus more strongly influences the seasonality of the total near-surface velocity. In contrast, the maximum near-surface northward flow in the northern cell along 10°W occurs during Jun-Nov for the drifter-Argo and GLORYS2V1 meridional velocities (Fig. 5.8a-d), consistent with the stronger seasonal variability of the near-surface ageostrophic component of meridional velocity south of 2°N along 10°W (Fig. 5.8e,f).

The observed and GLORYS2V1 mean southward displacement between the northern and southern cells, and the southward shift of the boundary from Dec-May to Jun-Nov, is due to the asymmetric structure of v_{ag} , and to a lesser extent v_g (Fig. 5.7 and Fig. 5.8). The equatorially asymmetric structure of the annual and seasonal mean v_{ag} is consistent with the asymmetric structure of the mean wind-driven

component of the near-surface meridional velocity. This can be qualitatively seen from the wind-driven component of meridional transport estimated using the simple equatorially-modified Ekman model applied by Perez et al. (2012) and the GLORYS2V1 surface zonal and meridional wind stress (τ_x , τ_y):

$$V_{ek} = \frac{r_s \tau_y - f \tau_x}{\rho_0 (f^2 + r_s^2)},$$

where ρ_0 is seawater density, f is the Coriolis parameter, and $r_s = (1.5 \text{ day})^{-1} \sim f$ at 3°N is the vertical shear dissipation rate. From the above equation, the location of the boundary between northward and southward wind-driven transport can be derived as the latitude where $V_{ek} = 0$ or $f = r_s \tau_y / \tau_x$ (note, this latitude varies linearly with the choice of r_s). For the prevailing southeasterly winds along 23°W , the long-term mean boundary between the northward and southward wind-driven transport lies at 1.70°S (black line in Fig. 5.9a). Along 10°W , the winds become more southerly, shifting the boundary between the northward and southward wind-driven transport further southward to 3.15°S (black line in Fig. 5.9c). Seasonal variations in the winds also appear to be partly responsible for the observed and simulated southward shift of the boundary between the northern and southern cells from Dec-May (Fig. 5.9a,c) to Jun-Nov (Fig. 5.9b,d).

Below 30 m depth, the winds exert less influence upon the meridional currents and this compensation between the seasonal variations of v_g and v_{ag} does not occur. Although there are some differences between the six-month mean ship-based ADCP (Fig. 5.6a,b) and GLORYS2V1 (Fig. 5.6c,d) meridional velocities along 23°W which may not be significant given the large observed standard errors, both show seasonal strengthening of the equatorward flow in the lower limb of the TCs between 1.5°N and 5°N in the northern cell, and to a lesser extent between 3°S and the equator in the southern cell during Jun-Nov (Fig. 5.6). The stronger southward flow between 1.5°N and 5°N in the lower limb of the northern cell during Jun-Nov also occurs along 10°W in GLORYS2V1 (not shown). Analysis of the six-month mean meridional velocity from the moored ADCPs and fixed-depth current meters at the nine sites along 23°W and 10°W (Fig. 5.10) provides a measure of confidence in the GLORYS2V1 results (Fig. 5.11). First, the flow in the subsurface limb of the northern cell indeed appears to be stronger during Jun-Nov (compare thick blue and red lines in Fig. 5.10e, Fig. 5.11e) - unfortunately, there are no moored ADCP data available at 4°N , 23°W where the simulated seasonal difference at the nine sites studied here is largest (compare thick blue and red lines in Fig. 5.11f). Second, the northern TC shifts further southward during Jun-Nov with the near-surface meridional velocity becoming more positive at the equator along both longitudes (Fig. 5.10c,h and Fig. 5.11c,h) as well as at 0.75°S and 0.75°N along 10°W (Fig. 5.10g,i and Fig. 5.11g,i). However, due to the large uncertainties associated with the observed six month mean meridional velocities at most of these sites (Fig. 5.10), only the observed seasonal differences at 0° , 10°W (Fig. 5.10h) may be significant.

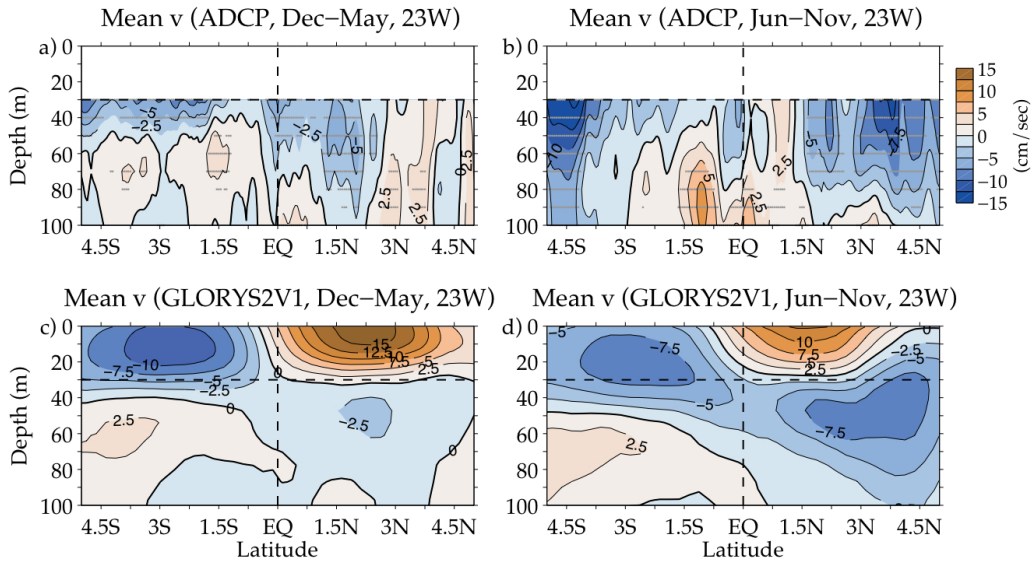


Fig. 5.6: Distribution of two-season mean (a)-(b) ship-based ADCP and (c)-(d) GLORYS2V1 meridional velocity along 23°W during Dec-May (left) and Jun-Nov (right). Gray dots in (a)-(b) indicate statistically significant values. Contour interval is 2.5 cm s^{-1} .

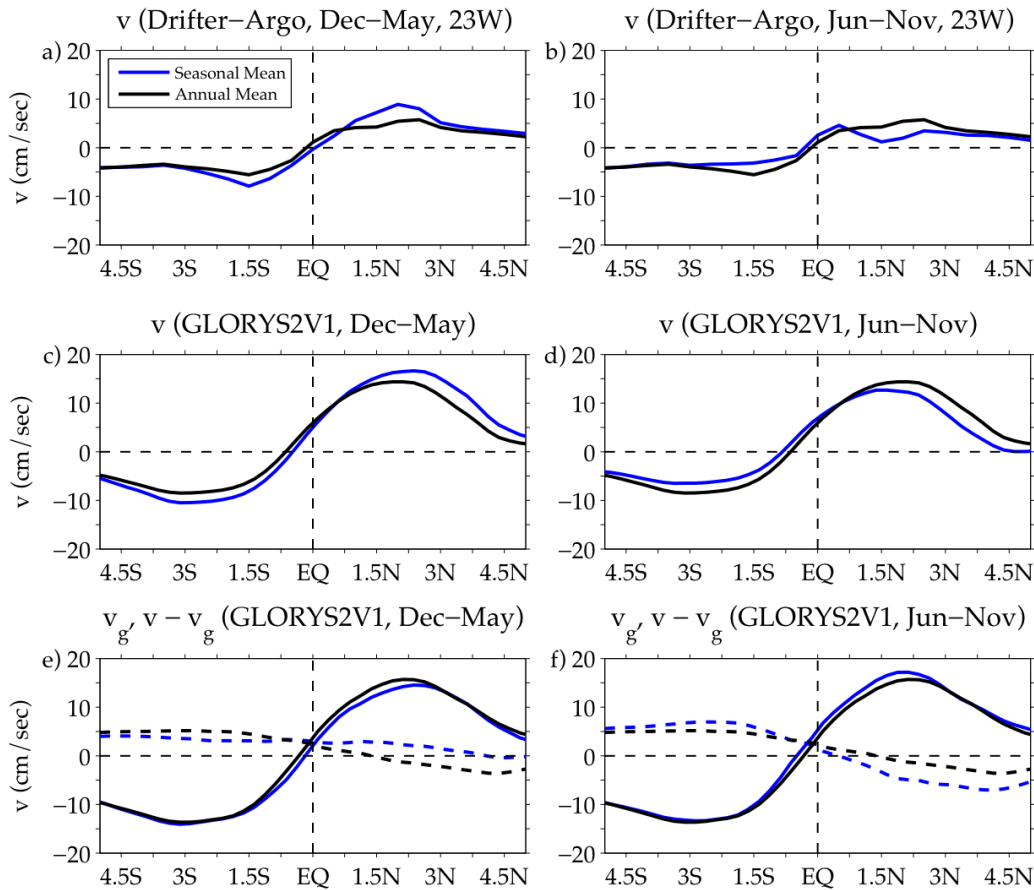


Fig. 5.7: Comparison of two-season mean near-surface (a)-(b) drifter-Argo and (c)-(d) GLORYS2V1 meridional velocity along 23°W during Dec-May (left) and Jun-Nov (right). Panels (e)-(f) show the simulated equatorially-modified geostrophic component of the meridional velocity, v_g , computed using the GLORYS2V1 sea surface height (dashed lines), and the ageostrophic component of meridional velocity, $v_{ag} = v - v_g$ (solid lines). For comparison, the long-term means are plotted in black and seasonal means are plotted in blue.

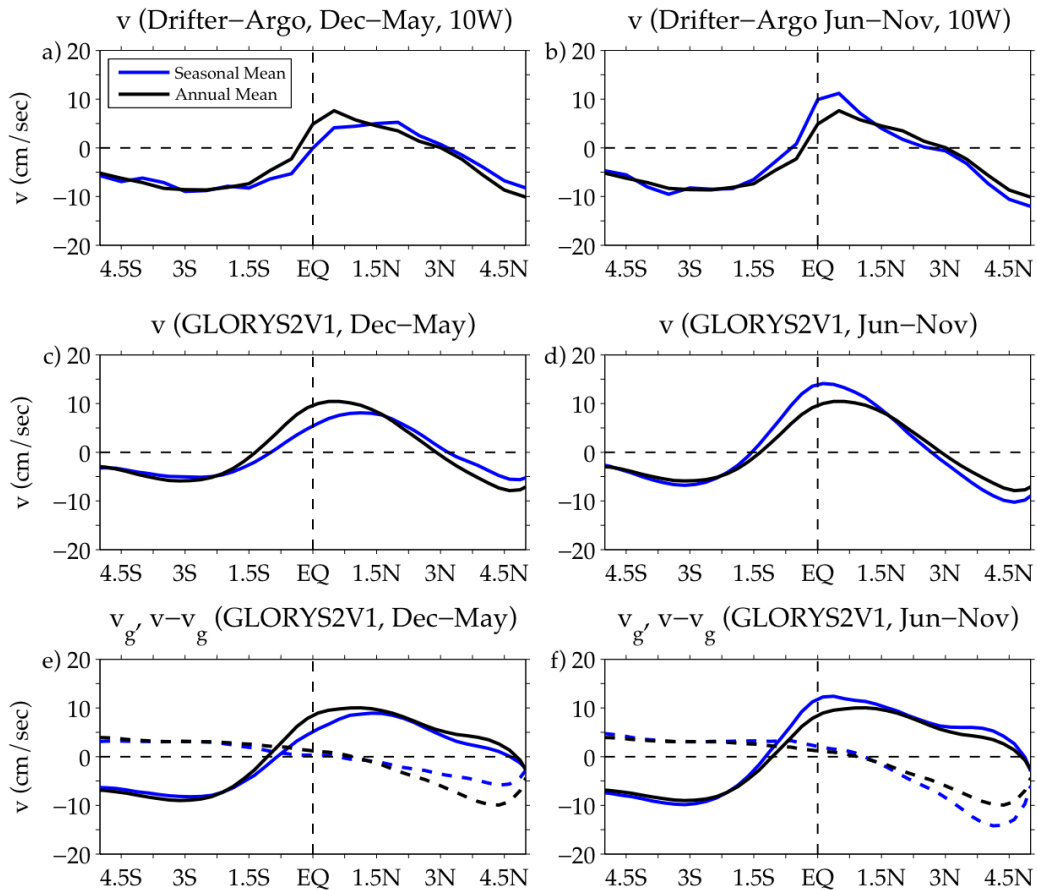


Fig. 5.8: Same as Fig. 5.7, except along 10°W .

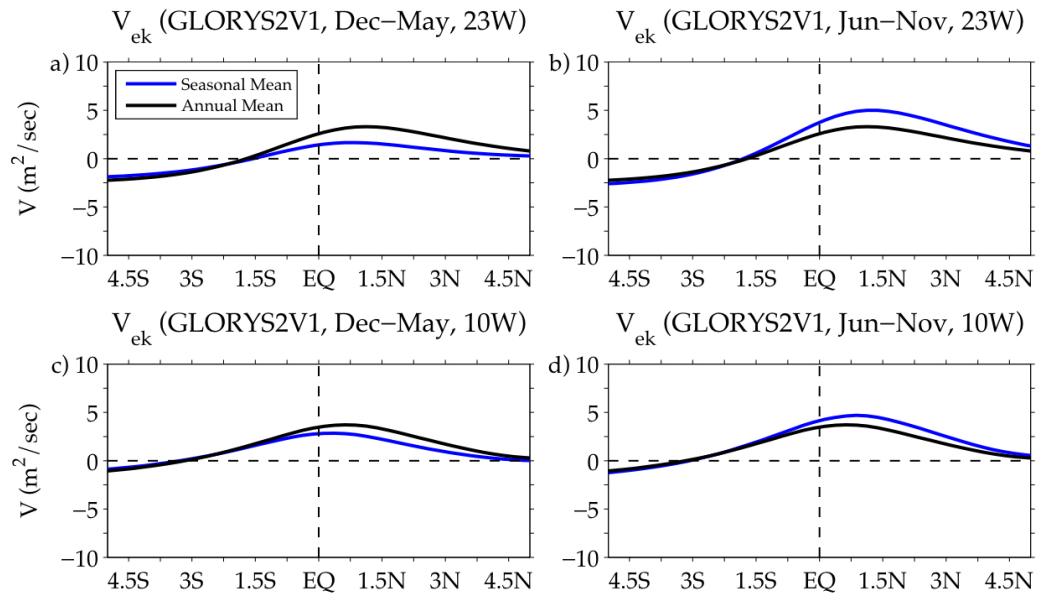


Fig. 5.9: Comparison of two-season mean equatorially-modified Ekman meridional transport computed using the GLORYS2V1 surface wind stress along (a)-(b) 23°W and (c)-(d) 10°W . For comparison, the long-term means are plotted in black and seasonal means are plotted in blue.

5.3 Summary and discussion

Since the late 1990s, several major field programs have been initiated to monitor the circulation, hydrography, and air-sea fluxes in the central and eastern equatorial Atlantic with moored arrays and cross-equatorial cruises. Here, shipboard and lowered ADCP velocity measurements collected by these programs were

averaged and combined with estimates of the mean near-surface meridional velocity derived from drifters and Argo float surface drifts to describe for the first time the mean cross-equatorial and vertical structure of the meridional currents along 23°W and 10°W, and to provide a new tool with which to assess the realism of the tropical Atlantic circulation in OGCMs, assimilation models, and coupled climate models. Data from moored ADCPs and fixed-depth current meters in the region, the satellite-derived OSCAR product, and the global ocean reanalysis GLORYS2V1 were additionally used to evaluate the mean meridional velocity estimated from the combined ADCP and drifter-Argo data (ADCP+D) along 23°W and 10°W.

Analysis of the ADCP+D long-term mean structure of meridional velocity confirmed that the dominant circulation features along these longitudes in the upper 100 m of the water column are the TCs, with near-surface poleward flow and subsurface equatorward flow that is stronger in the northern cell than it is in the southern cell. The thickness of the surface limb of the TCs decreases between 23°W and 10°W consistent with the eastward shoaling of the thermocline or pycnocline (e.g., Philander and Pacanowski (1986)). Moreover, the northern cell was observed to shift further south of the equator consistent with the more southerly orientation of the winds along 10°W noted in section 5.2.3, and a southward shift in maximum equatorial divergence and upwelling found in previous tropical Atlantic studies (e.g., Helber et al. 2007; Giordani and Caniaux 2011). Because of the deeper extent of the southern cell along both longitudes, the estimated mean meridional volume transport between 23°W and 10°W associated with the southern cell is stronger than that of the northern cell, that is -4.6 Sv compared with 2.3 Sv. The mean GLORYS2V1 meridional volume transport computed between 23°W and 10°W is very similar to the observed transport. Away from the continental boundaries, the magnitude of the transport scales approximately by the longitudinal width, with the transport between 23°W and 10°W being nearly half of the transport between 35°W and 10°W and exhibiting a similar meridional structure (Fig. 5.2c,d). The basin-wide GLORYS2V1 meridional transport is comparable to previously reported model estimates which typically range from 10 Sv to 15 Sv (e.g., Hazeleger et al. 2003; Lohmann and Latif 2007), and is strongly influenced by western boundary currents such as the North Brazil Current and Undercurrent and therefore does not scale by the longitudinal width of the integration (Fig. 5.2c).

The structure of the TCs derived from the observations was sensitive to whether the mean ship-based ADCP meridional velocity was linearly extrapolated from 30 m depth up to the surface using mean drifter-Argo or OSCAR meridional velocity, or ADCP-derived estimates of the mean vertical shear between 30 m and 40 m, with the best representation of the mean near-surface meridional currents resulting from vertical extrapolation to the mean drifter-Argo meridional velocity. However, based on comparisons with mean meridional velocities obtained from moored ADCPs and fixed-depth current meters, and GLORYS2V1, it is clear that more direct velocity measurements are needed near the maxima of poleward velocity in the surface limb of the TCs (between $\pm 1^\circ$ and $\pm 4^\circ$ of latitude) to better resolve the meridional flow and vertical current shear in the upper 30 m.

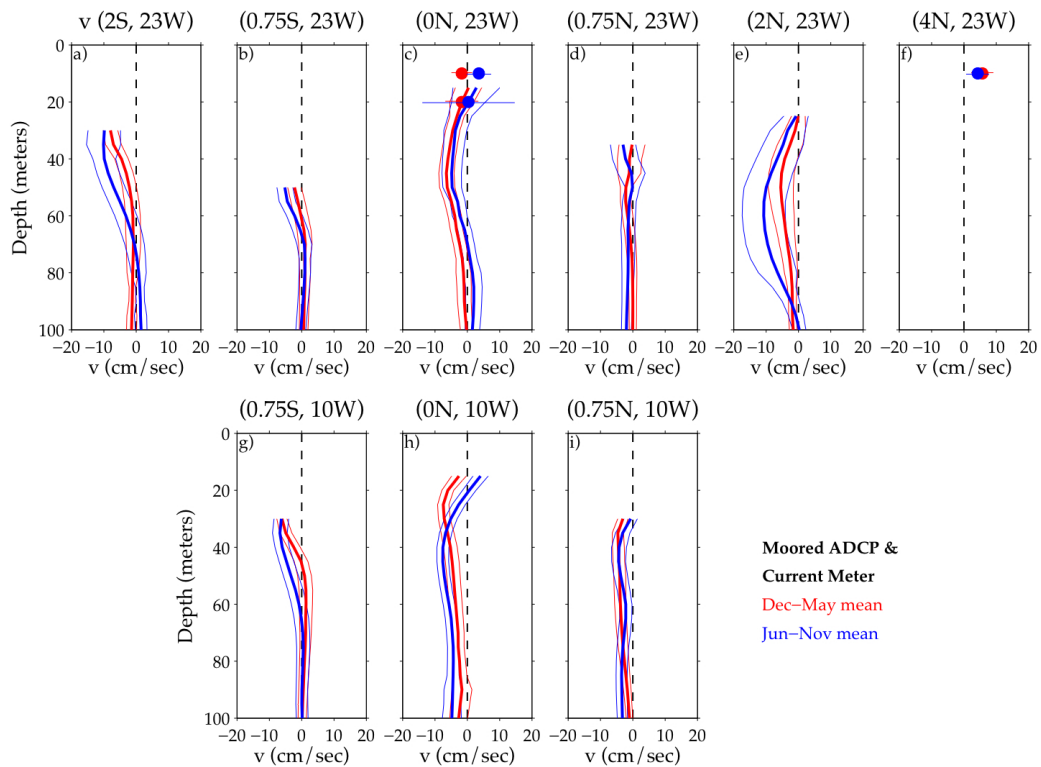


Fig. 5.10: Comparison of two-season mean meridional velocity derived from moored fixed-depth current meters (circles) and moored ADCPs (thick lines) at various latitudes along (a)-(f) 23°W and (g)-(i) 10°W. Red (blue) indicates mean during Dec-May (Jun-Nov). Thin lines denote the seasonal means \pm total errors for the moored ADCP measurements, and the error bars denote the seasonal means \pm total errors for the fixed-depth current meter measurements.

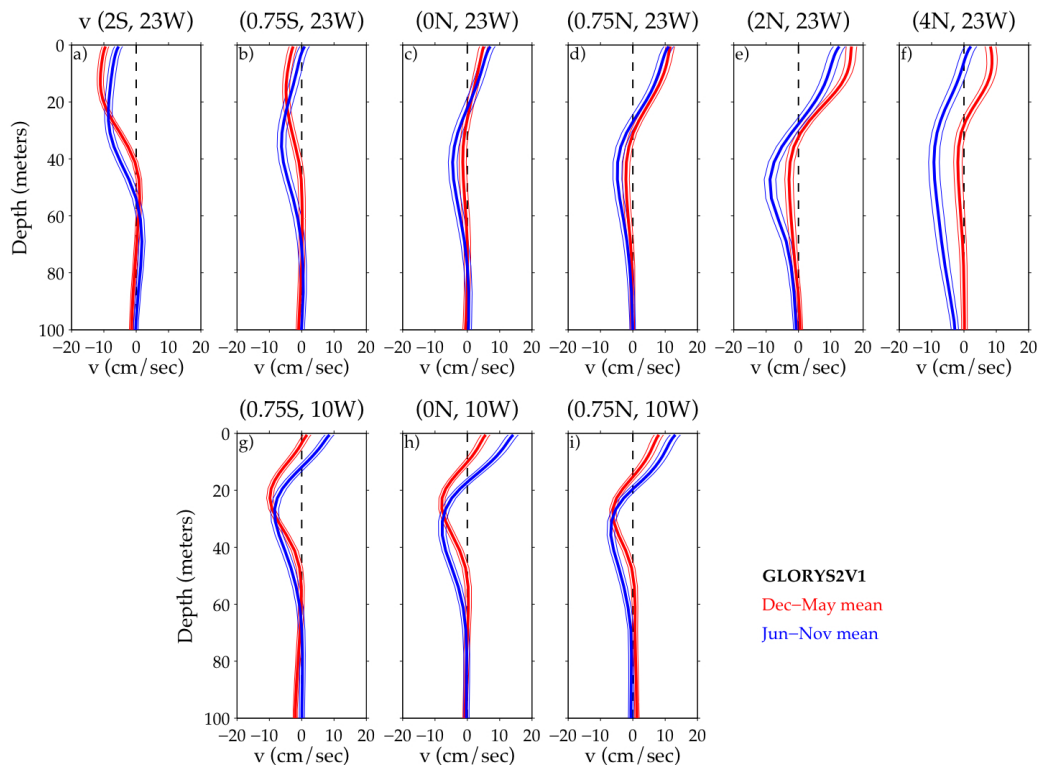


Fig. 5.11 Same as Fig. 5.10, except for GLORYS2V1 seasonal mean meridional velocities. Thin lines denote the seasonal means \pm standard errors (assuming a decorrelation time scale of 10 days) for the GLORYS2V1 meridional velocities.

Combined analysis of the two-season means estimated from the ship-based ADCP, drifter-Argo, and moored velocity data, as well as from GLORYS2V1 indicated that the maximum poleward velocity in the surface limb of the TCs intensifies during December to May along 23°W when the cold tongue is typically absent or weak, whereas the maximum equatorward flow in the subsurface limb of the northern cell intensifies during June to November along both 23°W and 10°W when the cold tongue is most pronounced in boreal summer. These seasonal differences appear to be due to compensation between the seasonal variations of the geostrophic and ageostrophic (wind-driven) components of meridional velocity in the surface limb of the TCs, and the seasonality of geostrophic meridional velocity in the subsurface limb of the TCs. However, more long-term direct current measurements are needed in the upper 100 m to examine the robustness of this result (i.e., reducing uncertainties due to the relatively small sample sizes), in particular between $\pm 1^\circ$ and $\pm 4^\circ$ of latitude where the mean meridional velocities associated with the mean locations of the TCs, as well as the velocity fluctuations due to TIWs, are both strongest.

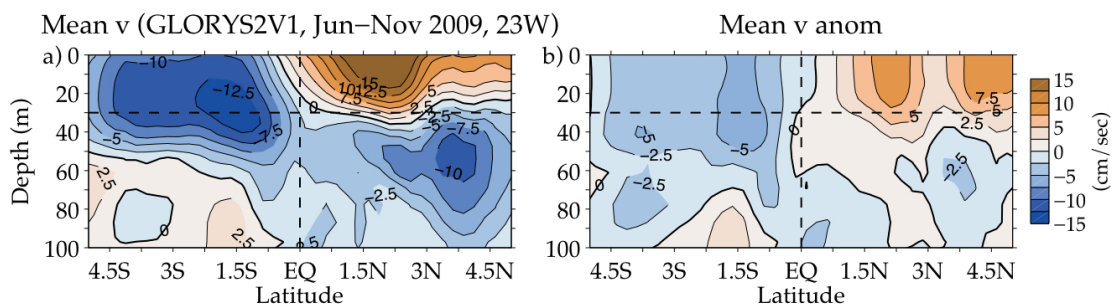


Fig. 5.12: Distribution of the (a) GLORYS2V1 mean meridional velocity along 23°W during Jun–Nov 2009 and (b) GLORYS2V1 meridional velocity anomaly relative to the two-season Jun–Nov mean shown in Fig. 5.6d. Contour interval is 2.5 cm s⁻¹.

During boreal summer, subsurface meridional currents in the central and eastern equatorial Atlantic can advect interannual wind-driven warm temperature anomalies induced immediately north of the equator southward and possibly trigger non-canonical Atlantic Niño events (Richter et al. 2013; Lübbecke 2013), and similarly advect corresponding cold anomalies southward and possibly trigger anomalous cooling events such as in May–July 2009 (Foltz et al. 2012; Brandt et al. 2013). Concurrent with the May–July 2009 cooling event, the poleward flow in the surface limb of the tropical cells and southward flow in the subsurface limb of the northern tropical cell both intensified in the global ocean reanalysis relative to the two-season mean (Fig. 5.12), but there were insufficient *in situ* measurements to determine whether this change occurred in the real ocean. With improved long-term measurements of meridional velocity in the tropical Atlantic, we will be able to examine more generally how the TCs themselves vary under such interannual wind forcing, and whether subsurface temperature anomalies generated during these events are advected by the seasonally strong or interannually intensified TCs.

6 Diapycnal heat flux and mixed layer heat budget within the Atlantic Cold Tongue

Authors: R. Hummels, M. Dengler, P. Brandt, M. Schlundt

SST variability in the tropical Atlantic is dominated by an annual signal formed by the seasonal appearance of the Atlantic cold tongue (ACT). During the development of the ACT in boreal spring/summer SSTs decrease by about 6°C. Towards the end of the year SSTs steadily increase completing the annual cycle (Fig. 6.1a). On the other hand, the net surface heat fluxes within this region are dominated by a semi-annual signal due to the meridional migration of the Inter Tropical Convergence Zone (ITCZ). The discrepancy between the semi-annual atmospheric forcing and the annual cycle of SSTs suggests ocean dynamics to be of fundamental importance within this region. Furthermore, the ACT is the oceanic region with strongest net atmospheric heat gain in the Atlantic (Josey et al. 1999). Hence, in order to reduce SST during ACT development, oceanic processes need to redistribute large amounts of heat to explain the observed seasonal decrease of SST. To further understand the seasonal cycle of SSTs within this region, an analysis of all individual contributions to the mixed layer (ML) heat budget is inevitable.

Several investigations of the ML heat budget in the ACT region already exist either relying on model simulations (Jouanno et al. 2011b; Peter et al. 2006) or observational data (Foltz et al. 2003; Hummels et al. 2013; Wade et al. 2011). Both approaches have their advantages and deficiencies. Model approaches can consistently evaluate the ML heat budget including all individual contributions. However, model results might be biased due to their sensitivity to the parameterization of unresolved physics, e.g. horizontal and vertical mixing. On the other hand, observational studies often lack information on individual terms of the budget, which cannot be estimated from the available data sets. In addition, some of the estimated terms may lack reliability due to a limited database in time and/or space.

Previous observational studies investigating the ML heat budget in the ACT region follow different approaches in order to exploit the existing data sets in the best possible way. Nevertheless, many of these studies lack information on the contribution of the diapycnal heat flux due to turbulent mixing at the base of the ML to the heat budget. Instead this term is assessed as the residual of the budget, which additionally includes all accumulated uncertainties (Foltz et al. 2003; Foltz et al. 2013; Wade et al. 2011). Model studies of the ACT as well as the Pacific cold tongue (PCT) have suggested that diapycnal mixing is an important contributor to the ML heat budget (Chang 1993; Jouanno et al. 2011b; Peter et al. 2006). In an observational study, Gouriou and Reverdin (1992) suggested diapycnal mixing to vary seasonally within the ACT.

It was only recently that measurement programs could indeed resolve seasonal variability of upper ocean turbulence: From multi-year moored microstructure temperature measurements Moum et al. (2013) demonstrated that diapycnal mixing indeed controls the seasonal cooling within the PCT at 140°W, while for the

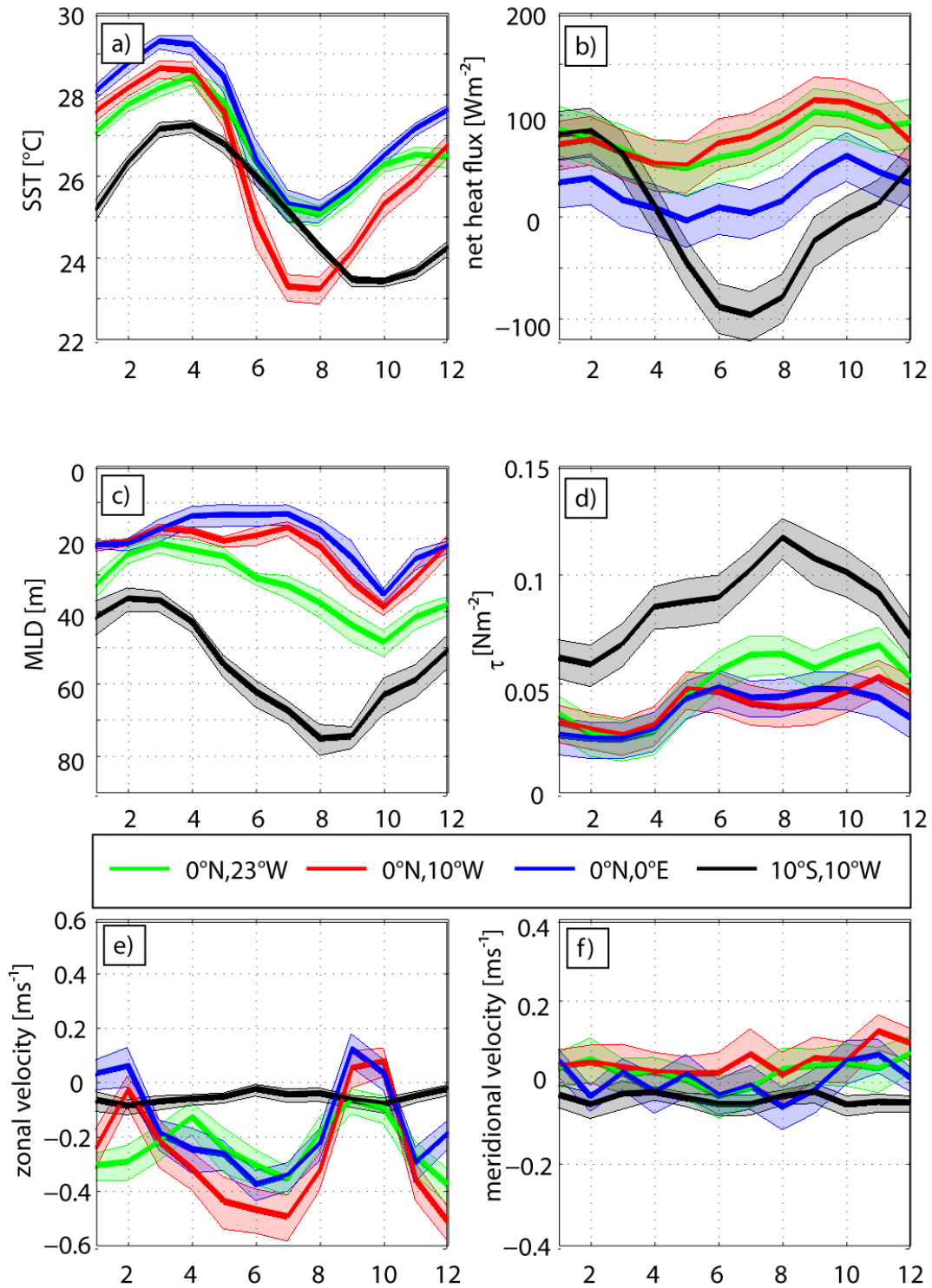


Fig. 6.1: Seasonal variability of different variables at the four different PIRATA buoy sites (color code is given in legend): a) SST (PIRATA), b) net surface heat flux corrected for the amount of heat penetrating the ML (TropFlux), c) MLD (PIRATA), d) wind stress magnitude (TropFlux), e) zonal surface velocities (Argo+drifter climatology), f) meridional surface velocities (Argo+drifter climatology). Error bars denote 95 % confidence limits.

equatorial ACT (i.e. within the equatorial belt 2°S-1.5°N, 23°W-2°E), Hummels et al. (2013) highlighted seasonal and regional differences in diapycnal heat flux from the ML into the upper thermocline using a multi-cruise microstructure profiling data set. Hummels et al. (2013) found that the ML heat loss due to diapycnal mixing is of

considerable magnitude and amounts to up to 90 W m^{-2} within the equatorial ACT region.

By solving the ML heat balance on the equator at 10°W , Hummels et al. (2013) showed that the diapycnal ML heat loss is the dominant cooling term for the ML heat budget during ACT development. In fact, they were able to balance the seasonal ML heat budget at this location for the period from May to November when incorporating estimates of the diapycnal heat flux. In the ACT as well as in the PCT region, turbulent mixing could be associated with shear instabilities (Gregg et al. 1985; Hummels et al. 2013). Within the entire equatorial ACT vertical shear of horizontal velocity is significantly elevated due to opposing currents, namely the westward-directed northern branch of the South Equatorial Current (nSEC) at the surface and the Equatorial Undercurrent (EUC) flowing eastward along the thermocline. Accordingly, the diapycnal heat flux estimated from individual cruises carried out at different locations within the equatorial ACT is elevated (Hummels et al. 2013). This suggests that diapycnal mixing could be important for the ML heat budget in the entire equatorial ACT region. The importance of diapycnal mixing for the ML heat budget associated with shear instabilities forced by the nSEC/EUC system within the equatorial ACT was previously diagnosed in numerical simulations (Jouanno et al. 2011a; Jouanno et al. 2011b).

However, elevated diapycnal heat flux appears to be confined to the equatorial band (2°S to 1°N) only. At the southern tip of the ACT at 10°S , 10°W , Hummels et al. (2013) find diapycnal ML heat loss to be considerably lower (their Fig. 15), which suggests other mechanisms are important to reduce SSTs in the off-equatorial ACT.

This study is motivated by the success of Hummels et al. (2013) in achieving a balance of the ML heat fluxes and tendency at the equator at 10°W between May and November during the times when estimates of the diapycnal heat flux were available and could be included. Our intention here is to clarify whether a closure of the ML heat budgets from different locations within the ACT can be achieved when explicitly incorporating estimates of the diapycnal heat flux from microstructure observations and to assess the relative contribution of the diapycnal ML heat loss to the budgets at the different locations. The diapycnal heat flux observations reported by Hummels et al. (2013) are complemented with some recent cruises and combined with long-term observations from the Prediction and Research moored Array in the Tropical Atlantic (PIRATA; Bourles et al. (2008)) and climatological products to estimate a seasonal climatology of the tendency and the flux terms contributing to the heat budget of the ML at different locations within the ACT. Furthermore, as microstructure data is only sparsely available, a parameterization for mixing based on stratification and shear is developed from the available data.

6.1. Data and methods

In order to accomplish a seasonal description of the ML heat budget within the ACT, several data sets are combined. A limiting factor is the availability of estimates of the diapycnal heat flux due to mixing processes across the base of the ML. This term is derived from estimates of the turbulent dissipation rates inferred from observations made by microstructure profilers during a multi-cruise program

(Hummels et al. 2013). During this program several meridional transects were frequently repeated during different stages of ACT development covering the absence (January-April), the development phase (April-July) and the mature phase (August-December) of the ACT (Caniaux et al. 2011). The highlighted transects were conducted across the equator (2°S - 1.5°N) along 23°W , 10°W and 2°E (see Tab. 2). At the equatorial position of these transects (or close to the transect in the case of the 2°E transect), atmospheric and oceanic PIRATA observations are available at high temporal resolution. Hence, all terms contributing to the ML heat budget will be estimated at the four PIRATA buoy sites at 0°N , 23°W ; 0°N , 10°W ; 0°N , 0°E and 10°S , 10°W . For the determination of the contribution of the heat flux due to advection additional information on surface velocities, SST and mixed layer depth (MLD) as well as their horizontal gradients are required from climatological products.

ACT phase	Time period of used MSS observations	Vessel and Cruise ID	Sections	Number of stations (2°S - 1.5°N)	Number of profiles (2°S - 1.5°N)
Absence	29/02-07/03/2008	N/O L'Atalante GEOMAR 4	23°W	16	78
Development	01/06-03/07/2006	N/O L'Atalante EGEE3	10°W (eq)	15	45
			10°W (south)	8	24
			2°E	8	43
			6°E	5	15
Development	17/06-01/07/2006	R/V Meteor M68/2	23°W	8	39
			10°W	7	21
Development	07/06-14/06/2007	N/O L'Antea EGEE5	2°E	8	24
			6°E	6	17
			23°W	17	50
Mature	12/09-14/09/2005	N/O Le Suroit EGEE2	10°W	8	25
Mature	04/09-24/09/2007	N/O L'Antea EGEE6	10°W	8	24
			0°E	9	29
			2°E	7	21
			6°E	7	21
Mature	20/11-29/11/2006	N/O L'Antea EGEE4	10°W	7	21
			2°E	8	24
Mature	02/11-13/11/2009	R/V Meteor M80/1	23°W	21	84
Mature	04/11-12/11/2012	R/V Maria S. Merian MSM22	23°W	5	10

Tab. 2: Spatial and temporal distribution of microstructure profiles available to this study. Usually, at least three microstructure casts were collected at each station. Each of those ensembles was used to infer diapycnal heat fluxes to include into the ML heat budgets (see section 6.2.3).

6.1.1. Shipboard observations

A unique data set of microstructure shear and temperature profiles along with conductivity-temperature-depth (CTD) profiles was collected on ten cruises to the ACT region during different stages of ACT development (Tab. 2). The multi-cruise program includes cruises of the French EGEE (Etude de la circulation océanique et des échanges océan-atmosphère dans le Golfe de Guinée) project (EGEE2-6) and the German projects Nordatlantik (M68/2, MSM18/2) and SFB754 (M80/1, GEOMAR4, MSM22). Four cruises (EGEE3, EGEE5, M68/2 and MSM18/2) were scheduled to coincide with the development of the ACT and onset of the West African Monsoon in boreal spring and early summer (end of May to July), while another two cruises (EGEE2 and EGEE6) were carried out during the mature phase of the monsoon (September-October), when the ACT is still well developed. Finally,

three cruises (EGEE4, M80/1 and MSM22) were conducted in November while the ACT was warming. Another cruise was undertaken during the absence of the ACT in March 2008 (GEOMAR4).

Due to the latitudinal extent of the EUC, meridional transect data collected in the equatorial belt between 2°S and 1.5°N are representative of the mixing activity at the equator (Hummels et al. 2013). Hence, to improve the statistics of the equatorial estimate of the diapycnal ML heat loss due to turbulence, all available profiles in this latitudinal range are used. The only stations evaluated outside the equatorial belt were collected near 10°S, 10°W during EGEE3. For more details on the cruises the reader is referred to Hummels et al. (2013).

The microstructure shear and temperature data were collected using different microstructure profilers (MSS90L and MSS90D) manufactured by Sea&Sun Technology in cooperation with ISW-Wassermesstechnik. All profilers were equipped with two shear sensors (airfoil), a fast temperature sensor (FP07), an acceleration sensor, tilt sensors and standard CTD sensors. For a detailed description of the instruments the reader is referred to Prandke and Stips (1998). The profilers were adjusted to descend at 0.5-0.6 m s⁻¹. Noise levels of turbulent dissipation rates from the microstructure profilers are better than 1×10⁻⁹ W kg⁻¹ for the MSS90L and better than 5×10⁻¹⁰ W kg⁻¹ for MSS90D (Prandke and Stips 1998; Schafstall et al. 2010).

The sampling strategy pursued for the different cruises differs in comparison to previous microstructure studies conducted in the equatorial Pacific. Instead of sampling at a single location for a period of several days to several weeks (Inoue et al. 2012; Lien et al. 1995; Moum et al. 1989; Moum et al. 2009; Peters et al. 1988), profiling was done at several locations during a single cruise usually separated by 0.5° latitude on the meridional transects. This was accomplished by integrating microstructure profiling into the CTD station program during all cruises. A minimum of 3 and up to 20 microstructure profiles were collected at a single station extending from the surface to between 150 m and 300 m depth. For this study a total of 615 profiles collected on 178 stations are used.

6.1.1.1. Microstructure data processing

Processing of microstructure data and further inferring eddy diffusivities (K_ρ) and diapycnal heat fluxes (J_h) out of the ML is explained in detail in Hummels (2012) and Hummels et al. (2013).

6.1.2. PIRATA data

For evaluating the ML heat budgets, incoming solar radiation, subsurface temperature time series, air temperature, relative humidity, wind speed and rainfall data from the PIRATA buoy sites at 23°W, 10°W and 0°E on the equator as well as at 10°S, 10°W were used. To determine the mean seasonal cycle, we used all available daily averages from 1997 to 2012.

6.1.3. Climatological products

6.1.3.1. Surface velocities

Near-surface velocities are constructed from a combination of the YoMaHa'07 (Lebedev et al. 2007) data set providing surface velocities from Argo float surface drifts and surface velocities from drifters (www.aoml.noaa.gov/phod/dac/). The combination of data from different platforms enhances the available data base, which is in general limited as the equatorial region is characterized by diverging poleward flow and drifters (and to some extent also ARGO floats) tend to leave the equatorial region shortly after their deployment. Drifters are designed to follow the mean currents of the upper 15 m due to the attachment of a drogue, while Argo floats drift at the surface. Some of the drifters lost their drogue after some time making their drift behavior similar to that of Argo floats. The used drifter data set was updated for the new meta data information, where the drogue loss dates were corrected (Lumpkin et al. 2013). The different platforms have different sensitivity to the wind slip that is accounted for as explained below. The Argo floats are corrected for the wind slip at the surface similar to the corrections applied to the undrogued drifters (Pazan and Niiler 2001) with differing coefficients A:

$$u_{corrected} = u_{uncorrected} - A W_x$$

$$v_{corrected} = v_{uncorrected} - A W_y,$$

where W_x and W_y are the zonal and meridional component of wind velocity (in units of m s^{-1}) from NCEP/NCAR Reanalysis 6-hourly winds. The coefficient A was set to $A1=1.14 \times 10^{-2}$ for the ARGO floats, $A2=1.64 \times 10^{-2}$ for undrogued drifters and $A3=7 \times 10^{-4}$ for drogued drifters as in Perez et al. (2013) to account for the different response of the observational platforms to the wind induced slip. The derived velocities were then averaged on a $1^\circ \times 1^\circ$ grid of latitude and longitude with an overlap of 2° in both directions to enlarge the amount of observations within the individual grid boxes.

For this study, investigating the contribution of the individual terms to the ML heat budget within the seasonal cycle, average monthly estimates of surface velocities are required. As drifters as well as ARGO floats can be captured within the vortices of TIWs, which act on intraseasonal timescales, the possible bias due to these intraseasonal phenomena needs to be eliminated. In order to derive unbiased monthly estimates required for this study the maximum amount of independent data points combining the drifter and ARGO data base is used: data of the individual drifters is available on a 6 hourly grid, which does not represent independent data. Moored observations from Perez et al. (2013) reveal a de-correlation time scale between 7 and 10 days for meridional velocity, which also agrees with the temporal resolution of the ARGO float data. Accordingly, the data of individual drifters were subsampled by averaging over 10 day periods and then combined with the ARGO data base. The use of shorter de-correlation time scales that is associated with a larger weight on drifter data relative to Argo float data results only in minor changes in the resulting advective heat flux as long as the de-correlation time scale is larger than 1 day.

6.1.3.2. SST

To accurately determine local horizontal SST gradients required for evaluating heat advection terms (see below) a SST climatology of higher resolution compared to the one available from Reynolds and Smith (1994) (1°x1°) was needed: Moum et al. (2013) described an underestimation of the meridional heat advection when using a SST climatology of 1° horizontal resolution. Hence here, monthly averages of satellite SSTs from the Tropical Microwave Imager (TMI) onboard the Tropical Rainfall Measuring Mission (TRMM) satellite (www.ssmi.com/tmi/) were used, which are available at a 0.25°x0.25° horizontal resolution. A monthly-mean SST climatology was produced by averaging the monthly SST observations between 1998 and 2012.

6.1.3.3. Surface heat fluxes

The individual contributions to the net surface heat flux at the ocean's surface from the recently developed TropFlux (Praveen Kumar et al. 2012) product are considered. This recent product was especially developed for the tropical oceans and the individual fluxes are available at daily or monthly resolution from 1979 to present on a 1°x1° grid. Monthly values are used to build an average long-term monthly climatology of the individual surface fluxes using data between 1997 and 2012 coinciding with the period of available PIRATA observations. The resulting climatological surface fluxes of the TropFlux product are then compared to the PIRATA observations after applying the COARE algorithm (Fairall et al. 2003). Additionally, climatological long wave radiation from the daSilva et al. (1994) surface marine atlas available on a 1° x 1° grid was used for comparison with the TropFlux product.

6.1.3.4. Mixed layer depth

Finally, to determine horizontal gradients of MLD (needed for the calculation of the entrainment term, see below), the ML climatology of de Boyer Montégut et al. (2004) was used in the estimate of the entrainment term. The long-term monthly means are only available at 2° resolution in both latitude and longitude, but are interpolated on a 1°x1° grid to match the resolution of the other variables.

6.1.4. Methodology

To assess the relative importance of the diapycnal heat fluxes on the ML heat budget, the individual terms of the budget are estimated. The heat balance equation for the ML in the following form was first introduced by Stevenson and Niiler (1983). Since then, it has been frequently used in observational studies evaluating the individual contributions to the ML heat budget (Foltz et al. 2003; Moisan and Niiler 1998; Wang and McPhaden 1999) and reads:

$$h \frac{\partial T}{\partial t} + h(\mathbf{v} \cdot \nabla T + \overline{\mathbf{v}' \cdot \nabla T'}) + (T - T_{-h}) w_{entrain} + \nabla \cdot \int_{-h}^0 \hat{\mathbf{v}} \hat{T} dz = \frac{q_{net} - q_{-h}}{\rho c_p}$$

where h represents the thickness of the ML, and \mathbf{v} and T are the vertically averaged velocity and temperature in the depth range between the surface and $-h$. \mathbf{v}' and T'

are the deviations from the temporal means and \hat{v} and \hat{T} are the deviations from the vertical average. The overbar of the third term indicates temporal averaging. $w_{entrain}$ is the entrainment velocity and T_{-h} is the temperature at the base of the ML. q_{net} denotes the net surface heat flux, and q_{-h} is the net heat loss through the base of the ML. Here, q_{-h} is determined from a combination of the penetrative shortwave radiation and the diapycnal heat flux at the base of the ML. From left to right the terms represent local heat storage, horizontal advection (divided into a mean and eddy term), entrainment, the vertical temperature/velocity covariance (e.g. due to baroclinic flow within the ML) and the combination of net atmospheric heating and vertical turbulent diffusion at the base of the ML. The vertical temperature/velocity covariance involves the correlation of the possible departures of horizontal velocity and temperature from their vertically and temporally averaged values in the ML. Swenson and Hansen (1999) estimated the heat flux due to this term considerably smaller than the other contributions and hence this term will be neglected in the following as also described in Foltz et al. (2003).

The evaluation of the individual terms closely follows the procedures described by Foltz et al. (2003). Seasonal cycles of different variables are obtained from daily PIRATA data, averaged on every given day of the year and subsequently averaged for each month of the year. The penetrative fraction of the shortwave radiation depends on the MLD and the optical transparency of seawater. Here, it is calculated via an e-folding decay following Wang and McPhaden (1999), who parameterized shortwave radiation absorbed in the ML as $Q_{abs} = Q_{short}(1 - 0.45e^{-h/25m})$. Latent and sensible heat fluxes were calculated from the PIRATA buoy data using the COARE algorithm (Fairall et al. 2003) for comparison with the TropFlux product, which uses the same algorithm. Mean horizontal advection is determined by multiplying the monthly mean velocities (calculated from the combined ARGO and drifter velocities) with climatological long-term SST gradients from the TMI satellite observations. The eddy term of horizontal advection is estimated indirectly from the residual between mean horizontal advection described above and total horizontal advection estimated as $h(\mathbf{v} \cdot \nabla T) = h \left(\frac{dT}{dt} - \frac{\partial T}{\partial t} \right)$ (Swenson and Hansen 1999). The total time derivative is obtained from drifter SSTs, whereas the local derivative is estimated from the average monthly TMI SSTs. The entrainment velocity can be expressed as $w_{entrain} = \frac{\partial h}{\partial t} + \nabla \cdot h\mathbf{v}$ (Stevenson and Niiler 1983) representing the local time derivative of the depth of the base of the ML from PIRATA temperature time series and a divergence term of the product of the base of the ML and surface velocity climatology.

MLDs were calculated from PIRATA subsurface temperature time series and taken from the MLD climatology of de Boyer Montégut et al. (2004). The climatology is built upon the temperature threshold criterion of 0.2°C. In the study of Foltz et al. (2003) MLDs are calculated with the temperature threshold criterion of 0.5°C, but using only the profiles between 5.00 and 7.00 local time as a reference for the threshold to avoid the influence of shallow diurnal mixed layers. Different temperature thresholds (0.2°C and 0.5°C) referenced against SSTs between 5.00 and 7.00 local

time as well as the temperature gradient criterion described in Lorbacher et al. (2006) for PIRATA subsurface temperatures have been evaluated and compared to the MLDs of the climatology of de Boyer Montégut et al. (2004) at the PIRATA locations. Best agreement was found for the temperature threshold of 0.5°C , which is therefore further used here to estimate MLDs from PIRATA subsurface temperatures.

6.2. Results

6.2.1. Seasonal variability at the PIRATA sites

Among the four considered PIRATA buoy locations, which are representative for different regions within the ACT, large seasonal variability in the background setting is observed. Common to all regions within the ACT is the strong cooling of SSTs starting around April/May (Fig. 6.1a). The strongest cooling is observed on the equator at 10°W , which is sometimes referred to as the center of the ACT (Jouanno et al. 2011b). The structure of the seasonal variability of SSTs at the western (23°W) and eastern (0°E) edge of the ACT on the equator is very similar to 10°W . However, the southern ACT region exhibits a slower cooling phase followed by a delayed and more rapid warming phase. Towards the end of the year SSTs recover to warm levels at all locations reaching their maximum levels in March/April again.

The seasonal cycle of net surface heat fluxes from the TropFlux product varies considerably within the ACT (Fig. 6.1b). The seasonal variation at all locations is mainly caused by variations in the incoming solar radiation and the latent heat flux, whereas the sensible heat flux and the outgoing long-wave radiation remain rather constant throughout the year (Foltz et al. 2003; Hummels et al. 2013). However, within the equatorial region, net surface heat flux is typically positive. In the western and central part of the equatorial ACT region (23°W and 10°W) the ML is warmed throughout the year by $50\text{-}100\text{ W m}^{-2}$. Note that here the net surface heat flux is calculated with the absorbed shortwave radiation, which is corrected for the amount of heat penetrating through the ML estimated from PIRATA sub-surface temperatures. Within the eastern equatorial ACT (0°E) the superposition of annual and semiannual cycles of the net surface heat fluxes leads to a net heat flux minimum from May to July when SSTs decrease. In the southern ACT region (10°S , 10°W) a strong annual cycle of net surface heat fluxes is observed, which includes a ML warming as well as a cooling phase. At this location the cooling phase of the ML due to a change in atmospheric forcing of nearly 200 W m^{-2} coincides with a decline of SSTs.

MLDs are in general shallow in the eastern equatorial Atlantic due to the shoaling thermocline. Accordingly, within the equatorial ACT region MLDs decrease from west (23°W) to east (0°E) (Fig. 6.1c). At all locations within the equatorial belt, MLDs exhibit a seasonal cycle with maximum MLDs of $40\text{-}50\text{ m}$ in boreal autumn and $15\text{-}20\text{ m}$ during boreal spring. Within the southern ACT region MLDs are generally larger than in the equatorial belt. In the south, the seasonal variation ranges from around 40 m in boreal winter/spring to maximum 80 m during boreal summer/autumn.

Winds in the ACT region are dominated by the westward trades (easterlies) surrounding the ITCZ, which migrates meridionally during the year. For the equatorial

ACT region this migration imprints an annual signal on the wind stress magnitude with strongest winds in August, when the ITCZ is at its northernmost position (Fig. 6.1d). A weaker semi-annual signal, which peaks in April/May and September/October is superimposed on the dominant annual pattern yielding a double peaked structure. The southern ACT region exhibits only an annual variation in wind stress, which peaks in August, increasing the latent heat flux during this period. This increased latent heat flux contributes to the strong cooling via net surface heat fluxes in the southern ACT (Fig. 6.1b).

Zonal surface velocities in the equatorial ACT region, determined from a combination of Argo float and surface drifter data, are subject to a relatively strong semi-annual cycle. This appears odd at first glance, as the wind forcing is dominated by the annual cycle with only a weak semi-annual imprint. However, the semi-annual cycle in zonal velocity was explained by the presence of a resonantly forced basin mode (Cane and Moore 1981; Ding et al. 2009; Thierry et al. 2004). The current dominating the equatorial region is the northern branch of the South Equatorial Current (nSEC) (Hummels et al. 2013; Lumpkin and Garraffo 2005), (Fig. 6.1e). Maximum westward velocities are observed during boreal summer of about 0.25-0.5 m s⁻¹ depending on the exact location within the equatorial belt. In the central and eastern equatorial Atlantic, zonal velocities even reverse in sign during the seasonal cycle. Due to the vanishing Coriolis parameter at the equator, meridional velocities might be directly forced by the meridional wind component. As winds at the equator have a southerly (from south to north) component and are largest in boreal summer and fall, meridional velocities are directed in the same direction (Rhein et al. 2010). This is also consistent with the results from Perez et al. (2013), where positive (northward) meridional velocities are found at the equator at 23°W and 10°W. However, their magnitude is significantly reduced compared to zonal velocities (Fig. 6.1f). In the southern ACT region zonal as well as meridional surface velocities are of reduced magnitude compared to the equatorial region and do not show a distinct seasonal variation. Surface velocities within this region are dominated by the Ekman flow. According to the steady trade winds (south-easterlies), the Ekman flow is directed towards the southwest throughout the year (Fig. 6.1e,f).

6.2.2. Turbulent mixing within the ACT

In this section, the new and unique data set of microstructure observations acquired in the central and eastern equatorial Atlantic (Hummels et al. 2013) is used to estimate the diapycnal ML heat loss directly, rather than relying on residual estimates of this quantity as has been done previously (Foltz et al. 2003; Foltz et al. 2013; Wade et al. 2011; Wang and McPhaden 1999). The main findings relevant for this study from Hummels et al. (2013) concerning the regional and seasonal variability of turbulent mixing are summarized in the following: Turbulent dissipation rates (ϵ) at the equator are significantly increased in the upper thermocline compared to off-equatorial locations (cf. Fig. 6.2a). Within the equatorial region turbulent dissipation rates in the upper thermocline are:

1. Elevated in the western equatorial ACT region in comparison to the eastern equatorial ACT region (cf. Fig. 6.2a);
2. Most intense mixing is observed in boreal summer in the whole equatorial ACT region;

Hummels et al. (2013) described a close correspondence between the seasonal and regional variability of background shear and stratification levels and ensemble mixing intensities, eddy diffusivities (K_ρ), and diapycnal heat fluxes (J_h): e.g. vertical shear squared of horizontal velocities ($S^2 = (\partial U/\partial z)^2 + (\partial V/\partial z)^2$) was found to reduce from 10°W towards the eastern equatorial ACT, while stratification (N^2) increased. This reduces the likelihood of shear instabilities to occur in the Gulf of Guinea and indeed turbulent parameters such as dissipation rates as well as diapycnal ML heat losses were observed to decrease in magnitude from the western equatorial region towards the east. Despite stronger zonal subsurface velocities at 23°W compared to 10°W (Brandt et al. 2011a), shear levels are reduced at 23°W compared to 10°W (Jouanno et al. 2011b). This can be explained by the shoaling of the EUC towards the east, which limits the depth range of opposite flowing currents, westwards at the surface and eastwards in the subsurface. The highest shear levels in the central equatorial ACT region correspond to highest mixing activity. Within the southern ACT, shear levels were significantly reduced due to the lack of strong current features and turbulent mixing was found to be low. The relation between background shear and stratification conditions and turbulent mixing activity will be further analyzed later in this study.

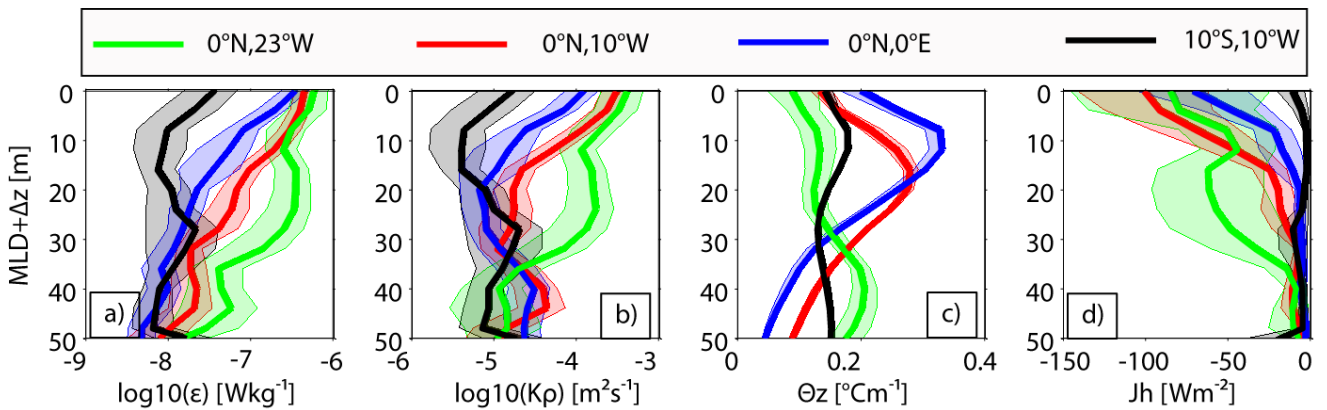


Fig. 6.2: Vertical profiles of turbulent parameters during summer (June/July) for the different locations within the ACT: a) dissipation rates of turbulent kinetic energy (ϵ), b) eddy diffusivities (K_ρ), c) gradient of potential temperature (θ_z) and d) diapycnal heat fluxes (J_h). Error bars are 95 % confidence limits, see Appendix C for details. Note that the depth range of the profiles shown in a-d is restricted to the upper thermocline, i.e. 0 corresponds to the ML depth and logarithmic abscissae scaling is used in panels a) and b). Note that the vertical temperature gradient is shown in c) as it is an important constituent in the formulation of the diapycnal heat flux.

According to the described variability in shear levels, average summer dissipation rates below the ML range from $3.5 \times 10^{-7} \text{ W kg}^{-1}$ in the eastern to $7 \times 10^{-7} \text{ W kg}^{-1}$ in the western equatorial ACT (Fig. 6.2a). In the southern ACT dissipation rates below the ML do not exceed $5 \times 10^{-8} \text{ W kg}^{-1}$. At a depth of 50 m below the ML, equatorial dissipation rates have dropped by about one order of magnitude (Fig.

6.2a). Inferred eddy diffusivities (section 6.1.1.1) just below the ML range from $1.2 \times 10^{-4} \text{ m}^2 \text{ s}^{-1}$ in the eastern to $7 \times 10^{-4} \text{ m}^2 \text{ s}^{-1}$ in the western equatorial ACT, while values in the southern ACT only reach $1.6 \times 10^{-5} \text{ m}^2 \text{ s}^{-1}$ at maximum. The magnitude and vertical structure of the observed turbulent parameters agrees rather well with those inferred from microstructure measurement programs carried out in the central equatorial Pacific (Gregg et al. 1985; Lien et al. 1995; Moum et al. 1989; Peters et al. 1988). However, in comparison to the central equatorial Pacific, Hummels et al. (2013) report for the equatorial ACT region a reduction in the night time enhancement of turbulence, which is referred to as deep cycle turbulence (Moum and Caldwell 1985). Nevertheless, to avoid possible biases due to an unevenly distributed sampling time of profiles during the day, mean profiles of turbulent parameters are derived here by separately averaging measurements collected during the day (08:00-20:00) and night (20:00-08:00) before calculating mean profiles. The average of the mean day and mean night profiles are then further incorporated into the ML heat budgets.

In order to obtain the turbulent contribution of diapycnal heat fluxes to the ML heat budget, the transition zone between the base of the ML and the stratified region below has to be accurately resolved. In the equatorial Atlantic as well as in the Pacific, profiles of the diapycnal heat flux are highly divergent below the ML. Maximum values are found at the base of the ML that rapidly decrease in deeper layers (Fig. 6.2d and Lien et al. 2008). In most of the mean profiles (Fig. 6.2d), diapycnal heat flux at 20 m below the ML is significantly reduced. Hence, the amount of heat being extracted from the ML into the interior ocean is characterized by the diapycnal heat flux in a rather narrow layer. Here, diapycnal ML heat loss is determined by averaging the diapycnal heat flux profiles in the interval MLD+5 m to MLD+15 m. The reason to use this averaging interval is to ensure values from within the ML to be excluded from the estimate as the method from Osborn (1980), which we use here, is only valid in stratified sheared flow. Due to strong variability in stratification within a few meters below the ML, and due to the fact that stratification for the Osborn parameterization needs to be calculated over a larger length scale than turbulent overturns (that can be as much as several meters due to the strong mixing there), we decided to use this depth interval. Due to the elevated vertical divergence of the heat flux profiles, this approach leads to estimates of diapycnal heat loss of the ML being biased low. The error of this approach can be estimated from the average heat flux profiles by extrapolating from MLD+10 m to the MLD. The extrapolation needs to be performed as the diapycnal heat flux obtained directly below the ML with the Osborn method cannot be considered reliable as explained above. Overall, the diapycnal heat flux reduces by about 30% at MLD+10 m compared to the value directly below the ML.

Note that the MLD from vertically high resolved CTD profiles was generally calculated using the temperature threshold criterion with $\Delta T = 0.2^\circ\text{C}$ compared to the SST. Heat flux profiles and inferred diapycnal ML heat losses were calculated separately for every station. Subsequently, these station averaged profiles of the different sections of an individual cruise between 2°S and 1.5°N were averaged in day and night ensemble (see above) to obtain a single estimate that was taken as

representative for diapycnal heat loss of the ML for the month in which the measurements were collected. Uncertainties for each individual estimate were calculated using Gaussian error propagation as described in Hummels et al. (2013).

6.2.3. Mixed layer heat budget

In the following, the contributions to the ML heat budget derived from PIRATA observations, climatological data sets as well as microstructure observations are combined at the four different locations within the ACT. Note that the individual contributions to the ML heat budget at 0°N , 10°W were already analyzed in Hummels et al. (2013). However, to achieve a consistent comparison between heat budgets at the different PIRATA locations, the analysis of the heat budget at 0°N , 10°W is repeated here partly using different data products (concerning the surface velocities and the net surface heat fluxes) compared to Hummels et al. (2013).

Several modeling as well as observational studies have addressed the ML heat budget in the eastern equatorial Atlantic previously (Foltz et al. 2003; Hummels et al. 2013; Jouanno et al. 2011b; Peter et al. 2006; Wade et al. 2011). Among these studies, the definition of high and low frequency advection terms, referred to as mean and eddy advection here (section 6.1.4), varied. Hence, in order to compare the results amongst the different studies it has to be clarified which oceanic processes are attributed to the different terms. As has been pointed out in the tropical Pacific analysis by Wang and McPhaden (1999) processes reflected in the eddy advection term close to the equator, particularly in the meridional component, significantly depend on the latitudinal averaging interval over which the heat budget analysis is performed. For local heat budgets or budgets performed for small regions around the equator (i.e. $\pm 2^{\circ}$ in latitude), the eddy advection warms the ML as the effect of Tropical Instability waves (TIWs) laterally advecting warm waters are explicitly resolved (Foltz et al. 2003; Jochum and Murtugudde 2006; Peter et al. 2006). When budgets are performed over a larger meridional extent, eddy advection will cool the ML as TIW contributions are averaged out and the Ekman divergence dominates. This study focuses on local heat budgets at the locations of the PIRATA buoys and thus requires evaluating the eddy heat fluxes as local as possible. Opposing this minimum regional extent requirement is the accuracy of velocity and SST gradient data, for which the statistical reliability of the individual variables increases when they are averaged over larger meridional intervals. As a compromise between locality and statistical reliability, a 2° latitudinal and longitudinal interval is

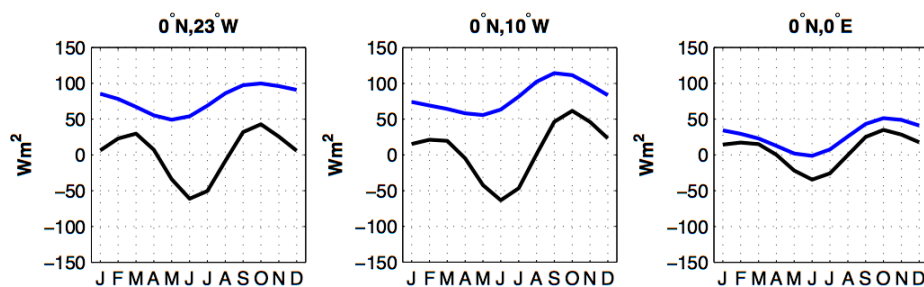


Fig. 6.3: Comparison of the net surface heat flux (absorbed shortwave radiation (corrected for the amount of shortwave radiation penetrating through the ML)+ latent heat flux + sensible heat flux + outgoing longwave radiation) in blue and the observed heat storage in black for the four different locations within the ACT.

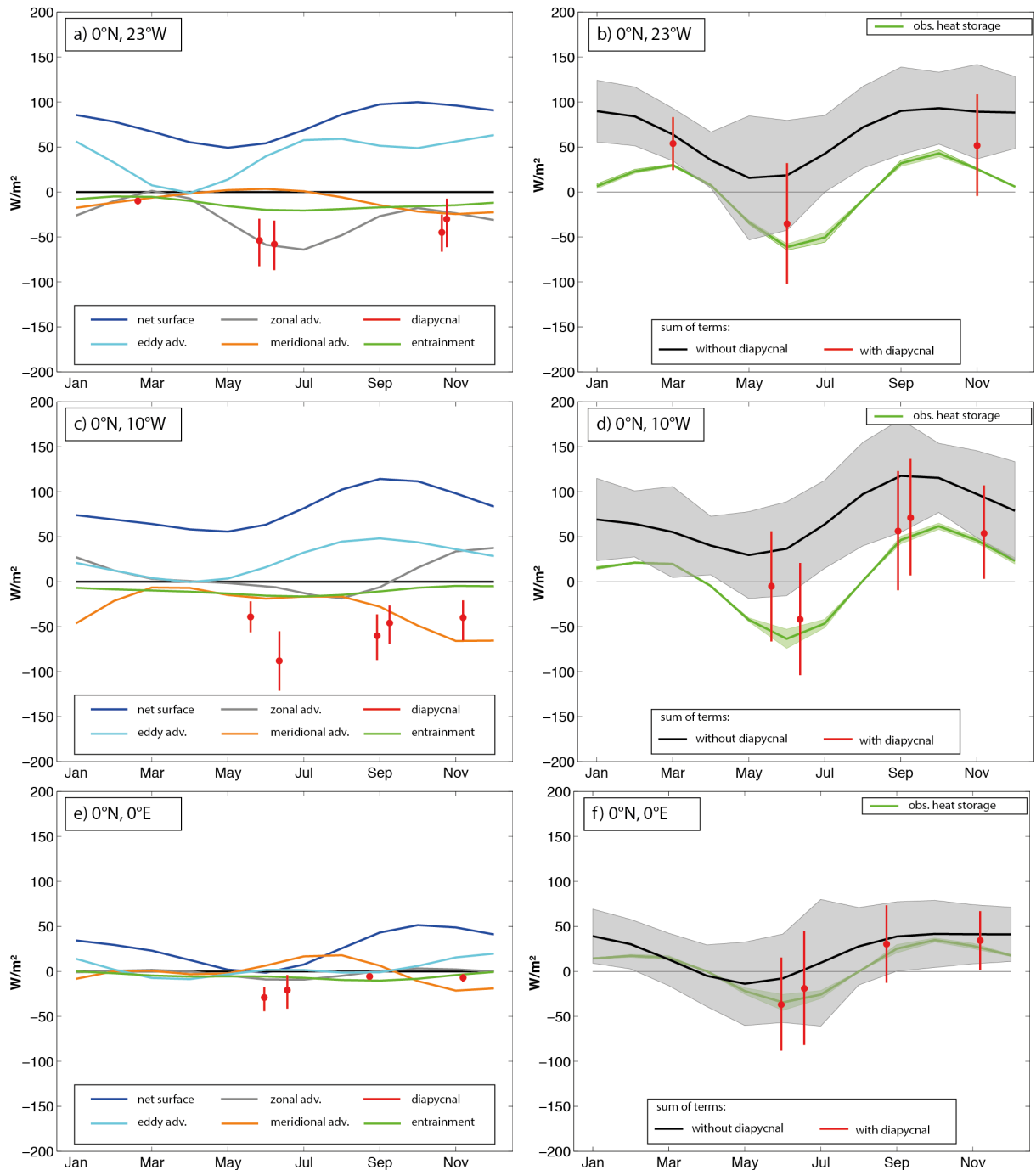


Fig. 6.4: Left panels: Individual contributions to the ML heat budget at the different locations within the ACT (color code explained in the legend). Vertical red lines denote 95% confidence limits for the diapycnal ML heat loss. Right panels: Sum of the individual contributions without (black) and with (red) the diapycnal ML heat loss; observed heat storage is in green. Grey shading denotes 95% confidence limits for the sum of terms excluding the diapycnal ML heat loss, red shading or vertical lines denote 95% confidence limits including the diapycnal ML heat loss;

used to evaluate mean and eddy advection terms. In doing so, the warming effect of TIWs will dominate the eddy advection term.

When the net surface heat flux is compared to the observed heat storage, large negative residuals are evident in the western (23°W) and central (10°W) equatorial ACT and a reduced residual in the eastern (0°E) equatorial ACT (Fig. 6.3, Fig. 6.4). In contrast, within the southern ACT region, SST variability during ACT development

can virtually be explained by the variability in net atmospheric forcing. Hence, the residuals in the equatorial region need to be explained by different oceanic processes, which probably also vary in their relative contribution within the seasonal cycle.

In the following, the respective contributions of atmosphere and ocean processes to the warming and cooling of the ML during the absence, development and mature phase of the ACT will be discussed. As the focus of this study is on the seasonal variability of the individual contributions to the ML heat budget, annual and semi-annual harmonics were fitted to the individual terms (besides of the diapycnal ML heat loss) before illustration (Fig. 6.4).

6.2.3.1. 0°N, 23°W

At the western edge of the ACT (23°W) in the central equatorial Atlantic, the ML is warmed by net atmospheric forcing (Fig. 6.1b, Fig. 6.4a) and by eddy heat advection. In the central equatorial Atlantic eddy heat advection is predominately controlled by TIWs (Jochum and Murtugudde 2006; Peter et al. 2006; Wang and McPhaden 1999). TIW activity here was reported enhanced in the beginning of the year, in boreal summer and autumn (Bunge et al. 2007; von Schuckmann et al. 2008), which agrees with periods of elevated eddy advection in this analysis (Fig. 5a). Cooling of the ML is achieved by subsurface processes (diapycnal mixing and entrainment) as well as mean heat advection (Fig. 6.4a).

During the *absence of the ACT* (January to April), the ML balance is dominated by net atmospheric forcing and eddy heat advection, the latter contributing to a warming of up to 50 W m^{-2} in January. During March and April, when the tropical Atlantic is uniformly warm and the meridional gradient of SST is very weak, the eddy heat advection reduces to zero.

During the *development phase of the ACT* (May to August) the net surface heat flux increases, mainly due to increased incoming solar radiation, which counteracts the observed cooling of SSTs. Eddy advection dominated by the effect of TIWs as discussed above contributes to the warming of the ML. However, there is a strong increase in ML cooling from zonal heat advection (60 W m^{-2}) and entrainment (25 W m^{-2}) during this phase. The elevated zonal advection term is due to the persistent westward flow (Fig. 6.1e) advecting cooler surface waters from the central ACT towards 23°W. In addition, elevated diapycnal heat loss at and below the ML further contributes to cool the ML: the two independent estimates for June from 2006 and 2011, 58 W m^{-2} (M68/2) and 54 W m^{-2} (MSM18/2) respectively, agree well. The cooling dominated by the diapycnal heat flux and zonal heat advection is strong enough to reduce SSTs despite the warming due to net surface heat fluxes and eddy advection.

Within the *mature phase of the ACT* (August to the end of the year) the net surface heat flux significantly warms the ML. Eddy advection still contributes significantly (50 W m^{-2}) to the warming. Cooling provided by zonal heat advection decreases at the beginning of the mature phase, due to the reduction in surface velocities associated with the nSEC (Fig. 6.1e). Towards the end of the year zonal heat advection re-intensifies in accordance with re-intensified zonal velocities

associated with the nSEC. The diapycnal heat flux during this period is still large. The two independent estimates for November from 2009 and 2012 yielded 45 W m^{-2} (MSM22) and 30 W m^{-2} (M80/1) respectively. The meridional heat advection increases within this phase due to increasing meridional velocities (Fig. 6.1) and increasing MLD (Fig. 6.1c). Entrainment still contributes a cooling of about 15 W m^{-2} during this phase. However, the gradual overall reduction of the cooling terms lead to a gradual increase in SSTs towards the end of the year.

Comparison of the sum of the individual terms contributing to the ML heat budget and the observed heat storage reveals a large residual of $30\text{-}100 \text{ W m}^{-2}$ throughout the year, if the contribution of the diapycnal heat flux is omitted (Fig. 6.4b). This was also reported in the recent study of Foltz et al. (2013). Similar residuals (around 80 W m^{-2}) have been reported in previous observational studies from the central equatorial Pacific (Wang and McPhaden 1999) as well as from the western equatorial ACT (Wade et al. 2011), where the diapycnal contribution could not be estimated. Including the resolved seasonal variability of the diapycnal heat flux into the sum of terms reduces the residual in boreal summer and November by more than a factor of 2 and closes the heat budget at least within the uncertainties (Fig. 6.4b). The diapycnal ML heat loss together with mean zonal advection are identified as the dominant contribution to the cooling of SSTs during ACT development at 0°N , 23°W .

6.2.3.2. 0°N , 10°W

In the center of the ACT (10°W) the ML is warmed by the atmosphere and eddy advection as was observed for 23°W . The ML is cooled by subsurface processes (diapycnal mixing and entrainment) as well as the meridional heat advection (Fig. 6.4c). Zonal heat advection at this site is significantly reduced in magnitude compared to the western edge of the ACT (23°W). Although westward surface velocities associated with the nSEC are also intensified at this location (Fig. 6.1e), the low zonal temperature gradient in the center of the ACT and shallow MLDs lead to reduced zonal heat advection compared to 23°W .

During the *absence of the ACT* (January to April) the ML heat budget at 10°W is dominated by net atmospheric forcing. The largest oceanic contribution is the meridional heat advection cooling the ML, which balances the warming via zonal heat advection and eddy advection. The meridional velocity is as explained previously a direct response to the meridional wind forcing. Although elevated ML cooling due to diapycnal heat fluxes is anticipated during this period, this study lacks observational support for this hypothesis.

Within the *development phase of the ACT* (May to August), the net heat flux from the atmosphere increases due to the reduction in latent heat flux due to reduced wind speed and an increase in the incoming solar radiation (Fig. 6.1b, Fig. 6.4c). Additional warming is provided by the eddy advection due to TIWs, similar as discussed for 23°W . However, strong subsurface cooling leads, despite these warming terms, to a cooling of the ML. The relative constitution of the subsurface cooling at this location differs from the observations at 23°W : Zonal heat advection is significantly reduced compared to 23°W , whereas entrainment is of similar magnitude

cooling the ML at a rate of about 20 W m^{-2} , which agrees with the results obtained by Rhein et al. (2010). The striking difference is the clear dominance of the diapycnal ML heat loss of up to 90 W m^{-2} over the other oceanic cooling contributions. As detailed in Hummels et al. (2013) elevated vertical shear of horizontal velocities increases the occurrence of shear instabilities leading to the elevated diapycnal heat fluxes during this phase.

During the *mature phase of the ACT* (August towards the end of the year) atmospheric warming stays on a rather high level. The cooling due to the diapycnal heat flux is still of considerable magnitude, but decreasing. The dominance of the diapycnal heat flux within the subsurface cooling terms reduces in favor of the meridional heat advection, which reaches 60 W m^{-2} towards the end of the year. This increase in meridional heat advection is due to enhanced meridional velocities presumably caused by increased southerly winds, temperature gradients and MLDs (Fig. 6.1). The warming effect of the eddy advection reduces during the mature phase and is accompanied by the zonal heat advection actually warming the ML towards the end of the year. This is due to the changing sign of the zonal velocity (the reversal of the nSEC between August and October; Fig. 6.1e) and the subsequent sign change for the zonal temperature gradient occurring in November and December (not shown). The gradual reduction in the total subsurface cooling leads to a gradual increase in SSTs during this phase.

Comparison of the sum of the individual terms of the ML heat budget to the observed heat storage reveals a large residual of up to 110 W m^{-2} when omitting the contribution of the diapycnal heat flux during boreal summer and autumn (Fig. 6.4d). This was already reported by Foltz et al. (2003), who performed a similar study at this location. Consideration of the diapycnal heat flux as a contributing term yields in a closure of the budget within the uncertainties from June to November. However, as further described below, ML cooling due to diapycnal mixing is likely to contribute to the ML budget also during the absence of the ACT.

6.2.3.3. $0^{\circ}\text{N}, 0^{\circ}\text{E}$

At the eastern edge of the ACT (0°E) the ML is mainly warmed by the net atmospheric forcing and cooled by the diapycnal heat flux (Fig. 6.4e). The other oceanic contributions do not exceed 20 W m^{-2} throughout the year. Zonal heat advection at this location is negligible throughout the year due to reduced zonal temperature gradients and MLDs (Fig. 6.1c), whereas entrainment acts to slightly cool the ML throughout the year, similar to what has been observed at 10°W . However, as pointed out above the net surface heat flux is significantly reduced in the eastern, equatorial ACT region compared to the more western and central locations (23°W , 10°W , Fig. 6.1b, Fig. 6.3). Accordingly, less subsurface cooling is required to decrease SSTs at this location.

During the *absence of the ACT* (January to April) in the beginning of the year the ML heat budget is determined by net atmospheric forcing and oceanic contributions do not exceed 10 W m^{-2} .

Incoming solar radiation reduces during *ACT development* (May to August) while the latent heat flux slightly increases, which leads to the reduction in net

surface heat fluxes during this period. Concurrently, the diapycnal heat flux as inferred from microstructure observations during June 2006 and 2007 increases to its maximum value at this location of 21 W m^{-2} and 29 W m^{-2} respectively and dominates the subsurface cooling (Fig. 6.4e). Note, that at this location the seasonal variability of the diapycnal heat flux was composed from available estimates at 0°N , 0°E as well as around 0°N , 2°E . MLDs are observed extremely shallow at this longitude (Fig. 6.1c). Hence, the additional subsurface cooling by diapycnal mixing, which superimposes on the reduced net surface heat flux, is sufficient for the strong decrease in SSTs. Eddy advection is negligible during this phase. At this longitude within the Gulf of Guinea TIWs have not been detected. Instead, Athie and Marin (2008) as well as the numerical simulation of Jouanno et al. (2013) suggest intraseasonal variability in the Gulf of Guinea dominated by wind-forced Yanai waves having long zonal wavelengths and a period between 10-20 days. From our analysis it seems that the effect of these waves with long zonal wavelengths on the eddy advection is significantly reduced compared to the effect of TIWs in the western equatorial ACT. Nevertheless they might contribute to enhance vertical shear of horizontal velocity and thereby favor diapycnal mixing at this location as suggested by Jouanno et al. (2013).

During the *mature phase of the ACT* (August to the end of the year), a similar evolution towards the end of the year is observed as at 10°W on the equator. Net surface heat fluxes increase due to the increase in the incoming solar radiation. Meridional and eddy heat advection both contribute about 20 W m^{-2} during this phase but with opposite sign. The cooling by the diapycnal heat flux reduces, which leads together with the increased warming by the atmosphere, to the retraction of the ACT towards the end of the year.

Comparison of the sum of individual terms to the ML heat budget and the observed heat storage reveals a residual of up to 30 W m^{-2} when omitting the contribution of the diapycnal heat flux (Fig. 6.4f), which is within the uncertainties at this location. However, if the diapycnal heat flux is included, the residual reduces minimum by a factor of 2 (Fig. 6.4f). Even if reduced in magnitude compared to the western and central equatorial region, the diapycnal heat flux provides the largest subsurface cooling term within the development phase of the ACT and hence seems to supply the essential contribution to cool SSTs.

No detailed observational study of the ML heat budget as far east as 0°E in the Gulf of Guinea has been published so far. Wade et al. (2011) determined the individual terms of the ML heat budget for considerable larger regions (about 5° latitude and 9° longitude). Their box 5, representative for a region including 0°N , 0°E , shows a considerable larger residual term of maximum 80 W m^{-2} during ACT development, which they associated with the diapycnal heat flux. Note, though that their box 5 extends until 6°W , where the diapycnal heat flux may still be elevated compared to 0°E . In addition, their estimate of the net surface heat flux within this box ranges from $50\text{-}120 \text{ W m}^{-2}$ and is above our estimates at 0°N , 0°E especially during ACT development (Fig. 6.1b). Thus, for their study a larger cooling by oceanic processes is required to match the observed heat storage.

6.3. Summary and discussion

A unique multi-cruise microstructure data set, observations from the PIRATA buoy network as well as climatological data sets are used to investigate the individual contributions to the seasonal ML heat budget at four different locations within the ACT region with a special focus on the role of the diapycnal heat flux. The ML budgets within different phases of the seasonal cycle associated with the absence, development and mature phase of the ACT are described. Microstructure observations allowed estimating the contribution of the diapycnal heat flux within the entire ACT region directly and not as a residual as has been done previously (Foltz et al. 2003; Foltz et al. 2013; Wade et al. 2011; Wang and McPhaden 1999). Here, the heat budgets are presented for four PIRATA buoy sites at 0°N , 23°W ; 0°N , 10°W ; 0°N , 0°E thus extending the work of Hummels et al. (2013) focusing on the heat budget at 0°N , 10°W . The major result is that the diapycnal heat flux is a dominant cooling term for the ML heat budget in the entire equatorial Atlantic during ACT development. Towards the eastern equatorial ACT region, the discrepancy between the net surface heat flux and the observed heat storage diminishes. Likewise the magnitude of diapycnal heat flux is reduced from the western, equatorial ACT towards the east in observations (Hummels et al. 2013) and models (Jouanno et al. 2011b). However, even in the eastern equatorial ACT it was found to be the largest contribution to ML cooling.

The dominance of the diapycnal ML heat loss within the entire equatorial region has been suggested from modeling studies (Jouanno et al. 2011b; Peter et al. 2006), but up to now was only assessed from direct observations for 0°N , 10°W (Hummels et al. 2013). Note that the results for 0°N , 10°W presented here are essentially the same as in Hummels et al. (2013) although different data sets are used for the surface velocities and the net surface heat fluxes. This points towards the fact that the obtained results concerning the individual contributions at this location are rather robust. Outside of the equatorial region, the variability of ML heat content within the ACT is set by net atmospheric forcing and horizontal advection.

The ML heat budget during the *development of the ACT* from May to August in the equatorial ACT region consists of the warming by net atmospheric fluxes and eddy advection and cooling by subsurface processes and horizontal advection. The cooling is dominated by the diapycnal heat flux at the base of the ML within the entire equatorial ACT. Eddy advection, which is associated with the lateral advection of heat by intraseasonal waves, moderates the cooling within the western and central equatorial ACT. Within the southern ACT region the cooling of SSTs during ACT development is driven by net atmospheric forcing.

During the *mature phase of the ACT* (August to the end of the year) net atmospheric forcing increases throughout the ACT region. Additional warming by eddy advection is still present. In the equatorial belt the cooling by the diapycnal heat flux decreases, while meridional heat advection becomes more important in cooling SST towards the end of the year.

During the *absence of the ACT* (January to April), the increase in ML heat content at all locations within the ACT is dominated by net atmospheric forcing. The

role of diapycnal heat fluxes during this period is hardly resolved from the multi-cruise data set. This will be further discussed below.

In general, the observed heat storage can be explained by the sum of terms, if the diapycnal heat flux is included. However, residuals between the sum of contributing terms remain especially within the western equatorial ACT at 0°N, 23°W. In addition, the uncertainties attributed to the sum of contributing terms are rather large. It should be noted though that here the 95 % confidence limits were presented, while in other studies only the standard error is considered. In the study of Foltz et al. (2003), the residual excluding the diapycnal ML heat loss at 23°W on the equator is of maximum 50 W m^{-2} and only present during the first half of the year. In a more recent study Foltz et al. (2013) revised this estimate using another surface velocity product. The differences between Foltz et al. (2003) and the results presented here can be attributed to extremely large zonal advection on the order of about 120 W m^{-2} during June-August and extremely low eddy advection from October to December, which reduce the residual in Foltz et al. (2003) during the second half of the year. Hence, the use of other surface velocity climatologies can lead to different results for the heat advection terms. This is also illustrated in Appendix B and demonstrates the necessity for improved surface velocity fields in order to get reliable estimates for the heat advection terms and their effect on the ML heat budget.

Unfortunately, and due to the scheduling of the microstructure measurement program the variability of the diapycnal heat flux during the absence of the ACT is not adequately resolved. However, Hummels et al. (2013) described a close agreement of the variability in the magnitude of turbulent parameters and the variability of large scale shear and stratification levels. Due to this good correspondence of vertical shear of horizontal velocities (S^2) and stratification (N^2) and the observed mixing intensities below the ML in the ACT region, Hummels (2012) proposed a simple relation of the form $\varepsilon = a \cdot Ri^b$ in order to estimate the seasonal variability of dissipation rates from observations of shear and stratification only. Here $Ri = N^2/S^2$ is the gradient Richardson number. The coefficients a and b were best fit to all available cruise data for the equatorial ACT region directly below the ML (MLD+5 m-MLD+20 m), which resulted in $a = 4 \times 10^{-8}$ and $b = -1.2$. To obtain this fit, shear was calculated from horizontal velocities observed with the vessel mounted ADCPs, which had a bin size of 8 m. This simple relation seemed to provide reasonable results in terms of magnitude and seasonal variation of the dissipation rates and further inferred diapycnal ML heat losses when applied to independent shear and stratification observations.

Independent observations of stratification were estimated from the subsurface measurements of temperature and salinity at fixed depths at the PIRATA buoys at 10°W and 23°W on the equator. Vertical shear of horizontal velocity was obtained from ADCPs moored in the proximity of the PIRATA buoy locations. Using the above mixing parameterization, the diapycnal ML heat loss on the equator at 23°W ranges on average between 22 W m^{-2} at the beginning of the year and 45 W m^{-2} during early summer (Fig. 6.5a). Here only data of 2002 and 2009-2012 were used, as within these years shear and stratification directly below the ML were adequately resolved. Maximum summer heat losses due to diapycnal mixing within the individual years

from this method range between 33 W m^{-2} and 67 W m^{-2} , which covers the range estimated directly from shipboard microstructure observations in summer (58 W m^{-2} and 54 W m^{-2}). Similar good correspondence is found at 10°W on the equator, where on average the parameterized diapycnal heat flux ranges between 40 W m^{-2} and 65 W m^{-2} , whereas individual summer maxima range between 70 W m^{-2} and 80 W m^{-2} compared to the maximum 90 W m^{-2} inferred from direct microstructure observations. Hence, this additional analysis tends to support the seasonal estimates obtained with the direct microstructure observations and could provide an estimate of the entire seasonal cycle of the diapycnal ML heat loss. In addition, the parameterized diapycnal ML heat losses suggest that even during the absence of the ACT the diapycnal ML heat loss is among the largest cooling terms in the western equatorial ACT. Incorporating these parameterized seasonal cycles of the diapycnal ML heat loss into the equatorial ML balances at 23°W and 10°W would lead to the closure of the ML heat budgets for the entire seasonal cycle within the uncertainties.

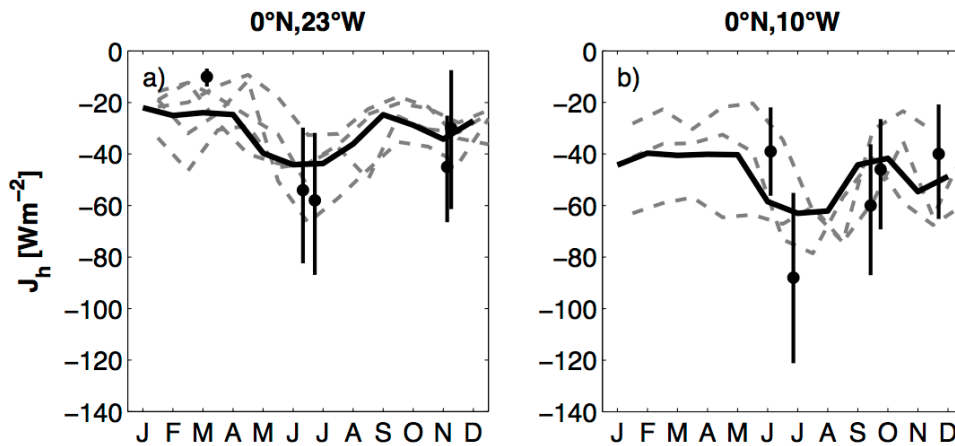


Fig. 6.5: Monthly averages of diapycnal ML heat loss estimated from shear and stratification observations at the PIRATA buoy sites $0^\circ\text{N}, 23^\circ\text{W}$ (a) and $0^\circ\text{N}, 10^\circ\text{W}$ (b) (heavy black lines averaged over the years 2002 and 2009-2012 for (a) and 2006-2007 and 2009 for (b)) and monthly averages of the individual years (dashed grey lines). Black circles mark the diapycnal ML heat loss estimated from microstructure observations together with their confidence limits as presented in Fig. 4.4a and c respectively.

7 Mixed layer heat and salinity budgets during the onset of the 2011 Atlantic cold tongue

Authors: M. Schlundt, P. Brandt, M. Dengler, R. Hummels, T. Fischer, K. Bumke, G. Krahnmann, J. Karstensen

Large-scale ocean-atmosphere interaction in the tropical Atlantic is an important driver of climate variability. It undergoes strong changes under current global warming conditions. Increasing sea surface temperatures (SSTs) (Deser et al. 2010; Xie et al. 2010) are associated with distinct changes in sea surface salinity (SSS) pattern (e.g. Durack and Wijffels 2010), which were predicted by climate models as the result of an increased hydrological cycle (e.g. Allen and Ingram 2002). However, the physical processes dominating the oceans' heat and salinity balances in the mixed layer (ML), which interact with the overlying atmosphere, are often poorly understood. A particular phenomenon in the Eastern Equatorial Atlantic (EEA) is the annual development of a region of cold SSTs. This so called Atlantic cold tongue (ACT) forms in boreal spring/summer, when the south easterly trades intensify (Philander and Pacanowski 1981), and retracts toward the end of the year resulting in uniformly warm SSTs within the tropical Atlantic. Minimum temperatures of about 22°C are reached within the "center" of the ACT at approximately 10°W (Jouanno et al. 2011b). This is a reduction of about 6°C compared to maximum SSTs occurring during late boreal winter and spring, before the onset of the ACT. The seasonal cycle of SST is most pronounced at this location. Towards the western and southern edges of the ACT the seasonal cycle of SST is still evident, but temperatures do not reach the minimum values found at 10°W at the equator. The interannual variability of the SSTs within the ACT is small in amplitude compared to the seasonal cycle. Nevertheless it is of climatic relevance: significant correlation was found between interannual variability of ACT and the West African Monsoon (WAM) (Brandt et al. 2011a; Caniaux et al. 2011).

A number of different processes lead to spatial and temporal variability of upper ocean temperatures and salinities on diurnal, intraseasonal, seasonal, interannual and longer time scales. Besides atmospheric forcing and horizontal advection through the currents, the ML is also influenced by vertical entrainment and diffusion through the ML base. However, the role of the different processes in the ML heat and ML salinity (MLS) budgets is still under debate.

In this study an extensive in-situ dataset is used to investigate the ML heat and salinity budgets concurrently. Hydrographic, oceanic microstructure, and atmospheric data collected during two expeditions on R/V Maria S. Merian (MSM) in spring/summer 2011 have been combined with simultaneous high-resolution temperature and salinity data from a glider swarm experiment. During this glider swarm experiment six gliders were deployed to measure hydrographic properties between 2°S and 2°N (one glider track was extended to 4°S) and between 23°W and 10°W. In the following we refer to the observational experiment as the "Cold Tongue Experiment" (CTE). The CTE data set is further augmented by temperature and

salinity profiles from Argo floats and time series from PIRATA buoys and subsurface moorings.

In contrast to former studies, that concentrated on single mooring locations or empirically defined boxes and examined seasonal ML heat budgets (Foltz et al. 2003; Hummels et al. 2013; Jouanno et al. 2011a; Peter et al. 2006; Wade et al. 2011), seasonal MLS budgets (Da-Allada et al. 2013), seasonal SST variability (Carton and Zhou 1997) or seasonal SSS variability (Bingham et al. 2012; Dessier and Donguy 1994), this study aims to estimate all terms contributing to the ML heat and MLS budgets as an average over the entire region

associated with the western ACT (Fig. 7.1). Due to the amount of ship time required to obtain such an extensive in-situ data set, the CTE covers only two months of the year 2011. The CTE was scheduled between May and July to focus on the processes responsible for the variability of SST and SSS during the development phase of the ACT.

7.1. Data and methods

To determine the various components of the ML heat and salinity budgets, observations of various parameters were required at adequate resolution, i.e. data for all heat and freshwater flux components between atmosphere and ocean, microstructure data to quantify oceanic mixing processes, ocean velocities and the hydrography of the ML itself. The strategy pursued here, which is explained in more detail below, requires complementing the in-situ data base with further products, such as satellite observations, reanalysis products for ocean-atmosphere heat and freshwater fluxes, surface and ML velocities and the output of a high-resolution assimilation model run. In this study, salinities are reported in practical salinity units (PSS-78).

7.1.1. Box-averaging strategy

In-situ data collected during the CTE indicate that the ML within the ACT region is characterized by relatively homogenous water mass. Elevated meridional temperature gradients limit the ACT region to the south between 3°S and 4°S and to the north between 1°N and 3°N. Maximum meridional temperature gradients from satellite SST at 3-day resolution were used to define the meridional extent of the ACT (Fig. 7.1). The zonal boundaries of the ACT box were set to 23°W and 10°W based on the availability of ship and glider data. To compare the distinct characteristics of the heat and salinity budgets of the ACT region, a second box located to the north of

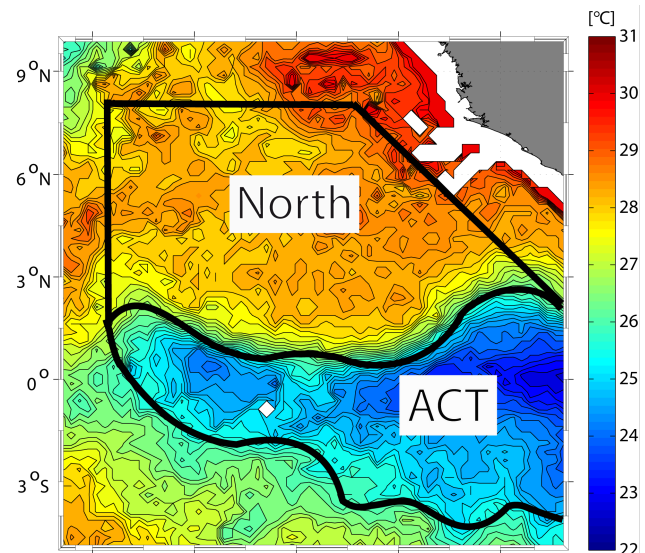


Fig. 7.1: Box edges (black lines) and SSTs from TMI (Background colors) between 14th and 17th of June 2011. “ACT” describes the area associated with the Atlantic cold tongue (ACT box), while the northern box is denoted “North”.

the ACT between the northern ACT boundary and a fixed boundary at 8°N (Fig. 7.1) was defined. Boxes used for the model analysis followed exactly the same approach. All individual contributions to the ML heat and salinity budgets were calculated either from individual profiles or from a regular 1°x1°-grid and subsequently averaged in the two boxes.

7.1.2. Ship data

During the two research cruises “MSM18/2” and “MSM18/3”, lasting from the 11th of May to the 11th of July, profiles with a conductivity, temperature and depth (CTD) probe were acquired, as well as continuous observations of the upper ocean temperature and salinity with a thermosalinograph (TSG) (Fig. 7.2). CTD profiling was performed with a SeaBird 911 CTD rosette system and measured salinity was calibrated against bottle salinity samples analyzed with a Guildline Autosol salinometer. The TSG data was recorded every minute using a SeaBird 38/45 system with an intake located at 6.5 m depth in the front of the ship. The TSG observations were calibrated against CTD data from 6-7 m depth and later considered as additional ML temperature (MLT) and MLS observations for the box and time averaging and for the comparison with satellite observations.

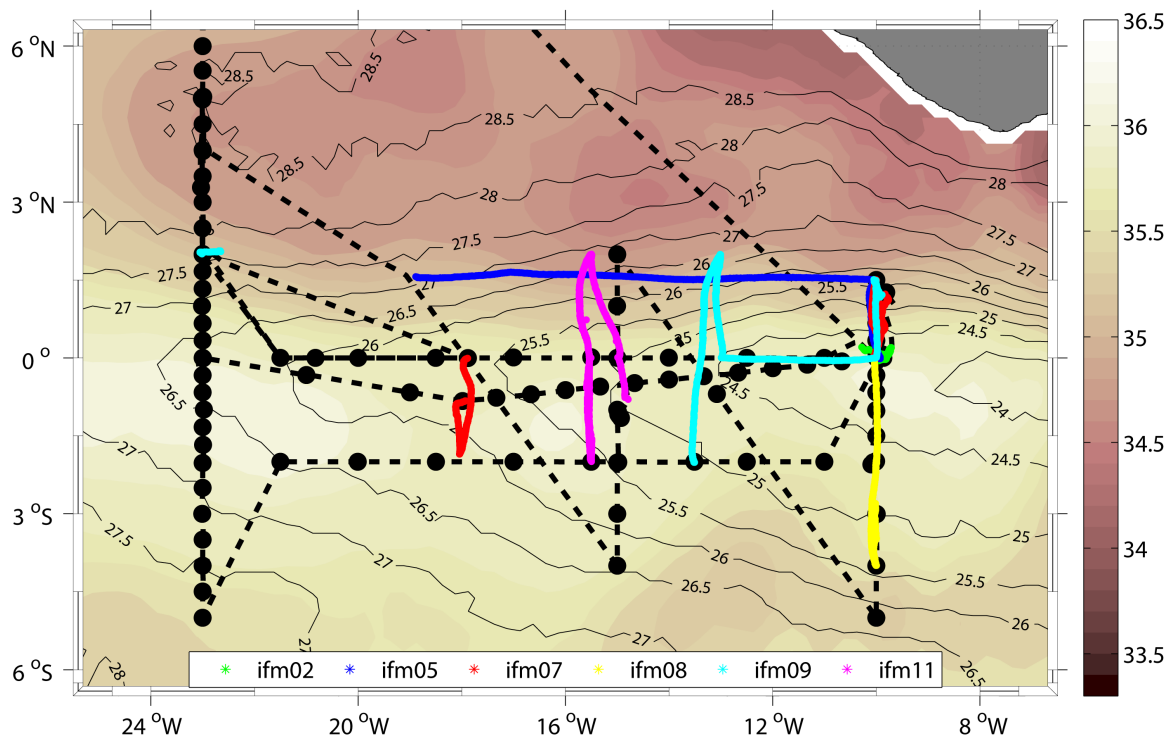


Fig. 7.2: Observations during the cold tongue experiment conducted between May and July 2011. Colored lines denote the glider tracks, dashed black lines show cruise tracks, and black dots are CTD stations. Background colors show 3-month mean SSS from SMOS with contour interval 0.1, while contour lines show 3-month mean SST from TMI in °C. Contour interval is 0.5 °C.

Along with the CTD profiles microstructure observations were performed at almost all stations. The microstructure data was collected using an MSS-90D profiler manufactured by Sea&Sun Technology. It was equipped with two shear sensors, a

fast temperature sensor, an acceleration sensor and a tilt sensor, plus a set of slower response standard CTD sensors. The data was sampled at a rate of 1024 Hz. A detailed description of the probe is given in Prandke and Stips (1998). From the observed velocity-microstructure it is possible to derive the dissipation rate of turbulent kinetic energy (TKE), from which the diapycnal fluxes of heat and salt can be estimated. The dissipation rate is calculated under the assumption of isotropic turbulence from the shear wavenumber spectrum ($E_{du'/dz}$). The spectrum is integrated between dynamically adapted wavenumber limits with $\varepsilon = 7.5 \nu \int_{k_{min}}^{k_{max}} E_{du'/dz}(k) dk$ to estimate the dissipation rate ε (ν is the kinematic viscosity of seawater). Due to the limited resolved wavenumber band, a variance loss correction is applied according to the universal Nasmyth spectrum (Oakey 1982). The derivation of dissipation rates followed here is described in detail in Schafstall et al. (2010) and Hummels et al. (2013).

Shipboard observations of atmospheric properties during CTE included measurements of the downward shortwave radiation flux with a pyranometer and the downward longwave radiation flux with a pyrgeometer every 2 seconds (for a description of the devices and the data processing see Kalisch and Macke (2012)). Precipitation was monitored using an optical disdrometer (Großklaus et al. 1998) and the ship's rain gauge (Hasse et al. 1998). A description of the analysis inferring precipitation from the ship's rain gauge is given by Bumke and Seltmann (2012). The reflected shortwave radiation was computed according to Taylor et al. (1996), while upward longwave radiation (F_{LW}^{\uparrow}) was calculated according to the Stefan-Boltzmann law, $F_{LW}^{\uparrow} = 0.97 \sigma SST^4$, where σ is the Boltzmann constant, assuming an emissivity of 0.97 for the sea surface. Turbulent heat fluxes and evaporation were computed from the ship's weather station data by using the parameterization of Bumke et al. (2014). They estimated the bulk transfer coefficients for latent and sensible heat and the drag coefficient with the inertial dissipation method and compared their fluxes with the fluxes estimated with latest version of the COARE algorithm (Fairall et al. (2003)). We also calculated the turbulent fluxes and the evaporation with the COARE algorithm which yielded only marginal differences in the final fluxes, similar to the findings of Bumke et al. (2014).

7.1.3. Glider data

Six autonomously operating Slocum electric gliders provided temperature and salinity profiles at approximately 3-4 km horizontal resolution and to maximum depths of 800 m. Altogether ten glider deployments, mostly along meridional sections (Fig. 7.2), were performed during the CTE, yielding in a total of about 5600 profiles. Thermal lag hysteresis in salinity calculations was corrected by applying the method of Garau et al. (2011), where four correction parameters are determined by minimizing the area between two temperature-salinity curves of successive CTD-casts.

7.1.4. Auxiliary datasets

7.1.4.1. Hydrographic data

Temperature and salinity profiles from Argo floats (provided by the US Global Ocean Data Assimilation Experiment (USGODAE)) and time series of temperature and salinity from the moored PIRATA buoys (provided by the Pacific Marine Environmental Laboratory (PMEL)) were used to further supplement the hydrographic dataset during the CTE as a part of a large hydrographic dataset.

7.1.4.2. Atmospheric data

Several atmospheric data products for the surface radiative and turbulent heat fluxes and the freshwater flux were compared. In particular, the data from the ERA-Interim reanalysis (Dee et al. 2011) from the European Centre for Medium-Range Weather Forecasts (ECMWF) was available for the net shortwave radiation, net longwave radiation, latent and sensible heat flux, evaporation and precipitation. They provide 12-hourly data at 0.75° resolution. The second product that provides all relevant surface fluxes is the NCEP2 reanalysis (Kanamitsu et al. 2002) from the National Center for Environmental Prediction (NCEP) with daily fields at 1.875° resolution. All radiative and turbulent heat fluxes together with evaporation are also available as TropFlux products (Praveen Kumar et al. 2012) on a 1° grid in the tropics (30°S-30°N) and at daily resolution. On the same spatial and temporal resolution latent heat flux and evaporation were taken from the Objectively Analyzed air-sea fluxes (OAFlux) data from Woods Hole Oceanographic Institute (Yu et al. 2008). All daily averaged datasets were compared with daily averages of onboard in-situ observations. The best agreement between the different radiative or turbulent fluxes and the ship-based observations was achieved with different data products. However, the best general agreement was achieved with the TropFlux product and the turbulent heat fluxes, evaporation, as well as net surface shortwave and longwave radiation are in the following taken from the TropFlux product.

Precipitation estimates were taken from the Advanced Microwave Scanning Radiometer (AMSR-E) onboard the NASA Aqua spacecraft, from the TRMM Microwave Imager (TMI) onboard the Tropical Rainfall Measurement Mission (TRMM) satellite, as well as from the Special Sensor Microwave Imager Sounder (SSMIS) F17 onboard the DMSP satellite. From all three products daily averages at a quarter-degree resolution were statistically compared against the direct shipboard observations with the method of Bumke et al. (2012). The analysis revealed by taking the statistical parameters into account, that the AMSR-E satellite precipitation product was closest to the observations and it was finally chosen.

7.1.4.3. SST and SSS data

SST data was taken from the TMI onboard the TRMM satellite to calculate horizontal SST gradients required to estimate the advective contribution to the heat budget.

Horizontal SSS gradients were calculated based on the SMOS data. SMOS SSS measurements on a 1°x1°-grid and with 10-day composites have, compared to Argo SSS, a current bias of ~0.3-0.4 (Boutin et al. 2012; Reul et al. 2012).

7.1.4.4. Velocity data

Surface velocities within the entire study region were required to estimate the advection terms. The Ocean Surface Current Analysis Real-time (OSCAR) product is used, which is derived from sea level measurements, wind stress and SST data (Lagerloef et al. 1999). This dataset represents vertically averaged geostrophic and Ekman velocities in the upper 30 m of the ocean (Bonjean and Lagerloef 2002). The filtered version of this dataset at a horizontal resolution of $1^{\circ} \times 1^{\circ}$ with a temporal resolution of 5-days is used here. Explanation and validation of the OSCAR product as well as error estimates are described in Johnson et al. (2007).

7.1.4.5. Mercator assimilation model

In addition to the observation based data products, we used the “Mercator Global operational System PSY2V4R2” model output in our analysis to estimate the horizontal advection terms and the entrainment. The model output corresponds to a simulation that assimilates SST and sea level anomaly (SLA) fields, temperature and salinity profiles, and a mean dynamic topography. Three-dimensional fields of zonal and meridional velocities, temperature and salinity are provided as output. The horizontal resolution is $1/12^{\circ} \times 1/12^{\circ}$ (9 km at the equator; decreasing poleward) with daily fields. There are 36 vertical levels in the first ~1000 meters. In the model, the vertical grid spacing changes from nearly one meter close to the surface to about 150 meters at 1000m depth (Lellouche et al. 2013).

7.1.4.6. Data for the mean seasonal cycle of MLS

The seasonal salinity budgets were estimated at the locations of three PIRATA buoys at the equator, 10°W and 23°W , and at 4°N , 23°W . A unique dataset of microstructure shear and temperature profiles and CTD salinity profiles was used to estimate the dissipation rates of TKE. The dataset was collected during 9 cruises to the ACT region carried out in different seasons between 2005 and 2012. A detailed description of data set and post-processing procedures are given in Hummels et al. (2013) and in Hummels et al. (2014). For this study, the dataset was supplemented by microstructure data from the R/V Maria S. Merian cruise MSM18/3. From this data set, profiles were used taken in the latitude range $\pm 2^{\circ}$ and in the longitude range $\pm 0.3^{\circ}$ relative to the nominal locations of the three selected PIRATA buoys.

All available buoy and mooring data, as the essential database for this part of the study, from January 1999 to December 2012 (first dates used: 01/30/1999 for $0^{\circ}\text{N}, 10^{\circ}\text{W}$; 03/07/1999 for $0^{\circ}\text{N}, 23^{\circ}\text{W}$; 06/12/2006 for $4^{\circ}\text{N}, 23^{\circ}\text{W}$) and several climatological products were used. Surface velocities were constructed from a combination of the YOMAHA'07 data set (Lebedev et al. 2007) and available surface drifter trajectories (Lumpkin and Garzoli 2005). The YOMAHA'07 velocities were derived from Argo float trajectories and provided by the Asia-Pacific Data Research Center and the International Pacific Research Center (APDRC/IPRC). A detailed description of the wind-slip correction and the construction of the combined velocity product is given in Perez et al. (2013).

The horizontal salinity gradients were constructed from the global monthly mean salinity dataset from the Japan Agency for Marine-Earth Science and

Technology (JAMSTEC). This dataset is derived from Argo float observations which are binned to $1^\circ \times 1^\circ$ monthly means from January 2001 ongoing (Hosoda et al. 2008). We used the data until December 2012. The periods of data coverage from satellite observations of SSS, SMOS started in November 2009 and Aquarius in July 2011, aren't long enough for a robust seasonal cycle.

Monthly means from AMSR-E precipitation (beginning in June 2002) and TropFlux evaporation (beginning in January 1999), and 3-day averages of SMOS SSS (beginning in January 2010) and TMI SST (beginning in January 2010), until December 2012 were used as well. The MLD climatology of de Boyer Montégut et al. (2004) was implemented to derive the horizontal gradients of the MLD. The MLDs were interpolated on a $1^\circ \times 1^\circ$ grid and the gradients were estimated with central differences on that grid.

7.1.5. Methodology

7.1.5.1. Heat and salinity budgets

The ML heat balance can be expressed as follows (Foltz et al. 2003; Stevenson and Niiler 1983)

$$\rho c_p h \frac{\partial T}{\partial t} = -\rho c_p h (\mathbf{u} \cdot \nabla T + \overline{\mathbf{u}' \cdot \nabla T'}) - \rho c_p w_e \Delta T + q_0 + R \quad (1)$$

T is the MLT, t is time, h is the MLD, \mathbf{u} is the ML-averaged horizontal velocity, \mathbf{u}' and T' are deviations from the temporal average (the temporal average is denoted with an overbar), $\Delta T = T - T_{-h}$ is the difference between T and the temperature at the base of the ML (T_{-h}) and w_e the entrainment velocity. ρ is the density of the ML, c_p the specific heat capacity at constant pressure and q_0 is the net heat flux through the ocean's surface corrected for the penetrative shortwave radiation through the ML base.

The local heat storage on the left hand side of equation (1) is balanced by horizontal temperature advection (divided into a mean and an eddy part), entrainment into the mixed layer, net surface heat flux and a residual term R . The residual represents the sum of all unresolved physical processes and the accumulation of errors from the other terms. The net heat flux at the ocean's surface is the sum of the net (incoming minus reflected) shortwave radiation - corrected for the amount penetrating below the ML -, the net longwave radiation, the latent heat flux and the sensible heat flux.

Similarly the balance for MLS is after e.g. Delcroix and Hénin (1991) given by:

$$h \frac{\partial S}{\partial t} = -h (\mathbf{u} \cdot \nabla S + \overline{\mathbf{u}' \cdot \nabla S'}) - w_e \Delta S + (E - P)S + R \quad (2)$$

S is the MLS, S' is the deviation from the temporal average, E is the evaporation, P is the precipitation, and $\Delta S = S - S_{-h}$ is the difference between S and the salinity at the base of the ML (S_{-h}). The first term on the right hand side of equation (2) describes the horizontal advection of salinity (divided into a mean and an eddy part) and the second term represents salinity entrainment through the ML base. The third term is the freshwater flux through the ocean's surface, while R again represents the residual including the sum of all unresolved physical processes and the accumulated errors from the other terms.

According to Stevenson and Niiler (1983) the entrainment velocity can be defined as

$$w_e = H\left(\frac{\partial h}{\partial t} + w_{-h} + \mathbf{u} \cdot \nabla h\right). \quad (3)$$

The entrainment velocity thereafter is the sum of the local change in MLD with time, the vertical velocity w_{-h} at the ML base and the horizontal advection of MLD ($\mathbf{u} \cdot \nabla h$). Only the upward movement (entrainment) in equation (3) was considered because downward movement (detrainment) does not affect the temperature or the salinity in the ML. This constraint was implemented with the use of the Heaviside unit function: $H(x) = (1, x \geq 0 \text{ and } 0, x < 0)$.

In this contribution, the different terms of equation (1) and (2) were estimated for the two boxes described in section 2.1 for the period of the CTE using 10 day time steps as well as for the PIRATA buoy sites at 4°N and the equator at 23°W and at the equator at 10°W using monthly-averaged data. The different methodologies used to determine the individual contributions are described in the following.

7.1.5.2. Methodology to derive heat and salinity budget terms

This section describes the calculation of the individual quantities and terms from the equations (1) and (2). For all quantities the calculation for the CTE is described at first and followed by the calculation for the mean seasonal cycles at the PIRATA buoys.

Mixed layer depth

The ML can be defined as the surface layer of constant potential density and hence the depth where the density starts to increase is the MLD. Another definition of the ML is a surface layer of constant temperature. Here, the depth where the temperature starts decreasing is called isothermal layer depth (ILD). The ILD was determined as the depth at which temperature is 0.5°C lower than the temperature averaged between 2 and 6 meters depth. The MLD was defined as the depth where the potential density has increased equivalently to a temperature decrease of 0.5°C while salinity and pressure are held constant. The required potential density increase was about 0.15 kg m⁻³, slightly varying with SSS. We avoided effects of diurnal cycles in MLD/ILD for the temporal averaging of fluxes through the ML base by using these definitions. Diurnal cycles were present when using 0.2°C ILD-criterion (corresponding to a MLD-criterion of ~0.06 kg m⁻³). No significant difference between MLD and ILD was found in the high resolution glider data at all locations. Therefore the simpler temperature criterion was chosen for our definition of the MLD.

To estimate the seasonal cycles the daily mean MLDs were averaged for all days of the year using all available data from January 1999 to December 2012. Afterwards monthly means were constructed. From these the temporal evolution of the MLD was calculated as well.

Horizontal advection

For the CTE, horizontal advection was not separated into mean and eddy contribution, because the time period of the CTE was too short. Here total advection

of heat and salinity were estimated 1) by combining velocities from the OSCAR product with horizontal temperature and salinity gradients from satellites respectively and 2) from the Mercator assimilation model output. Horizontal gradients of satellite SST and SSS were calculated using central differences of the $1/4^\circ$ gridded data set that were subsequently averaged onto the OSCAR-native $1^\circ \times 1^\circ$ grid. Finally, the $1^\circ \times 1^\circ$ advection terms were spatially averaged for the two boxes described in section 7.1.1.

Velocities from the Mercator assimilation model were averaged in the upper 30 m using trapezoidal integration in order to be comparable to the OSCAR estimates. Advection of heat and salinity were then estimated on the $1/12^\circ \times 1/12^\circ$ grid and subsequently averaged for the two boxes described above. Finally, the advective terms from the OSCAR/satellite product and from the model were temporally-averaged as 10-day means.

A comparison of the spatially averaged advection terms in the two boxes showed that zonal heat and salinity advection determined from the model output was smaller compared to those determined from the OSCAR/satellite product (not shown). The main reason for the difference is the generally weaker zonal velocity of the Mercator assimilation model output compared to the OSCAR estimates for the CTE period.

To obtain a mean seasonal cycle of horizontal salinity advection, mean and eddy advection were calculated separately at the PIRATA buoy sites. For the mean salinity advection, monthly mean velocities were calculated on a $1^\circ \times 1^\circ$ grid from all available float and drifter data. The monthly mean horizontal gradients of SSS from float observations were calculated with central differences on the same $1^\circ \times 1^\circ$ grid and afterwards averaged for the mean seasonal cycle. Note, that the salinity climatology captures only the time from January 2001 to December 2012.

Eddy salinity advection, $(\overline{\mathbf{u}' \cdot \nabla S'})$, was estimated for the equatorial moorings by assuming a correlation between temperature and salinity fluctuations. Using the eddy temperature advection $(\overline{\mathbf{u}' \cdot \nabla T'})$ the eddy salinity advection was calculated via

$$\overline{\mathbf{u}' \cdot \nabla S'} \approx \overline{\mathbf{u}' \cdot \nabla T'} \frac{\delta S}{\delta T}. \quad (4)$$

The eddy temperature advection is calculated indirectly as the residual of the mean horizontal advection, estimated with the mean TMI SST and the aforementioned mean velocities (Hummels et al. 2014), and the total horizontal advection, estimated by the difference between total time derivative and local time derivative of SST (Swenson and Hansen 1999). The total time derivative of SST is calculated from SST changes along Lagrangian drifter trajectories. The local time derivative is estimated from monthly averaged TMI SSTs. The regression of SSS and SST $(\frac{\delta S}{\delta T})$ was calculated on a monthly basis by using three years (2010-2012) of 3-day averages of satellite SSS and SST observations in a box $2.5^\circ \times 2.5^\circ$ around the buoy locations and daily PIRATA SSS and SST observations from 1999 to 2012. The regression coefficient for one climatological month is calculated separately for the satellite and the buoy observations by taking the slope of the regression line of all pairs of SSS and SST observations in the particular month in all years. Finally the monthly mean of the monthly satellite and buoy regression coefficients are used. The

two independent estimates of the regression of SSS and SST are very similar with regard to their seasonal cycle and their annual means.

Entrainment

Entrainment was calculated from the Mercator assimilation model output only. There were no observational vertical velocity estimates available for the period of the CTE. The vertical velocity at the ML base was calculated using the continuity equation $w_{-h} = h(\nabla \cdot \mathbf{u})$. Horizontal gradients of ML velocity and MLD were estimated with central differences on the $1/12^\circ \times 1/12^\circ$ model grid. Local changes in MLD were derived on a daily basis.

Entrainment for the mean seasonal cycles at the PIRATA buoy locations was calculated from the MLD gradients, the horizontal divergence of the monthly mean horizontal velocities and the local time derivative of the MLD.

Surface heat and freshwater fluxes

All atmospheric datasets were re-gridded linearly on a $1^\circ \times 1^\circ$ grid and for the surface freshwater flux combined with box- and time-averaged MLS and MLD. The penetrative shortwave radiation was calculated following Wang and McPhaden (1999) assuming an exponential decay of surface shortwave radiation with 25 m e-folding depth for the North box and 15 m for the ACT box. The smaller e-folding depth (i.e. stronger absorption of shortwave radiation) in the ACT region follows from enhanced chlorophyll concentrations near the equator (e.g. Grodsky et al. 2008).

For the seasonal cycles of the surface freshwater flux monthly means of all atmospheric datasets were used and averaged in mean months of the year. These were combined with monthly means of MLS and MLD estimated with the PIRATA buoy data.

Diapycnal diffusivities and fluxes

In regions where the stratification is dominated by temperature the diapycnal diffusivities of heat and mass are similar ($K_h = K_\rho$, e.g. Peters et al. (1988)). Using the observed dissipation rates the diapycnal diffusivity of mass was estimated following Osborn (1980)

$$K_\rho = \Gamma \varepsilon N^{-2} \quad (5)$$

N^2 is the buoyancy frequency and Γ is the turbulent mixing efficiency. Γ is set constant to 0.2, which is commonly used in several other studies (e.g., Moum et al. (1989); Hummels et al. (2013)). Further, the diapycnal heat flux was estimated using

$$J_{heat} = -\rho c_p K_\rho \frac{\partial T}{\partial z} \quad (6)$$

For shear-driven turbulence the diapycnal diffusivity of salt (K_S) is equal to the diapycnal diffusivity of heat (e.g., Osborn and Cox (1972); Osborn (1980); Schmitt et al. (2005)) and, thus, equal to the diapycnal diffusivity of mass ($K_S = K_h = K_\rho$). With this assumption the diapycnal salt flux was calculated using

$$J_{salt} = -K_\rho \frac{\partial S}{\partial z} \quad (7)$$

Diapycnal diffusivities, vertical temperature gradients, and vertical salinity gradients were averaged vertically in this study between 5 and 15 meters below the ML base. The upper boundary was chosen to exclude ML values from the average. Lien et al. (2008) and Hummels et al. (2013) showed that the diapycnal heat flux is highly divergent in the vertical and rapidly decreases below the ML base. Therefore, the average within the narrow layer between 5 and 15 meters below the ML base was used. Due to the limited amount of microstructure profiles available and the large variability inherent in turbulent mixing in the ocean, diapycnal fluxes were averaged for two periods: (1) the first half of the CTE (May until mid-June) and (2) the second half of the CTE (mid-June/July). To these two periods will be referred later in section 3, when the ML budgets are described. For the seasonal cycles monthly means of the diapycnal salt flux were calculated. Uncertainties of the fluxes were estimated from error propagation and boot strapping as detailed in Hummels et al. (2013).

7.2. Results

7.2.1. The ACT in boreal summer 2011

7.2.1.1. Surface observations of temperature and salinity

The long-term observations of SST and SSS at the PIRATA buoy sites at 23°W and 10°W on the equator can be used to investigate the exact timing of ACT development during 2011 with respect to the climatological cycles (Fig. 7.3). At 23°W (western part of ACT region) SST (Fig. 7.3a) and SSS (Fig. 7.3b) in 2011 align well with the average seasonal cycle. In contrast, in the center of the cold tongue at 10°W, the onset of the cooling was approximately one week earlier and the cooling was stronger in 2011 compared to the climatology (Fig. 7.3c). Similar, SSS exhibited an earlier and stronger increase this year (Fig. 7.3d). The comparison shows that the time period of our experimental campaign (May-July 2011) was well chosen in terms of studying the processes during cold tongue development as well as covering the entire cooling period in the center of the ACT. However, a large SSS increase occurred before the CTE that was not covered by our measurements.

The onset and spreading of the ACT in boreal summer 2011 is apparent in the monthly equatorial SST evolution (Figs. 6a, c, e, and g). The strongest cooling, resulting in minimum temperatures of less than 22°C, was found at the equator at around 10°W. In June and July the negative SST anomaly expanded further to the west- and southwest, but with a weaker intensity. The monthly satellite data showed a strong increase in SSS in the EEA from April to May (Figs. 6b and d) followed by a period of nearly constant SSS (Figs. 6f and h). Within the northern box (Fig. 7.1), a reduction of SSS occurred from April through June, which is associated with the northward migration of the ITCZ. From June to July, SSS increased in the southern part of that region (2°-5°N).

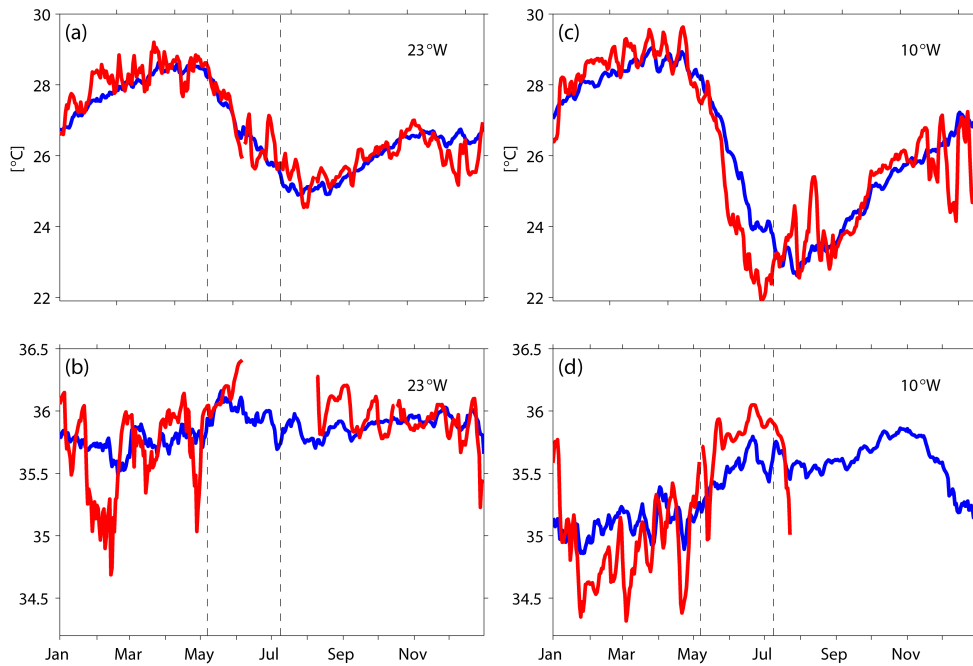


Fig. 7.3: Mean seasonal cycle (blue) of SST (a, c) and SSS (b, d) for the PIRATA buoy at 23°W at the equator (left; a, b) and 10°W at the equator (right; c, d) based on averaging all data from beginning of the measuring period (SST/SSS at 23°W: 7th of March 1999; SST at 10°W: 15th of September 1997; SSS at 10°W: 29th of January 1999) to the end of 2012. The red line indicates SST and SSS in 2011, while the dashed vertical black lines mark the beginning and end of the CTE.

7.2.1.2. Vertical structure of temperature and salinity

Subsurface hydrographic changes during ACT development at 10°W were monitored with high vertical and temporal resolution using glider (Fig. 7.5) and moored temperature and salinity recorders. Surface cooling, as evident from the satellite SSTs, was also clearly visible in the gliders' CTD measurements (Fig. 7.5a). In addition, the high vertical-resolution of those data revealed a shoaling of the MLD during the first month of observations (Fig. 7.5c).

The temporal evolution of the vertical salinity structure was more complex. At the beginning of the time series a pronounced salinity maximum was present below a rather fresh ML (Fig. 7.5b). The salinity maximum is related to the eastward transport of saline water from the western Atlantic within the EUC occurring during spring (Johns et al. 2014; Kolodziejczyk et al. 2014). A strong increase in MLS was observed with the onset of the cold tongue, while the subsurface salinity maximum was reduced. The simplest explanation would be a vertical redistribution and mixing of salinity through exchange processes across the ML base. However, advective processes played the dominant role as will be shown below. MLS remained elevated during the further development of the cold tongue, whereas in the beginning of July the subsurface salinity maximum reappeared. Typically, MLDs are shallowest in tropical upwelling regions (e.g., de Boyer Montégut et al. (2007)). Indeed, at the survey site, MLD never exceeded 30m, but a clear diurnal cycle is visible when using a smaller temperature criterion ($dT=0.2^{\circ}\text{C}$) for the MLD than chosen for the ML budgets, i.e. $dT=0.5^{\circ}\text{C}$ (Fig. 7.5c). The abrupt increase in MLT and decrease in MLS

on May 14th (Fig. 7.5a and b) was a remarkable event in the temperature and salinity time series, which counteracted the trends expected from the cold tongue development. Satellite SST distributions from this period (not shown) suggested that the anomaly was caused by the propagation of a TIW that moved the SST front, here defined as the maximum meridional SST gradient at 10°W, north of the ACT southward (Fig. 7.5d).

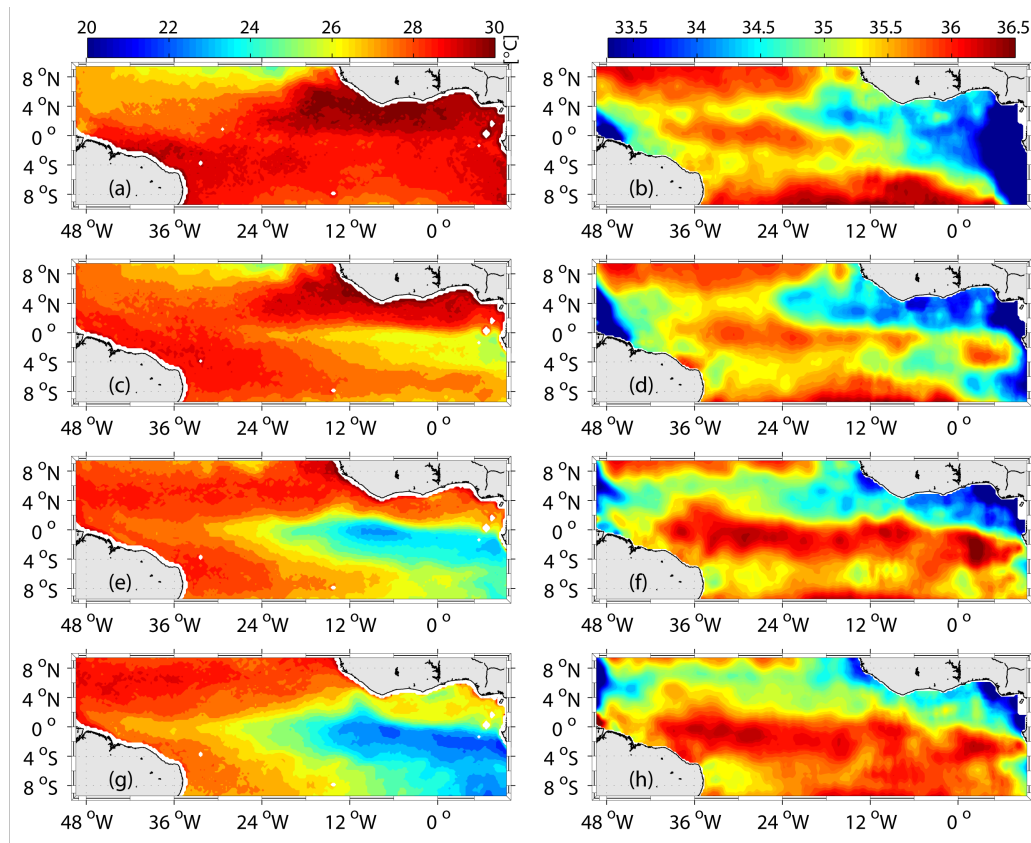


Fig. 7.4: Monthly mean fields of SST (a, c, e, g) from TMI and SSS (b, d, f, h) from SMOS. Upper row is April (a, b), top middle row is May (c, d), lower middle row is June (e, f) and lower row is July (g, h).

The glider surveys along meridional or zonal sections (Fig. 7.2) exhibit a mixture of temporal and spatial variability. One glider was assigned to profile along a meridional section at 15.5°W between 2°S and 2°N (Fig. 7.6d). The glider crossed the SST front on June 10th, stayed north of the front, and crossed back on June 18th (Fig. 7.6d). The first crossing of the front was clearly visible in the freshening of the ML in association with increased temperatures (Fig. 7.6a and b). North of the front, a diurnal cycle in MLD (using the 0.2°C criterion) is not evident (Fig. 7.6c). The glider was close to the equator and crossed the EUC core with the subsurface salinity maximum three times: at the beginning of the section, around the 10th of June, and at the end of June (Fig. 7.6b and d). North and south of the equator and away from the EUC the subsurface salinity maximum was weak or not present.

To further investigate the spatial and temporal distribution and evolution of the subsurface salinity maximum, the glider and CTD data were supplemented with CTD data from a French PIRATA cruise (PIRATA-FR21) and Argo float profiles. The

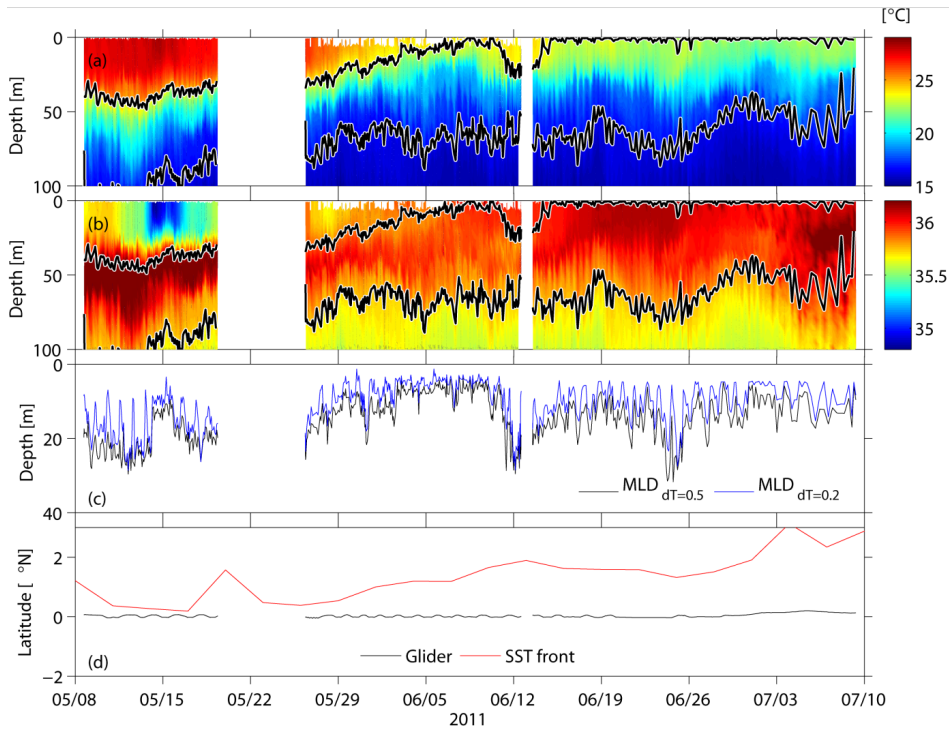


Fig. 7.6: Time series of glider ifm02 of temperature (a), salinity (b), MLD (c) and latitudinal position (black; d). In panels (a) and (b) the potential density surfaces 24.5 and 26.2 are denoted in black. In panel (d) the latitude of the SST front at 10°W is denoted in red. The glider profiled all the time close to the PIRATA buoy at 10°W. The two gaps in the time series stem from recoveries for battery exchanges.

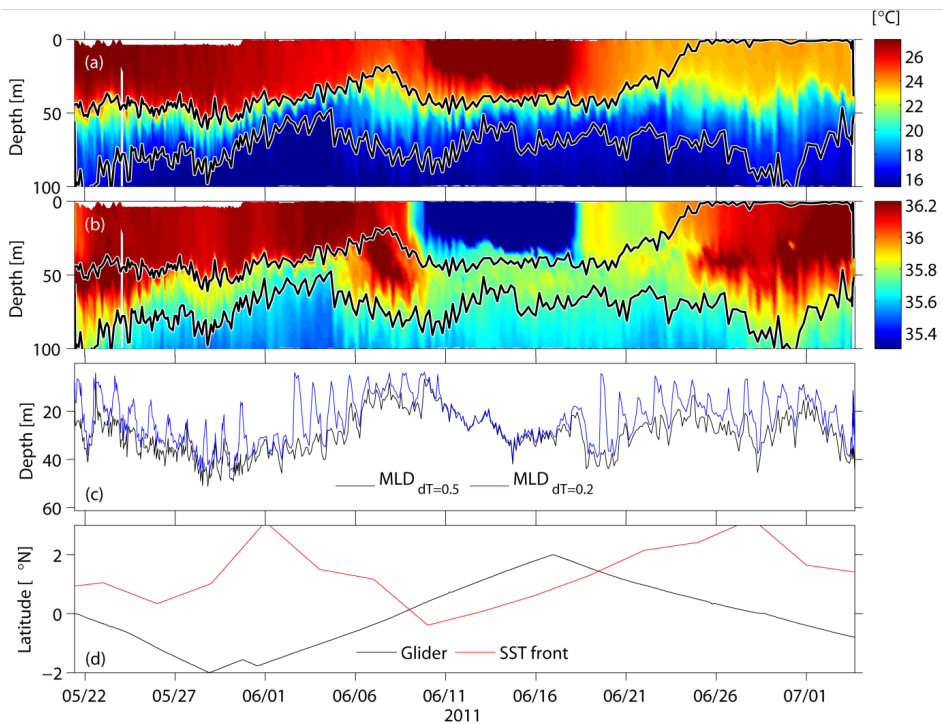


Fig. 7.5: Same as Fig. 7.5, except for glider ifm11 profiling along a meridional section at about 15.5°W.

results revealed a general reversal of the upper-ocean vertical salinity gradient (Fig. 7.7). At the beginning of the CTE the thermocline layer (TL; defined with the potential density range: $24.5 \leq \sigma_\theta \leq 26.2$) was more saline than the ML in the entire equatorial ACT region (Fig. 7.7a). This is due to the fact that the TL contains the EUC core that

is advecting high saline waters from the west during this period. However, south of the equator the ML was saltier than the TL during May and beginning of June (Fig. 7.7b-d). This reversed vertical salinity gradient weakened later at the end of June and the beginning of July, when MLS and the TL-salinity became equal in the ACT region (Fig. 7.7e and f). Note, that during June and July the upper boundary of the TL ($\sigma_\theta = 24.5$) reached the sea surface (Fig. 7.5b and Fig. 7.6b). The described variability of the vertical salinity gradient is independent of the measurement device and visible in glider profiles as well as CTD and Argo float profiles. Taking the mean seasonal cycle of the salinity difference between ML and TL from Argo it is obvious that the difference changes sign in boreal summer (Fig. 7.7g). While the mean seasonal cycle of the difference is a robust feature, its magnitude depends on the latitudinal boundaries used for averaging.

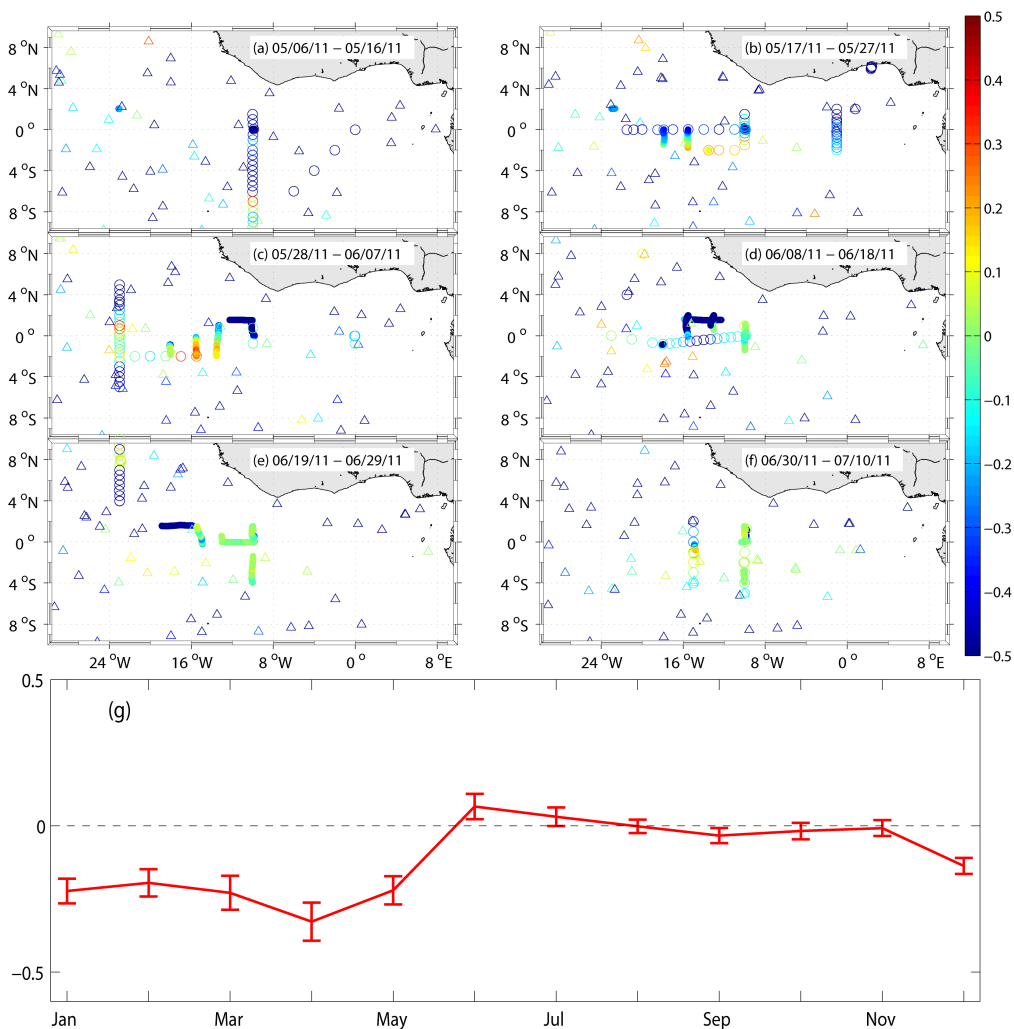


Fig. 7.7: (a-f) Salinity difference between MLS and maximum salinity in the upper thermocline layer below the ML ($24.5 \leq \sigma_\theta \leq 26.2$ or $\sigma_{MLD} \leq \sigma_\theta \leq 26.2$ if $\sigma_{MLD} > 24.5$) from glider profiles (filled circles), shipboard CTD profiles (open circles), and Argo float profiles (triangles) for the CTE. (g) Mean salinity difference between MLS and maximum salinity in the upper thermocline layer ($24.5 \leq \sigma_\theta \leq 26.2$) from all Argo float profiles from the years 2000-2012 in boxes with the longitudinal boundaries 23°W and 10°W and the latitudinal boundaries 2°S and 1°N. Red bars denote the standard error of the mean of all profiles in the box within one month.

7.2.2. Heat budget

The contributions of the different processes (equation 1) to the ML heat budget in the North box (Fig. 7.8a and b) and the ACT box (Fig. 7.8c and d) are described in the following. Since this study describes focuses on the cold tongue development, we start with the ACT box.

7.2.2.1. ACT box

Absorbed shortwave radiation in the ACT ranged from 194 ± 36 to 226 ± 36 Wm^{-2} . The variability is caused by the variability of cloud cover and ML thickness. The latent and sensible heat fluxes as well as the net surface longwave radiation cooled the ML throughout the CTE (Fig. 7.8c). The net surface longwave radiation in the ACT box was nearly constant (ranging from 42 ± 10 to 55 ± 10 Wm^{-2}) during the CTE due to the balance of outgoing and downward longwave radiation. Outgoing longwave radiation slightly weakened with decreasing SSTs and the downward longwave radiation weakened with the reduction of clouds. The latent heat flux ranged between a maximum of 110 ± 21 Wm^{-2} and a minimum of 78 ± 21 Wm^{-2} . The variability was predominantly associated with varying winds. The magnitude of the sensible heat flux from the ocean to the atmosphere was the smallest compared to the aforementioned heat fluxes with a mean of 2 ± 3 Wm^{-2} . The resulting net surface heat flux warmed the ML during the whole CTE with a mean of 61 ± 43 Wm^{-2} .

The strong heat loss of the ACT ML in boreal summer can only be explained by ocean dynamics. Zonal heat advection played an important role for ML cooling during the CTE with strongest cooling of -63 ± 25 Wm^{-2} at the end of May, while meridional heat advection was a minor contributor to cooling with a maximum of -5 ± 11 Wm^{-2} . Similar results were obtained for the Mercator assimilation model, where meridional heat advection showed a maximum contribution of -12 ± 1 Wm^{-2} . Entrainment consistently cooled the ML with a mean -8 ± 1 Wm^{-2} resulting from high vertical velocities in combination with a weak positive vertical temperature gradient below the ML.

In accordance with the reduced SST, the ML heat content tendency in the ACT box was negative during the entire CTE period (Fig. 7.8d). The tendency was weakly negative during early May, but strongly negative during the period end of May to early June, when the ML locally lost up to -144 ± 15 Wm^{-2} of heat. Without considering diapycnal mixing (Fig. 7.8d), the mixed layer heat tendency cannot be explained by the sum of processes described above.

The diapycnal heat flux determined from the microstructure data was elevated during the first period of the CTE from the second half of May to the beginning of June. For this period, a mean flux of -111 ± 16 Wm^{-2} was estimated that reduced in magnitude to -49 ± 9 Wm^{-2} during the second half of the CTE (Fig. 7.8c). Unfortunately, microstructure observations were not continuously available for the entire CTE period within the ACT box thus longer averaging periods had to be used to estimate representative diapycnal heat flux contributions. The elevated diapycnal heat flux during the first period of the CTE resulted from elevated turbulent eddy diffusivities that persisted despite increased upper-ocean stratification during this period.

The magnitude and temporal variability of the sum of the individual heat flux contributions including the diapycnal heat flux (Fig. 7.8d) agrees well with the magnitude and temporal variability of the heat content tendency. This indicates that within the uncertainties, the heat budget in the ACT region was closed utilizing the above flux estimates for the sampled period.

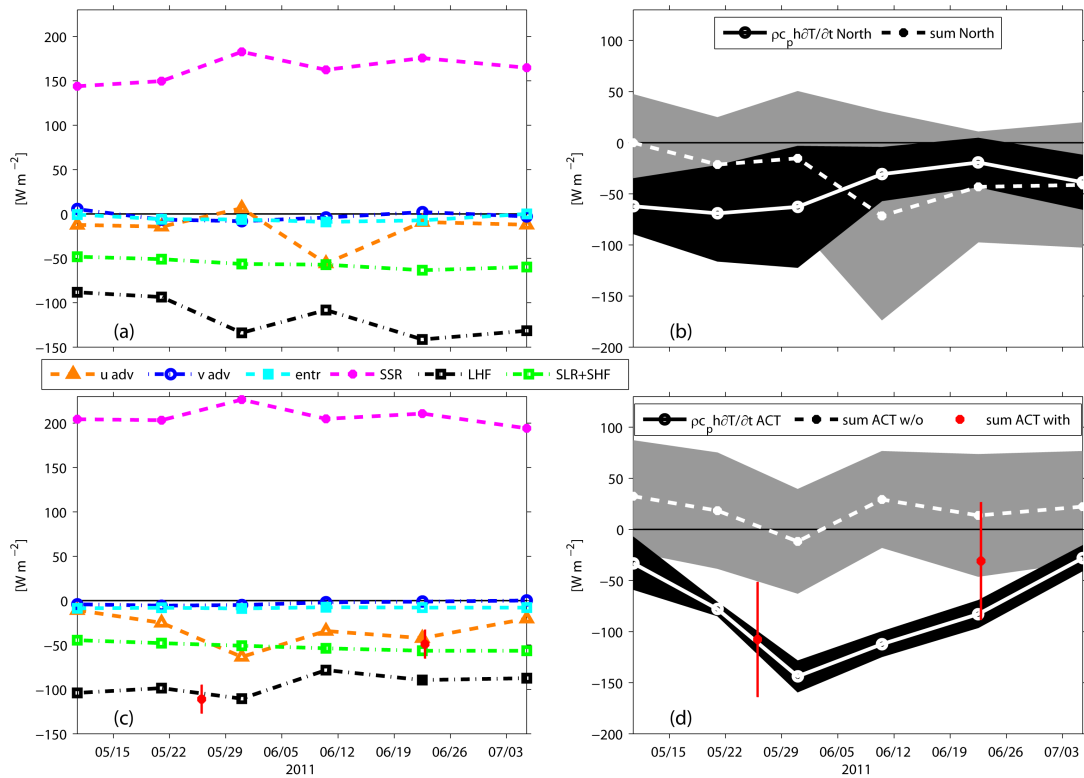


Fig. 7.8: The contribution of each term to the ML heat budget (a and c) and the local heat tendency and the sum of the terms (b and d) for the northern box (top) and for the ACT box (bottom). The different contributions in (a) and (c) are zonal (u adv) and meridional (v adv) heat advection, entrainment (entr), net surface shortwave radiation corrected for the penetrative part (SSR), latent heat flux (LHF) and the sum of net surface longwave radiation (SLR) and sensible heat flux (SHF). The contribution of diapycnal mixing in (c) is shown with the red dots (each dot is representative for the averaging period of about one month). In (d) the sum without (sum ACT w/o; dashed-dotted line) and with (sum ACT with; red dots) diapycnal mixing is shown. The black shadings in (b) and (d) are the uncertainty of the observed heat changes. The grey shadings in (b) and (d) are the accumulation of all errors of the different processes.

7.2.2.2. Northern box

The dominant processes contributing to the heat balance of the northern box differ from those dominating the ACT heat balance. In particular, the net surface heat flux was comparably lower and even changed sign during the CTE. Absorbed shortwave radiation ranged from 144 ± 35 to $183 \pm 35 \text{ Wm}^{-2}$ and was mainly balanced by the heat loss due to the other atmospheric fluxes (sum ranging from -142 ± 24 to $-205 \pm 24 \text{ Wm}^{-2}$) (Fig. 7.8a). However, the net surface heat flux warmed the ML in the beginning of the CTE with $8 \pm 42 \text{ Wm}^{-2}$, while it cooled the ML during the rest of the experiment with a minimum of $-29 \pm 42 \text{ Wm}^{-2}$ at the end of the CTE. This was mainly caused by the increased cooling contribution of the latent heat flux due to the increased wind.

Zonal heat advection significantly contributed to cooling of the ML only during the beginning of June ($-56\pm 68 \text{ Wm}^{-2}$), but was small during the rest of the CTE period. The contribution of meridional heat advection to ML cooling in the northern box was in general small with a minimum value of $-8\pm 49 \text{ Wm}^{-2}$. The high uncertainties for the advection terms result, on the one hand, from the velocity error, estimated through comparison of OSCAR velocities with velocities from moored measurements and, on the other hand, from uncertainties of estimating the horizontal temperature gradients from the satellite data. The contribution of entrainment ranged from $-1\pm 2 \text{ Wm}^{-2}$ to -9 ± 2 during the whole CTE and is not important for ML cooling. The diapycnal heat flux was not estimated for the northern box due to missing data.

The ML heat content tendency was negative throughout the CTE (Fig. 7.8b). The negative tendency was largest at the end of May/beginning of June ($-70\pm 47 \text{ Wm}^{-2}$) while it was smallest ($-19\pm 24 \text{ Wm}^{-2}$) at the end of June. During the whole CTE period and within the given uncertainties, the sum of the aforementioned individual flux terms balances the ML heat content tendency.

7.2.3. Salinity budget

The contributions of the different processes (equation 2) to the MLS budget in the North box (Fig. 7.9a and b) and in the ACT box (Fig. 7.9c and d) are described in the following. As for the heat budget, we start with the ACT box.

7.2.3.1. ACT box

Evaporation in the ACT region increased MLS constantly at a rate between 0.16 ± 0.03 and 0.20 ± 0.05 per month (mth^{-1}), while precipitation reduced the MLS only weakly in the beginning of May (Fig. 7.9c). The contribution of precipitation to MLS changes during the development of the ACT was negligible, due to the position of the ITCZ further to the north (Fig. 7.9c). Hence the difference E-P is at this location dominated by evaporation.

By far, the largest absolute contribution to the MLS budget was by zonal advection. In May and the beginning of June 2011 negative salinity anomalies were transported into the ACT within the westward branches of the SEC. Minimum salinity advection occurred in early June contributing to a freshening of $-0.70\pm 0.37 \text{ mth}^{-1}$. However, zonal advection exhibited elevated variability throughout the CTE and almost disappeared in the middle of June when it contributed to a weak salinity increase of $0.01\pm 0.01 \text{ mth}^{-1}$.

Meridional salinity advection increased MLS in May and the beginning of June 2011 with a maximum contribution of $0.11\pm 0.20 \text{ mth}^{-1}$ (Fig. 7.9c). During the rest of the CTE, the contribution of meridional advection was weak. Entrainment also played a minor role for salinity changes in the ML during the CTE with a maximum value of $0.03\pm 0.01 \text{ mth}^{-1}$. As vertical velocities used for the entrainment estimates in the salinity and the heat budgets are the same, the minor role of entrainment in the salinity budget is due to the small vertical salinity gradients below the ML as pointed out in section 7.2.1.

The diapycnal salt flux inferred from microstructure observations increased MLS by $0.10\pm 0.01 \text{ mth}^{-1}$ during the first period of the CTE (Fig. 7.9c). It decreased in

June and locally partly changed sign in the end of June/beginning of July around 10°W , according to a local change in sign of the vertical salinity gradient (Fig. 7.5b). However, the average diapycnal salt flux determined from all data collected between the second week of June and the end of the CTE resulted in a very weak salt flux of $0.01\pm 0.01 \text{ mth}^{-1}$ (Fig. 7.9c).

The MLS in the ACT box increased with the cold tongue onset in May 2011, with a maximum tendency of $1.24\pm 0.65 \text{ mth}^{-1}$ (Fig. 7.9d). This tendency reduced during the further expansion of the cold tongue and was followed by a period of weak ML freshening. With the data sets available for this study, the salinity content change during cold tongue development could not be fully balanced by the individual flux contributions, although contributions due to diapycnal mixing were evaluated here. The latter accounted for some of the salinity content increase observed during the beginning of the experiment, but an unresolved residual remained.

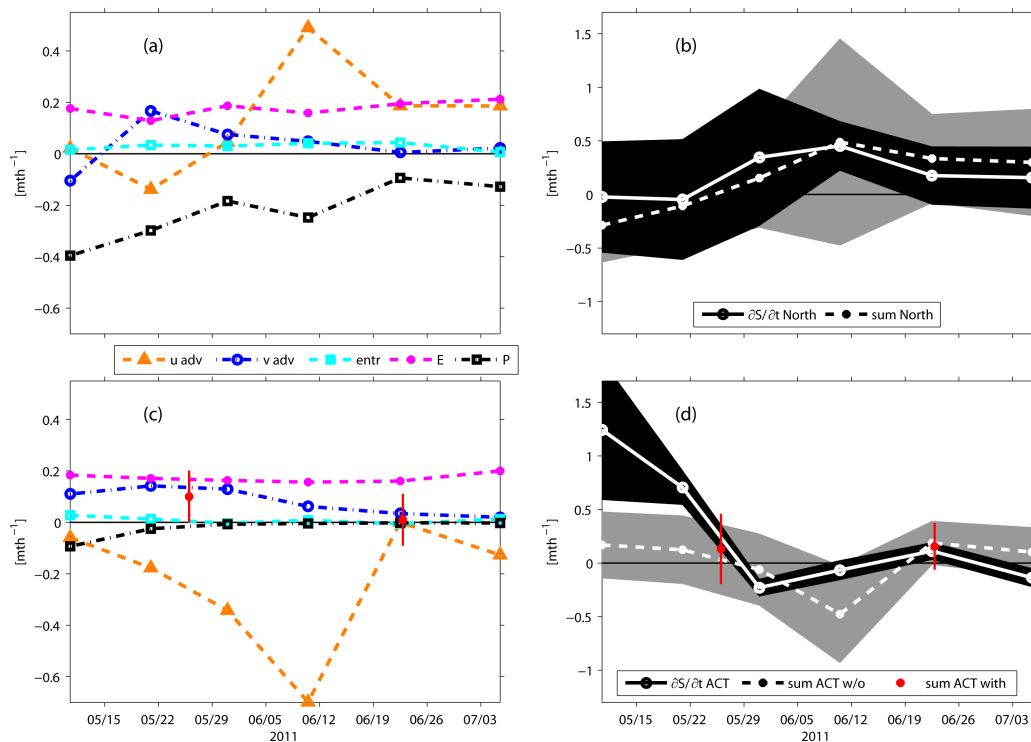


Fig. 7.9: The contribution of each term to the MLS budget (a and c) and the local salinity tendency and the sum of the terms (b and d) for the northern box (top) and for the ACT box (bottom). The different contributions in (a) and (c) are zonal (u adv) and meridional (v adv) salinity advection, entrainment (entr), evaporation (E) and precipitation (P). The contribution of diapycnal mixing in (c) is shown with the red dots (each dot is representative for the averaging period of about one month). In (d) the sum without (sum ACT w/o; dashed-dotted line) and with (sum ACT with; red dots) diapycnal mixing is shown. The black shadings in (b) and (d) are the uncertainty of the observed salinity changes and the grey shadings in (b) and (d) are the accumulation of all errors of the different processes.

7.2.3.2. Northern box

Evaporation in the northern box was similar to the evaporation in the ACT box and weakly increasing during the CTE from 0.13 ± 0.03 to $0.21\pm 0.06 \text{ mth}^{-1}$. In analogy to the latent heat flux, this increase was caused by the increasing wind speed. The main source of freshwater in the northern box during the CTE was precipitation (Fig.

7.9a). The ITCZ occupied parts of the northern box during the CTE, which led to an elevated freshwater input of predominantly convective rainfall resulting in a maximum salinity decrease of $-0.40 \pm 0.11 \text{ mth}^{-1}$ at the beginning of May. Hence, the difference E-P was negative during most parts of the CTE and only changed sign in the second half of June.

Similar to the ACT box, zonal advection played a key role in salinity changes for the northern box (Fig. 7.9a). During May, westward flow transported negative salinity anomalies into the northern box from the east leading to a minimum of zonal salinity advection of $-0.14 \pm 0.12 \text{ mth}^{-1}$. Later in June, elevated zonal salinity advection of up to $0.49 \pm 0.6 \text{ mth}^{-1}$ contributed to increase MLS. This is caused by positive salinity advection with the nSEC, which was strong during June. However, this contribution is uncertain due to the misrepresentation of TIWs in the OSCAR product. Meridional salinity advection contributed to increase MLS during May and June except at the beginning of the CTE in early May. Northward flow transported salty water from the cold tongue into the northern box with a maximum contribution of $0.17 \pm 0.35 \text{ mth}^{-1}$. Entrainment derived from model output was weak during the CTE with a maximum contribution of $0.04 \pm 0.01 \text{ mth}^{-1}$ in mid-June. The diapycnal salt flux was not estimated for the northern box due to missing data.

In the northern box, MLS tendency was positive during the whole CTE except for a weak freshening during the beginning of the experiment (Fig. 7.9b). The MLS tendency was balanced within the uncertainties by the sum of precipitation, evaporation, horizontal advection, and entrainment during most of the CTE period.

7.2.4. The CTE in the seasonal cycle

In order to incorporate the different contributions to the ML budgets inferred during the CTE into a broader perspective, we compare the results obtained for the period of the CTE to the mean seasonal cycle of the contributions to the ML budgets estimated at three PIRATA buoy locations within our study area. For the salinity budget, the seasonal cycles of the individual contributions are estimated in the following at the three PIRATA buoy sites at 23°W and 10°W on the equator, as well as 4°N , 23°W (Fig. 7.10). The seasonal ML heat budgets at these locations were already examined in various previous studies (Foltz et al. 2003; Foltz et al. 2013; Hummels et al. 2013). Hence, the results of the CTE concerning the ML heat budgets are compared to the results of these previous studies as part of section 7.3.

7.2.4.1. Mean seasonal mixed layer salinity budgets

4°N , 23°W

The variability of precipitation dictates the mean seasonal cycle of MLS tendency at the PIRATA buoy site at 4°N , 23°W . It follows a semiannual cycle caused by the seasonal migration of the ITCZ (Fig. 7.10a). During May-July the contribution weakens due to the northward migration of the ITCZ. However, although it is reduced during this period, precipitation was the dominant contributor to MLS changes in the northern box during the CTE (Fig. 7.9a). Monthly mean evaporation is nearly constant over the year, but reduced compared to evaporation at the two

equatorial locations. Hence, the net surface freshwater flux at 4°N, 23°W is predominantly determined by the semiannual cycle of precipitation and is only positive in July and August, when precipitation is strongly reduced.

The seasonal cycle of zonal advection at the buoy site is weak and follows the seasonal cycle of the NECC, which strengthens from its minimum eastward velocity during boreal spring to maximum eastward velocities in July (e.g., Richardson and Reverdin (1987); Goes et al. (2013)). The monthly mean zonal advection during May–July at the buoy site is much weaker than suggested for the northern box during the CTE period in 2011. In particular, the variability of zonal advection included a change in sign during the CTE, which is not captured in the seasonal estimate at the buoy location.

Meridional advection has its maximum in late fall/early winter and is the main contributor for the increase of the MLS this period (Fig. 7.10a). Eddy salinity advection exhibits a weak semiannual cycle with a freshening contribution in April/May and from October to December. During the latter period, eddy salinity advection is elevated but negative, leading to a decrease of MLS content. The sum of the seasonal cycle of meridional salinity advection and eddy salinity advection, dominated by the meridional eddy advection due to the TIWs, at the mooring site is small in boreal summer, which is similar to the total meridional salinity advection estimated during the CTE. The sum during May is negative, indicating negative total meridional salinity advection, which was not determined from the data collected during the CTE period. During June and July the sum is positive, indicating a total meridional salinity advection similar to the results obtained for the same period of the CTE.

Entrainment is weak throughout the year and exhibits a maximum in spring. During this period, it represents the largest contribution to increase MLS. During the CTE, the entrainment in the northern box was similarly weak. The diapycnal salt flux is negligible throughout the year, at least during the resolved periods. The sum of the contributing terms balances the observed salinity tendency within the uncertainties over the entire year at the PIRATA buoy at 4°N, 23°W (Fig. 7.10b). Although the seasonal cycle was evaluated locally, the results generally agree with the findings during the CTE pointing towards the fact that the salinity variability observed during the CTE is typical for this season (Fig. 7.9b, Fig. 7.10b).

0°N, 23°W

From January to May precipitation exceeds evaporation at the equatorial PIRATA buoy at 23°W representing the western ACT region (Fig. 7.10c). Later in the year precipitation is negligible and nearly constant evaporation yields a positive surface freshwater flux during that part of the year. Similarly, in 2011 during the CTE period from May to July, the influence of precipitation on the MLS budget was weak in the ACT region and a positive freshwater flux due to excess evaporation with only weak variability was indicated. This freshwater flux contributed to a MLS increase, comparable to the climatological freshwater flux from May to July (Fig. 7.10c).

The zonal salinity advection at the buoy site is negative throughout the year representing a significant contribution to the total salinity budget. It is characterized

by a weak semiannual cycle that peaks in boreal summer and winter. The negative salinity advection during early boreal summer is consistent with the results from the CTE period, but weaker in magnitude. Meridional salinity advection exhibits a maximum in boreal winter and represents the largest positive flux contribution to the MLS budget. Eddy salinity advection reduces MLS content at 23°W and is largest in the boreal winter months. At the end of spring, the contribution is negligible but is again relevant during summer. The sum of the seasonal cycle of mean meridional advection and eddy salinity advection at the buoy site is small in boreal summer. Due to the fact that eddy variability at 23°W is dominated by TIWs and the meridional gradients exceed the zonal ones, eddy advection is presumed to consist mostly of the meridional eddy component. The small magnitude of the total meridional heat advection agrees with the results from the CTE (Fig. 7.10c), however, the sign differs to the CTE results, where weak positive meridional heat advection is found.

Within the seasonal cycle, entrainment at the PIRATA buoy at 23°W has its maximum during May and June (Fig. 7.10c) when it contributes to a salinity increase. During the rest of the year, its contribution is weak. Within the ACT and during the CTE period in 2011, the weak salinity difference between the ML and below the ML resulted in weak entrainment contributions to MLS changes, albeit elevated entrainment velocities.

The diapycnal salt flux calculated from individual cruise data exhibits elevated variability within the seasonal cycle at 23°W. Strongest diapycnal salt flux, leading to a MLS increase occur during February-March. Additionally, diapycnal salt fluxes are elevated in June and November. In May and July, its contribution at 23°W is weak. The results for June and July are comparable to the CTE results from 2011, when the diapycnal salt flux led to a MLS increase in June and had a negligible contribution in July.

The seasonal cycle of the salinity tendency at the equatorial PIRATA buoy at 23°W is weak, but shows a positive tendency during spring, which reduces and even reverses towards July (Fig. 7.10d). The weak variability of the MLS tendency is generally captured by the sum of the contributing terms. In February and March, the salinity-increasing contribution of diapycnal mixing decreases the imbalance between tendency and the sum of fluxes. During this period, large freshening contributions result from zonal advection, eddy advection as well as precipitation while the diapycnal flux increases MLS together with meridional advection and evaporation. Although the seasonal cycle was evaluated locally, the results generally agree with the findings during the CTE pointing towards the fact that the salinity variability observed during the CTE is typical for this season (Fig. 7.9d, Fig. 7.10d). However, some flux contributions may vary locally within the ACT during the seasonal cycle.

0°N, 10°W

In winter and early spring, the mean seasonal cycles of evaporation and precipitation at the equatorial PIRATA buoy site at 10°W are comparable in magnitude, resulting in a weak surface freshwater flux (Fig. 7.10e). During the rest of the year, evaporation exceeds precipitation, thus the surface freshwater flux contributes to increase MLS. This is comparable to the freshwater flux in the ACT

region during the CTE period. Additionally, comparable results of the surface freshwater flux were obtained by Da-Allada et al. (2013) for the GG, suggesting that the surface freshwater flux is a large-scale phenomenon during this period.

Zonal advection is the largest contributing term to the mean seasonal cycle of the MLS balance at the equator at 10°W. It acts to reduce MLS and is most pronounced from December to July. Later in the year, its contribution weakens (Fig. 7.10e). Although zonal advection at 23°W is reduced compared to 10°W, zonal advection in the ACT region during the CTE period is of similar magnitude compared to 10°W and also shows a similar temporal evolution. This freshening contribution to the MLS balance can be explained by negative salinity advection mainly associated with the westward current branches, the northern SEC (nSEC) and the central SEC (cSEC). However, as will be discussed in section 7.3, the seasonal evolution of zonal salinity advection is predominantly controlled by the seasonal evolution of zonal MLS gradients. In general, the spring/early summer dominance of zonal advection in the MLS budget found here also agrees with recent results from a model study of the MLS balance in the GG region reported by Da-Allada et al. (2013).

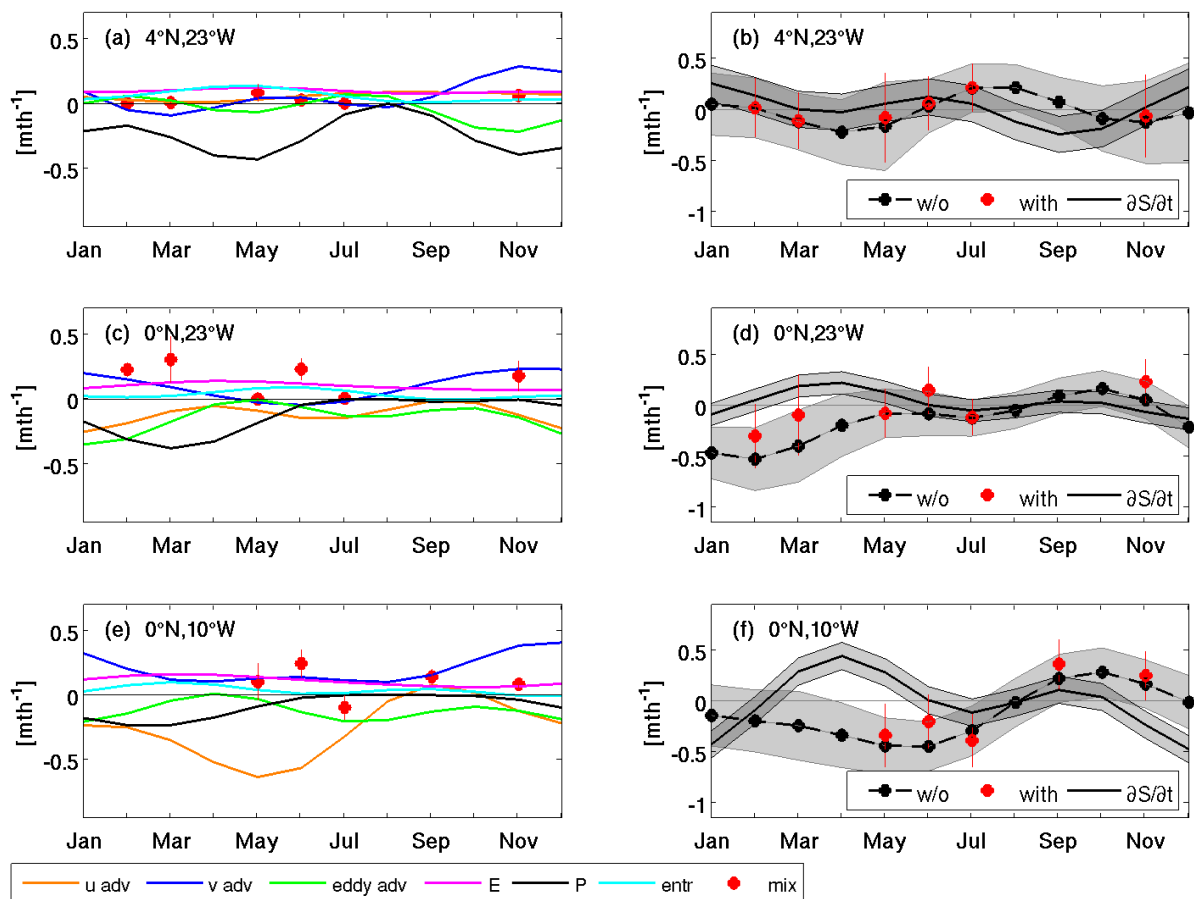


Fig. 7.10: Seasonal cycles of the contributing terms to the MLS budget (left) and the comparison of the local salinity tendency and the sum of the contributing terms (right) at three PIRATA buoys. The different contributions in (a), (c) and (e) are zonal (u adv), meridional (v adv) and eddy (eddy adv) salinity advection, evaporation (E), precipitation (P), entrainment (entr) and diapycnal mixing (mix). Black dashed-dotted lines (right panels) are the sum without diapycnal mixing and red dots are the sum with diapycnal mixing. The grey shadings in (b), (d) and (f) are the accumulation of all errors of the different processes and the error of the salinity tendency.

Similar to the results from 23°W, the contribution of meridional advection to the MLS budget has a maximum in late fall/early winter. During this period, the meridional salinity advection represents the dominant MLS source at 10°W (Fig. 7.10e). Magnitude and phase of eddy salinity advection at 10°W is also very similar to 23°W. It exhibits a semiannual cycle with minimum in December/January and July/August. The sum of the seasonal cycle of meridional salinity advection and eddy salinity advection at the buoy site is again small (cf. 23°W) in boreal summer, which is similar to the total meridional salinity advection estimated during the CTE. Also as for 23°W, the sum during June and July is negative, indicating freshening due to meridional salinity advection, which was not found during the CTE.

The seasonal cycle of entrainment at the PIRATA buoy at 10°W has its maximum in March and April contributing to the MLS increase during this period (Fig. 7.10e). During the rest of the year the contribution of entrainment is weak. This is consistent with the estimate of entrainment during the CTE, when the contribution of entrainment was rather negligible due to weak salinity differences between the ML and below the ML albeit rather strong entrainment velocities. Weak positive and negative entrainment contributions to MLS changes were obtained due to changes in sign of the vertical salinity gradient below the ML.

The diapycnal salt flux at the 10°W-PIRATA buoy increases the MLS in May and June, followed by a freshening contribution during July. Later in September and November again a positive salt flux from the subsurface layer into the ML through diapycnal mixing was observed. The findings for June and July are comparable with the CTE results that showed a positive diapycnal salt flux, leading to a MLS increase during June, followed by a negligible contribution to the MLS budget in July 2011.

The observed MLS increase during May 2011 in the ACT region is identifiable in the seasonal cycle of the salinity tendency at 10°W (and 23°W) as well (Fig. 7.10f). This increase weakens during June and July in the central ACT region. The MLS increase at the equatorial PIRATA buoy site at 10°W is not explained by the considered processes from equation (2). The remaining residual indicates either a missing source of salinity or an overestimate of the freshening contributions (Fig. 7.10f). Observed diapycnal mixing in May and June provide a positive salt flux into the ML and thus reduces the residual, leading to a balanced salinity budget within the uncertainties at least during June. From March through May, vertical salinity gradients between the ML and the thermocline are largest (cf. Fig. 7.7). It is thus likely that diapycnal mixing during this period contribute to increase MLS and thus decrease the residual. However, so far no microstructure observations from 10°W during these months are available. The remaining imbalance between the sum of terms and the observed salinity tendency at this location also coincides with periods of highly elevated zonal advection (March to July) and periods of elevated meridional advection (September to December). Possibly, the remaining imbalance is caused by an overestimation of these terms, which is either caused by overestimated horizontal velocities or horizontal salinity gradients. As the same velocity product did not cause imbalances in the ML heat budget at this location in another study (Hummels et al. 2014), it could be argued that the zonal and meridional salinity gradients are still not sufficiently well resolved by Argo floats.

7.3. Summary and discussion

Within the present study, the physical processes responsible for MLT and MLS changes during cold tongue development in 2011 have been investigated using an extensive set of in-situ and satellite data, reanalysis products and assimilation model output. In contrast to other studies evaluating the ML heat and salinity budget at individual locations or empirically defined boxes, the strategy pursued here was to evaluate the individual contributions to the ML budgets in two boxes representing the western ACT region and a region to the north of it. The boundary between the two boxes was defined by the temporally varying maximum of the meridional SST gradient. In general, the results concerning the ML heat budget agree with previous studies of the same region (Hummels et al. 2013; Jouanno et al. 2011b; Wade et al. 2011), despite the different approaches regarding box-averaged or local budgets. The diapycnal heat flux stands out as the dominant cooling term during ACT development, which has been inferred here from microstructure observations distributed within the ACT box. This finding is in agreement with previous studies (Hummels et al. 2013; Jouanno et al. 2011b). It also gives confidence that the chosen region for averaging is adequate to investigate the contributions to the ML budgets representative for the western ACT.

The MLS budget has to our knowledge not been investigated within this region before. MLS tendency is positive during ACT development. However, diapycnal mixing played only a minor role in the MLS budget. This is due to a rather weak vertical salinity gradient in the western ACT during the period of the CTE, which partly even changed sign. The horizontal salinity advection, especially its zonal component, represents the dominant contribution to the MLS budget. Contrary to the MLT budget, the MLS budget is partly not closed within the estimated uncertainties, although considering diapycnal flux contributions. This suggests the presence of unaccounted errors in the MLS budget that might result from the used products or methodology. In summary, tendencies and major flux contributions to MLT and MLS within the CTE period from May to July 2011 were:

ACT box

- The heat content tendency of the ML was negative throughout the CTE period. The net surface heat flux constantly warmed the ML. Dominant cooling terms were diapycnal mixing through the ML base and zonal advection associated with the transport of cold water from the GG. The sum of these contributions balanced the observed MLT changes within the uncertainties.
- MLS tendency was positive at the beginning of the CTE in May and became close to zero in June and July. Evaporation exceeded precipitation throughout the CTE. Horizontal salinity advection was the dominant contributor to ML freshening from May to mid-June. Entrainment was negligible throughout the CTE. The contribution of diapycnal mixing was relatively small. The sum of these contributions balanced the observed MLS changes within the uncertainties in June and the beginning of July. A

residual between observed MLS changes and the sum of all contributions remained during May.

Northern box

- Heat content tendency was negative during the CTE but considerably lower when compared to the ACT box. Net surface heat flux was small, warming the ML at the beginning of the CTE and cooling the ML afterwards. Horizontal heat advection cooled the ML during the entire CTE, except at the end of June, when advection weakly warmed the ML. Entrainment weakly cooled the ML throughout the CTE. The sum of these contributions balanced the observed MLT changes within the uncertainties.
- The MLS decreased during May and increased later in June and July. Precipitation was the main contributor to MLS changes during the beginning of the CTE in May, when zonal and meridional advection cancelled out each other. In June and July, when precipitation and evaporation were of similar magnitude, horizontal salinity advection, mainly the zonal component, was the main contributor to the MLS increase, particularly in the beginning of June. The observed MLS tendency was balanced within the uncertainties by the sum of resolved flux contributions.

To address the generality of the results obtained during the period of the CTE, the mean seasonal cycle of the contributions to the MLS budget was evaluated at three PIRATA buoy locations, on the equator at 23°W and 10°W and at 4°N, 23°W. Overall, the dominant flux contributions determined at the buoy positions for the CTE period agreed well in magnitude and phase with the box averaged flux contributions. At the equatorial buoy site at 10°W, zonal salinity advection is the dominant term contributing to a freshening of the ML from December to July (Fig. 7.10e) and the magnitude of the contribution is a factor of two larger in the central ACT region at 10°W compared to the western ACT region at 23°W (Fig. 7.10c). Precipitation and meridional eddy advection also significantly contribute to a freshening of the ML within the ACT region throughout the year. Meridional advection, entrainment and evaporation contribute to increase MLS. Finally, diapycnal mixing increases salinity predominantly from November to June and is negligible during the other month of the year. The results emphasize that the MLS tendency is largely balanced by ocean processes and to a lesser extent by the net surface freshwater flux (see Fig. 7.10).

Furthermore, the evaluation of the mean seasonal cycles at the PIRATA buoy locations emphasized that zonal salinity advection is the main contributor to the MLS budget in the western ACT during the first half of the year. Two major branches of the SEC, the nSEC slightly north of the equator (mean position: ~1°N at 10°W and ~2°N at 23°W) and the cSEC south of the equator (mean position: ~3-4°S at 10°W and ~4°S at 23°W) (see e.g., Lumpkin and Garzoli (2005); Brandt et al. (2006); Kolodziejczyk et al. (2009)) provide negative salinity advection. However, its contribution rapidly weakens towards the end of June. Due to the fact that the two branches of the SEC are still present during this period, the strong weakening of zonal salinity advection results from a decrease of the zonal salinity gradient. In fact,

a large MLS increase in the EEA in June and July 2011 was observed in the SMOS SSS (Fig. 7.4). As evaporation increases MLS in the central and EEA homogeneously, the elevated MLS in the EEA must have their origin in subsurface processes. Recently, Kolodziejczyk et al. (2014) conjectured vertical diffusion toward the sea surface in the GG occurring between May and August as the fate of the high-saline thermocline waters that are transported eastward within the EUC during the spring period (Johns et al. 2014). This requires enhanced diapycnal mixing in the GG from late boreal spring through summer, which was indeed indicated by numerical simulations with a general circulation model (Jouanno et al. 2011a).

Although the salinity flux into the ML associated with diapycnal mixing was weak during the CTE it is in general a salinity-increasing contributor to the MLS budget of the ACT. This is due to the fact that the EUC core is generally associated with a subsurface salinity maximum and hence diapycnal mixing acts to increase MLS. Surprisingly though on some stations in the central ACT region diapycnal mixing partly contributed to decrease MLS in boreal summer. These local freshening events are due to the local reversal of the vertical salinity gradient below the ML. The question arises which processes are responsible for the reversal of the vertical salinity gradient. According to the findings of Jouanno et al. (2011a) and as hypothesized in recent studies by Kolodziejczyk et al. (2014) and Johns et al. (2014) a possible explanation is that a part of the additional salt in the ML was previously entrained or mixed from the thermocline layer in the GG (and parts of the central ACT) upwards, simultaneously eroding the salinity maximum of the EUC. Evaporation further increased the MLS, finally leading to a strong reduction or reversal of the vertical salinity gradient below the ML. Differing meridional displacements of existing meridional salinity gradients in the ML and the EUC below due to TIWs might as well contribute to local changes in the vertical salinity gradient below the ML, which is illustrated by the glider section at the PIRATA buoy at the equator, 10°W.

Strong local differences of vertical gradients and diapycnal diffusivities at the base of the ML within the ACT box were observed. Diapycnal fluxes calculated by using box-averages of vertical gradients and diapycnal diffusivities do not agree with the box-average of locally calculated diapycnal fluxes due to a correlation of vertical gradients and diapycnal diffusivities. Similarly diapycnal mixing as conjectured from box-averaged budget residuals might become erroneous when averaging over larger regions. Microstructure observations as they are used here are still rather sparse. To get more reliable estimates on the variability in space and time of the diapycnal heat and salt fluxes at the ML base other observational platforms have to be used with higher spatial and/or temporal resolution such as e.g. gliders equipped with microstructure sensors or moored microstructure measurements.

For the calculation of the horizontal advection, surface or upper ocean currents are necessary together with horizontal gradients of MLT and MLS. To estimate box-averages of the advection a velocity product is needed with a high temporal and spatial resolution within the entire box. In this study the OSCAR product is used, which is estimated from satellite observation and not directly constrained by observations. In particular in the equatorial band OSCAR velocities strongly deviate

from subsurface ADCP velocities measured at PIRATA locations (not shown) and also from velocities of the MERCATOR assimilation model. The discrepancy in the velocity products results in a large uncertainty of the box-averaged horizontal advection for the CTE.

A general good agreement between in-situ SSS and SMOS SSS was shown for the cold tongue region with an estimated accuracy of satellite SSS similar to the previous studies (Boutin et al. 2012; Boutin et al. 2013; Reul et al. 2012). In regions strongly affected by precipitation, substantial differences between SSS and MLS were observed (not shown) that introduce additional uncertainty when using SSS for studying ML processes. However, the steadily improving SSS measurements are the basis for improving the MLS budget particularly by better constraining individual contributions due to the different atmospheric and oceanic processes in dynamically varying regions.

Together with several previous studies the present study improved our understanding of the seasonal and intraseasonal variability of temperature and salinity within the ML in the central equatorial Atlantic. The interesting question regarding the contribution of different processes to interannual variations of ML properties and thus to a deterministic or stochastic behavior of climate relevant SST variability remains to be addressed in future studies.

Acknowledgements

The studies collected here were funded and supported by a number of programs, which are listed below:

- Deutsches Bundesministerium für Bildung und Forschung (BMBF) as part of the projects NORDATLANTIK, RACE, MIKLIP, SOPRAN, SACUS
- Deutsche Forschungsgemeinschaft as part of the Sonderforschungsbereich 754 "Climate-Biogeochemistry Interactions in the Tropical Atlantic", and as part of the Emmy Noether Programme
- U.S. National Science Foundation under awards OCE0623552 and OCE1129874
- European Community's Sixth Framework Research Programme
- European Community's Seventh Framework Programme
- National Oceanic and Atmospheric Administration (NOAA), cooperative agreement NA10OAR4320143
- NOAA's Climate Program Office
- NOAA's Atlantic Oceanographic and Meteorological Laboratory
- NOAA's Global Drifter Programme NA10OAR4320156

References

- Allen MR, Ingram WJ (2002) Constraints on future changes in climate and the hydrologic cycle *Nature* 419:224-232 doi:10.1038/nature01092
- Antonov JI et al. (2010) World ocean atlas 2009, volume 2: salinity. In: Levitus S (ed) NOAA atlas NESDIS 69. U.S. Government Printing Office, Washington, DC, p 184 pp
- Arhan M, Treguier AM, Bourles B, Michel S (2006) Diagnosing the annual cycle of the equatorial undercurrent in the Atlantic Ocean from a general circulation model *J Phys Oceanogr* 36:1502-1522 doi:10.1175/Jpo2929.1
- Athie G, Marin F (2008) Cross-equatorial structure and temporal modulation of intraseasonal variability at the surface of the Tropical Atlantic Ocean *J Geophys Res-Oceans* 113 doi:10.1029/2007jc004332
- Athie G, Marin F, Treguier AM, Bourles B, Guiavarc'h C (2009) Sensitivity of near-surface Tropical Instability Waves to submonthly wind forcing in the tropical Atlantic Ocean *Model* 30:241-255 doi:Doi 10.1016/J.Ocemod.2009.06.016
- Atlas R, Hoffman RN, Ardizzone J, Leidner SM, Jusem JC, Smith DK, Gombos D (2010) A Cross-calibrated, Multiplatform Ocean Surface Wind Velocity Product for Meteorological and Oceanographic Applications *B Am Meteorol Soc* 92:157-174 doi:10.1175/2010BAMS2946.1
- Barnett TP (1983) Interaction of the Monsoon and Pacific trade-wind system at interannual time scales. Part I: The equatorial zone *Mon Weather Rev* 111:756-773 doi:10.1175/1520-0493(1983)111<0756:lotmap>2.0.Co;2
- Barnier B, Marchesiello P, De Miranda AP, Molines J-M, Coulibaly M (1998) A sigma-coordinate primitive equation model for studying the circulation in the South Atlantic. Part I: Model configuration with error estimates *Deep Sea Research Part I: Oceanographic Research Papers* 45:543-572 doi:[http://dx.doi.org/10.1016/S0967-0637\(97\)00086-1](http://dx.doi.org/10.1016/S0967-0637(97)00086-1)
- Barnier B et al. (2006) Impact of partial steps and momentum advection schemes in a global ocean circulation model at eddy-permitting resolution *Ocean Dynam* 56:543-567 doi:10.1007/s10236-006-0082-1
- Benkiran M, Greiner E (2008) Impact of the Incremental Analysis Updates on a Real-Time System of the North Atlantic Ocean *J Atmos Ocean Tech* 25:2055-2073 doi:10.1175/2008JTECHO537.1
- Berger H, Treguier AM, Perenne N, Talandier C (2014) Dynamical contribution to sea surface salinity variations in the eastern Gulf of Guinea based on numerical modeling *Climate Dynamics* (submitted)
- Bingham FM, Foltz GR, McPhaden MJ (2012) Characteristics of the seasonal cycle of surface layer salinity in the global ocean *Ocean Sci* 8:915-929 doi:10.5194/os-8-915-2012
- Blanke B, Delecluse P (1993) Variability of the Tropical Atlantic Ocean Simulated by a General Circulation Model with Two Different Mixed-Layer Physics *J Phys Oceanogr* 23:1363-1388 doi:10.1175/1520-0485(1993)023<1363:VOTTAO>2.0.CO;2
- Blanke B, Arhan M, Lazar A, Prévost G (2002) A Lagrangian numerical investigation of the origins and fates of the salinity maximum water in the Atlantic *Journal of Geophysical Research: Oceans* 107:3163 doi:10.1029/2002JC001318

- Bloom SC, Takacs LL, da Silva AM, Ledvina D (1996) Data Assimilation Using Incremental Analysis Updates Mon Weather Rev 124:1256-1271 doi:10.1175/1520-0493(1996)124<1256:DAUIAU>2.0.CO;2
- Böning CW, Kröger J (2005) Seasonal variability of deep currents in the equatorial Atlantic: a model study Deep Sea Research Part I: Oceanographic Research Papers 52:99-121 doi:<http://dx.doi.org/10.1016/j.dsr.2004.06.015>
- Bonjean F, Lagerloef GSE (2002) Diagnostic model and analysis of the surface currents in the tropical Pacific Ocean J Phys Oceanogr 32:2938-2954 doi:10.1175/1520-0485(2002)032<2938:dmaao>2.0.co;2
- Bourles B et al. (2007) African Monsoon Multidisciplinary Analysis (AMMA): special measurements in the tropical Atlantic CLIVAR Exch Lett 41 12 no2:7-9
- Bourles B et al. (2008) The PIRATA program: History, accomplishments, and future directions B Am Meteorol Soc 89:1111-1125 doi:10.1175/2008bams2462.1
- Bourlès B, D'Orgeville M, Eldin G, Gouriou Y, Chuchla R, DuPenhoat Y, Arnault S (2002) On the evolution of the thermocline and subthermocline eastward currents in the Equatorial Atlantic Geophys Res Lett 29:32-31-32-34 doi:10.1029/2002GL015098
- Boutin J, Martin N, Xiaobin Y, Font J, Reul N, Spurgeon P (2012) First Assessment of SMOS Data Over Open Ocean: Part II-Sea Surface Salinity IEEE Transactions on Geoscience and Remote Sensing 50:1662-1675 doi:10.1109/tgrs.2012.2184546
- Boutin J, Martin N, Reverdin G, Yin X, Gaillard F (2013) Sea surface freshening inferred from SMOS and ARGO salinity: impact of rain Ocean Sci 9:183-192 doi:10.5194/os-9-183-2013
- Brandt P, Schott FA, Provost C, Kartavtseff A, Hormann V, Bourles B, Fischer J (2006) Circulation in the central equatorial Atlantic: Mean and intraseasonal to seasonal variability Geophys Res Lett 33 doi:10.1029/2005gl025498
- Brandt P, Hormann V, Bourles B, Fischer J, Schott FA, Stramma L, Dengler M (2008) Oxygen tongues and zonal currents in the equatorial Atlantic J Geophys Res-Oceans 113 doi:10.1029/2007jc004435
- Brandt P et al. (2010) Changes in the ventilation of the oxygen minimum zone of the tropical North Atlantic J Phys Oceanogr 40:1784-1801 doi:10.1175/2010jpo4301.1
- Brandt P et al. (2011a) Equatorial upper-ocean dynamics and their interaction with the West African monsoon Atmos Sci Lett 12:24-30 doi:10.1002/Asl.287
- Brandt P, Funk A, Hormann V, Dengler M, Greatbatch RJ, Toole JM (2011b) Interannual atmospheric variability forced by the deep equatorial Atlantic Ocean Nature 473:497-500 doi:10.1038/Nature10013
- Brandt P et al. (2012) Ventilation of the equatorial Atlantic by the equatorial deep jets J Geophys Res-Oceans 117 doi:10.1029/2012jc008118
- Brandt P et al. (2013) Tropical Atlantic Climate Experiment (TACE) CLIVAR Exch 18:26-31

- Brandt P, Funk A, Tantet A, Johns W, Fischer J (2014) The Equatorial Undercurrent in the central Atlantic and its relation to tropical Atlantic variability *Clim Dyn*:1-13 doi:10.1007/s00382-014-2061-4
- Brodeau L, Barnier B, Treguier A-M, Penduff T, Gulev S (2010) An ERA40-based atmospheric forcing for global ocean circulation models *Ocean Model* 31:88-104 doi:<http://dx.doi.org/10.1016/j.ocemod.2009.10.005>
- Bumke K, Fennig K, Strehz A, Mecking R, Schröder M (2012) HOAPS precipitation validation with ship-borne rain gauge measurements over the Baltic Sea *Tellus A* 64 doi:10.3402/tellusa.v64i0.18486
- Bumke K, Seltmann J (2012) Analysis of Measured Drop Size Spectra over Land and Sea *ISRN Meteorology* 2012:10 doi:10.5402/2012/296575
- Bumke K, Schlundt M, Kalisch J, Macke A, Kleta H (2014) Measured and Parameterized Energy Fluxes Estimated for Atlantic Transects of R/V Polarstern *Journal of Physical Oceanography* 44:482-491 doi:10.1175/jpo-d-13-0152.1
- Bunge L, Provost C, Kartavtseff A (2007) Variability in horizontal current velocities in the central and eastern equatorial Atlantic in 2002 *J Geophys Res-Oceans* 112 doi:10.1029/2006jc003704
- Cane MA, Moore DW (1981) A Note on Low-Frequency Equatorial Basin Modes *J Phys Oceanogr* 11:1578-1584 doi:10.1175/1520-0485(1981)011<1578:ANOLFE>2.0.CO;2
- Cane MA, Sarachik ES (1983) Equatorial oceanography *Reviews of Geophysics and Space Physics* 21:1137-1148
- Caniaux G, Giordani H, Redelsperger J-L, Guichard F, Key E, Wade M (2011) Coupling between the Atlantic cold tongue and the West African monsoon in boreal spring and summer *Journal of Geophysical Research: Oceans* 116:C04003 doi:10.1029/2010JC006570
- Carton JA, Zhou Z (1997) Annual cycle of sea surface temperature in the tropical Atlantic Ocean *Journal of Geophysical Research: Oceans* 102:27813-27824 doi:10.1029/97jc02197
- Chang P (1993) Seasonal cycle of sea surface temperature and mixed layer heat budget in the tropical Pacific Ocean *Geophys Res Lett* 20:2079-2082 doi:10.1029/93GL02374
- Coëtlogon Gd, Janicot S, Lazar A (2010) Intraseasonal variability of the ocean — atmosphere coupling in the Gulf of Guinea during boreal spring and summer *Quarterly Journal of the Royal Meteorological Society* 136:426-441 doi:10.1002/qj.554
- Cromwell T, Montgomery RB, Stroup ED (1954) Equatorial Undercurrent in Pacific Ocean revealed by new methods *Science* 119:648-649 doi:10.1126/Science.119.3097.648
- Da-Allada CY, Alory G, du Penhoat Y, Kestenare E, Durand F, Hounkonnou NM (2013) Seasonal mixed-layer salinity balance in the tropical Atlantic Ocean: Mean state and seasonal cycle *Journal of Geophysical Research: Oceans* 118:332-345 doi:10.1029/2012JC008357
- Dai A, Trenberth KE (2002) Estimates of freshwater discharge from continents: Latitudinal and seasonal variations *Journal of Hydrometeorology* 3:660-687 doi:10.1175/1525-7541(2002)003<0660:eofdfc>2.0.co;2

- daSilva A, Young AC, Levitus S (1994) Atlas of surface marine data 1994, volume 1.: Algorithms and procedures. Tech Rep 6, US Department of Commerce, NOAA, NESDIS
- de Boyer Montégut C, Madec G, Fischer AS, Lazar A, Iudicone D (2004) Mixed layer depth over the global ocean: an examination of profile data and a profile-based climatology *J Geophys Res* 109 doi: doi:10.1029/2004JC002378
- de Boyer Montégut C, Mignot J, Lazar A, Cravatte S (2007) Control of salinity on the mixed layer depth in the world ocean: 1. General description *Journal of Geophysical Research: Oceans* 112:C06011 doi:10.1029/2006jc003953
- Dee DP et al. (2011) The ERA-Interim reanalysis: configuration and performance of the data assimilation system *Quarterly Journal of the Royal Meteorological Society* 137:553-597 doi:10.1002/qj.828
- Delcroix T, Hénin C (1991) Seasonal and interannual variations of sea surface salinity in the tropical Pacific Ocean *Journal of Geophysical Research: Oceans* 96:22135-22150 doi:10.1029/91jc02124
- Deser C, Phillips AS, Alexander MA (2010) Twentieth century tropical sea surface temperature trends revisited *Geophysical Research Letters* 37:L10701 doi:10.1029/2010gl043321
- Dessier A, Donguy JR (1994) The sea surface salinity in the tropical Atlantic between 10°S and 30°N—seasonal and interannual variations (1977–1989) *Deep Sea Research Part I: Oceanographic Research Papers* 41:81-100 doi:10.1016/0967-0637(94)90027-2
- Ding H, Keenlyside NS, Latif M (2009) Seasonal cycle in the upper equatorial Atlantic Ocean *Journal of Geophysical Research: Oceans* 114:C09016 doi:10.1029/2009JC005418
- Duing W et al. (1975) Meanders and long waves in the equatorial Atlantic *Nature* 257:280-284
- Durack PJ, Wijffels SE (2010) Fifty-Year Trends in Global Ocean Salinities and Their Relationship to Broad-Scale Warming *Journal of Climate* 23:4342-4362 doi:10.1175/2010jcli3377.1
- Dutrieux P, Menkes CE, Vialard J, Flament P, Blanke B (2008) Lagrangian Study of Tropical Instability Vortices in the Atlantic *J Phys Oceanogr* 38:400-417 doi:10.1175/2007JPO3763.1
- Fairall CW, Bradley EF, Hare JE, Grachev AA, Edson JB (2003) Bulk parameterization of air-sea fluxes: Updates and verification for the COARE algorithm *J Climate* 16:571-591 doi:10.1175/1520-0442(2003)016<0571:bpoasf>2.0.co;2
- Ferry N, Parent L, Garric G, Barnier B, Jourdain NC, Group M (2010) Mercator global Eddy permitting ocean reanalysis GLORYS1V1: description and results *Mercator Ocean Q Newsl* 36:15-27
- Fischer J, Brandt P, Dengler M, Müller M, Symonds D (2003) Surveying the Upper Ocean with the Ocean Surveyor: A New Phased Array Doppler Current Profiler *J Atmos Ocean Tech* 20:742-751 doi:10.1175/1520-0426(2003)20<742:STUOWT>2.0.CO;2
- Foltz GR, Grodsky SA, Carton JA, McPhaden MJ (2003) Seasonal mixed layer heat budget of the tropical Atlantic Ocean *J Geophys Res-Oceans* 108 doi:Artn 3146
Doi 10.1029/2002jc001584
- Foltz GR, Carton JA, Chassignet EP (2004) Tropical instability vortices in the Atlantic Ocean *Journal of Geophysical Research: Oceans* 109:C03029 doi:10.1029/2003JC001942

- Foltz GR, McPhaden MJ, Lumpkin R (2012) A strong Atlantic Meridional Mode event in 2009: The role of mixed layer dynamics *J Climate* 25:363-380 doi:10.1175/Jcli-D-11-00150.1
- Foltz GR, Schmid C, Lumpkin R (2013) Seasonal cycle of the mixed layer heat budget in the Northeastern Tropical Atlantic Ocean *J Climate* 26:8169-8188 doi:10.1175/JCLI-D-13-00037.1
- Gaillard F, Autret E, Thierry V, Galaup P, Coatanoan C, Loubrieu T (2009) Quality Control of Large Argo Datasets *J Atmos Ocean Tech* 26:337-351 doi:10.1175/2008JTECHO552.1
- Ganachaud A, Wunsch C (2000) Improved estimates of global ocean circulation, heat transport and mixing from hydrographic data *Nature* 408:453-457 doi:10.1038/35044048
- Garau B, Ruiz S, Zhang WFG, Pascual A, Heslop E, Kerfoot J, Tintore J (2011) Thermal Lag Correction on Slocum CTD Glider Data *Journal of Atmospheric and Oceanic Technology* 28:1065-1071 doi:10.1175/jtech-d-10-05030.1
- Garzoli SL (1987) Forced oscillations on the equatorial Atlantic Basin during the seasonal response of the Equatorial Atlantic Program (1983–1984) *Journal of Geophysical Research: Oceans* 92:5089-5100 doi:10.1029/JC092iC05p05089
- Giarolla E, Nobre P, Malagutti M, Pezzi LP (2005) The Atlantic Equatorial Undercurrent: PIRATA observations and simulations with GFDL Modular Ocean Model at CPTC *Geophys Res Lett* 32 doi:10.1029/2004gl022206
- Giordani H, Caniaux G (2011) Diagnosing vertical motion in the Equatorial Atlantic Ocean *Dynam* 61:1995-2018 doi:10.1007/s10236-011-0467-7
- Goes M, Goni G, Hormann V, Perez RC (2013) Variability of the Atlantic off-equatorial eastward currents during 1993–2010 using a synthetic method *Journal of Geophysical Research: Oceans* 118:3026-3045 doi:10.1002/jgrc.20186
- Gouriou Y, Reverdin G (1992) Isopycnal and diapycnal circulation of the upper equatorial Atlantic Ocean in 1983–1984 *Journal of Geophysical Research: Oceans* 97:3543-3572 doi:10.1029/91JC02935
- Greatbatch RJ, Brandt P, Claus M, Didwischus SH, Fu Y (2012) On the width of the equatorial deep jets *J Phys Oceanogr* 42:1729-1740 doi:10.1175/Jpo-D-11-0238.1
- Gregg MC, Peters H, Wesson JC, Oakey NS, Shay TJ (1985) Intensive measurements of turbulence and shear in the equatorial undercurrent *Nature* 318:140-144 doi:10.1038/318140a0
- Grodsky SA, Carton JA, Provost C, Servain J, Lorenzetti JA, McPhaden MJ (2005) Tropical instability waves at 0°N, 23°W in the Atlantic: A case study using Pilot Research Moored Array in the Tropical Atlantic (PIRATA) mooring data *Journal of Geophysical Research: Oceans* 110:C08010 doi:10.1029/2005JC002941
- Grodsky SA, Carton JA, McClain CR (2008) Variability of upwelling and chlorophyll in the equatorial Atlantic *Geophysical Research Letters* 35:L03610 doi:10.1029/2007gl032466
- Großklaus M, Uhlig K, Hasse L (1998) An optical disdrometer for use in high wind speeds *Journal of Atmospheric and Oceanic Technology* 15:1051-1059 doi:10.1175/1520-0426(1998)015<1051:aodfui>2.0.co;2

- Han W, Webster PJ, Lin J-L, Liu WT, Fu R, Yuan D, Hu A (2008a) Dynamics of Intraseasonal Sea Level and Thermocline Variability in the Equatorial Atlantic during 2002–03 *J Phys Oceanogr* 38:945-967 doi:10.1175/2008JPO3854.1
- Han WQ, Webster PJ, Lin JL, Liu WT, Fu R, Yuan DL, Hu AX (2008b) Dynamics of intraseasonal sea level and thermocline variability in the equatorial Atlantic during 2002-03 *J Phys Oceanogr* 38:945-967 doi:10.1175/2008jpo3854.1
- Hasse L, Grossklaus M, Uhlig K, Timm P (1998) A ship rain gauge for use in high wind speeds *Journal of Atmospheric and Oceanic Technology* 15:380-386 doi:10.1175/1520-0426(1998)015<0380:asrgfu>2.0.co;2
- Hazeleger W, de Vries P (2003) Fate of the equatorial undercurrent in the Atlantic. Interhemispheric water exchange in the Atlantic ocean, vol 68. Elsevier Oceanography,
- Hazeleger W, de Vries P, Friocourt Y (2003) Sources of the Equatorial Undercurrent in the Atlantic in a High-Resolution Ocean Model *J Phys Oceanogr* 33:677-693 doi:10.1175/1520-0485(2003)33<677:SOTEUI>2.0.CO;2
- Helber RW, Weisberg RH, Bonjean F, Johnson ES, Lagerloef GSE (2007) Satellite-Derived Surface Current Divergence in Relation to Tropical Atlantic SST and Wind *J Phys Oceanogr* 37:1357-1375 doi:10.1175/JPO3052.1
- Hisard P, Morlière A (1973) La terminaison du contre-courant équatorial subsuperficiel atlantique (courant de Lomonosov) dans le Golfe de Guinée, *Sér Océanogr* XI:455-464
- Hisard P, Hénin C (1987) Response of the equatorial Atlantic Ocean to the 1983–1984 wind from the Programme Français Océan et Climat Dans l'Atlantique equatorial cruise data set *Journal of Geophysical Research: Oceans* 92:3759-3768 doi:10.1029/JC092iC04p03759
- Hormann V, Brandt P (2007) Atlantic Equatorial Undercurrent and associated cold tongue variability *J Geophys Res-Oceans* 112 doi:10.1029/2006jc003931
- Hormann V, Brandt P (2009) Upper equatorial Atlantic variability during 2002 and 2005 associated with equatorial Kelvin waves *J Geophys Res-Oceans* 114 doi:10.1029/2008jc005101
- Hormann V, Lumpkin R, Perez RC (2013) A Generalized Method for Estimating the Structure of the Equatorial Atlantic Cold Tongue: Application to Drifter Observations *J Atmos Ocean Tech* 30:1884-1895 doi:10.1175/JTECH-D-12-00173.1
- Hosoda S, Ohira T, Nakamura T (2008) A monthly mean dataset of global oceanic temperature and salinity derived from Argo float observations. *JAMSTEC Rep Res Div* 8:47-59
- Hummels R (2012) On the variability of turbulent mixing within the upper layers of the Atlantic Cold Tongue region. PhD, Universitätsbibliothek Kiel
- Hummels R, Dengler M, Bourlès B (2013) Seasonal and regional variability of upper ocean diapycnal heat flux in the Atlantic cold tongue *Progress in Oceanography* 111:52-74 doi:10.1016/j.pocean.2012.11.001
- Hummels R, Dengler M, Brandt P, Schlundt M (2014) Diapycnal heat flux and mixed layer heat budget within the Atlantic Cold Tongue under revision in *Climate Dynamics*

- Inoue R, Lien RC, Moum JN (2012) Modulation of equatorial turbulence by tropical instability wave J Geophys Res-Oceans 117 doi:10.1029/2011JC007767
- Jochum M, Murtugudde R (2006) Temperature advection by tropical instability waves J Phys Oceanogr 36:592-605 doi:10.1175/jpo2870.1
- Johns WE, Brandt P, Bourlès B, Tantet A, Papapostolou A, Houk A (2014) Zonal structure and seasonal variability of the Atlantic Equatorial Undercurrent Clim Dyn:1-23 doi:10.1007/s00382-014-2136-2
- Johnson ES, Bonjean F, Lagerloef GSE, Gunn JT, Mitchum GT (2007) Validation and Error Analysis of OSCAR Sea Surface Currents Journal of Atmospheric and Oceanic Technology 24:688-701 doi:10.1175/jtech1971.1
- Johnson GC, McPhaden MJ, Firing E (2001) Equatorial Pacific Ocean Horizontal Velocity, Divergence, and Upwelling* J Phys Oceanogr 31:839-849 doi:10.1175/1520-0485(2001)031<0839:EPOHVD>2.0.CO;2
- Johnson GC, Sloyan BM, Kessler WS, McTaggart KE (2002) Direct measurements of upper ocean currents and water properties across the tropical Pacific during the 1990s Progress in Oceanography 52:31-61 doi:10.1016/S0079-6611(02)00021-6
- Josey SA, Kent EC, Taylor PK (1999) New insights into the ocean heat budget closure problem from analysis of the SOC air-sea flux climatology J Climate 12:2856-2880 doi:10.1175/1520-0442(1999)012<2856:niitoh>2.0.co;2
- Jouanno J, Marin F, du Penhoat Y, Molines JM, Sheinbaum J (2011a) Seasonal Modes of Surface Cooling in the Gulf of Guinea Journal of Physical Oceanography 41:1408-1416 doi:10.1175/jpo-d-11-031.1
- Jouanno J, Marin F, du Penhoat Y, Sheinbaum J, Molines JM (2011b) Seasonal heat balance in the upper 100 m of the equatorial Atlantic Ocean J Geophys Res-Oceans 116 doi:10.1029/2010jc006912
- Jouanno J, Marin F, du Penhoat Y, Molines J-M (2013) Intraseasonal Modulation of the Surface Cooling in the Gulf of Guinea J Phys Oceanogr 43:382-401 doi:10.1175/jpo-d-12-053.1
- Kalisch J, Macke A (2012) Radiative budget and cloud radiative effect over the Atlantic from ship-based observations Atmos Meas Tech 5:2391-2401 doi:10.5194/amt-5-2391-2012
- Kanamitsu M, Ebisuzaki W, Woollen J, Yang SK, Hnilo JJ, Fiorino M, Potter GL (2002) NCEP-DOE AMIP-II reanalysis (R-2) Bulletin of the American Meteorological Society 83:1631-1643 doi:10.1175/bams-83-11-1631
- Katz EJ (1984) Basin wide thermocline displacements along the equator of the Atlantic in 1983 Geophys Res Lett 11:729-732 doi:10.1029/GL011i008p00729
- Kolodziejczyk N, Bourlès B, Marin F, Grelet J, Chuchla R (2009) Seasonal variability of the Equatorial Undercurrent at 10 degrees W as inferred from recent in situ observations J Geophys Res-Oceans 114 doi:10.1029/2008JC004976
- Kolodziejczyk N, Marin F, Bourlès B, Gouriou Y, Berger H (2014) Seasonal variability of the equatorial undercurrent termination and associated salinity maximum in the Gulf of Guinea Climate Dynamics:1-22 doi:10.1007/s00382-014-2107-7

- Lagerloef GSE, Mitchum GT, Lukas RB, Niiler PP (1999) Tropical Pacific near-surface currents estimated from altimeter, wind, and drifter data *Journal of Geophysical Research: Oceans* 104:23313-23326 doi:10.1029/1999jc900197
- Lebedev KV, Yoshinari H, Maximenko NA, Hacker PW (2007) YoMaHa'07: Velocity data assessed from trajectories of Argo floats at parking level and at the sea surface IPRC Technical Note No.4(2):16p
- Legeckis R (1977) Long Waves in the Eastern Equatorial Pacific Ocean: A View from a Geostationary Satellite *Science* 197:1179-1181 doi:10.1126/science.197.4309.1179
- Legeckis R, Reverdin G (1987) Long waves in the equatorial Atlantic Ocean during 1983 *Journal of Geophysical Research: Oceans* 92:2835-2842 doi:10.1029/JC092iC03p02835
- Lellouche JM et al. (2013) Evaluation of global monitoring and forecasting systems at Mercator Océan *Ocean Sci* 9:57-81 doi:10.5194/os-9-57-2013
- Lien RC, Caldwell DR, Gregg MC, Moum JN (1995) Turbulence variability at the equator in the central Pacific at the beginning of the 1991–1993 El Niño *Journal of Geophysical Research: Oceans* 100:6881-6898 doi:10.1029/94JC03312
- Lien RC, D'Asaro EA, Menkes CE (2008) Modulation of equatorial turbulence by tropical instability waves *Geophys Res Lett* 35 doi:10.1029/2008gl035860
- Liu Z, Philander SGH, Pacanowski RC (1994) A GCM Study of Tropical–Subtropical Upper-Ocean Water Exchange *J Phys Oceanogr* 24:2606-2623 doi:10.1175/1520-0485(1994)024<2606:AGSOTU>2.0.CO;2
- Locarnini RA et al. (2010) World Ocean Atlas 2009, Volume 1: Temperature. In: Levitus S (ed) NOAA Atlas NESDIS 68. U.S. Government Printing Office, Washington, DC, p 184 pp
- Lohmann K, Latif M (2007) Influence of El Niño on the Upper-Ocean Circulation in the Tropical Atlantic Ocean *J Climate* 20:5012-5018 doi:10.1175/JCLI4292.1
- Lorbacher K, Dommenges D, Niiler PP, Köhl A (2006) Ocean mixed layer depth: A subsurface proxy of ocean-atmosphere variability *Journal of Geophysical Research: Oceans* 111:C07010 doi:10.1029/2003JC002157
- Lübbecke JF (2013) Climate science: Tropical Atlantic warm events *Nature Geosci* 6:22-23
- Lumpkin R, Speer K (2003) Large-scale vertical and horizontal circulation in the North Atlantic Ocean *J Phys Oceanogr* 33:1902-1920
- Lumpkin R, Garraffo Z (2005) Evaluating the decomposition of tropical Atlantic drifter observations *J Atmos Ocean Tech* 22:1403-1415 doi:10.1175/jtech1793.1
- Lumpkin R, Garzoli SL (2005) Near-surface circulation in the Tropical Atlantic Ocean Deep Sea Research Part I: Oceanographic Research Papers 52:495-518 doi:10.1016/j.dsr.2004.09.001
- Lumpkin R, Grodsky SA, Centurioni L, Rio M-H, Carton JA, Lee D (2013) Removing Spurious Low-Frequency Variability in Drifter Velocities *J Atmos Ocean Tech* 30:353-360 doi:10.1175/JTECH-D-12-00139.1

- Madec G (2008) NEMO ocean engine. Note du pole de modélisation, Institut Pierre-Simon Laplace (IPSL), France, No 27
- Malanotte-Rizzoli P, Hedstrom K, Arango H, Haidvogel DB (2000) Water mass pathways between the subtropical and tropical ocean in a climatological simulation of the North Atlantic ocean circulation *Dynam Atmos Oceans* 32:331-371 doi:10.1016/S0377-0265(00)00051-8
- Marin F, Caniaux G, Bourles B, Giordani H, Gouriou Y, Key E (2009) Why were sea surface temperatures so different in the eastern equatorial Atlantic in June 2005 and 2006? *J Phys Oceanogr* 39:1416-1431 doi:10.1175/2008jpo4030.1
- McCreary JP, Lu P (1994) Interaction between the subtropical and equatorial ocean circulations - the subtropical cell *J Phys Oceanogr* 24:466-497
- Menkes CE et al. (2002) A whirling ecosystem in the equatorial Atlantic *Geophys Res Lett* 29:48-41-48-44 doi:10.1029/2001GL014576
- Mercier H, Arhan M, Lutjeharms JRE (2003) Upper-layer circulation in the eastern Equatorial and South Atlantic Ocean in January–March 1995 *Deep Sea Research Part I: Oceanographic Research Papers* 50:863-887 doi:[http://dx.doi.org/10.1016/S0967-0637\(03\)00071-2](http://dx.doi.org/10.1016/S0967-0637(03)00071-2)
- Metcalf WG, Voorhis AD, Stalcup MC (1962) The Atlantic Equatorial Undercurrent *J Geophys Res* 67:2156-2202 doi:10.1029/JZ067i006p02499
- Moisan JR, Niiler PP (1998) The Seasonal Heat Budget of the North Pacific: Net Heat Flux and Heat Storage Rates (1950–1990) *J Phys Oceanogr* 28:401-421 doi:10.1175/1520-0485(1998)028<0401:TSHBOT>2.0.CO;2
- Molinari RL, Bauer S, Snowden D, Johnson GC, Bourles B, Gouriou Y, Mercier H (2003) A comparison of kinematic evidence for tropical cells in the Atlantic and Pacific oceans. In: Goni GJ, Malanotte-Rizzoli P (eds) IAPSO special issue: interhemispheric water exchange in the Atlantic Ocean. Elsevier Oceanography Series 68, pp 269-286
- Moum JN, Caldwell DR (1985) Local Influences on Shear-Flow Turbulence in the Equatorial Ocean *Science* 230:315-316 doi:10.1126/science.230.4723.315
- Moum JN, Caldwell DR, Paulson CA (1989) Mixing in the equatorial surface layer and thermocline *Journal of Geophysical Research: Oceans* 94:2005-2022 doi:10.1029/JC094iC02p02005
- Moum JN, Lien RC, Perlin A, Nash JD, Gregg MC, Wiles PJ (2009) Sea surface cooling at the Equator by subsurface mixing in tropical instability waves *Nat Geosci* 2:761-765 doi:10.1038/ngeo657
- Moum JN, Perlin A, Nash JD, McPhaden MJ (2013) Seasonal sea surface cooling in the equatorial Pacific cold tongue controlled by ocean mixing *Nature* 500:64-67 doi:10.1038/nature12363
- Niiler PP, Paduan JD (1995) Wind-Driven Motions in the Northeast Pacific as Measured by Lagrangian Drifters *J Phys Oceanogr* 25:2819-2830 doi:10.1175/1520-0485(1995)025<2819:WDMITN>2.0.CO;2
- Oakey NS (1982) Determination of the Rate of Dissipation of Turbulent Energy from Simultaneous Temperature and Velocity Shear Microstructure Measurements *J Phys Oceanogr* 12:256-271 doi:10.1175/1520-0485(1982)012<0256:DOTROD>2.0.CO;2

- Okumura Y, Xie S-P (2006) Some Overlooked Features of Tropical Atlantic Climate Leading to a New Niño-Like Phenomenon* J Climate 19:5859-5874 doi:10.1175/JCLI3928.1
- Osborn TR, Cox CS (1972) Oceanic fine structure Geophysical Fluid Dynamics 3:321-345 doi:10.1080/03091927208236085
- Osborn TR (1980) Estimates of the Local Rate of Vertical Diffusion from Dissipation Measurements J Phys Oceanogr 10:83-89 doi:10.1175/1520-0485(1980)010<0083:EOTLRO>2.0.CO;2
- Pacanowski RC, Philander SGH (1981) Parameterization of Vertical Mixing in Numerical-Models of Tropical Oceans J Phys Oceanogr 11:1443-1451 doi:Doi 10.1175/1520-0485(1981)011<1443:Povmin>2.0.Co;2
- Pazan SE, Niiler PP (2001) Recovery of Near-Surface Velocity from Undrogued Drifters J Atmos Ocean Tech 18:476-489 doi:10.1175/1520-0426(2001)018<0476:RONSVF>2.0.CO;2
- Perez R et al. (2013) Mean meridional currents in the central and eastern equatorial Atlantic Clim Dyn:1-20 doi:10.1007/s00382-013-1968-5
- Perez RC, Kessler WS (2009) Three-Dimensional Structure of Tropical Cells in the Central Equatorial Pacific Ocean* J Phys Oceanogr 39:27-49 doi:10.1175/2008JPO4029.1
- Perez RC, Cronin MF, Kessler WS (2010) Tropical Cells and a Secondary Circulation near the Northern Front of the Equatorial Pacific Cold Tongue* J Phys Oceanogr 40:2091-2106 doi:10.1175/2010JPO4366.1
- Perez RC, Lumpkin R, Johns WE, Foltz GR, Hormann V (2012) Interannual variations of Atlantic tropical instability waves J Geophys Res-Oceans 117 doi:Artn C03011 Doi 10.1029/2011jc007584
- Peter AC et al. (2006) A model study of the seasonal mixed layer heat budget in the equatorial Atlantic J Geophys Res-Oceans 111 doi:10.1029/2005jc003157
- Peters H, Gregg MC, Toole JM (1988) On the parameterization of equatorial turbulence Journal of Geophysical Research: Oceans 93:1199-1218 doi:10.1029/JC093iC02p01199
- Philander SGH, Pacanowski RC (1981) The oceanic response to cross-equatorial winds (with application to coastal upwelling in low latitudes) Tellus 33:201-210
- Philander SGH, Pacanowski RC (1986) A model of the seasonal cycle in the tropical Atlantic Ocean Journal of Geophysical Research: Oceans 91:14192-14206 doi:10.1029/JC091iC12p14192
- Polo I, Lazar A, Rodriguez-Fonseca B, Arnault S (2008) Oceanic Kelvin waves and tropical Atlantic intraseasonal variability: 1. Kelvin wave characterization J Geophys Res-Oceans 113 doi:10.1029/2007jc004495
- Prandke H, Stips A (1998) Test measurements with an operational microstructure-turbulence profiler: Detection limit of dissipation rates Aquatic Sciences 60:191-209 doi:10.1007/s000270050036
- Praveen Kumar B, Vialard J, Lengaigne M, Murty VSN, McPhaden MJ (2012) TropFlux: air-sea fluxes for the global tropical oceans-description and evaluation Clim Dyn 38:1521-1543 doi:10.1007/s00382-011-1115-0

- Provost C, Arnault S, Chouaib N, Kartavtseff A, Bunge L, Sultan E (2004) TOPEX/Poseidon and Jason equatorial sea surface slope anomaly in the Atlantic in 2002: Comparison with wind and current measurements at 23W *Mar Geod* 27:31-45 doi:10.1080/01490410490465274
- Qiao L, Weisberg RH (1995) Tropical instability wave kinematics: Observations from the Tropical Instability Wave Experiment *Journal of Geophysical Research: Oceans* 100:8677-8693 doi:10.1029/95JC00305
- Qiao L, Weisberg RH (1997) The zonal momentum balance of the equatorial undercurrent in the central Pacific *J Phys Oceanogr* 27:1094-1119
- Redelsperger J-L, Thorncroft CD, Diedhiou A, Lebel T, Parker DJ, Polcher J (2006) African Monsoon Multidisciplinary Analysis: An International Research Project and Field Campaign *B Am Meteorol Soc* 87:1739-1746 doi:10.1175/BAMS-87-12-1739
- Reul N et al. (2012) Overview of the First SMOS Sea Surface Salinity Products. Part I: Quality Assessment for the Second Half of 2010 *IEEE Transactions on Geoscience and Remote Sensing* 50:1636-1647 doi:10.1109/tgrs.2012.2188408
- Reynolds RW, Smith TM (1994) Improved Global Sea Surface Temperature Analyses Using Optimum Interpolation *J Climate* 7:929-948 doi:10.1175/1520-0442(1994)007<0929:IGSSTA>2.0.CO;2
- Rhein M, Dengler M, Sultenfuss J, Hummels R, Huttli-Kabus S, Bourles B (2010) Upwelling and associated heat flux in the equatorial Atlantic inferred from helium isotope disequilibrium *J Geophys Res-Oceans* 115 doi:10.1029/2009jc005772
- Richardson PL, Reverdin G (1987) Seasonal cycle of velocity in the Atlantic North Equatorial Countercurrent as measured by surface drifters, current meters, and ship drifts *Journal of Geophysical Research-Oceans* 92:3691-3708 doi:10.1029/JC092iC04p03691
- Richter I, Behera SK, Masumoto Y, Taguchi B, Sasaki H, Yamagata T (2013) Multiple causes of interannual sea surface temperature variability in the equatorial Atlantic Ocean *Nat Geosci* 6:43-47 doi:10.1038/Ngeo1660
- Roemmich D, Gilson J (2009) The 2004–2008 mean and annual cycle of temperature, salinity, and steric height in the global ocean from the Argo Program *Progress in Oceanography* 82:81-100 doi:<http://dx.doi.org/10.1016/j.pocean.2009.03.004>
- Schafstall J, Dengler M, Brandt P, Bange H (2010) Tidal-induced mixing and diapycnal nutrient fluxes in the Mauritanian upwelling region *J Geophys Res-Oceans* 115 doi:10.1029/2009jc005940
- Schlundt M et al. (2014) Mixed layer heat and salinity budgets during the onset of the 2011 Atlantic cold tongue *Journal of Geophysical Research: Oceans*:n/a-n/a doi:10.1002/2014JC010021
- Schmitt RW, Ledwell JR, Montgomery ET, Polzin KL, Toole JM (2005) Enhanced diapycnal mixing by salt fingers in the thermocline of the tropical Atlantic *Science* 308:685-688 doi:10.1126/science.1108678
- Schott FA, Fischer J, Stramma L (1998) Transports and pathways of the upper-layer circulation in the western tropical Atlantic *J Phys Oceanogr* 28:1904-1928 doi:10.1175/1520-0485(1998)028<1904:TAPOTU>2.0.CO;2
- Schott FA et al. (2003) The zonal currents and transports at 35°W in the tropical Atlantic *Geophys Res Lett* 30:1349 doi:10.1029/2002GL016849

- Schott FA, McCreary JP, Johnson GC (2004) Shallow overturning circulations of the tropical-subtropical oceans. In: Wang C, Xie S-P, Carton JA (eds) Earth Climate: The Ocean-Atmosphere Interaction. Geophysical Monograph 147. American Geophysical Union, Washington, DC, pp 261-304
- Simmons A, Uppala S, Dee D, Kobayashi S (2007) ERAInterim: new ECMWF reanalysis products from 1989 onwards ECMWF Newsl 110:25-35
- Snowden D, Molinari RL (2003) Subtropical cells in the Atlantic ocean: an observational summary. Interhemispheric water exchange in the Atlantic Ocean, vol 68. Elsevier Oceanography,
- Steger JM, Carton JA (1991) Long waves and eddies in the tropical Atlantic Ocean: 1984–1990 Journal of Geophysical Research: Oceans 96:15161-15171 doi:10.1029/91JC01316
- Stevenson JW, Niiler PP (1983) Upper Ocean Heat Budget During the Hawaii-to-Tahiti Shuttle Experiment J Phys Oceanogr 13:1894-1907 doi:10.1175/1520-0485(1983)013<1894:UOHBDT>2.0.CO;2
- Stramma L, Schott F (1999) The mean flow field of the tropical Atlantic Ocean Deep Sea Research Part II: Topical Studies in Oceanography 46:279-303 doi:[http://dx.doi.org/10.1016/S0967-0645\(98\)00109-X](http://dx.doi.org/10.1016/S0967-0645(98)00109-X)
- Subramaniam A, Mahaffey C, Johns W, Mahowald N (2013) Equatorial upwelling enhances nitrogen fixation in the Atlantic Ocean Geophys Res Lett 40:1766-1771 doi:10.1002/grl.50250
- Swenson MS, Hansen DV (1999) Tropical Pacific ocean mixed layer heat budget: The Pacific cold tongue J Phys Oceanogr 29:69-81 doi:10.1175/1520-0485(1999)029<0069:tpomlh>2.0.co;2
- Taylor JP, Edwards JM, Glew MD, Hignett P, Slingo A (1996) Studies with a flexible new radiation code. II: Comparisons with aircraft short-wave observations Quarterly Journal of the Royal Meteorological Society 122:839-861 doi:10.1002/qj.49712253204
- Thierry V, Treguier A-M, Mercier H (2004) Numerical study of the annual and semi-annual fluctuations in the deep equatorial Atlantic Ocean Ocean Model 6:1-30 doi:[http://dx.doi.org/10.1016/S1463-5003\(02\)00054-9](http://dx.doi.org/10.1016/S1463-5003(02)00054-9)
- Tranchant B, Testut C-E, Renault L, Ferry N, Birol F, Bresseur P (2008) Expected impact of the future SMOS and Aquarius Ocean surface salinity missions in the Mercator Ocean operational systems: New perspectives to monitor ocean circulation Remote Sensing of Environment 112:1476-1487 doi:<http://dx.doi.org/10.1016/j.rse.2007.06.023>
- Treguier AM et al. (2001) An eddy-permitting model of the Atlantic circulation: Evaluating open boundary conditions Journal of Geophysical Research: Oceans 106:22115-22129 doi:10.1029/2000JC000376
- Tuan Pham D, Verron J, Christine Roubaud M (1998) A singular evolutive extended Kalman filter for data assimilation in oceanography Journal of Marine Systems 16:323-340 doi:[http://dx.doi.org/10.1016/S0924-7963\(97\)00109-7](http://dx.doi.org/10.1016/S0924-7963(97)00109-7)
- Verstraete J-M (1992) The seasonal upwellings in the Gulf of Guinea Progress in Oceanography 29:1-60 doi:[http://dx.doi.org/10.1016/0079-6611\(92\)90002-H](http://dx.doi.org/10.1016/0079-6611(92)90002-H)

- Visbeck M (2002) Deep Velocity Profiling Using Lowered Acoustic Doppler Current Profilers: Bottom Track and Inverse Solutions* J Atmos Ocean Tech 19:794-807 doi:10.1175/1520-0426(2002)019<0794:DVPULA>2.0.CO;2
- von Schuckmann K, Brandt P, Eden C (2008) Generation of tropical instability waves in the Atlantic Ocean J Geophys Res-Oceans 113 doi:10.1029/2007jc004712
- Wacongne S (1989) Dynamical regimes of a fully nonlinear stratified model of the Atlantic equatorial undercurrent Journal of Geophysical Research: Oceans 94:4801-4815 doi:10.1029/JC094iC04p04801
- Wacongne S, Piton B (1992) The near-surface circulation in the northeastern corner of the South Atlantic ocean Deep Sea Research Part A Oceanographic Research Papers 39:1273-1298 doi:[http://dx.doi.org/10.1016/0198-0149\(92\)90069-6](http://dx.doi.org/10.1016/0198-0149(92)90069-6)
- Wade M, Caniaux G, du Penhoat Y (2011) Variability of the mixed layer heat budget in the eastern equatorial Atlantic during 2005-2007 as inferred using Argo floats J Geophys Res-Oceans 116 doi:Artn C08006
Doi 10.1029/2010jc006683
- Wang CZ (2005) Subthermocline tropical cells and equatorial subsurface countercurrents Deep-Sea Res Pt I 52:123-135 doi:10.1016/j.dsr.2004.08.009
- Wang WM, McPhaden MJ (1999) The surface-layer heat balance in the equatorial Pacific Ocean. Part I: Mean seasonal cycle J Phys Oceanogr 29:1812-1831 doi:10.1175/1520-0485(1999)029<1812:tslhbi>2.0.co;2
- Weisberg RH, Hickman JH, Tang TY, Weingartner TJ (1987) Velocity and temperature observations during the seasonal response of the Equatorial Atlantic Experiment at 0°, 28°W J Geophys Res-Oceans 92:5061-5075 doi:10.1029/Jc092ic05p05061
- Weisberg RH, Weingartner TJ (1988) Instability Waves in the Equatorial Atlantic Ocean J Phys Oceanogr 18:1641-1657 doi:10.1175/1520-0485(1988)018<1641:IWITEA>2.0.CO;2
- Xie S-P, Deser C, Vecchi GA, Ma J, Teng H, Wittenberg AT (2010) Global Warming Pattern Formation: Sea Surface Temperature and Rainfall* Journal of Climate 23:966-986 doi:10.1175/2009jcli3329.1
- Yu L, Jin X, Weller RA (2008) Multidecade Global Flux Datasets from the Objectively Analyzed Air-sea Fluxes (OAFux) Project: Latent and Sensible Heat Fluxes, Ocean Evaporation, and Related Surface Meteorological Variables. Woods Hole Oceanographic Institution OAFux Project Technical Report (OA-2008-01):1-64
- Zhang DX, McPhaden MJ, Johns WE (2003) Observational evidence for flow between the subtropical and tropical Atlantic: The Atlantic subtropical cells J Phys Oceanogr 33:1783-1797 doi:10.1175/2408.1